POLITECNICO DI MILANO

DEPARTMENT OF CHEMISTRY, MATERIALS AND CHEMICAL ENGINEERING
"GIULIO NATTA"

DOCTORAL PROGRAMME IN INDUSTRIAL CHEMISTRY AND CHEMICAL
ENGINEERING

STUDY OF STRUCTURE AND DYNAMICS OF PROTIC IONIC LIQUIDS (PILs) AS ELECTROLYTES AND COMPONENTS FOR POLYMER ELECTROLYTES

Doctoral Dissertation of:

Giselle de Araujo Lima e Souza

Supervisor:

Prof. Dr. Andrea Mele

Co-supervisor

Dr. Maria Enrica Di Pietro

ENEA Tutor:

Dr. Giovanni Battista Appetecchi

2022 – XXXV Cycle

Abstract

THE use of energy storage devices is exponentially growing,

especially for mobile devices and the transportation sector, therefore the development of optimized systems is the key to the successful and entire transition to renewable energy sources. Nowadays, lithium-ion batteries (LIBs) are the technology of choice for most electrochemical applications thanks to their high specific energy, high efficiency, and long cycle life. However, safety is still an issue, and some electrolyte components must be improved.

Recently, protic ionic liquids (PILs) emerged as potential electrolyte components in LIBs. When replacing flammable and volatile organic solvents, PILs are expected to improve the safety and performance of electrochemical devices. For implementing PILs as electrolyte components, a challenging task is still to understand the key factors governing their physicochemical and transport properties.

To this end, this PhD work deeply investigates the effects of the structural features and intermolecular interactions on the properties of promising PILs based on the 1,8-diazabicyclo-[5,4,0]-undec-7-ene (DBUH$^+$) cation and the (trifluoromethanesulfonyl-nonafluorobutylsulfonyl)imide (IM14$^-$), trifluoromethanesulfonate (TFO$^-$) and bis(trifluoromethanesulfonyl)imide (TFSI$^-$) anions. Here, a complete characterization of the PILs by using multinuclear NMR methods and different physicochemical analyses provided a comprehensive understanding of the features governing the properties of the selected PILs. The initial results unveiled the peculiar behavior of DBUH-IM14 in terms of macroscopic properties, which may be related to the structural characteristics of IM14$^-$ anion, such as the

presence of a C4 perfluorinated chain, the asymmetric distribution of the F atoms at the side of the sulfonylimide functional group, the steric hindrance, the capability of establishing fluorinated domains in the bulk liquid, etc.

Yet, to promote the application of the PILs as electrolyte components, an in-depth understanding of the role played by the ions in the bulk system became crucial to scaling their transport properties. In this regard, both neat PILs and PIL-based electrolytes (DBUH-IM14, DBUH-TFSI and DBUH-TFO doped with lithium salt containing the same anion, i.e., LiTFO, LiIM14, and LiTFSI) were investigated by conductivity, diffusion and relaxation NMR. These techniques allowed the achievement of a broad overview of the ion dynamics of these systems. Accordingly, the presence of Li^+ showed a peculiar effect on the dynamics of DBUH-IM14, and from the molecular point of view, DBUH-IM14 electrolytes deserve further investigation.

It is known that polymer electrolytes can further improve the safety issues of the LIBs. Besides, polymer electrolytes are shapable materials and can improve the volumetric design concerns associated with liquid electrolytes. Then, to expand the application of PILs as innovative electrolyte components, the selected PILs were confined into a polymeric matrix using poly(methyl methacrylate) (PMMA) as a polymer host. Through the thermal analysis and solid-state NMR, this work could probe the structural features and molecular level interactions between the ions and the PMMA. The combined approach showed that (i) even when housed by the polymeric matrix, the PIL retains some internal mobility, and (ii) DBUH-IM14 has a stronger interaction with the polymeric matrix than DBUH-TFSI and DBUH-TFO.

The unpredictable behavior of DBUH-IM14-polymeric system prompted to further investigate the transport properties of DBUH-IM14-based polymer electrolytes. Then, the effect of PILs confinement onto their transport properties was probed by pulsed field gradient NMR and fast field cycling NMR. When blended with PMMA, a marked slowing of the overall dynamics was observed. In the case of the polymer electrolyte system, Li^+ showed a minor effect on the $DBUH^+$ dynamics, whereas rotational and translational dynamics of the $IM14^-$ anion was quite responsive to the presence of Li^+. Still, a descriptive model is currently being developed to fully explain the transport properties and relaxation profiles of these systems.

From all the achievements of this PhD work, I can certainly state that DBUH-IM14-based electrolytes are of interest in LIB application and the structural features and nature of the intermolecular interactions in the $IM14^-$ anion play a crucial role in their molecular and macroscopic properties.

Acknowledgements

T HIS endeavour would not have come to fruition without the

assistance and kindness of several individuals. I would like to start by expressing my deepest gratitude to my supervisor Dr. Andrea Mele for the patient guidance, encouragement, and loyal assistance which make possible the realization of this work.

There are no proper words to express my deep gratitude for my co-supervisor Dr. Maria Enrica di Pietro who generously and constantly spent her time giving guidance, encouragement, suggestion, and comments throughout this PhD work. She has been supportive since I began working on my PhD activities, kindly explaining to me every detail about NMR experiments. Marica has also supported me professionally and emotionally throughout the challenging path to finishing this thesis. I am proud to have had the opportunity to work with her; she has my endless gratitude.

I would like to thank my committee members Dr. Monika Schönhoff and Dr. Patrick Judeinstein for letting my defense be an enjoyable moment, and for their availability to review my work and for the opportunity they gave me to improve this dissertation.

I am also grateful to Dr. Franca Castiglione, without her guidance and continuous assistance, this work would have been exponentially more difficult.

I would also like to extend the acknowledgement to Dr. Giovanni Battista Appetecchi with whom I had the opportunity to work for a short term in ENEA. I thank him for providing me with a cooperative

atmosphere at work and insightful comments on my project during all these years. I also would like to acknowledge Dr. Alessandro Triolo for sharing his knowledge and expertise about ionic liquids.

I would also like to acknowledge again Dr. Monika Schönhoff who have been supportive and insightful since my research stay in the University of Muenster. All my gratitude to Maleen Middendorf for faithfully dedicating her time guiding me during my research stay and Martin Lorenz for the fun time we had working and socializing together.

I would like to thank Dr. Patricia Fazzio Martins Martinez from the University of Campinas which continuously provided encouragement and was always willing to assist me in any way she could throughout the research project.

My grateful thanks are also extended to Dr. Steven Greenbaum who welcomed me for a short stay in Hunter College and Dr. Phill Stallworth for his willingness to give his time so generously. I am endlessly grateful to Dr. Carla Cecilia Fraenza who kindly offered her invaluable expertise in FFC and for being a source of encouragement, help and inspiration to me. I also would like to acknowledge the GIDRM for the generous Mobility Grant with made possible my secondment at Hunter College.

I would like to thank Katia De Vettori for providing much needed assistance with administrative tasks of the PhD School, reminding me of impending deadlines, and keeping my work running smoothly.

A warm word for my colleagues from Politecnico di Milano: Valeria Vanoli, Asia Pietrowiska, Alberto Mannu, Walter Panzeri with whom I have spent great and challenging time during the last three years.

Last, but not least, a very special word of thanks goes for my family, my beloved dog Johnny and my fiancé Gabriel Luis whose have been a never-ending source of love, encouragement, and motivation. My gratitude for them can hardly be expressed in words. I dedicate this thesis to you.

Contents

Introduction

1.1. Energy storage devices: state-of-the-art technology and its hurdles

The extensive use of fossil fuels increased CO_2 emissions at a constant rate in the last decades, resulting in a rise in global temperature which is associated with a series of dramatic climate changes[1,2]. Then, efficient energy storage devices such as batteries, fuel cells, and supercapacitors have been extensively explored as an alternative to overcome environmental issues[1]. The use of energy storage devices is exponentially growing, especially for mobile devices and the transportation sector, and the development of optimized systems is the key to the successful and entire transition to renewable energy sources.

Nowadays, lithium-ion batteries (LIBs) are the technology of choice for most electrochemical applications thanks to their high specific energy, high efficiency, and long life[3]. The term "lithium-ion batteries" refers to the general charge storage mechanism, involving lithium ions that are shuttling back and forth between the negative and positive electrodes, which are serving as host matrices for these cations (Figure 1.1). Basically, during the discharge of the LIBs, an oxidation reaction takes place at the anode producing positively charged lithium ions (Li^+) and negatively charged electrons (e^-). The Li^+ ions move through the electrolyte and the electrons move through the external circuit; then, they recombine with the cathode material in a reduction reaction. The reactions during discharge lower the chemical potential of the cell, so discharging transfers energy from the cell to an external circuit. When plugging in the

device for the charging process, the opposite happens: Li^+ and e^- move from the cathode and are received by the anode. During the charging process, the external circuit provides electric energy which is then stored as chemical energy in the cell.
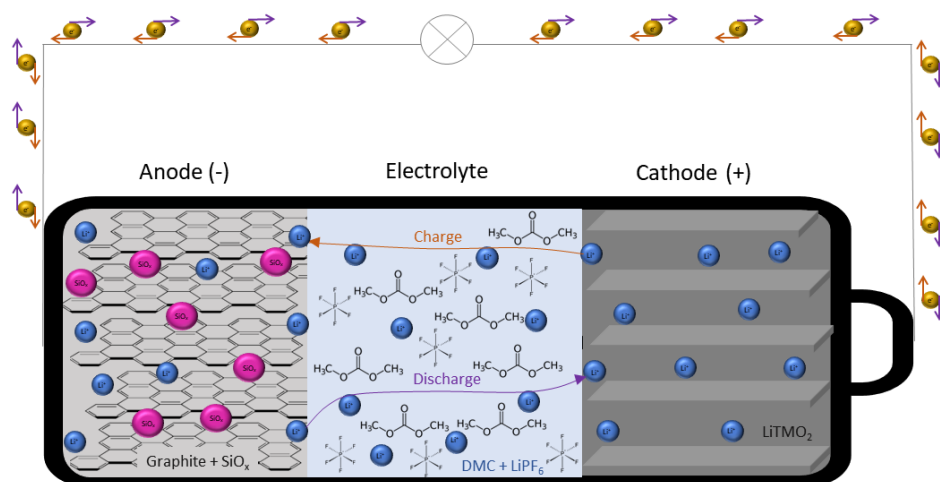
Figure 1.1. Schematic representation of the LIB components.

Current state-of-the-art cell components of LIBs (Figure 1.1) include: [4]

- a composite of graphite -sometimes containing silicon oxide (SiO_x) as active material- for the negative electrode (anode)

- a liquid electrolyte based on organic carbonates (such as dimethyl carbonate, DMC) as solvents, and a conducting lithium salt (usually lithium hexafluorophosphate, $LiPF_6$)

- a layered lithium transition metal oxide ($LiTMO_2$; TM = Ni, Mn, Co, and potentially other metals) as active material for the positive electrode.

Even if the current state-of-art LIBs components are very efficient, there are still concerns preventing the large-scale application of LIBs. The most urgent and serious issue in LIBs technology is related to safety. The commonly used electrolytes contain critical components that detriment the safety of LIBs. Generally, lithium-ion batteries electrolytes are comprised of a mixture of linear organic carbonates as solvents, (e.g., dimethyl carbonate (DMC), ethyl methyl carbonate (EMC), and diethyl carbonate (DEC)) combined with cyclic additives, such as fluoroethylene carbonate (FEC) or vinylene carbonate (VC), and dissolved thermally unstable Li salts (usually $LiPF_6$)[5]. These combinations afford superior ionic conductivity (up to 10^{-2} S cm^{-1} at room temperature)[6] and long-cycle stability[7]. However, two major drawbacks related to electrolytes have to be addressed:

(i) The organic carbonates are highly flammable and volatile; then, thermal, mechanical or electrical abuse conditions may lead to an

2

uncontrolled chain of events, such as thermal runaway, cell venting, fire and, sometimes, explosion[8,9].

(ii) The electrolyte burning causes decomposition of the lithium salt, $LiPF_6$ (stable up to 105 °C, or lower temperature, according to the amounts of moisture present[10]). Such decomposition releases highly toxic HF gases[8].

Thus, developing safer electrolytes is needed for further improvements of the safety of the LIBs technology and the growth of this technology.

1.2. Alternative electrolytes: ionic liquids and thermally stable lithium salts

Many approaches are under study with the aim of reducing safety hazards of the electrolyte components[9]. In this regard, researchers were highly oriented towards the replacement of both $LiPF_6$ and the organic carbonates.

Among the numerous alternative lithium salts proposed, lithium bis(trifluoromethanesulfonyl)imide (LiTFSI)[11] and lithium bis(fluorosulfonyl) imide (LiFSI)[12] have gained the most attention from both academia and industry thanks to their considerable high thermal stability. Nowadays, hundreds of tons of LiTFSI and LiFSI have been produced and are used as co-salt for lithium-ion batteries.

On the other side, to improve the safety of the liquid electrolytes, the replacement of carbonate solvents with non-flammable ionic liquids (ILs) has been intensively investigated[13]. ILs are molten salts displaying a melting point below 100 °C[14,15], constituted by an organic cation and an organic/inorganic anion. The exceedingly low melting point is the effect of a particularly low lattice enthalpy, in turn related to the irregular shape of the cations (and anions in some cases), to the delocalized electric charge and to the highly polarizable character of both anions and cation. These features sum up in the so-called *ions packing frustration*, leading to crystal lattices easily disrupted by the thermal motion[16,17].

Usually, ILs are recognized for their favorable physical chemical properties such as good transport properties, high thermal stabilities, low flash point, large electrochemical stabilities, low flammability, and low volatility[18–20]. Clearly, this set of properties makes ILs potential candidates to replace organic solvents currently used in electrochemical devices resulting in improved safety in case of overheating/overcharging[21].

Basically, to work as an efficient electrolyte in LIBs, the IL-lithium salt mixture needs to meet at least a few requirements: (i) reasonable high ionic conductivity ($\geq 10^{-3}$ S.cm^{-1}), to assure sufficiently high Li$^+$ transport properties through the electrolyte; (ii) wide electrochemical stability to allow Li$^+$ reversible intercalation without any relevant degradation; and (iii) high thermal stability to allow safe utilization at high temperature. Up to now, many combinations of cation and anion have been proposed to tailor the properties of an IL for a target application (Figure 1.2). However, considering the (at present) significantly high cost and complicated synthesis of ILs, such electrolytes have not been commercially used in LIBs yet.
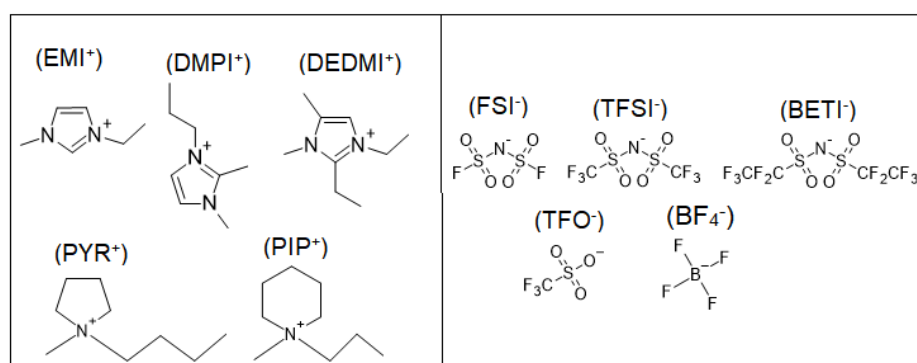
Figure 1.2. Chemical structure of the most common IL cations 1-ethyl-3-methylimidazolium (EMI$^+$), 1,2-dimethyl-3-propylimidazolium (DMPI$^+$), 1,2-diethyl-3,5-dimethylimidazolium (DEDMI$^+$), N-butyl-N-methylpyrrolidinium (PYR$^+$), N-methyl-N-propylpiperidinium (PIP$^+$), and anions bis(fluorosulfonyl)imide (FSI$^-$), bis(trifluoromethanesulfonyl)imide (TFSI$^-$), bis(pentafluoroethanesulfonyl)imide (BETI$^-$), trifluoromethanesulfonate (TFO$^-$), tetrafluoroborate (BF$_4^-$), used as electrolyte components.

Depending on their chemical structure, ILs can be divided into different classes. Among them, two of the most important ones are aprotic (AILs) and protic (PILs) ionic liquids. Basically, the main difference between them relies on the nature of the constituents: PILs contain one (or more) acidic, exchangeable proton in the cation moiety (e.g. protonated N-alkylimidazolium cations, protonated tertiary amines; Figure 1.3), while AILs do not have exchangeable protons on the cationic species (e.g. the common N-methyl, N-alkylimidazolium cations; Figure 1.2)[22].

The main general advantage of PILs, when compared to the AILs, is their easy synthesis. In most cases, AILs are synthesized through a two-step process involving alkylation followed by an anion exchange yielding the main product and intermediates[23]. Then, AILs synthesis requires purification/separations steps which are time and energy-demanding[24]. On the other hand, PILs can be easily synthesized by a single neutralization reaction between a Brønsted acid and a Brønsted base (Figure 1.4)[25,26]. For this

reason, the synthesis of PIL is often considered easier compared to that of AILs and, thus, more suitable for the establishment of mass production, favoring the large-scale application.
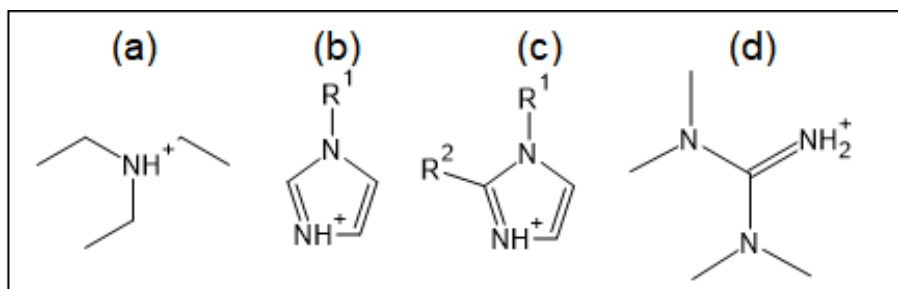
Figure 1.3. Example of commonly used PILs cations (a) triethylammonium. (b) 1-alkylimidazolium, (c) 1-alkyl-2-alkylimidazolium, and (d) 1,1,3,3-tetramethylguanidinine.
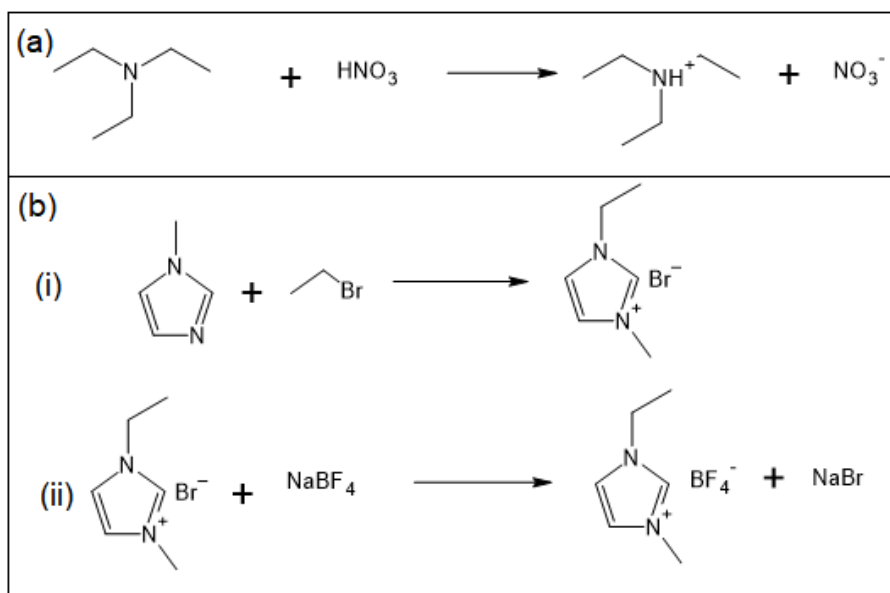
Figure 1.4. Schematic representation of the synthesis of a (a) PIL by a neutralization reaction and (b) AIL by a (i) alkylation reaction followed by an (ii) anion exchange reaction.

1.3. Protic ionic liquids: promising next-generation electrolyte components

Until the last decade, most studies focused on developing ILs for LIBs electrolytes have been performed utilizing AILs[27,28]. The justification for PILs not being considered a feasible strategy for safer electrolyte components is related to the relatively low electrochemical stability and potential reactivity of the acidic proton towards alkali metals, including lithium[29]. However, the scenario changed in 2013, with the introduction of PILs as electrolytes for LIBs[27] and the realization of stable devices with good

performances comparable to those achievable with AILs[30,31]. Remarkably, Menne et al. successfully showed that a PIL-based electrolyte, formed by 1 M LiTFSI in Et₃NHTFSI, displays a conductivity comparable to that of AILs and an electrochemical stability window large enough to allow the realization of LIBs[31]. Since then, the interest in using PILs in energy storage devices has been increasing (Figure 1.5), and now, PILs are quoted as promising candidates for electrolyte components by the scientific community[32–35].
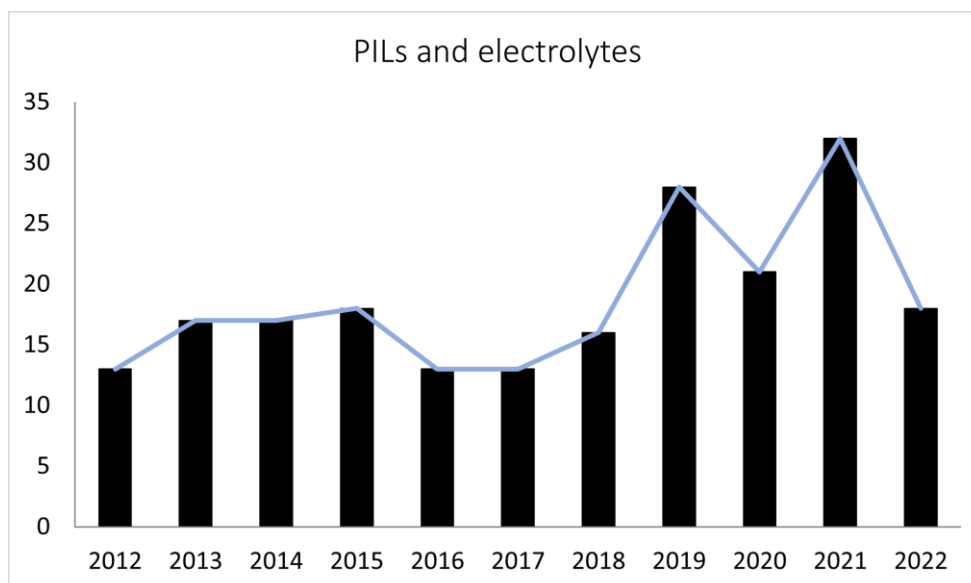
Figure 1.5. Number of publications including the terms ''protic ionic liquids'' and "electrolytes" in title, abstract and keywords, available on Scopus. Accessed on 24 November 2022

As mentioned previously, the development of safer electrolytes is of high priority in the research for advanced batteries. Further improvements in electrolytes can be achieved by confining the liquid electrolyte in a solid or semi-solid (gel) matrix using polymers forming alternative electrolytes. The development of PILs-based polymer electrolytes is interesting for several reasons: (i) the immobilization of PILs inside of a polymer network reduces the risk of leakage typical for other liquid electrolytes, therefore further improving the safety of systems and their cycle life[36]; (ii) the use of solid or semi-solid electrolytes contributes to implementing complex electrochemical architectures (including flexible), which in turn offer new opportunities for improving electrochemical devices[37,38]; (iii) the use of a solid electrolyte incorporating a PIL is also a strategy to overcome the limitation related to the high reactivity of these ILs toward alkali metals which is particularly appealing for the direct use of PILs in lithium metal batteries

contributing to the development of the next generation of high energy density batteries[39].

In 2020, for the first time, a PIL-based crosslinked polymer electrolyte was successfully used for the realization of lithium-metal batteries. The solid electrolyte system was formed by poly(ethylenoxide) (PEO), encompassing the PIL 1-butylpyrrolidinium bis(trifluoromethanesulfonyl)imide (PyrH4TFSI) and the lithium salt LiTFSI. This innovative battery showed almost full specific capacity output and stable cycling at different current rates at room temperature[39]. Also, in 2020, Marie et al.[40] investigated ionogel systems constituted by PIL confined in silica materials. This study has shown that the presence of the acidic proton influences the macro/microscopic properties of the ionogel. Besides, it reveals the strong impact of the acidity of a PIL on the chemistry occurring at the interface of the host, bringing knowledge for a better choice of host network for the confinement of the PIL, given the further applications as a solid or semi-solid electrolyte[40]. Finally, a recent study has demonstrated the application of ionogel electrolyte based on triethylammonium bis(trifluoromethanesulfonyl)imide (TEAH-TFSI) and of poly(vinylidene fluoride) (PVDF) for the development of high-performance micro-supercapacitors[41]. All these works open up new avenues for developing PILs-based polymer electrolytes seeking the improvement and safety of energy storage devices.

1.4. Seeking the unicorn?

Beyond the simplistic misconception that ILs – and PILs specifically – may address all of the issues related to LIB, it is clear that the tremendous potential of PILs for the next generation of devices for energy production and storage will be exploitable only after a thorough understanding of their fundamental physical chemistry. The atomistic description of electrolytes and polymer electrolytes is fully integrated into the eco-system of the electrochemical research and represents the main motivation of this PhD project. This thesis is structured as follows: *Chapter 2* describes the initial work focused on the protonation status of the PILs, as well as the characterization of the neat systems in terms of thermal, electrochemical, and rheological properties. Then, in *Chapter 3*, I further explore the PILs electrolytes in terms of translational diffusion, rotational motion and ionicity, to understand their transport properties to scale up their electrochemical applications. Finally, in *Chapter 4*, I expand the investigations to polymeric systems looking to the structural and intermolecular features of the polymer-PIL binary systems. Among the studied systems, the best suited was explored as PIL-based

polymer electrolytes, and the effects of confinement in the molecular motions was accessed using different NMR spectroscopy techniques. By exploring various experimental techniques and having a clear picture of the features governing the transport properties of the PILs and PIL electrolytes, I hope to contribute to the improvement of the current electrolytes technologies.

CHAPTER 2

Protic Ionic Liquids – Synthesis and Characterization

2.1. Introduction

The use of LIBs has significantly increased in our society during the last decades. Still, many efforts have been devoted to overcoming their major drawbacks, i.e. relatively low thermal stability of $LiPF_6$ and high flammability of the organic carbonate solvents, thus enhancing their safety and consequently expanding their application[13].

Easily synthesized by a single neutralization reaction, PILs are a promising alternative for replacing organic electrolytes. The presence of acidic protons on the cations, very often of N-H type, introduces the possibility of establishing H-bonds among the IL components, thus adding a new source of intermolecular interactions, along with the conventional Coulombic and dispersion forces observed for AILs[42,43]. The possibility of a network of intermolecular interactions based on H-bonding is a strong peculiarity of PILs.

The recent developments of PILs as electrolyte components underline how crucial is to investigate the features governing their physicochemical properties to tailor them as suitable solvents for electrochemical applications.

Among all the possible ion combinations to form a PIL, the 1,8-diazabicyclo-[5,4,0]-undec-7-ene (DBU, see Figure 2.1a for molecular formula) super-strong base is an attractive cation precursor due to its large size and strong charge delocalization on the N─C=N frame[44]. Watanabe's group has systematically

investigated a set of DBU-based PILs, finding that the thermal stability and the transport properties of those PIL families depend on the pK$_a$ difference (ΔpK$_a$) between the acid-base pair used as precursors[45,46]. Even though DBU is an excellent proton acceptor to form stable PILs, it has also been shown that pairing this base with weaker acids (e.g. acetic acid) can lead to incomplete proton transfer resulting in a poorly ionic system[47]. Then, a crucial step when selecting the precursor of a DBU-based PIL is to choose a strong enough acid to favor the proton transfer converting all neutral species into ions. Usually, a ΔpK$_a$ value equal to 15 is set for PILs based on DBU, but the threshold ΔpKa value is still under discussion[48].

Considering the acid strength as a key factor when selecting a PIL precursor, we proposed the following anions as the PILs constituents:

- (bis(trifluoromethanesulfonyl)imide (TFSI$^-$)
- (trifluoromethanesulfonyl-nonafluorobutylsulfonyl)imide (IM14$^-$)
- trifluoromethanesulfonate (TFO$^-$).

The molecular formulae of the corresponding acids are shown in Figure 2.1.

It has been reported that those anions lead to distinguished intermolecular interactions within the bulk PILs such as hydrogen bonding and attractive interactions between the fluorinated domains[49,50]. In turn, these specific intermolecular interactions are expected to affect the physicochemical properties of the PILs. Thus, to further characterize the select PILs in view of their application as electrolyte components, I intend to investigate the role played by the structural features of the anion in their microscopic and macroscopic properties.
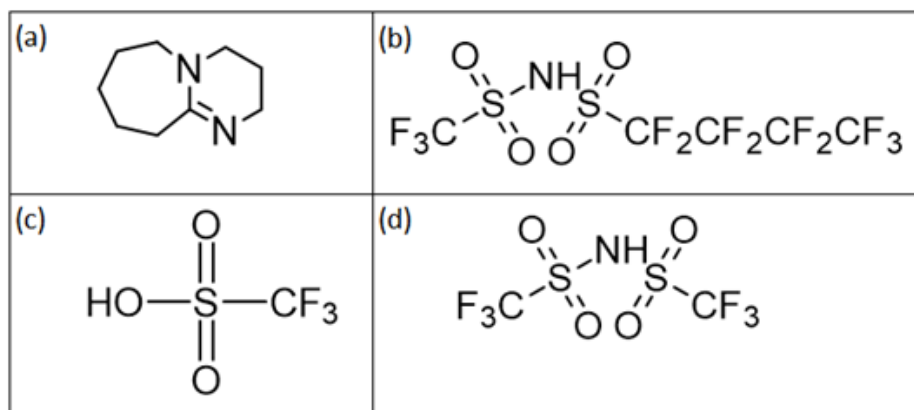
Figure 2.1. Structure of the PILs' precursors: DBU base (a) and the three acids HIM14 (b), HTFO (c) and HTFSI (d).

The overarching goal of this part of the PhD project is the synthesis and in-depth characterization of the selected DBU-based PILs and the understanding of the features governing their properties, aiming at their application as electrolyte components. For this purpose, the following specific objectives were established:

- Synthesis and purification of the PILs: DBUH-IM14, DBUH-TFSI, and DBUH-TFO.

- Evaluation of the protonation status by using multinuclear 1D NMR methods.

- Physicochemical characterization of the PILs by thermal analyses, density, viscosity, and conductivity measurements.

2.2. Materials and Methodology

2.2.1. Synthesis of the PIL samples

1,8-diazabicyclo[5.4.0]undec-7-ene (DBU, 98%), trifluoromethylsulfonic acid (HTFO, 99%), and nitric acid (HNO$_3$, 65 wt.% solution in water) were purchased from Sigma-Aldrich. Lithium bis(trifluoromethanesulfonyl)imide salt (LiTFSI, > 99.9 wt %) and acidic (trifluoromethanesulfonyl)(nonafluorobutanesulfonyl)imide (HIM14, 60 wt.% solution in water) were provided by 3M.

The synthesis of DBUH-TFO and DBUH-IM14 consisted of a standard neutralization reaction. The acid was counted in 3 wt.% excess to ensure the full protonation of the DBU. The acid was added dropwise to the base under stirring, and kept in a cooling water/ice bath to avoid sudden temperature increase and unexpected oxidation.

The DBUH-TFSI was synthesized by reacting DBU with nitric acid for neutralization, yielding DBUH-NO$_3$. Then, DBUH-TFSI was formed by a metathesis reaction using LiTFSI dissolved in water. The crude DBUH-based PILs were rinsed several times with deionized water to remove water-soluble impurities, acid excess and, for DBUH-TFSI, water-soluble LiNO$_3$ and the excess of LiTFSI.

Finally, all PILs were vacuum dried at 323 K for at least 1 hour and then, at 373 K for at least 18 hours and stored in an Ar atmosphere glove box (VAC, [O$_2$] < 1 ppm, [H$_2$O] < 1 ppm). The schematic representation of the synthesis of the DBU-based PILs is shown in Figure 2.2.
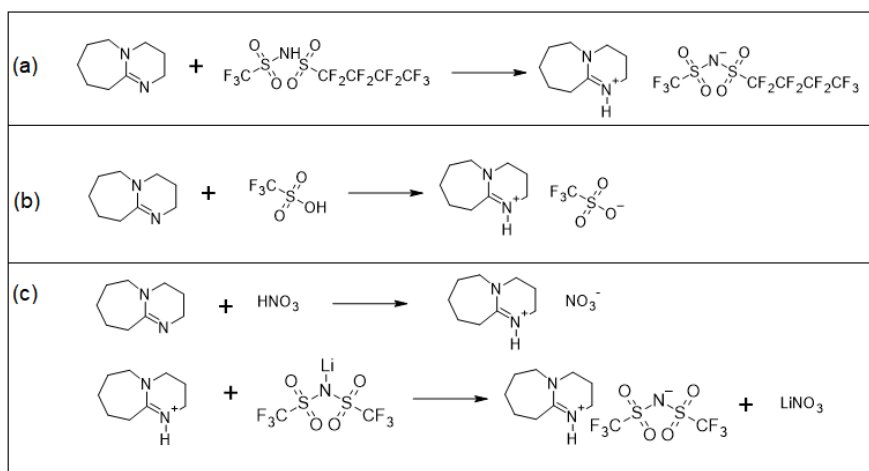
Figure 2.2. Schematic representation of the synthesis of the (a) DBUH-IM14, (b) DBUH-TFO and (c) DBUH-TFSI.

2.2.2. Purification of the PIL samples

The dry PIL samples were submitted to an additional purification procedure using activated charcoal as a sorbent (Sigma-Aldrich Darco-G60) and ethyl acetate (98 %, Sigma Aldrich) as solvent. Before being used in the purification step, the activated charcoal was boiled in deionized water for at least 1 hour (water:carbon weight ratio equal to 20:1). Then, the activated charcoal was vacuum filtered using a nylon filter membrane (pore size < 0.2 µm), equipped with a water pump. The pretreatment procedure of the sorbent was repeated at least 4 times before its final use. After the pretreatment, the activated charcoal and the ethyl acetate were added to the PIL (PIL:carbon weight ratio equal to 2:1), and the final mixture was continuously stirred at room temperature for at least 3 hours. The sorbent was removed by vacuum filtration using a Millipore hydrophilic polyamide filter (pore size < 0.2 µm), and the ethyl acetate was evaporated in a desiccator under a vacuum. Finally, the PILs were vacuum dried (< 1 mbar in oil-free pump) at 323 K for at least 1 hour and then, at 373 K for at least 18 hours. The purified PILs were stored in an Ar atmosphere glove box (VAC, $[O_2]$ < 1 ppm, $[H_2O]$ < 1 ppm).

2.2.3. UV-Vis measurements

The effectiveness of the purification procedure described above was qualitatively accessed by UV-Vis spectrophotometry. UV-Vis spectroscopy is an analytical technique that measures the amount of discrete wavelengths of UV or visible light that are absorbed by or transmitted through a sample in comparison to a reference or blank sample[51]. Basically, the experiment starts from a light source that emits light across a wide range of wavelengths. The light passes through a selector, and only certain wavelengths of light

pass through a sample. Then, a detector is used to convert the light which has passed through the sample into a readable electronic signal. Finally, the electronic signal is recognized and the output is sent to a computer for processing (see Figure 2.3 for a schematic representation)[51]. The absorbance recorded expresses how much light has passed through a sample. This property is influenced by the sample composition, potentially providing qualitative or quantitative information about unknown components into the sample.
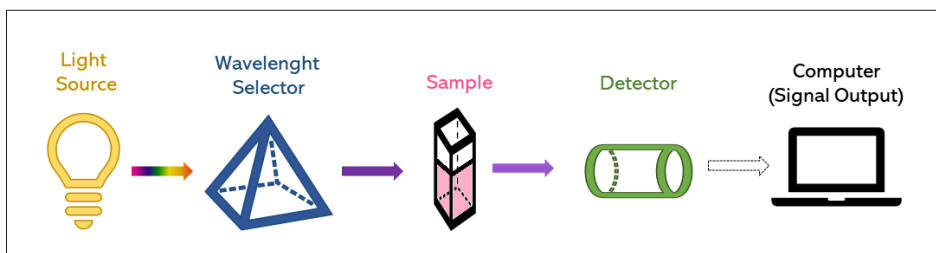
Figure 2.3. Simplified schematic representation of the main components involved in UV-Vis spectrophotometry.

The UV-Vis spectra of the PILs, before and after purification, were recorded using a Shimadzu UV-1800 spectrophotometer in a 1 cm quartz cuvette with a path length of 2 mm. The measurements were performed in the 190–700 nm wavelength range (resolution of 0.5 nm) at room temperature. All the samples were diluted in ethanol until the concentration of 20% (v/v).

2.2.4. NMR measurements

NMR spectroscopy comprises a wide range of measurement techniques and its basic principles are widely known in the academic community. For an introduction to NMR spectroscopy, the interested reader is referred to the available comprehensive literature[52], while here, I briefly describe the NMR experiments applied in this chapter.

A standard 1D-sequence (*zg* pulse sequence in the Bruker library) was used in this work for ^{1}H and ^{15}N acquisitions (Figure 2.4a). Basically, the sample is placed in a magnetic field B_0, causing the precession of individual nuclear magnetic moments around the z-axis and according to the quantum mechanical selection rules. The thermal equilibrium is described by the vector sum of the individual magnetic moments, leading to the bulk magnetization **M**, aligned along the positive z-axis and with a null component on the xy-plane. To manipulate the bulk magnetization, a specific radio frequency pulse (RF), B_1, at appropriate frequency is applied along the x or y axis, i.e., perpendicular to the main magnetic field B_0. Consequently, the **M** vector rotates by a given *flip angle β* along the x or y axis (Eq. 2.1) [52]:

$$\beta = \gamma B_1 t_p \qquad\qquad\qquad (2.1)$$

with γ the gyromagnetic ratio and t_p the pulse length (P1 in Figure 2.4a).

Then, the stray field B_0 induces the free precession of the magnetization in the xy-plane. The motion of the magnetization is characterized by the frequency of precession – the Larmor frequency – and by the relaxation of the **M** vector to equilibrium (see *Chapter 3* for further description of nuclear relaxation). The overall motion is quite complex, and it is referred to as nutation. The free precession components on the xy-plane induce a current in the receiver coils placed in phase with x- and y-axis. The collected signal is a damped oscillation called Free Induction Decay (FID). This time-domain signal is then digitized and transformed to the frequency domain spectrum via discrete fast Fourier Transform [52].

A 1D experiment with heteronuclear decoupling is similar to a regular 1D experiment but incorporates a RF train pulse in the second channel to provide the heteronuclear scalar decoupling. In this chapter, ^{15}N spectra with inverse gated decoupling (*zgig* pulse sequence in the Bruker library) were employed, where ^{1}H decoupling is executed during acquisition only, using a composite pulse decoupling (CPD) scheme (Figure 2.4b).

Finally, the Insensitive Nuclei Enhanced by Polarization Transfer (INEPT) experiment (*ineptnd* pulse sequence in Bruker library) was applied to increase the ^{15}N sensitivity (natural abundance 0.364%) by antiphase magnetization transfer from the reservoir of the most abundant nucleus (^{1}H) via ^{15}N-^{1}H spin coupling, resulting in a coupled ^{15}N-nucleus NMR spectrum[53] (Figure 2.4c).
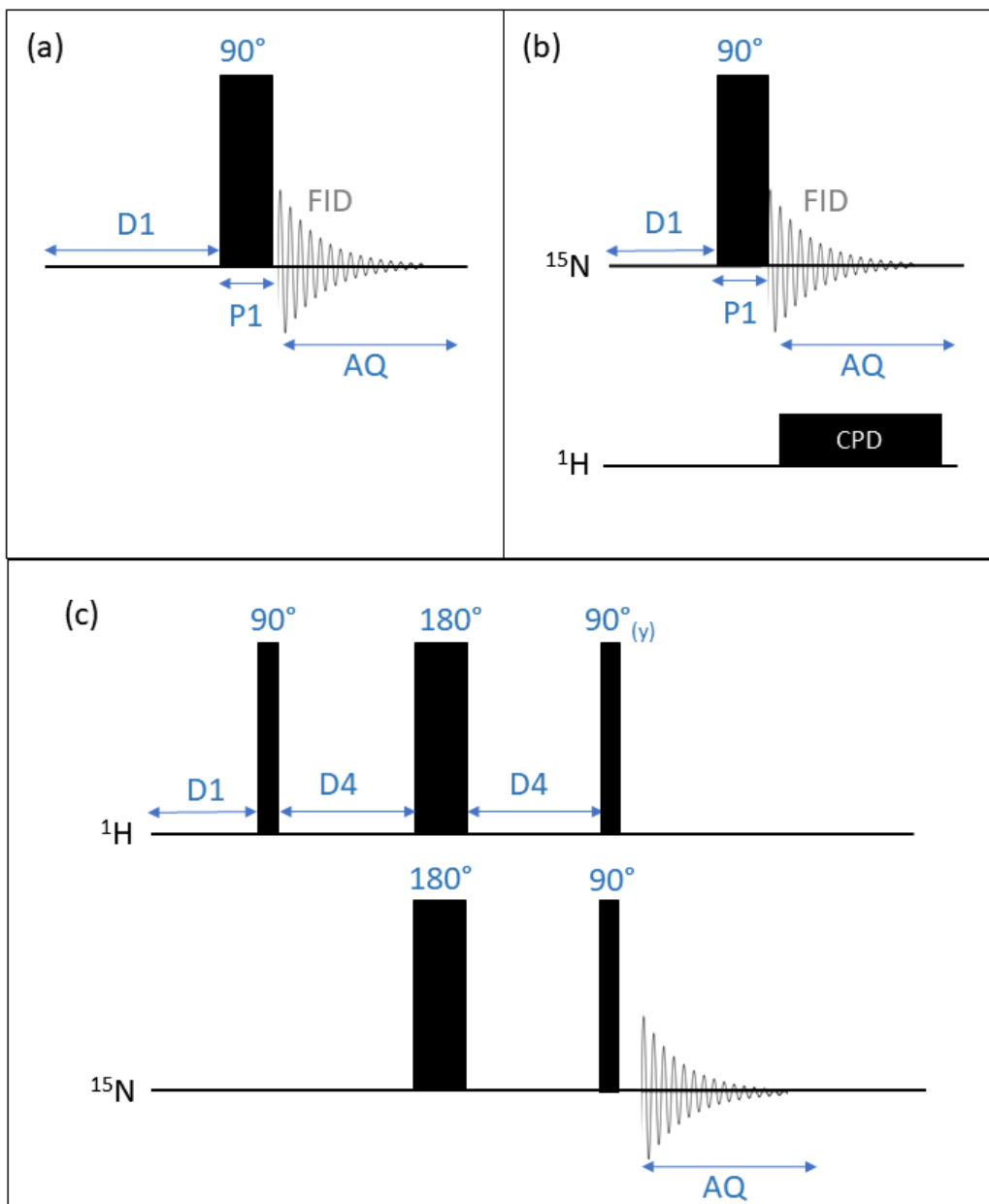
Figure 2.4. Schematic representation of the (a) zg, (b) zgig and (c) ineptnd pulse sequences, where D1 represents the relaxation delay, D4 a delay equal to $1/(4J_{NH})$, P1 represents the 90° pulse length, AQ is the acquisition time and CPD is the composite pulse decoupling scheme.

The PIL samples were placed in 5 mm NMR tubes and flame-sealed in a controlled environment (dry-room, relative humidity < 0.1% at 293 K) to prevent any contamination and air contact. All the NMR tubes contained a flame-sealed capillary tube of deuterated DMSO (DMSO-d_6) as a reference/lock solution.

^1H and ^{15}N NMR experiments of the pure PILs were performed at 11.74 T with a Bruker NEO 500 console equipped with a direct observe 5 mm pulsed-field z-gradient BBFO iProbe. For each sample, the probe was carefully tuned, and the 90° pulses were calibrated. The sample temperature was set and controlled using a variable temperature control unit using air gas flow. Standard Bruker library programs were used for the measurements.

^{1}H and ^{15}N NMR spectra were acquired over a temperature range from 298 K to 373 K for DBUH-TFO and DBUH–IM14, and from 313 K to 373 K for DBUH-TFSI, with steps of 5 K, 10 K, or 15 K depending on the type of analysis, and a minimum of 30 minutes allowed for thermal equilibration.

Shortly before the ^{15}N spectra were collected, the PILs were externally referenced to the standard sample of 90% formamide in DMSO-d_6 by setting its ^{15}N resonance to 112.7 ppm. The ^{15}N spectra were collected with and without ^{1}H decoupling, the latter allowing the direct observation of the one-bond spin-spin coupling ($^{1}J_{N-H}$). A WALTZ-64 decoupling scheme with a power level of 0.34 W was used for the ^{1}H decoupling. The standard notation ^{15}N-{^{1}H} is used to indicate ^{15}N acquisition with ^{1}H broadband decoupling.

The ^{15}N INETP experiments allowed a faster and more accurate measurement of the $^{1}J_{N-H}$ over the whole temperature range.

All experimental details are reported in Table 2.1.

Table 2.1. Experimental details of the ^{15}N-{^{1}H} NMR, ^{15}N NMR and ^{15}N INEPT NMR spectra*.

^{15}N-{^{1}H} NMR				
	DBUH-TFSI	DBUH-IM14	DBUH-TFO	DBU (free base)
Temperature (K)	308	308	308	308
NS	178	4096	96	256
TD	32768	8192	32768	32768
SW (ppm)	70.46	147.24	70.46	246.62
D1 (s)	10.0	2.0	10.0	10.0
^{15}N NMR				
	DBUH-TFSI	DBUH-IM14	DBUH-TFO	
Temperature (K)	318	305	305	
NS	13312	13312	3000	
TD	16384	16384	32768	
SW (ppm)	147.24	147.24	70.46	
D1 (s)	3.0	3.0	10.0	
^{15}N INEPT NMR				
	DBUH-TFSI	DBUH-IM14	DBUH-TFO	
Temperature range (K)	303-373	298-373	298-368	
NS	256	256	128	
TD	32768	32768	32768	
SW (ppm)	98.65	147.24	98.65	
D1 (s)	3.0	3.0	3.0	

*NS: number of scans; TD: time domain - number of raw data points; SW: spectral width; D1: relaxation delay between scans.

2.2.5. DSC analysis

Differential scanning calorimetry (DSC) is a common technique to determine the phase transitions and the procedure to establish the thermal events in ILs using DSC is well described in the literature[54]. Basically, the DSC technique is applied to detect phase transitions by monitoring the difference in the heat flow of two crucibles (one empty working as a reference and one loaded with the sample under investigation) at the same temperature conditions. Both DSC crucibles are heated and cooled at the same rate. The difference in the heat flow applied to maintain both, the sample and reference, at the same temperature is then measured. By plotting the heat flow as a function of temperature, one can observe the energy difference of an endothermic or exothermic process. From the heating scan, it is possible to determine the temperature involved in different thermal events by using the characteristic shape of the phase transition such as melting (T_m), cold-crystallization (T_{c-c}) and glass-transition (T_g) as exemplified in Figure 2.5[55].
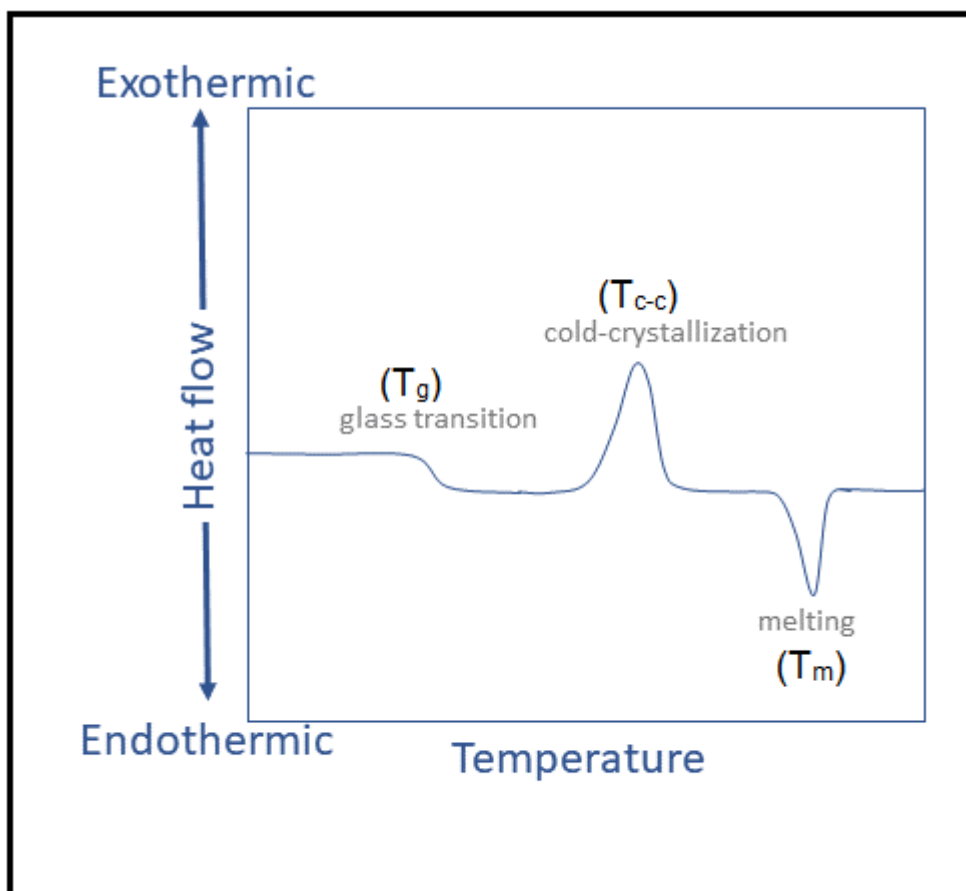
Figure 2.5. Schematic representation of the possible thermal events detected during a heating DSC scan.

Thermal properties of the PIL samples were analyzed with a DSC 1 instrument (Mettler Toledo), equipped with a liquid nitrogen cooling system during my secondment at the University of Campinas - Brazil. About 10 mg of the PIL samples were weighed using a

microanalytical balance MX5 (Mettler Toledo) and tightly sealed in a standard aluminium crucible.

The PILs liquid at room temperature, DBUH-IM14 and DBUH-TFO, were subjected to the same temperature program. First, the samples were cooled down to 153 K, with isothermal treatment at this temperature for 2 minutes. Then, they were heated up to 323 K. The heating and cooling scan rates were 10 K.min^{-1}. An additional evaluation was performed on both samples, fully crystallizing them before the heating scan. Thus, the PILs were subjected to a refrigeration cycle from 153 K until their cold-crystallization temperature in the DSC instrument. Then, the thermograms were recorded during the heating scan from 153 K to 323 K at 10 K.min^{-1}.

For the DBUH-TFSI sample, solid at room temperature, the protocol was slightly different. The sample was initially heated from 298 K to 323 K, at 10 K.min^{-1}, with isothermal treatment at this temperature for 2 minutes. Then, the sample was cooled to 153 K at 2 K.min^{-1} and kept at 153 K for 5 minutes, for the crystallization process. Finally, the sample was heated to 323 K at a scan rate of 2 K.min^{-1}. The DSC thermograms were recorded during the last heating scan.

In this thesis work, the melting point (T_m) was determined as the extrapolated onset temperatures of an endothermic peak during the heating (or reheating) scan. The cold crystallization temperature (T_{cc}) was defined as the onset of an exothermic peak upon heating from a subcooled liquid state to a crystalline solid phase. The glass transition temperature (T_g) was obtained as the midpoint of a small heat capacity change upon heating (or reheating) from the amorphous glass state to a liquid phase.

2.2.6. TGA analysis

Thermogravimetric analysis (TGA) is a technique for measuring the change of mass in a sample with temperature, providing information about thermal stability. The TGA analysis is performed by placing a sample in an open crucible that is then lowered into a furnace under a controlled atmosphere containing a microbalance. Plotting the mass change (i.e., the weight loss) vs. temperature (Figure 2.6a), one can extract information regarding the temperature related to the onset of a mass change, which occurs due to different reactions taking place with increasing the temperature during the reaction interval[56]. The TGA experiment can be performed as (i) a dynamic TGA, using a linear rate of increasing temperature (e.g. 10 K.min^{-1}), or an isothermal TGA, using isotherms, where the temperature is kept constant for a certain interval while the sample weight is recorded as a function of time[57]. Exemplification of dynamic and isothermal degradation thermograms are shown in Figure 2.6a-b.
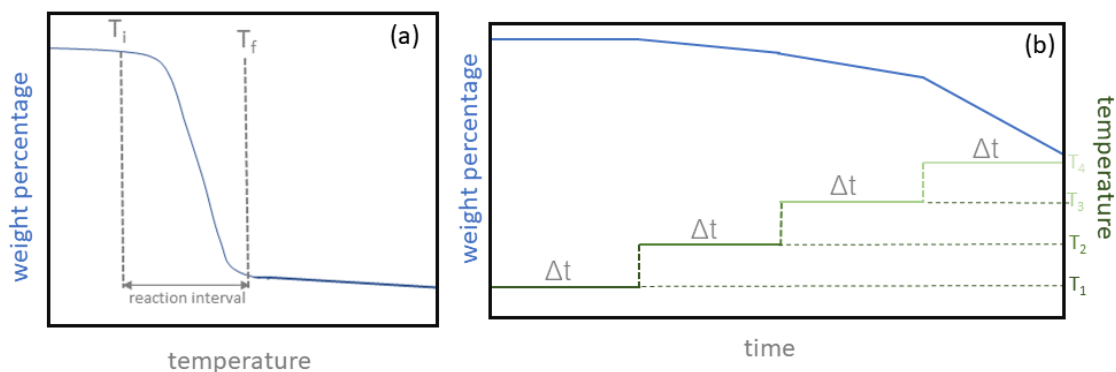
Figure 2.6. Schematic representation of (a) dynamic TGA, where the sample is heated at a constant rate and the weight loss is recorded as a function of temperature, with T_i and T_f representing the onset and end of the reaction interval, respectively; and (b) isothermal TGA where the temperature (T_i) is kept constant for a certain interval (Δt) and the sample weight loss is recorded as a function of time.

In this thesis, the thermal stability of the three PIL samples was assessed in nitrogen and synthetic air using the instrument TGA/DSC1 from Mettler Toledo with the STARe Thermal Analysis Software 10.00 during my secondment at the University of Campinas - Brazil. During the experiment, the gas flow rate was settled at 100 ml.min^{-1} to avoid external contamination from the atmosphere. Then, open alumina crucibles containing 10–15 mg of PIL were scanned. Initially, the thermal stability was investigated by heating the samples from room temperature up to 873 K at the heating scan of 10 K.min^{-1}.

The decomposition temperature (T_d) is frequently defined as the onset temperature or the temperature where the mass loss is 3%[58]. However, a better approach is based on estimating the T_d taking the minimum of the TGA derivative curve (DTG)[59]. In the present work, the derivative method (DTG) was applied to determine the decomposition temperatures of the PILs studied. Besides, the samples were evaluated by isothermal TGA in synthetic air to obtain more profound information on the stability at higher temperatures. In the isothermal TGA, the sample was heated at 10 K.min^{-1} until a specific temperature (isotherm) and kept at this condition for 40 min. Specifically the PILs were submitted to the following isotherms temperatures:

- DBUH-IM14: 523 K, 548 K, 573 K, 598 K
- DBUH-TFSI: 573 K, 598 K, 623 K
- DBUH-TFO: 548 K, 573 K, 598 K, 563 K

The degradation temperature was assigned as the same as the isotherm where practical weight loss (3% of mass weight loss) occurs.

2.2.7. Density

Density is a physical property of matter defined as the mass to volume ratio. A standard methodology for determining the density is via a mechanically oscillating U-tube. The experimental procedure consists of filling a glass U-tube with a known volume of sample and according to the change of the resonance frequency, the tube oscillates depending on the mass, automatically giving the density values as the output. When measuring viscous samples without correcting for viscosity, the resulting densities are slightly overestimated. Therefore, the density meter provider recommends to activate the automatic viscosity correction when measuring samples with a viscosity > 7 mPa.s[60]. For the PILs investigated, the automatic viscosity correction was activated, giving more accurate results.

Density measurements of DBUH-TFSI were performed under Ar atmosphere in a glove box (VAC, $[O_2]$ < 1 ppm, $[H_2O]$ < 1 ppm). The densities were recorded using the density meter DDM2910 from Rudolph Research Analytical in 5 K steps.

The other two samples, DBUH-IM14 and DBUH-TFO, were manipulated without a controlled environment and the air exposure was minimized as much as possible. The densities of those two samples were measured using the density meter DM45 Delta Range from Mettler Toledo in 10 K steps. For all PILs, the samples were allowed to equilibrate for at least 15 minutes before the measurements.

2.2.8. Viscosity

Viscosity is the measure of the internal friction of a fluid. This friction becomes apparent when a layer of fluid is made to move in relation to another layer. The greater the friction, the greater the amount of force required to cause this movement, which is called "shear". Shearing occurs whenever the fluid is physically moved or distributed. Highly viscous fluids, therefore, require more force to move than less viscous materials. The velocity gradient which measures the change in speed at which the intermediate layers move with respect to each other is called "shear rate". The force per unit area required to produce the shearing action is referred to as "shear stress". When dividing the shear stress by the shear rate, one can get the viscosity of the sample[61].
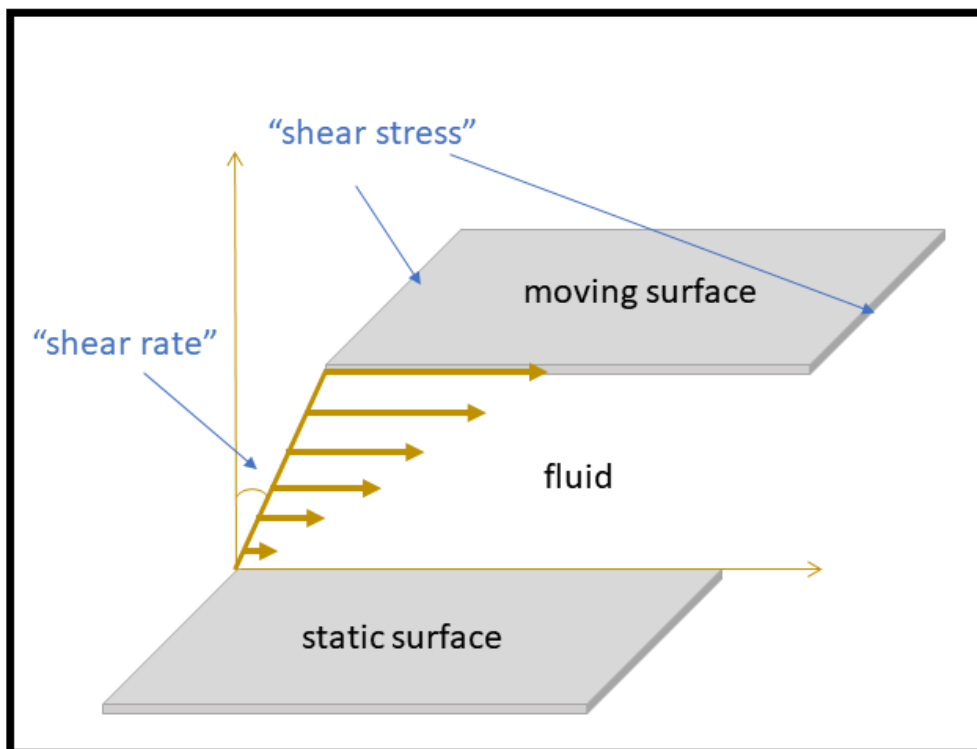
Figure 2.7. Schematic representation of the shear rate and shear stress involved in the viscosity measurement of a fluid.

The viscosity measurements of the three PILs studied in this thesis were carried out in a controlled environment (dry-room, relative humidity < 0.1% at 293 K) to prevent any contamination and air contact. The measurements were performed using a MCR 102 Rheometer (Anton Paar) in a plate-plate geometry (PP25/DI/Ti rotor) with a 100 μm gap. The temperature was controlled using a Peltier-heated P-PTD200/DI base plate and an H-PTD200 actively heated geometry housing. The viscosities values were measured from the loading temperature (i.e., 293 K for DBUH-IM14 and DBUH-TFO, and 303 K for DBUH-TFSI) up 373 K, with a 5 K temperature step. A 10 minutes thermal equilibration was considered for each step, and the viscosity was recorded with a constant shear rate of 10 s^{-1}. All the measurements were performed in triplicates.

2.2.9. Conductivity

The ionic conductivity represents how fast the ions can move within the electrolyte when exposed to an electric field[62]. For ionic conductors as ILs, the method generally applied for the investigation of the ion transport properties, including ionic conductivity, is the Electrochemical Impedance Spectroscopy (EIS). Basically, EIS allows the determination of the frequency-dependent resistance, the impedance $\hat{Z}$, of a conducting material. Because the quantity $\hat{Z}$ contains magnitude and phase information, it can be represented as a complex number with real Z' and imaginary Z'' components[62]. Mathematical definitions about Z' and Z'' can be found in the

literature, and they will not be explored in this dissertation, because here, the focus is the interpretation of the data obtained[63].

Two complementary graphs are commonly used to fully represent this complex dataset when acquiring information by varying the applied frequency (ω): Nyquist and Bode plots (Figure 2.8a and 2.8b, respectively). The Nyquist plot represents the modulus of Z according to the real Z' and imaginary components Z'', following the Eq. 2.2.

$$|Z(\omega)| = \sqrt{(Z')^2 + (Z'')^2} \hspace{3cm} (2.2)$$

and the Bode plot describes the phase angle (ϕ) as a function of the applied frequency (ω) (Eq. 2.3)

$$\phi(\omega) = \tan^{-1}\frac{Z'}{Z''} \hspace{3cm} (2.3)$$

These related plots provide visual hints in the analysis of experimental data. For data interpretation, it is useful to model the electrochemical system as an equivalent circuit model. When measuring the ionic conductivity of ILs using ion-blocking electrodes and starting from the fully crystallized state (IL in the solid state), the equivalent circuit described in the Figure 2.8c is employed for fitting the impedance spectra. This circuit contains an $(RC)_1$ element, (i.e., combination of a resistor and capacitor in parallel), represented by a semicircle at high-medium frequencies starting from the axes origin, and a capacitor (C_2) associated to the inclined straight-line observed at low frequencies. Here, $(RC)_1$ represents the resistance (R_1, related to the semicircle diameter) and the geometrical capacitance (C_1) associated to the electrolyte, whereas C_2 describes the double-layer capacitance due to charge accumulation at the electrolyte/electrode interfaces[62,64]. Note that a cell phase element (CPE) was used to represent the non-ideal capacitances which may be caused by inhomogeneity and porosity of the electrochemical materials and interfaces[62].

When the IL sample turns liquid (going from the solid to the liquid state), i.e., above the melting temperature, the Nyquist and Bode plots assume the shape as described in Figure 2.8d and 2.8e, respectively. The Nyquist diagram shows only the inclined straight-line associated to the double-layer capacitance (C_2). The disappearance of high-medium frequencies semicircle is due to the drastic reduction of the electrolyte resistance (i.e., the frequency of the semicircle points, inversely proportional to the electrolyte resistance, is above the maximum value achievable by the equipment). In this case, the complex part of the impedance, -jZ'', exhibits a minimum approaching zero, before it increases at higher frequencies. The frequency ω_{dc}, at which this minimum occurs, corresponds to the real impedance where Z' is frequency independent. Therefore, the distance of the high frequency intercept

with the real axis (Z') from the axes origin gives the electrolyte resistance (R1). As expected, the R1 value is rather low compared to that observed in the solid state (Figure 2.8a) due to the relevant increase of ion conduction. The related equivalent circuit model (Figure 2.8f) reduces the electrolyte resistance (R1) connected in series with the double-layer capacitance (C2).
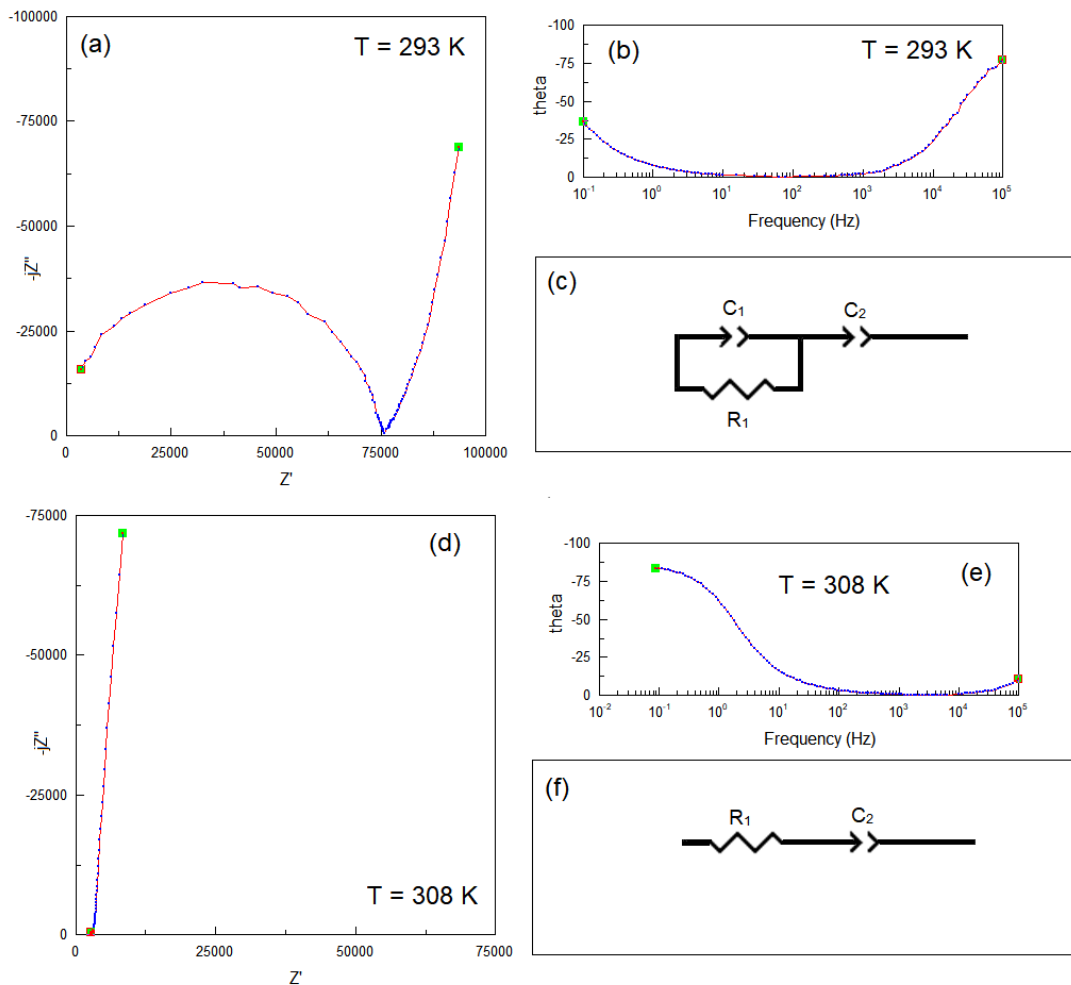
Figure 2.8. (a) Nyquist and (b) Bode plots of the DBUH-IM14 obtained at 293 K; (c) equivalent circuit model used to fit the experimental data obtained at 293 K; (d) Nyquist and (e) Bode plot of the DBUH-IM14 obtained at 308 K; (f) equivalent circuit model used to fit the experimental data obtained at 308 K.

The measurements of the specific conductivity of the PILs investigated in this thesis was performed during my short research stay at ENEA. The specific conductivity was determined using a Frequency Response Analyzer (F.R.A) combined with a potentiostat-galvanostat Parstat 2273. The complex impedance spectra were recorded in the frequency range of 100 kHz to 1 Hz. Before the measurements, the PIL samples were housed in sealed glass conductivity cells equipped with two porous platinum electrodes under an Ar atmosphere in a dry glove box (VAC, $[O_2] <$ 1 ppm, $[H_2O] <$ 1 ppm). In sequence, the cells were dipped (1 minute) in liquid nitrogen to fully crystallize the PILs. Then, they were kept in the climatic chamber at 233 K for at least 18 hours, allowing the sample to thermally equilibrate. After that, the conductivity was

measured in 5 K steps by running a heating scan at 1 K h^{-1} from 233 K to 373 K. The specific conductivity was determined by resolving the Nyquist plots of the impedance data using the software Zview, or extracting the Z' from the complex plot. After extracting the value of the R_1, representing the resistance of the electrolyte, the values of the specific conductivity σ were obtained using Eq. 2.4:

$$\sigma = K \frac{1}{R_1}$$ (2.4)

where, K is the cell constant (previously determined with KCl solutions having known conductivity values). Note that the constant K is an experimentally determined parameter, which accounts for the cell geometry (area, shape and porosity of electrodes, electrodes' distance, etc.). Only in particular cases, i.e., satisfying all these conditions (electrodes having identical shape and surface, electrodes perfectly faced and parallel, electrodes perfectly smooth), the cell constant may be assumed as the ratio between the electrodes' distance and surface. The uncertainty for the measured specific conductivity is 10 %.

2.3. Results

2.3.1. The effectiveness of the purification

The synthesis of PILs with no trace impurities is key to their application. The protocol reported in the literature for preparing DBU-based PILs consists of distillation the DBU base before its use, whereas the acid is handled as received without any further purification[46]. Accordingly, only the impurities derived from one precursor are removed. Indeed, very strong and volatile acids, such as HTFO, require distillation at elevated temperatures (around 162 °C) to be purified, demanding specific apparatus and considerable high energy consumption[65]. Then, in my thesis work, I propose an alternative methodology to directly purify the final product using activated charcoal as a sorbent. This strategy has been already applied for AILs[66] and is advantageous as it applies in a one-pot procedure to the final PIL (i.e., both conjugated acid and base are simultaneously purified).

UV-Vis spectrophotometry is an efficient method for assessing the purity level of an IL[67], therefore this technique was used to qualitatively check the effectiveness of the purification procedure applied (Figure 2.9). The peaks in the range of 250-500 nm are ascribable to colored impurities in the PILs[67]. In all the unpurified samples (black solid lines), absorption peaks of 0.18, 0.25, and 0.65 (in arbitrary units a.u.) are found around 300 nm for DBUH-TFSI, DBUH-IM14, and DBUH-TFO, respectively. Conversely, no peaks relative to those impurities are detected in the absorption spectrum

of the purified samples (blues dashed lines). Therefore, the results demonstrated the effectiveness of the purification method applied here for PILs, through the adsorption of the colored impurities on the surface of active charcoal.
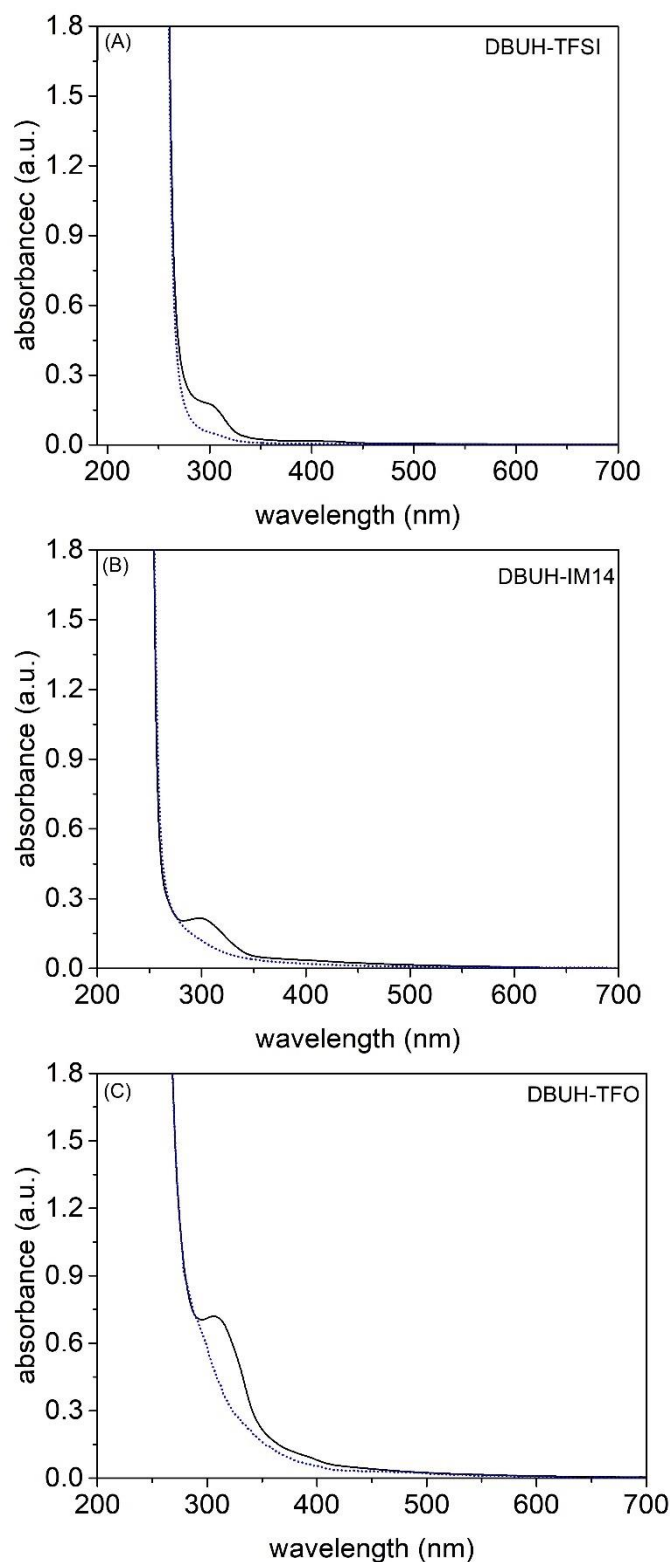
Figure 2.9. UV-Vis spectra of the unpurified (black solid lines) and purified (blue dashed lines) obtained for DBUH-TFSI (a), DBUH-IM14 (b), DBUH-TFO (c).

An easy-to-detect effect of impurities is on the thermal stability of PILs. It is well-known that ILs are exceptionally thermally stable systems, having considerably high decomposition temperatures

(i.e., above 250 °C)[58]. However, the impurities present in the bulk liquid can catalyze the decomposition process, lowering their thermal stability[68]. Here, I qualitatively accessed the effect of the impurities in the thermal stability of the DBUH-IM14 through a bench flame test. The experimental procedure consisted in weighing about 1 g of PIL sample, purified and not purified, in a watch glass and heating it using a lighter flame gun. Recording the process (Figure 2.10), it was observed the appearance of colored degradation products due to the flame exposure much earlier for the unpurified DBUH-IM14 (after 13 seconds) than for the purified one (around 29 seconds). This qualitative experiment supports the catalytic effect of the impurities in the degradation process of PILs, highlighting the importance of the purification procedure before their physicochemical characterization.
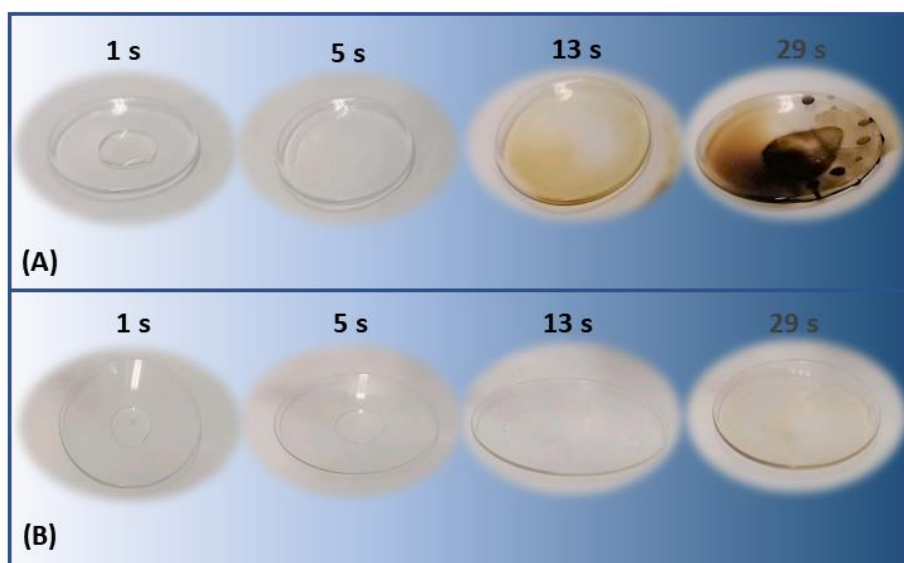
Figure 2.10. Qualitative evaluation of the degradation process of the unpurified (a) and purified (b) DBUH-IM14.

2.3.2. Protonation status of the synthesized PILs: ^{1}H and ^{15}N NMR measurements

As mentioned in *Section 2.1*, PILs are formed by a neutralization reaction between a Brønsted acid and a Brønsted base (Eq. 2.5):

$$HA + B \rightleftharpoons BH^+ + A^- \qquad (2.5)$$

Where *HA* is the Brønsted acid, *B* is the Brønsted base, BH^+ is the cation (protonated base) and A^- is the anion (deprotonated acid).

The literature often reports on the estimate of the degree of proton transfer by using the difference between the aqueous pK_a values of the acid and the base (ΔpK_a)[69]. This approach intends to numerically quantify a threshold value of ΔpK_a that can be generalized to guarantee the PIL formation, where the number of neutral species in the final system is negligible. Specifically,

Yoshizawa et al.[70] proposed that ΔpK_a should be higher than 10 to ensure a complete proton transfer; MacFarlane et al. achieved 99% proton transfer in systems with ΔpK_a = 4[71]; Watanabe suggested a ΔpK_a higher than 15 to get fully ionic systems in PILs based on DBU base[46]. Clearly, there are some discrepancies in the definition of a threshold value for the ΔpK_a. Moreover, the pK_a values are meaningful only in aqueous systems, and the approach does not take into account the acid strength in the IL environment[59]. This is why proton affinity (PA) has been also suggested as a more reliable indicator of the degree of proton transfer[72], with lower PA of the anion translating into stronger associated acid, but it is unclear how it correlates with the macroscopic behaviour of the whole system yet. Regardless of the ongoing debate, both the ΔpK_a and PA approaches can be used with caution to predict or at least describe the proton transfer behaviour of a PIL according to its precursors.

The choice of the precursors of this thesis work is meant to obtain fully ionic PILs (i.e., to achieve a full proton transfer). Indeed, DBU is a super-base with pK_a = 13.4[46], while HTFO and HTFSI are very strong acids (HTFO, pK_a = -7, PA = 305 kcal.mol^{-1}); HTFSI, pK_a = -10, PA = 294 kcal.mol^{-1})[46,72]. pK_a and PA of the HIM14 acid are still unknown in the literature, even if it is claimed to display an acidic strength comparable to other similar imide super-acids (e.g., HTFSI)[49]. Given the role played by acid strength on PIL's formation, it is worth quantifying exactly the acidity strength of the HIM14, and I propose here an indirect method based on ^{1}H and ^{15}N NMR measurements. A general trend reported in the literature is that the chemical shift of the exchangeable proton is shifted upfield (to lower ppm values) with the increase of the acid strength of the precursor [46,72]. For the investigated PILs, the ^{1}H and ^{15}N NMR spectra and the chemical shift assignment are displayed in Figures 2.11-2.13.
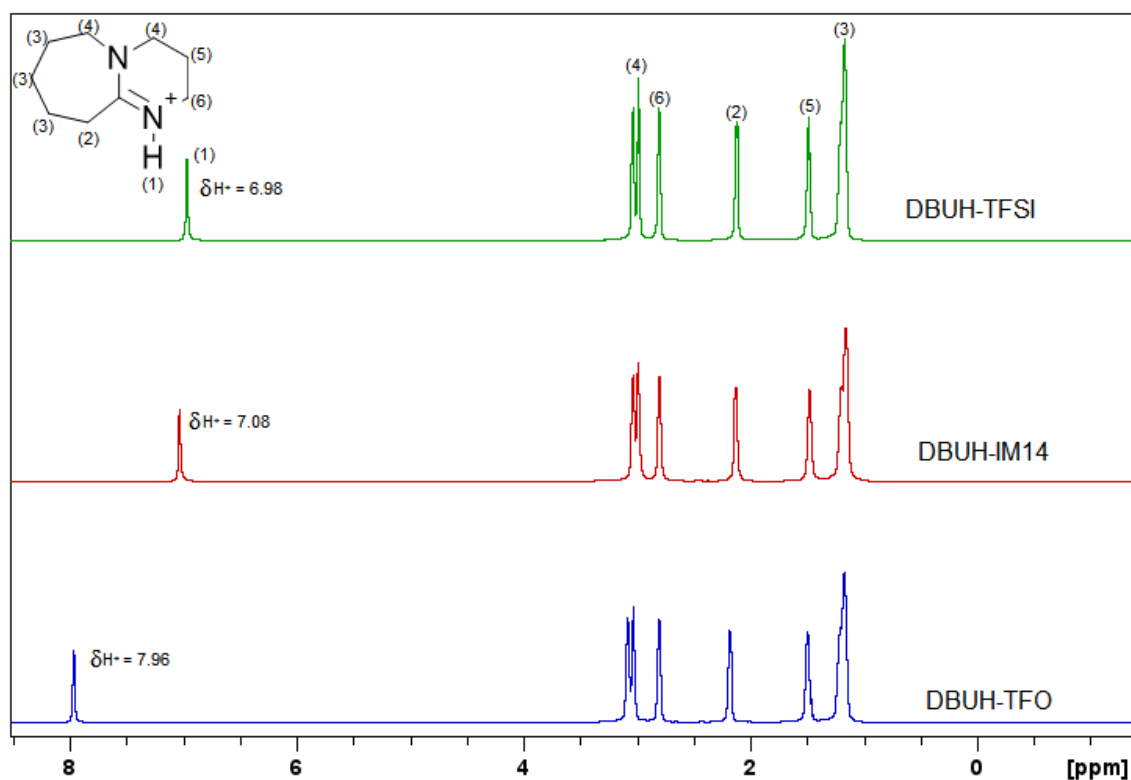
Figure 2.11. 1D ^{1}H NMR spectra and chemical shift assignment of the PILs investigated at 338 K.

The ^{1}H signals appearing in the spectral region between 1 and 3 ppm are assigned to the C-H protons of the DBU backbone (molecular formula and atom numbering in Figure 2.11). The most deshielded signal corresponds to the acidic exchangeable proton available on the DBUH$^+$ cation.

As shown in Figure 2.11 for DBUH-TFO and DBUH-TFSI, the chemical shift of the exchangeable proton is decreased (shielding effect, i.e., it moves upfield or to lower frequencies) as the ΔpK_a of the PIL increases (ΔpK_a(DBUH-TFO) = 20.4; ΔpK_a(DBUH-TFSI) = 23.4[46]). Such an upfield shift is related to the extent of the acidic dissociation of the N-H exchangeable proton. Accordingly, the chemical shift difference between the acidic proton and the most shielded proton, i.e., the CH$_2$(3) group of the DBU[73], ($\Delta\delta$(^{1}H)) has been chosen as a marker of protonation and an indirect indicator of the acid strength (Table 2.2). Given $\Delta\delta$(^{1}H) measured for DBUH-IM14 is the same as DBUH-TFSI, it can be safely assumed that pK_a and PA of HIM14, and in general its acidic strength, are very close to those of HTFSI.

Remarkably, no signal was detected in the 10–20 ppm spectral range (Figure 2.12), ruling out the presence of the free acid in the system. Note, for instance, that a peak at 16.3 ppm has been detected in the PIL formed by DBU and trifluoracetic acid (DBUH-TFA, ΔpK_a = 12.9 [46]) indicating that a full protonation status was not achieved, probably due to the exchange between the H$^+$ and two trifluoroacetic anions[44].
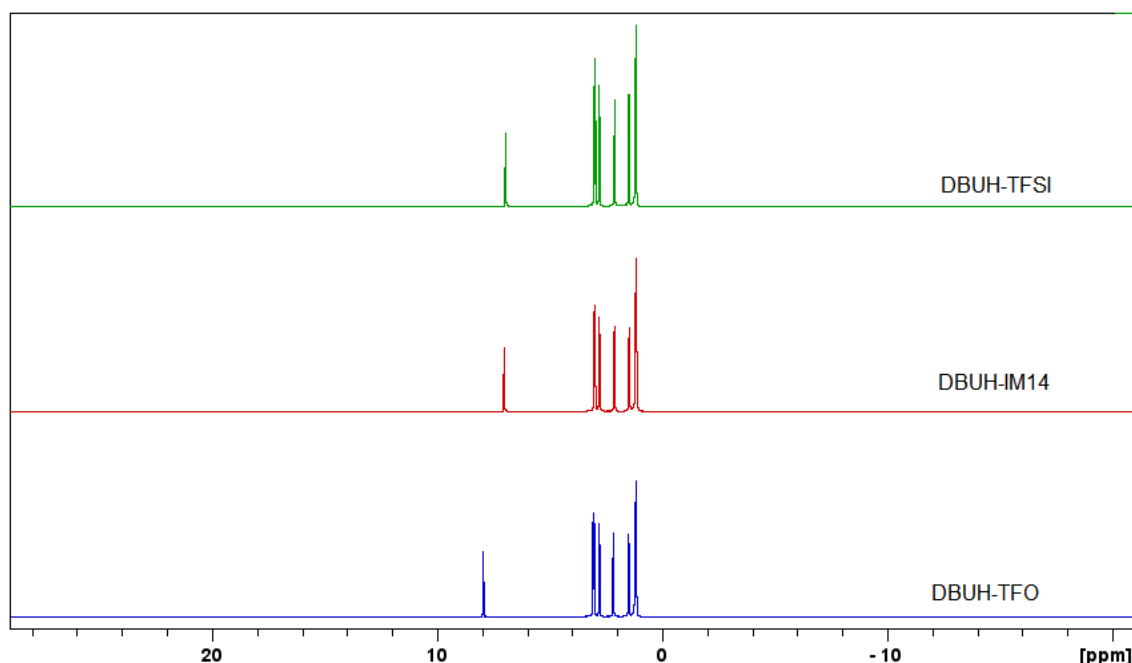
Figure 2.12. 1D ^{1}H NMR spectra and chemical shift assignment of the PILs investigated at 338 K with spectral width up to 20 ppm.

The protonation status found for the investigated PILs via ^{1}H spectra was also confirmed by the proton-decoupled ^{15}N NMR spectra recorded at 308 K and displayed in Figure 2.13. The spectrum of the free base (DBU) shows two signals at 87.7 ppm and 212.0 ppm assigned to the amino (N1) and imino (N2) nitrogen, respectively[44]. Upon protonation, the signal of the imino (N2) nitrogen is significantly shielded (110.2 ppm, 110.2 ppm and 111.4 ppm for DBUH-IM14, DBUH-TFSI and DBUH-TFO, respectively), while the amino nitrogen (N1) in the β position with respect to the protonation site shows a strong downfield shift (122.6 ppm, 122.7 ppm, 122.0 ppm for DBUH-IM14, DBUH-TFSI and DBUH-TFO, respectively), in agreement with the charge and electron density delocalization onto the N-C=N moiety. A similar trend was shown by Angell et al.[74] in the case of the protonation of 1,3-dimethyl-2-imidazolidinone (DMI). The ^{15}N chemical shift variation at N2 between the protonated and the free base ($\Delta\delta(^{15}N)$) is around 100 ppm for the three PILs (see Table 2.2), confirming the full protonation of the imino nitrogen[44]. Again, $\Delta\delta(^{15}N)$ of DBUH-IM14 is very close to that of DBUH-TFSI, indicating that the HIM14 acidity is comparable to that of HTFSI. The nitrogen nuclei belonging to IM14$^-$ and TFSI$^-$ anions were detected at 142.8 ppm and 139.0 ppm, respectively.
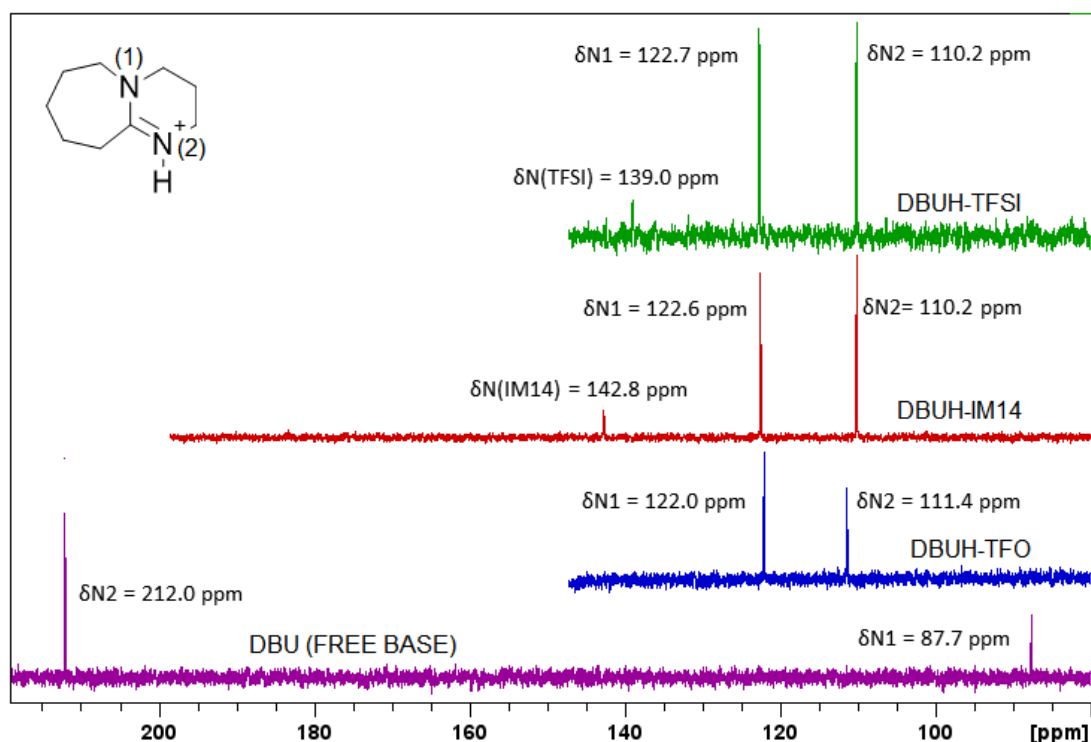
Figure 2.13. 1D ^{15}N-{^{1}H} NMR spectra and the chemical shift assignments of the PILs investigated at 308 K.

Overall, the observed trends in ^{1}H and ^{15}N chemical shift data are in line with the known and expected proton donor ability of the acids and proton acceptor character of the DBU base, as shown in Table 2.2. Indeed, both the chemical shift difference $\Delta\delta(^1$H) and $\Delta\delta(^{15}$N) of DBUH-IM14 are very close to those of DBUH-TFSI, indicating that the acidic strength of HIM14 is comparable to that of HTFSI. This finding is particularly relevant as pK_a and PA of HIM14 have not been reported yet and considering that HIM14 is an important precursor of PILs with reduced melting point, likely due to the asymmetry of the fluorinated chains linked to the sulphonamide group in the IM14$^-$ anion[75]. Other DBU-based PILs having very strong acids as a precursor, such as DBUH-TFSI and DBUH-TFO, are actually solid at room temperature (see *Section 2.3.3*), thus hampering their technical application at ambient conditions[76].

Table 2.2. Correlation between ^{1}H and ^{15}N NMR resonances with ΔpK_a of the PILs studied.*

PIL	$\Delta\delta(^1$H) [a] ppm	$\Delta\delta$(N2) [b] ppm	ΔpK_a	Anion PA kcal/mol
DBUH-TFO	6.79	100.6	20.4 [c]	305 [d]
DBUH-TFSI	5.80	101.8	23.4 [c]	294 [d]
DBUH-IM14	5.87	101.8	$\simeq$23.4	$\simeq$294

[a] $\Delta\delta(^1$H) = δH$^+$ − δCH$_2$(3) at 338 K; [b] $\Delta\delta$(N2) = |δ(N2)$_{(DBUH+)}$ − δ(N2)$_{(DBU)}$| at 308 K; [c] Ref.[46]; [d] Ref.[72]. * Standard uncertainties u are u($\Delta\delta(^1$H)) = 0.05 ppm; u($\Delta\delta$(N2)) = 0.1 ppm and u(T) = 0.1 K.

The 1D ^{15}N NMR spectra run without proton decoupling shown in Figure 2.14 served as unambiguous evidence for the exclusive protonation of the imino nitrogen (N2). In all samples, the signal appearing around 110 ppm is a well-resolved doublet with a one-bond ^{1}J$_{N-H}$ scalar coupling constant of about 98 Hz, which is

consistent with the formation of N-H covalent bond upon protonation[44]. Thus, the doublet multiplicity of the N2 signal is the direct spectroscopic evidence of the formation of the stable DBUH$^+$ cation on the NMR time scale investigated for all the PILs studied. From a kinetic viewpoint, the detection of kinetically stable and well-defined signal splitting due to $^1J_{N-H}$ scalar coupling means that the rate of proton exchange is slower than the timescale associated to the spin-spin coupling, i.e., here slower than ~ 10 ms.
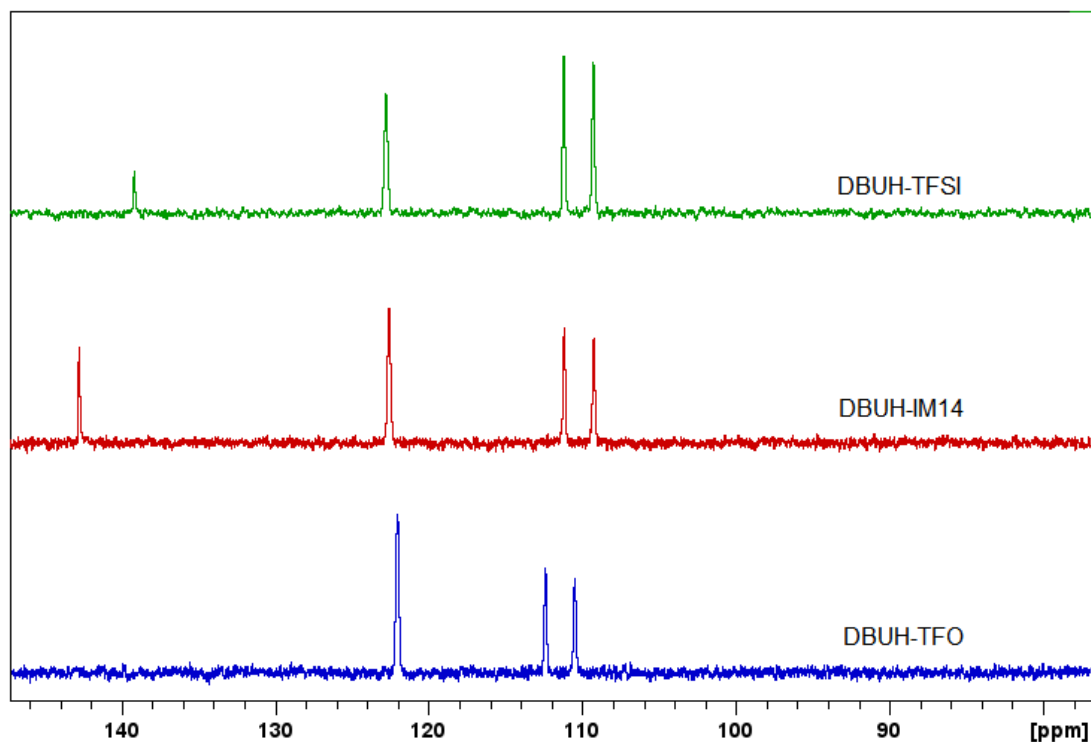
Figure 2.14. 1D ^{15}N NMR spectra acquired without proton decoupling at 318 K for DBUH-TFSI, and 305 K for DBUH-IM14, and DBUH-TFO.

The ^{15}N chemical shift of the amino and imino nitrogen was also measured in a large range of temperatures to evaluate if the kinetic stability is retained with the temperature increase (Figure 2.15). Only a small linear variation in the ^{15}N chemical shift is detectable in both signals assigned to nitrogen nuclei of DBUH$^+$ (Figure 2.15 a-b). No significant or discontinuous ^{15}N chemical shift change of the nitrogen signal of TFSI$^-$ and IM14$^-$ anions were detected in the same temperature range (Figure 2.15c). The main conclusion is that the extent of protonation remains constant with increasing temperature, indicating that imino nitrogen of DBU base (N2) is fully protonated within the explored temperature range.
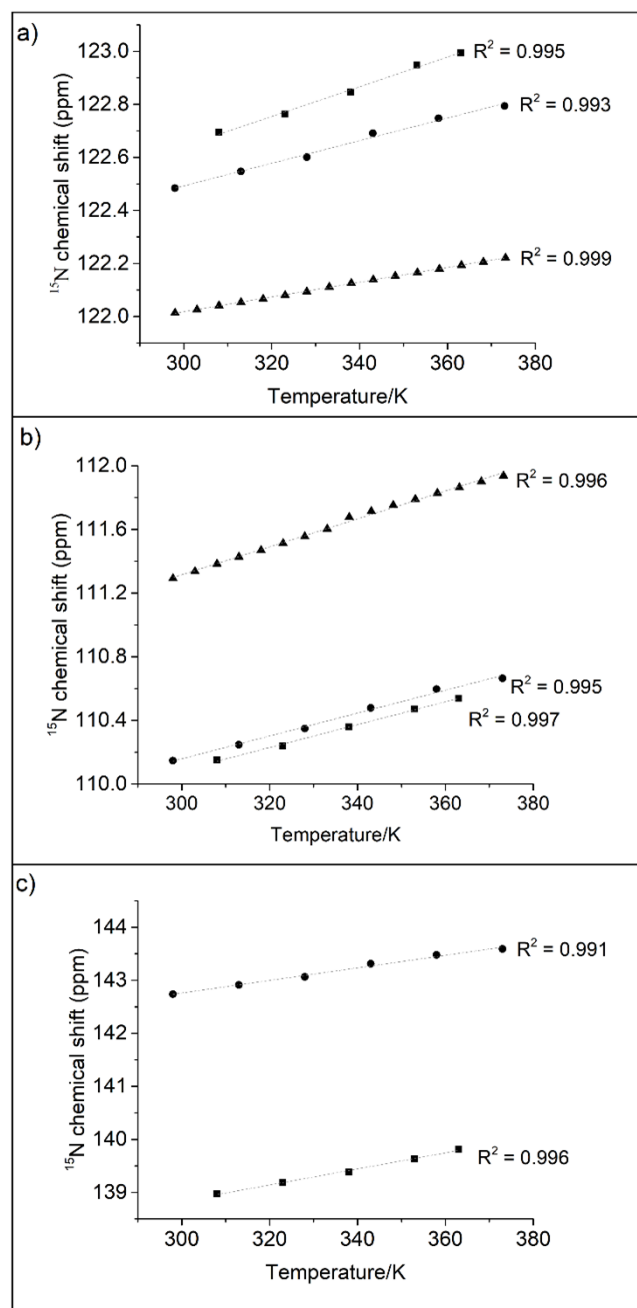
Figure 2.15. ^{15}N chemical shift of the (a) imino (N2), (b) amino (N1) and (c) imide nitrogen for the (■) DBUH-TFSI (●) DBUH-IM14 and (▲) DBUH-TFO, as measured from ^{15}N-{^{1}H} NMR spectra as a function of temperature.

The thermal stability of the N-H bond between the imino nitrogen and the acidic proton is also confirmed by ^{15}N INEPT experiments (Figure 2.16), which revealed an approximately constant of 98 Hz $^{1}J_{N-H}$ in the temperature range investigated for all the PILs studied. Thus, the INEPT evidenced the thermal stability of the N-H bond in the full temperature range evaluated, confirming that the proton residence time on the imino N remained above the order of 10 ms range in the explored temperature range.

The extensive NMR evaluation performed provides evidence that all the PILs studied here are formed by a very strong acid, favoring the complete proton transfer, and leading to a system with a negligible

content of neutral species and stable in the whole temperature interval investigated.
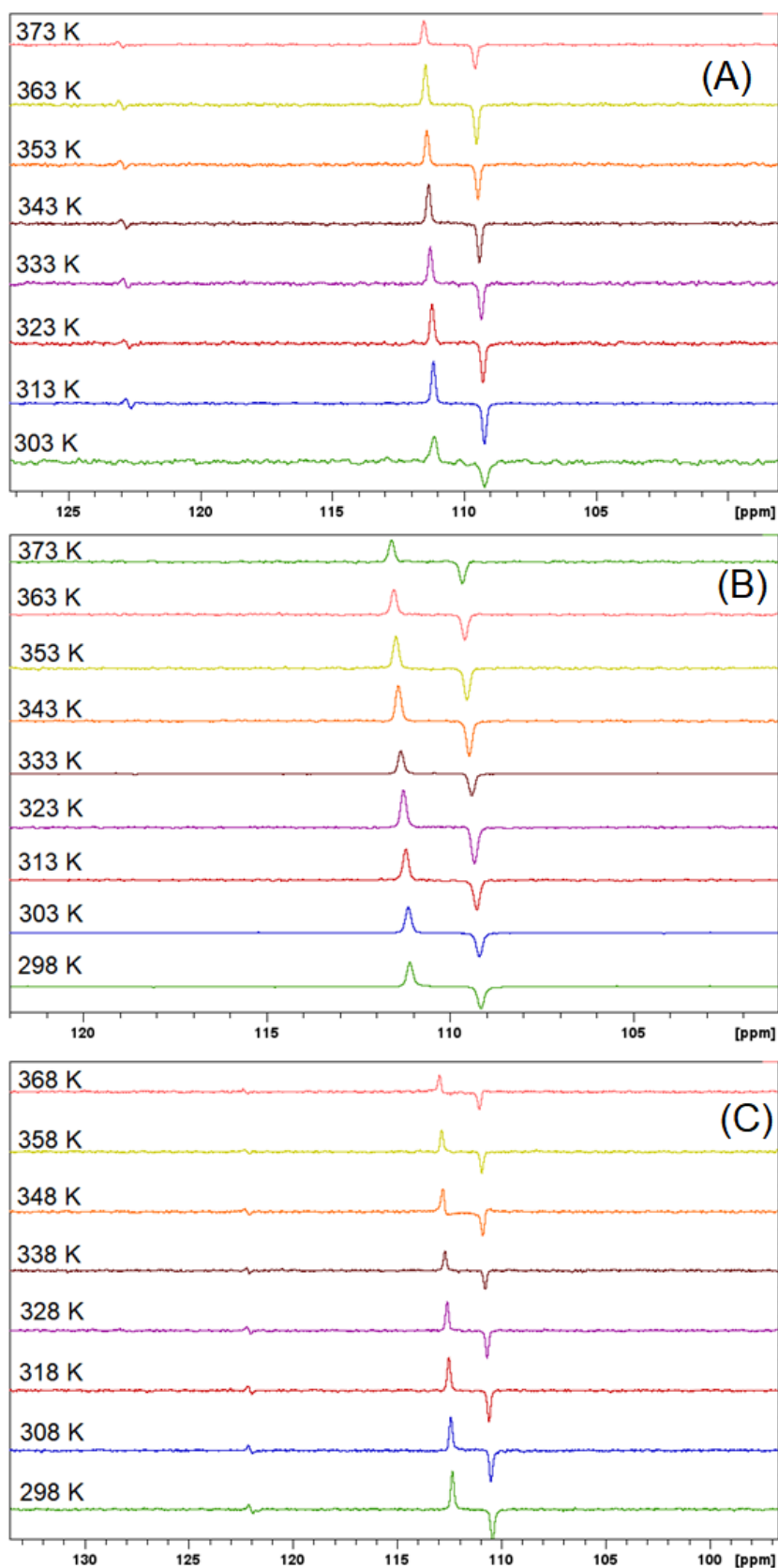
Figure 2.16. ^{15}N INEPT spectra recorded for DBUH-TFSI (a) DBUH-IM14 (b) and DBUH-TFO (c), as a function of temperature.

2.3.3. The effect of water on the PILs

Recent studies have been trying to rationalize the water effects on the properties of PILs[77,78]. For instance, some works revealed an enhancement of conductivity due to the presence of water in PILs[33], and some others addressed the correlation between local structure and transport properties in H_2O/PIL binary systems[79,80].

In this framework, this thesis work intends not only to evaluate if impurities, including water traces, have a significant effect on the intermolecular properties of DBU-based PILs, but also to disentangle the effect of water and other unknown impurities. To this end, the PILs were investigated in the following states:

(i) samples unpurified (i.e., no purification step with activated charcoal) and wet (i.e., doped with 3600 ppm of water), acronym $PIL_{(u/w)}$;

(ii) samples unpurified (i.e., no purification step with activated charcoal) and dried (water content < 200 ppm), acronym $PIL_{(u/d)}$;

(iii) samples purified (i.e., purification step with activated charcoal) and dried (water content < 200 ppm), acronym $PIL_{(p/d)}$.

^{15}N NMR was used here to gain insights into the effect of water and other impurities on the three PILs.

After running ^{15}N NMR coupled experiments (Figure 2.17), the signal in the high field region of the DBUH-TFO spectrum is a well-resolved doublet of about 98 Hz, regardless of the presence of humidity and/or impurities (Figures 2.17a-c, in red). The doublet multiplicity is due to the one-bond $^1J_{N-H}$ scalar coupling constant of N-H covalent bond upon protonation, as described previously.

Conversely, the peak shape of the N-H signal shows significant differences in the two PILs with a sulfonylimide anion (DBUH-TFSI and DBUH-IM14) in the presence of water/impurities. Indeed, the sharp doublet observed for purified and dry samples (Figures 2.17f and 2.17h) is replaced by a broad singlet in the unpurified and wet samples (Figures 2.17d and 2.17g), thus indicating a change in the residence time of the N-H proton as detected in the NMR timescale. The comparison between DBUH-TFSI$_{(u/w)}$ and DBUH-TFSI$_{(u/d)}$ allows disentangling the effect of water and unknown impurities. Figure 2.17e shows indeed an unmistakable $^1J_{N-H}$ of approximately 98 Hz for the imine nitrogen in the case of the unpurified and dried DBUH-TFSI sample. This unambiguously indicates that water is responsible for a such kinetic effect of the N-H proton, hence in DBUH-TFSI$_{(u/w)}$ there must be a moderately fast exchange of that proton with water. Even though the ^{15}N coupled spectrum for the DBUH-IM14$_{(u/d)}$ is not available, the similarity between the two

34

sulfonylimide anions suggests the two PILs likely have the same behavior.

Overall, the spectra of Figure 2.17 indicate that the impurities – even at the trace level of the examined samples – do not affect the kinetics of the N-H proton exchange of the PILs. At this stage, we may formulate the hypothesis of a selective, possibly catalytic, effect of water on the N-H kinetic stability of PILs based on sulfonylimide anions vs the triflate based PIL.

The selective water effect on the N-H kinetic stability as a function of the nature of the anion may stem from a different intermolecular network of these systems, i.e., triflate based vs sulfonylimide based DBUH-PILs. As reported in the literature[49], DBUH-TFO has a "robust", highly directional hydrogen bonding network and the TFO⁻ anion may be strongly interacting with the water molecules. Similar findings have been detected by Raman spectra in the PIL $C_2HImTFO$[77], supporting the interaction scheme described above.

The scenario is different for DBUH-TFSI and DBUH-IM14, which contain a less oriented hydrogen bonding network due to the presence of imide anion[50,76]. For such TFSI-based PILs, it has been shown that water establishes stronger interactions with the cation (as well as weaker interaction with the anion)[77]. This point leads to the conclusion that the water molecules can facilitate the N-H exchange via direct interaction with the protonation site of the DBUH cation. Indeed, for imide-based PILs, we observed that water affects the residence time of the acidic proton located on the DBUH⁺ cation, possibly through hydrogen bonding. Note that the interaction between the water molecules and the exchangeable proton is not strong enough to deprotonate the base. Actually, in such a case the magnetic environment of the imino ^{15}N would dramatically change with consequent chemical shift variations which are not observed. The overall conclusion is that the presence of water, at the concentrations here studied (3600 ppm), has a mere kinetic effect on the N-H exchange rate.
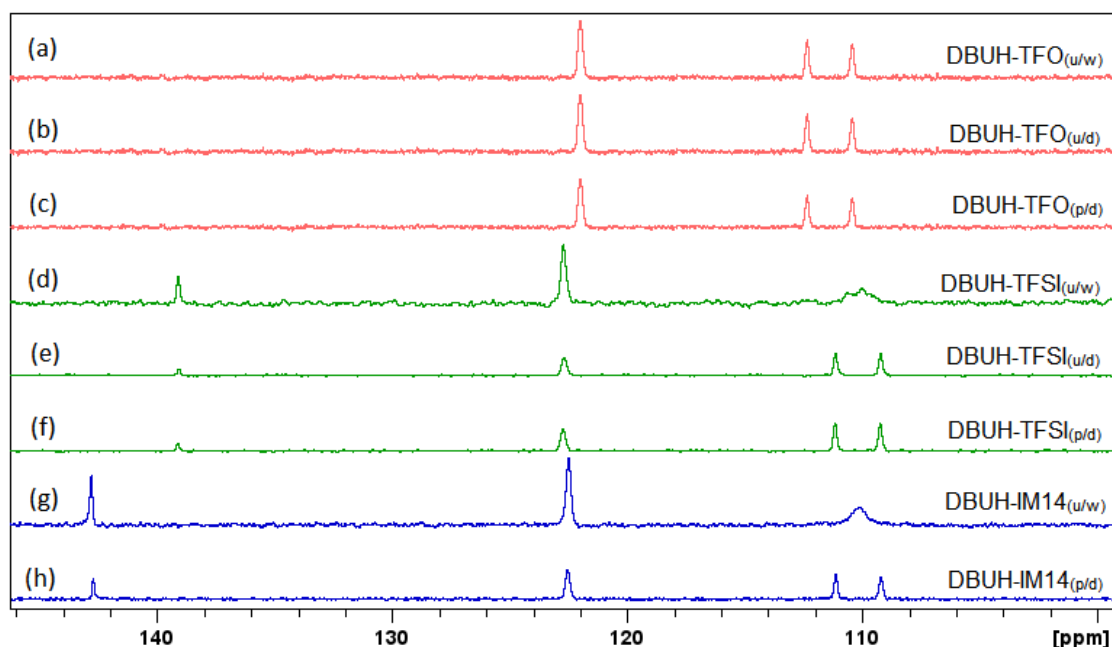
Figure 2.17. ^{15}N coupled spectra of the PILs samples at the investigated conditions. For DBUH-TFO and DBUH-IM14, spectra were collected at 305 K. For DBUH-TFSI, spectra were recorded at 318 K. The subscripts in the parentheses contain the indication of the state of purification-dryness (u: unpurified; p: purified; w: wet; d: dry), as described above.

To get more accurate measurements of the $^{1}J_{N-H}$, I performed ^{15}N INEPT experiments over a wide temperature range, in both $PIL_{(u/w)}$ and $PIL_{(p/d)}$ for the DBUH-TFSI and DBUH-TFO samples (Figure 2.18). For the DBUH-TFO, no change of $^{1}J_{N-H}$ with T was observed in both the dried and wet samples. For the DBUH-TFSI, the $^{1}J_{N-H}$ of the dried PIL is approximately constant (almost equal to 98 Hz), while a linear decrease of the $^{1}J_{N-H}$ with increasing temperature was observed for the wet PIL (empty squares in Figure 2.18). The linear dependence of the coupling constant with the temperature experimentally indicates that the N-H proton experiences a progressive increase in the exchange rate. A similar temperature dependence of the coupling constant was also qualitatively observed for the DBUH-IM14$_{(u/w)}$ by ^{15}N NMR coupled spectra (Figure 2.19).

The insights gathered from the nitrogen-proton scalar coupling confirm the previous findings:

- for the triflate-based PIL, DBUH-TFO, $^{1}J_{N-H}$ does not change with T, probably because (i) DBUH^{+} is already strongly interacting with the TFO^{-} anion by means of highly oriented hydrogen bonds[76], and (ii) the water molecules are mainly interacting with the TFO^{-} anion[77] and do not have access to the protonation site.

- for the sulfonylimide based PILs, DBUH-TFSI and DBUH-IM14, $^{1}J_{N-H}$ changes with T. probably because (i) DBUH^{+} is less strongly interacting with the TFSI/IM14-anion through of a less oriented hydrogen bond, and (ii) the water molecules establish stronger

36

interactions with the DBUH⁺ cation, thus affecting the protonation site.
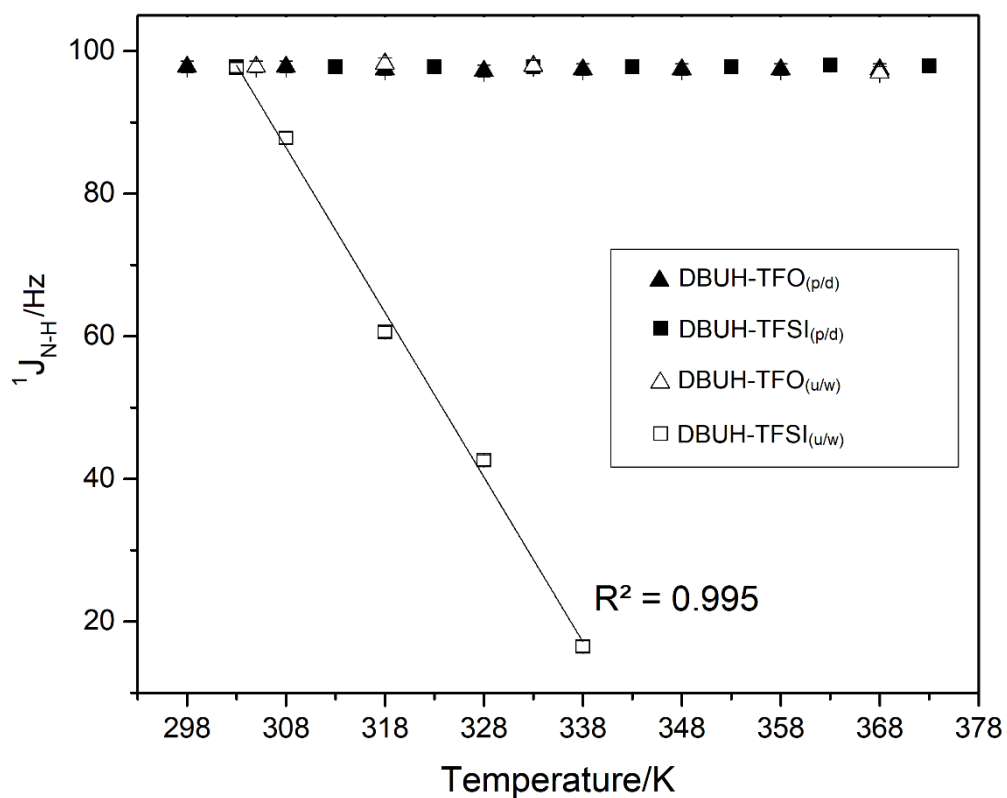
Figure 2.18. $^1J_{N-H}$ coupling constant for the purified and dried PILs and unpurified and dried PILs as a function of temperature measured via ^{15}N INEPT experiments.
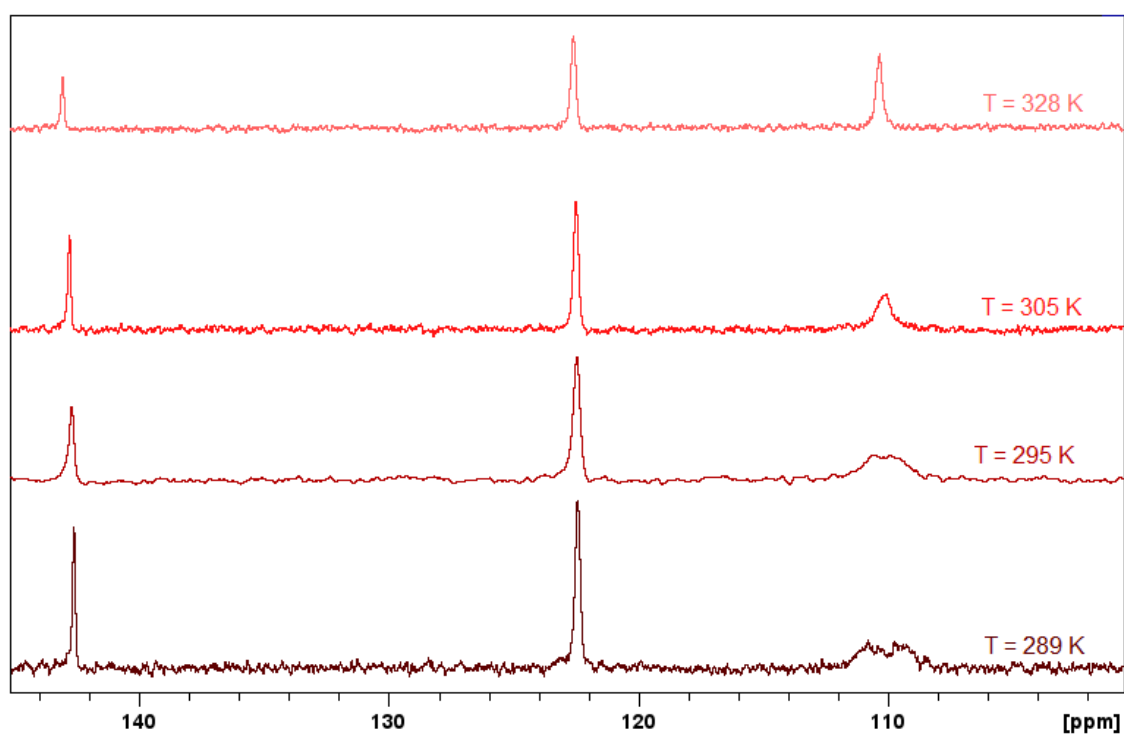
Figure 2.19. ^{15}N coupled NMR spectra of the sample DBUH-IM14$_{(u/w)}$ as a function of temperature.

2.3.4. DSC analysis

The thermal analysis of the selected systems is of pivotal importance to know the boundary conditions in view of a target application, and even more in electrochemical storage devices. In the present thesis work, the thermal transitions of all the PILs were evaluated by means of DSC (Figure 2.20-2.22).
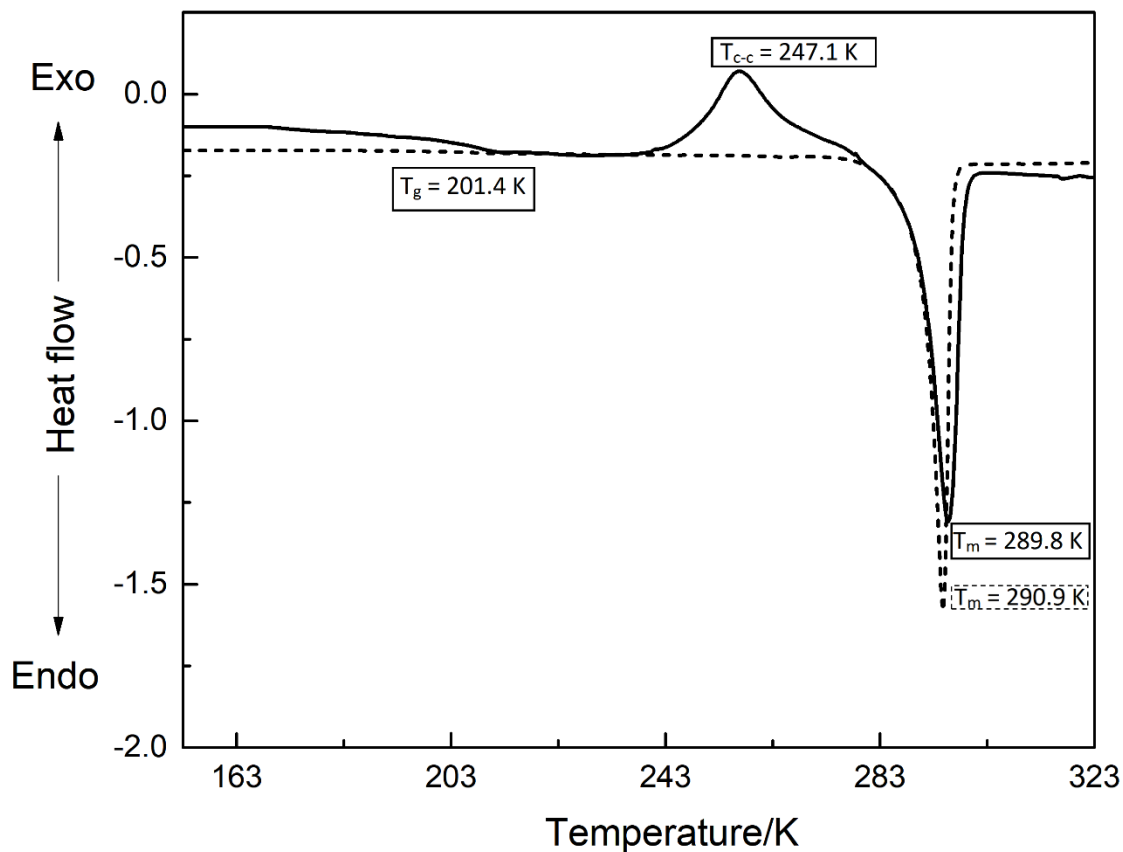
Figure 2.20. DSC traces of the DBUH-IM14 where the solid line represents the first heating scan and the dotted line represents the last heating scan after 3 full heating-cooling cycles, recorded at the scan rate 10 K.min^{-1}.
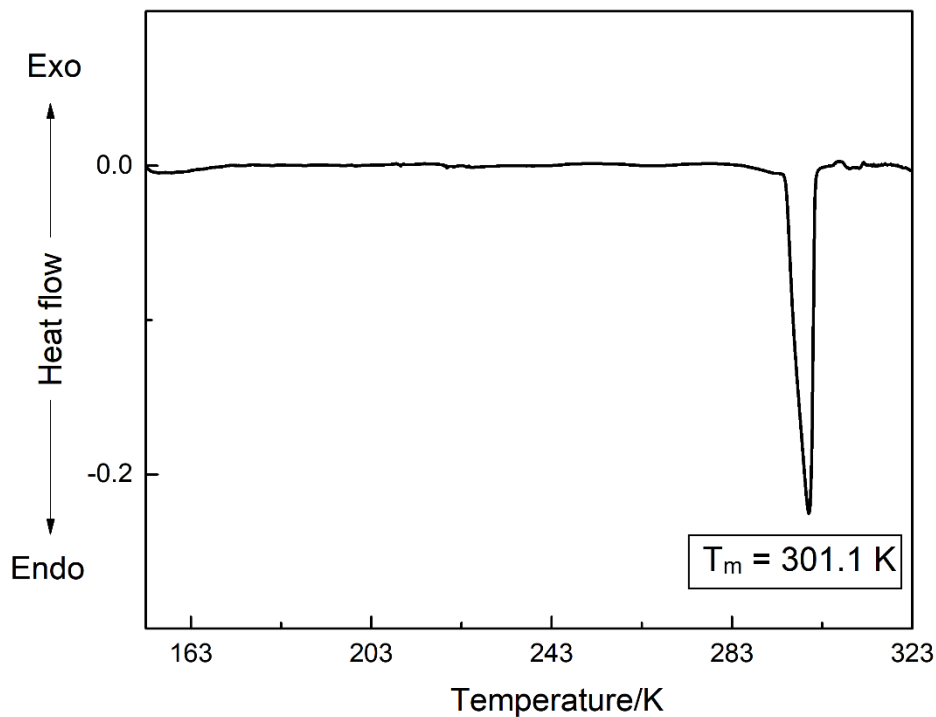
Figure 2.21. DSC trace of the DBUH-TFSI recorded at the scan rate 2 K.min^{-1}.
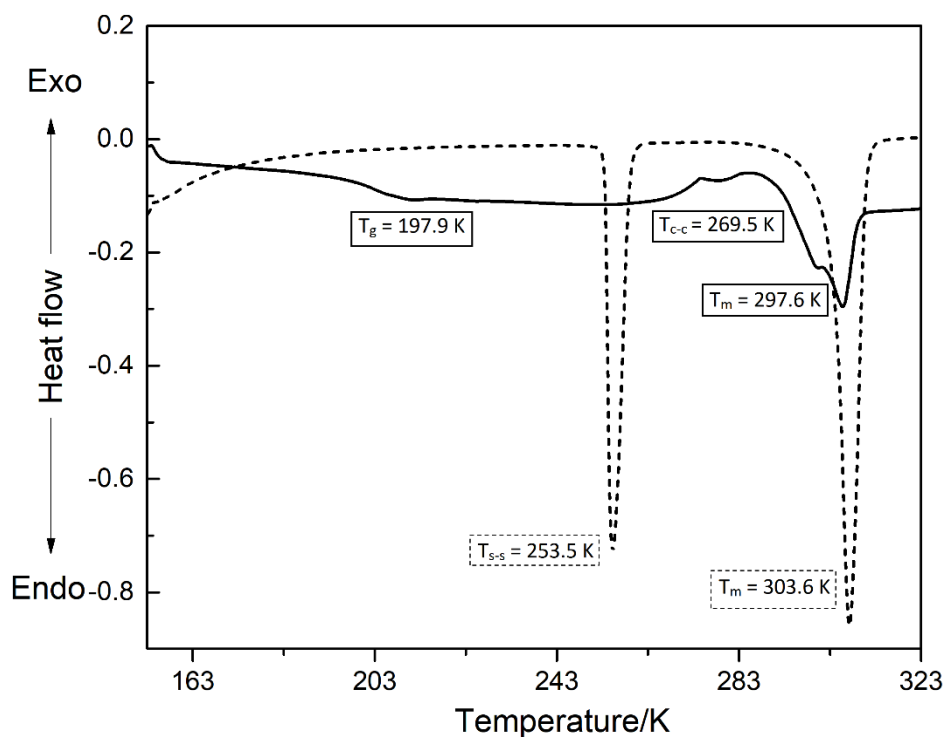
Figure 2.22. DSC traces of the DBUH-TFO where the solid line represents the first heating scan and the dotted line represents the last heating scan after 3 full heating-cooling cycles, recorded at the scan rate 10 K.min^{-1}.

Starting from the DBUH-IM14, the first heating scan shows a glass transition (T_g) at 201.4 K, followed by cold crystallization (T_{c-c}) at 247.1 K, and finally the melting transition at 289.8 K (Figure 2.20,

solid line). In the cold crystallization event, a subcooled liquid crystallizes upon heating above the glass transition state to a crystalline solid. In other words, at temperatures higher than T_g, the subcooled liquid actually crystallizes upon heating. Such thermal feature has already been reported in the case of some TFSI-containing ILs, whereas for IM14-based ILs having similar cations the cold-crystallization event was not detected[81]. The cold-crystallization event can be associated with the ability of the molecules to undergo rapid temperature-dependent conformational rearrangements[82]. For the DBUH-IM14, the cold-crystallization feature observed using a scan rate of 10 K.min^{-1}, may be related to its asymmetrical fluorine-containing chain organization (CF$_3$ and C$_4$F$_9$ moieties are located on the opposite sides of the di-alkyl-sulfonylimide frame) which confers to the system some conformational flexibility, as previously reported in the literature[49,83]. After applying refrigeration cycles, a fully crystalline system was achieved, suppressing the cold-crystallization feature. At those conditions (Figure 2.20, dotted line), the melting point of DBUH-IM14 was nearly equal to the previous one (T_m = 290.9 K).

It is worth highlighting that IM14-based ILs generally exhibit no solid-phase transition (i.e., no melting feature) as the uneven distribution of the fluorinated chains in the IM14$^-$ anion – i.e. C4 perfluorobutyl and C1 trifluoromethyl on the two sides of the (bis)sulfonylimide functional group – prevents the crystallization process[75]. For instance, IM14-based AILs having quaternary ethyl ammonium (Et$_4$N$_+$), N-ethyl-N-methyl imidazolium (EMI$_+$), and N-alkyl-N-methyl pyrrolidinium (PYR$_{1A+}$) as cations were reported to be unable to crystallize during the DSC analysis despite the repeated refrigeration cycles at low temperature, and only the glass transition feature could be detected in the range 193 K to 218 K. Probably, the different behavior between the DBUH-IM14 and the other IM14-based ILs is due to the higher hydrogen bonding capability of the PIL with respect to the conventional AILs.

DBUH-TFSI (Figure 2.21) does not undergo glass transition, at least under the presently chosen cooling rate (2 K.min^{-1}). This behavior is quite common for TFSI-based ILs and can be related to the symmetric nature of the anion geometry that easily drives the sample towards its crystalline phase. Here, the thermal profile of DBUH-TFSI (Figure 2.21) shows the melting at 301.1 K, in good agreement with the value 298.2 K reported by Miran et al.[46], considering the different scan rate used in the two cases. Given the distribution of the electronic charge, rather low melting points are generally observed for TFSI-containing AILs which are, generally, liquid at room temperature[75]. Nevertheless, DBUH-TFSI shows, so far, one of the lowest melting point reported for TFSI-based PILs, as indicated by the melting points of some representative PILs: pyrazinium-TFSI,T_m = 346 K; morpholinium-TFSI, T_m = 336 K;

pyridinium-TFSI, T_m = 333 K; tetramethylguanidinium-TFSI, T_m = 322 K, pyrrolidinium-TFSI, T_m = 307 K [48,84]). According to the literature, the variability between the melting point of TFSI-containing PILs may stems from the extent of H-bonding, in turn depending on the structure of the cations, which influences the ion-pair binding, and thus affects their phase transition temperature[48].

The DSC curves recorded for the DBUH-TFO (Figure 2.22) indicate that the thermal history of the sample substantially affects its thermal properties. The glass transition (T_g = 197.9 K) observed during the first heating scan (Figure 2.22, solid line) suggests that the sample tends to crystallize only at a slow cooling rate, and upon a cooling rate of 10 K.min^{-1} the glassy state is formed. The slightly different value of T_g (212.1 K) reported in the literature for the same sample[46] can be explained by the different thermal histories during the crystallization procedure (i.e., different cooling rates and isothermals treatments). Upon heating, above the glass transition, the supercooled liquid undergoes a cold crystallization (T_{c-c} = 269. 5 K) and finally melts at 297.6 K, which well matches the value of 296.2 K reported by Miran et al.[46]. To precisely determine the melting point of DBUH-TFO, refrigeration cycles were performed to fully crystallize the sample. The fully crystalline state was achieved once the glass transition and the cold crystallization features disappeared in the last heating scan (Figure 2.22, dashed line). The DSC trace reveals a solid-solid phase transition at 253.5 K. A similar thermal event has been already reported in the case of TFO-based ILs[85]. Finally, the sample undergoes melting at 303.6 K. The increase of 7.7 K in the melting point when the sample is fully crystallized can be related to the reduction of the mobility of the ions due to the confinement effect produced by the crystallization, and the highly oriented hydrogen bonds into this PIL[50,76].

Table 2.3 summarizes the temperatures of the phase transitions events obtained for the studied PILs. A comparison of the different melting temperatures of the three PILs indicates that the ion sizes and the intermolecular interactions play a significant role on the phase transition temperature. In the fully crystalline state, the melting temperature follows the order DBUH-TFO > DBUH-TFSI > DBUH-IM14. Considering the nature of the intermolecular interactions on these PILs, one would expect a similar melting point for the DBUH-TFSI and DBUH-IM14. However, a crucial aspect is introduced here by the large and asymmetrical IM14$^-$ anion, because it hinders lattice formation, consequently decreasing the melting temperature of the system[86]. From a practical point of view, DBUH-IM14 has a plus in respect to the other systems because it is liquid at room temperature. This feature expands its possible range of applications, especially as non-volatile electrolyte component[87] in electrochemical devices.

Table 2.3. Summary of the temperatures of phase transitions events obtained for the studied PILs using DSC.

PIL	T_g (K)	T_{c-c} (K)	T_{s-s} (K)	T_m (K)
DBUH-TFO	197.9	269.5	253.5[a]	297.6[b]; 303.6[c]
DBUH-TFSI	-	-		301.1
DBUH-IM14	201.4	247.1		289.8[b]; 290.9[c]

[a] Solid-solid transition temperature obtained in the last heating scan after 3 full heating-cooling cycles; [b] melting point obtained in the first heating scan; [c] melting point obtained in the last heating scan after 3 full heating-cooling cycles.

2.3.5. TGA analysis

It is known that the state-of-the-art organic carbonate solvents used as electrolyte components in LIBs possess poor thermal stability, thus causing safety issues[88]. Then, when selecting and/or designing PILs as electrolyte components, a fundamental property of the chosen system is its thermal stability. In this thesis, the degradation temperature (T_d) of the selected PILs was accessed by means of thermogravimetric analysis in nitrogen and synthetic air atmospheres (Figures 2.23-2.24 and Table 2.4).
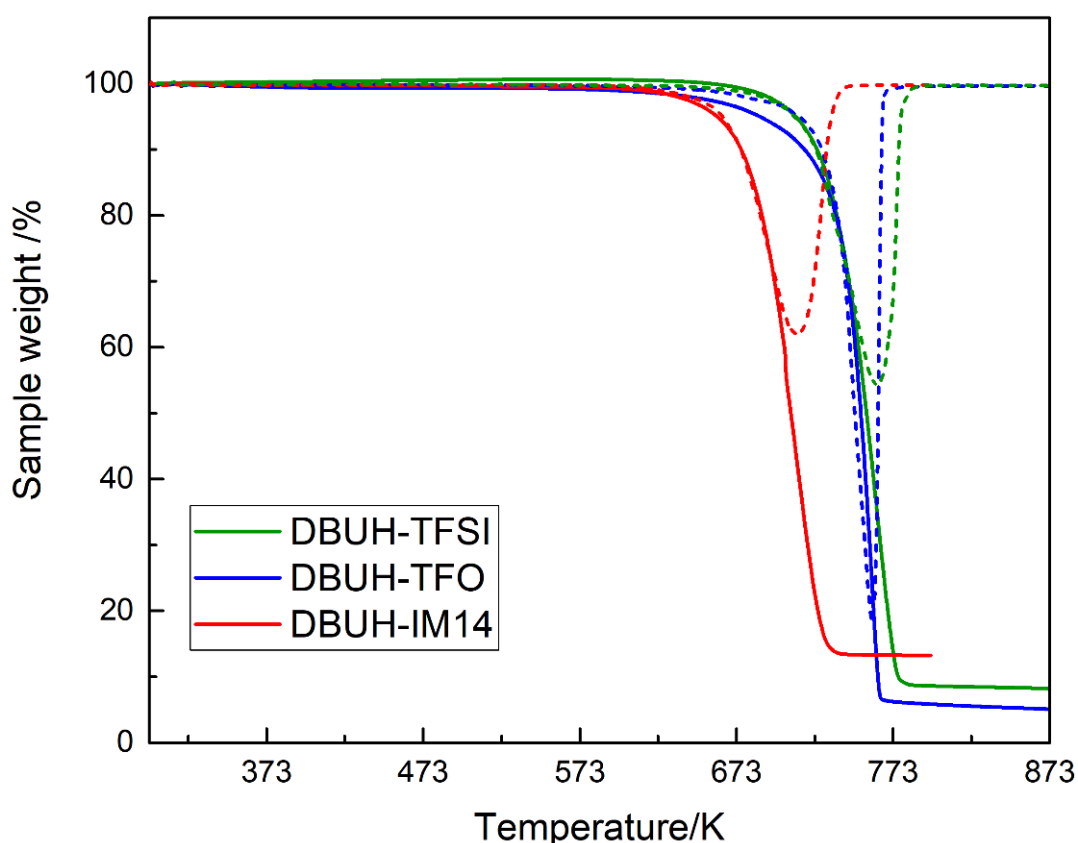
Figure 2.23. Dynamic TGA of the studied PILs in nitrogen performed using heating rate of 10 K.min^{-1} under N_2 atmosphere. Dashed lines correspond to the DTG curves.
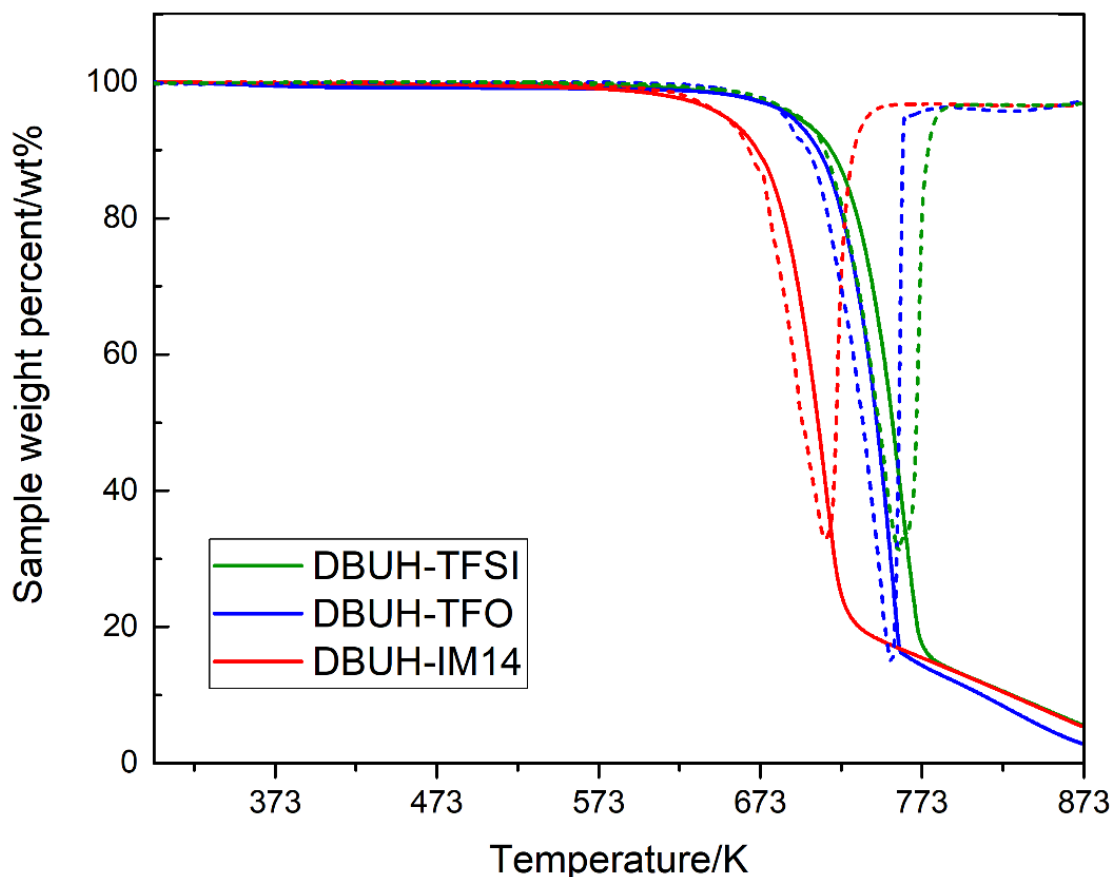
Figure 2.24. Dynamic TGA of the studied PILs in nitrogen performed using heating rate of 10 K.min^{-1} under synthetic air atmosphere. Dashed lines correspond to the DTG curves.

The thermograms of Figs. 2.23 and 2.24 show that, in both atmospheres, the decomposition process occurs around 710 K for DBUH-IM14 and 760 K for DBUH-TFSI and DBUH-TFO. The reported thermograms also show that the presence of oxygen (as in the air atmosphere tests) has almost no effect on the T_d of the PILs (maximum discrepancy equal to 7 K, see Table 2.4), in line with other examples of ILs from the literature[89,90]. According to the literature, the almost negligible effect of oxygen on the degradation temperature of ILs may be due to the short exposure time (i.e., 1 hour of exposure using a scan rate of 10 K.min^{-1}) and the lower reactivity of the material itself with the oxidative atmosphere[91].

Considering the degradation temperature obtained in this thesis and the values available in the literature[46], it is clear that the PILs synthesized and purified following the previous protocol *(Section 2.2.2)* show a significantly increased thermal stability. For instance, the values of the T_d measured in this thesis for purified DBUH-TFO and DBUH-TFSI are 49 and 36 K higher than the corresponding values reported in the literature (see Table 2.4 for bibliographic reference). This difference might be due to the different impurities content of the samples which we may speculate having a catalytic effect on the decomposition process[68]. Overall, these data support

the qualitative evaluation reported in *Section 2.3.1* and underlines the relevance of the application of a strict protocol for the purification of the PILs as described in *Section 2.2.2*.

For the PILs investigated, the thermal stability follows the order DBUH-TFSI ≈ DBUH-TFO > DBUH-IM14. In the literature, it is already stated that TFSI⁻ anion confers the highest thermal stability to the ILs, although some TFO-based ILs also have excellent thermal stability[89]. The high thermal stability found for DBUH-TFSI may be related to the relatively bulky structure and delocalized electron density of the TFSI⁻ anion[92], whereas in the case of DBUH-TFO the stronger hydrogen bonds into the system may be playing a significant role on raising its thermal stability[46,49].

Surprisingly, DBUH-IM14 was the least thermally stable system. Given DBUH-IM14 is characterized by a degree of proton transfer as high as DBUH-TFSI (*Section 2.3.2*), comparable temperatures of degradation of these two systems are reasonably expected. Indeed, a correlation between T_d values and the ΔpK_a of PILs is reported in the literature[46]. However, in the case of DBUH-IM14, the perfluoroalkyl chains seem to play a crucial role in decreasing the lattice potential energy and consequently lowering the thermal stability. A lower thermal stability of IM14-based ionic liquids, as compared to the TFSI homologues (sharing the same cation), was also previously observed also in ammonium ILs[93]. Despite being the least thermally stable PIL investigated here, it is important to stress that DBUH-IM14 still displays a T_d far above 673 K (400 °C), which enables its usage in high-temperature applications, including energy storage devices.

The results obtained with TGA not only provide a ranking of the thermal stability of the examined PILs, but also give information on how the structural features and the intermolecular interactions may affect the thermal stability of the materials. However, it should be pointed out that the generally fast scan rate used in the measurements may lead to an overestimation of the real degradation temperature[90]. To further investigate the thermal behavior of the PILs under prolonged heating time, isothermal TGA experiments were performed in synthetic air (Figure 2.25). The results reveal lower stability of the PILs with respect to that obtained by the dynamic TGA experiments, with a difference of more than 150 K (Table 2.4). More in detail, a practical weight loss (higher than 3% wt) is observed already above 548 K, 573 K and 573 K for DBUH-IM14, DBUH-TFO, and DBUH-TFSI, respectively. Still, the degradation temperature of the studied PILs is in the same range of the AILs[90,94], confirming that they are a suitable alternative for applications requiring inert systems at very high temperatures.
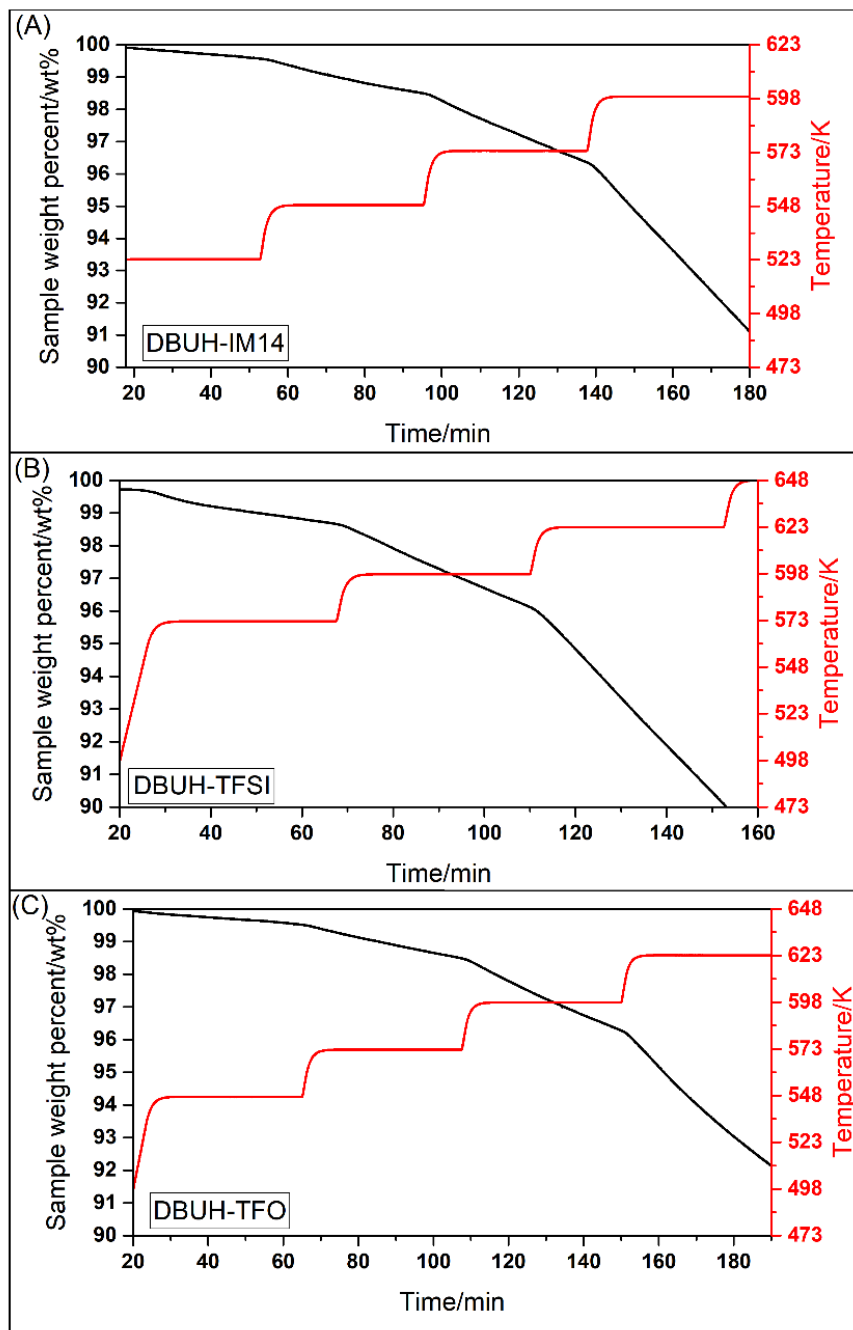
Figure 2.25. Isothermal TGA of the studied PILs samples in synthetic air.

Table 2.4. Summary of the degradation temperatures of the PILs investigated here, obtained using different techniques.*

PIL	$T_{d(air)}$ (K)	$T_{d(N2)}$ (K)	$T_{d(ISO-TGA)}$ (K)	T_{d-ref} (K)
DBUH-TFSI	762	760	573	724
DBUH-TFO	760	753	573	704
DBUH-IM14	712	713	548	

$T_{d(air)}$ corresponds to the degradation temperature obtained under synthetic air atmosphere; $T_{d(N2)}$ corresponds to the degradation temperature obtained under nitrogen atmosphere; $T_{d(ISO-TGA)}$ corresponds to the degradation temperature obtained by isothermal TGA (where 3% of weight loss was detected); T_{d-ref} corresponds to the degradation temperature reported in the literature obtained in N_2 atmosphere [46].

45

2.3.6. Density measurements

The density (ρ) of the studied PILs was measured as a function of temperature. The experimental values are presented in Table 2.5 and plotted in Figure 2.26. For all the PILs, the density was fitted to a linear equation in the range of temperature evaluated, showing a decrease with increasing temperature (best-fit parameters are reported in Table 2.6).

For the DBUH-IM14, a graphical comparison between the experimental data and the available literature reveals almost no difference[76]. Indeed, the deviations from those data are lower than the standard uncertainty of the measurement (0.001 g.cm^{-3}). Conversely, the density values of DBUH-TFO and DBUH-TFSI reported by Miran et al.[46] show a considerable deviation from those reported in the present thesis (0.005 g.cm^{-3} at 298 K and around 0.01 g.cm^{-3} at 308 K for DBUH-TFO; 0.018 at 308 K for DBUH-TFSI). These differences may stem from a different purification treatment of the PILs, since the presence of impurities frequently reduces the density of ionic liquids[95].

For the DBU-based PILs investigated here the densities decreased in the order [IM14$^-$] > [TFSI$^-$] > [TFO$^-$]. This trend supports the statement that the nature of the anion influences the density of an ionic liquid[96]. Indeed, DBUH-IM14, the only PIL liquid at room temperature, shows the higher density due to its ion-pair packing ability, which prevents an ordered electrostatic net structure as a result of its steric hindrance [76].

Table 2.5. Densities values of the PIL samples.*

	DBUH-IM14	DBUH-TFO	DBUH-TFSI	
Temperature (K)	Density (g.cm^{-3})	Density (g.cm^{-3})	Temperature (K)	Density (g.cm^{-3})
298.15	1.580	1.349	308.15	1.470
308.15	1.570	1.341	313.15	1.466
318.15	1.559	1.334	318.15	1.461
328.15	1.548	1.326	323.15	1.457
338.15	1.538	1.318	328.15	1.452
348.15	1.527	1.310	333.15	1.448
358.15	1.516	1.302	338.15	1.443
			343.15	1.439
			348.15	1.434
			353.15	1.430
			358.15	1.425
			363.15	1.421
			368.15	1.416

* Standard uncertainties are 0.05 K and 0.001 g.cm^{-3} for the temperature and densities, respectively.
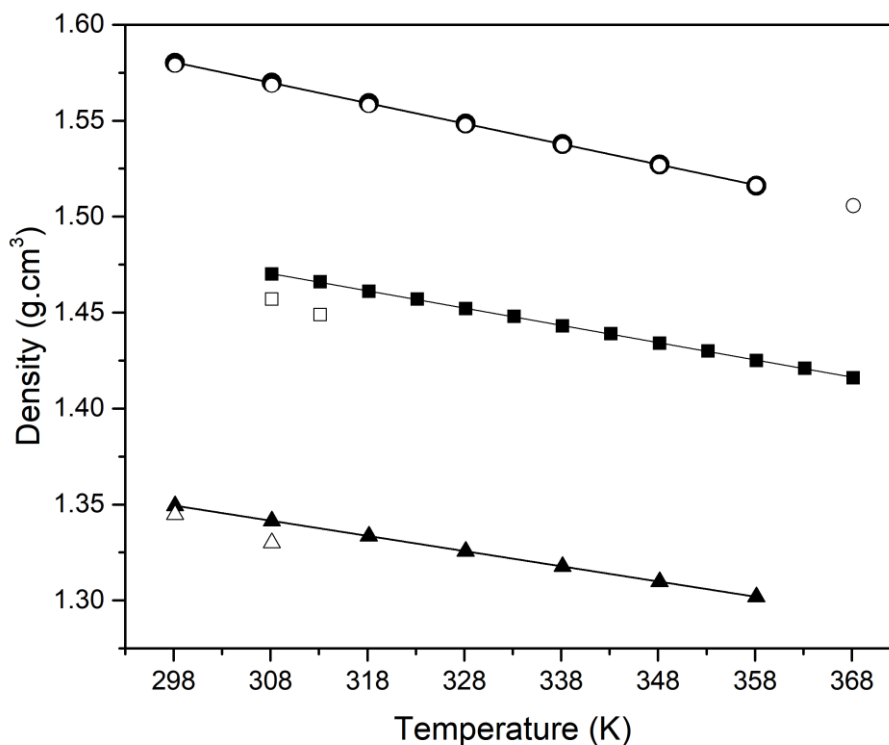
Figure 2.26. Densities of the PILs (■) DBUH-TFSI (●) DBUH-IM14 and (▲) DBUH-TFO, as a function of temperature. The values for (□)DBUH-TFSI (○) DBUH-IM14 and (Δ) DBUH-TFO correspond to the values fitted from the literature [46]. Standard uncertainties for the temperature and densities are 0.05 K and 0.001 g.cm^{-3}, respectively.

Table 2.6. Linear fit parameters of the density of the studied PILs.

		$\rho = \rho_0 - aT(K)$			
PIL	T range (K)	a (g.cm^3. K^{-1})	ρ_0 (g.cm^3)	R^2	M (g.mol^{-1})
DBUH-IM14	298 - 358	$10.7 \cdot 10^{-4}$	1.898	0.999	583.4
DBUH-TFSI	308 – 368	$9.00 \cdot 10^{-4}$	1.758	0.999	433.4
DBUH-TFO	298 – 358	$7.92 \cdot 10^{-4}$	1.586	0.999	302.3

2.3.7. Viscosity

It is well known that IL's viscosity is dependent on the ion-ion interactions, such as Coulombic and van der Waals interactions, and hydrogen bonding. Greater interactions lead to higher viscous systems [22].

In general, several factors act in determining the viscosity of PILs or AILs, and they can be summarized as follows:

(i) the viscosity increases with increasing alkyl chains length through stronger dispersive interactions[25];

(ii) the anion's charge delocalization, as in the case of (poly)fluorinated anions, decreases the viscosity by weakening hydrogen bonding network[97];

(iii) the changes on the structure of the anion have a far more marked effect on the viscosity than the same changes to the cation structure[97];

(iv) less viscous systems can be obtained through a very "malleable" charge network (i.e., the formation of positive−negative charge-alternating chains or networks)[98].

Here, the viscosity of the studied PILs is discussed in terms of their structural features and intermolecular interactions.

For all systems the viscosity decreases with increasing temperature (Table 2.7 and Figure 2.27). The temperature-dependence of the data is described by the Vogel–Fulcher–Tammann (VFT)[99] equation (Eq. 2.6).

$$\eta = \eta_o exp\left[\frac{B}{T - T_0}\right] \qquad (2.6)$$

where η_o (mPa.s), B (K), and T_0 (K) are adjustable parameters. The best-fit parameters are reported in Table 2.8.

Table 2.7. Viscosity data of the studied PILs.

	Viscosity (mPa.s)		
Temperature (K)	DBUH-IM14	DBUH-TFO	DBUH-TFSI
293	1364	3417	
298	881	2118	
303	592	1369	201
308	410	919	147
313	292	633	111
318	213	448	85
323	159	326	67
328	120	242	53
333	93	184	44
338	74	142	36
343	59	111	31
348	48	88	25
353	39	71	21
358	33	58	18
363	27	48	16
368	23	40	14
373	20	34	12

*Relative standard uncertainty of the viscosity is 0.08; standard uncertainty of the temperature is 0.5 K.

Table 2.8. VFT fit parameters of the viscosity of the studied PILs.

PIL	η_0 (mPa.s)	B (K)	T_0 (K)	R^2
DBUH-TFO	0.0604	1200.2	183.5	0.9999
DBUH-TFSI	0.0891	944.2	180.7	0.9999
DBUH-IM14	0.0605	1098.5	183.6	0.9999
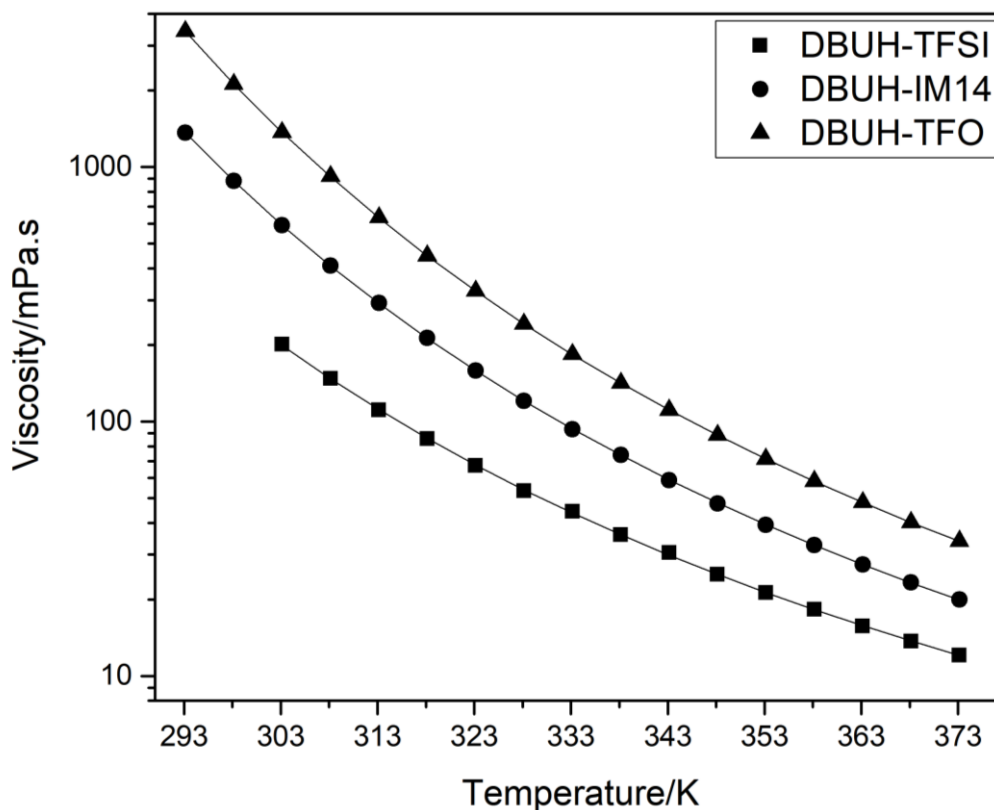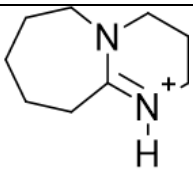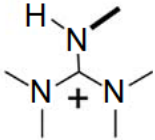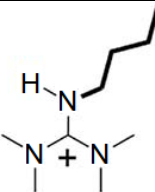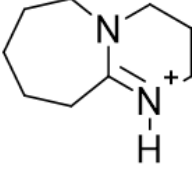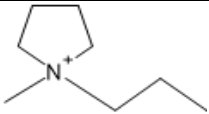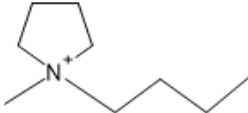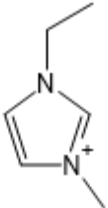
Figure 2.27. Viscosity of the PILs studied. Solid lines correspond to the VFT fitting.

The viscosity trend follows the order: DBUH-TFSI < DBUH-IM14 < DBUH-TFO, with DBUH-TFO 2.4 times more viscous than DBUH-IM14 at ambient temperature and almost 7 times more viscous than DBUH-TFSI at 303 K. If we take into account the interplay of the structural features and molecular interactions in concurring to the measured viscosity[100], the highest viscosity observed in the case of DBUH-TFO can be ascribed to the strong hydrogen bonds between the protonated DBU-cation and the triflate anion[76]. Such strong interactions also explain the higher viscosity reported in the literature for AILs containing the triflate anion TFO[-] with respect to the analogues having the sulfonylimide anion TFSI[-] (Table 2.9A)[84].

The comparison of DBUH-TFSI to DBUH-IM14 is interesting, as those two PILs have comparable hydrogen bonding properties. A viscosity increase is observed with increasing the anion size (i.e., on passing from TFSI[-] to IM14^{-}), thus reflecting again the key role played by the structural features of the large IM14^{-} anion with

uneven fluorine-pool distribution and its capability to generate perfluorocarbon domains[83]. The same effect has been reported in the literature in AILs having either TFSI⁻ or IM14⁻ as the anion (see Table 2.9B). For a given cation, a 4-fold to 6-fold increase in viscosity has been observed at 293 K on passing from TFSI to IM14[75].

Table 2.9. Comparison of viscosity data of DBU-based PILs with selected AILs with structural similarities at specified T.

A. Comparison AILs vs PILs with triflate or sulfonylimide anion (effect of H-bond)				
PIL	Viscosity (mPa.s)	T (K)	Reference	Cation Structure
DBUH-TFSI	201	303	Present work	
DBUH-TFO	1369	303	Present work	
DBUH-TFO	2118	298	Present work	
C₁HTMG-TFSI	66.4	298	[84]	
C₁HTMG-TFO	171.4	298	[84]	
C₄HTMG-TFSI	88.2	298	[84]	
C₄HTMG-TFO	233.9	298	[84]	

B. Comparison AILs vs PILs with sulfonylimide anions (effect of fluorous domains)				
AIL	Viscosity (mPa.s)	T (K)	Reference	Cation Structure
DBUH-TFSI	201	303	Present work	
DBUH-IM14	592	303	Present work	
DBUH-IM14	1364	293	Present work	
PYR₁₃-TFSI	72.0	293	[75]	
PYR₁₃-IM14	300	293	[75]	
PYR₁₄-TFSI	95.0	293	[75]	
PYR₁₄-IM14	560	293	[75]	
EMI-TFSI	36.0	293	[75]	
EMI-IM14	150	293	[75]	

2.3.8. Ionic and molar conductivities

Given the relevance of high charge transport for electrochemical applications, a deep understanding of the features governing the ionic conductivity (σ) of the selected PILs is crucial to optimize their application as electrolyte components. In the present thesis work, the mobility of ionic carriers was investigated using electrochemical impedance spectroscopy (EIS) and the obtained data are reported in Table 2.10 and Figure 2.28.

Below the melting point, the DBU-based PILs showed low ionic conductivity in the range of 10^{-7} S.cm^{-1} (i.e., σ(DBUH-IM14) = 7.51·10^{-7} at 288 K; σ(DBUH-TFO) = 4.61·10^{-7} at 298.15 K and σ(DBUH-TFSI) = 7.03·10^{-7} at 308.15 K). A sharp increase of the specific conductivity indicates the complete melting of the PILs samples, as previously observed for some bis(perfluoroalkylsulfonyl)imide-based ionic liquids[75].

The investigated DBU-based PILs show good ionic conductivity (i.e., in the order of 10^{-3} S.cm^{-1} at 328 K) comparable to other PILs and AILs reported in the literature [84,101,102]. Here is worth pointing out that DBUH-IM14 is the only system within the set of PILs studied in this thesis showing a considerable high ionic conductivity (10^{-4} S.cm^{-1}) at 298 K. This value is comparable to the specific conductivity of IM14-based AILs and it can be appealing for electrochemical applications at reduced temperatures[75].
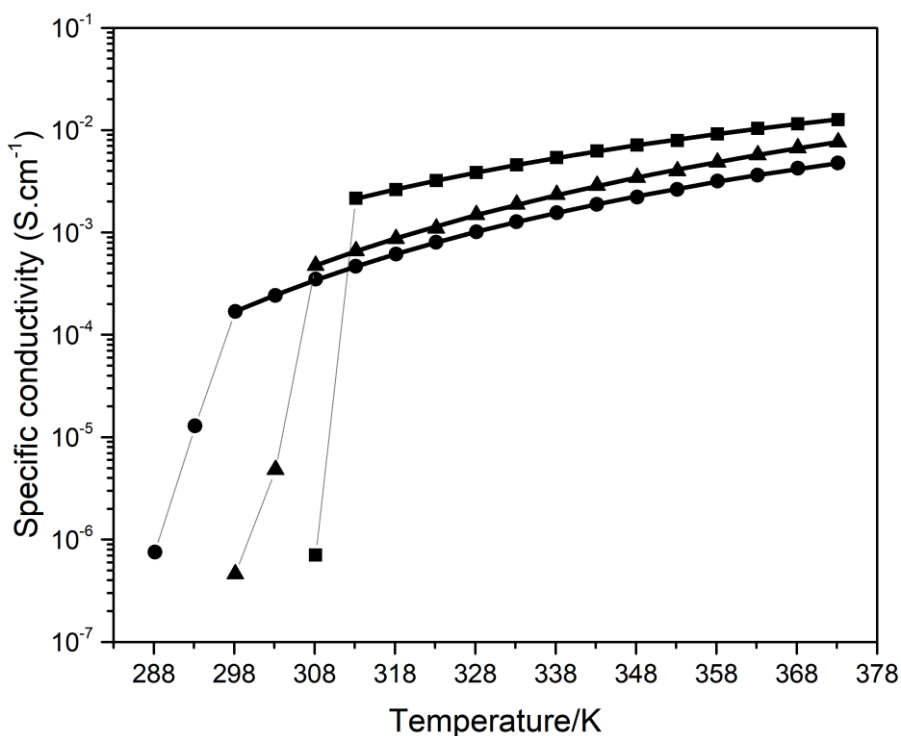
Figure 2.28. Specific conductivity σ of the PILs (■) DBUH-TFSI (●) DBUH-IM14 and (▲) DBUH-TFO, as a function of temperature. Black solid lines correspond to the VFT fitting.

Table 2.10. Specific conductivity σ of the studied PILs.

Temperature (K)	Specific conductivity (S.cm^{-1})		
	DBUH-IM14	DBUH-TFO	DBUH-TFSI
288.15	$7.51 \cdot 10^{-7}$		
293.15	$1.29 \cdot 10^{-5}$		
298.15	$1.69 \cdot 10^{-4}$	$4.61 \cdot 10^{-7}$	
303.15	$2.42 \cdot 10^{-4}$	$4.81 \cdot 10^{-6}$	
308.15	$3.50 \cdot 10^{-4}$	$4.78 \cdot 10^{-4}$	$7.03 \cdot 10^{-7}$
313.15	$4.68 \cdot 10^{-4}$	$6.61 \cdot 10^{-4}$	$2.15 \cdot 10^{-3}$
318.15	$6.15 \cdot 10^{-4}$	$8.71 \cdot 10^{-4}$	$2.62 \cdot 10^{-3}$
323.15	$8.02 \cdot 10^{-4}$	$1.10 \cdot 10^{-3}$	$3.21 \cdot 10^{-3}$
328.15	$1.01 \cdot 10^{-3}$	$1.49 \cdot 10^{-3}$	$3.85 \cdot 10^{-3}$
333.15	$1.27 \cdot 10^{-3}$	$1.89 \cdot 10^{-3}$	$4.58 \cdot 10^{-3}$
338.15	$1.55 \cdot 10^{-3}$	$2.35 \cdot 10^{-3}$	$5.38 \cdot 10^{-3}$
343.15	$1.88 \cdot 10^{-3}$	$2.87 \cdot 10^{-3}$	$6.23 \cdot 10^{-3}$
348.15	$2.22 \cdot 10^{-3}$	$3.45 \cdot 10^{-3}$	$7.13 \cdot 10^{-3}$
353.15	$2.63 \cdot 10^{-3}$	$3.98 \cdot 10^{-3}$	$7.92 \cdot 10^{-3}$
358.15	$3.18 \cdot 10^{-3}$	$4.85 \cdot 10^{-3}$	$9.17 \cdot 10^{-3}$
363.15	$3.62 \cdot 10^{-3}$	$5.73 \cdot 10^{-3}$	$1.04 \cdot 10^{-2}$
368.15	$4.22 \cdot 10^{-3}$	$6.71 \cdot 10^{-3}$	$1.15 \cdot 10^{-2}$
373.15	$4.75 \cdot 10^{-3}$	$7.65 \cdot 10^{-3}$	$1.27 \cdot 10^{-2}$

* Relative standard uncertainty of the specific conductivity is 0.1; standard uncertainty of the temperature is 0.05 K.

In the temperature range in which the samples are in the liquid state, the temperature dependencies of the ionic conductivity (σ) follow the VFT equation (Eq.2.7) (typical of IL materials)[75]:

$$\sigma = \sigma_0 \exp\left[\frac{-B}{T - T_0}\right] \qquad (2.7)$$

where σ_0 (S cm^{-1}), B (K), and T_0 (K) are adjustable parameters. The best-fit parameters for the VFT model of the specific conductivity data are listed in Table 2.11, while the graphical representation of the experimental and fitted data is shown in Figure 2.28 as black solid lines.

Table 2.11. VFT fit parameters of the ionic conductivity σ.

PIL	T range (K)	σ_0 (S.cm^{-1})	B (K)	T_0 (K)	R^2
DBUH-TFSI	313 - 373	0.50	674.12	189.51	0.999
DBUH-TFO	308 – 373	1.30	950.27	188.02	0.999
DBUH-IM14	298 – 373	0.45	806.86	195.77	0.999

When the samples are in the liquid state, their specific conductivity decreases in the order DBUH-TFSI > DBUH-TFO > DBUH-IM14, which is not in line with the fluidity (reciprocal viscosity, η^{-1}) trend DBUH-TFSI > DBUH-IM14 > DBUH-TFO (*Section 2.3.7*). Hence, lower ionic conductivity is detected in the bulk liquid of DBUH-IM14 when compared to DBUH-TFO, despite the higher fluidity of the former. Note that the assumption of the direct proportionality between the conductivity and the fluidity was proposed for fully dissociated ions, and recently, MacFarlane et al.[103] pointed out that the ion size factor should also be considered. Clearly, the long and asymmetrical fluorinated chain of IM14$^-$ plays a crucial role in lowering the ionic conductivity of this PIL.

Once obtained the ionic conductivity and the density of the PILs, I extend the evaluation to their molar conductivity (Λ) via Eq. (2.8):

$$\Lambda = \frac{\sigma}{\rho} MM \qquad (2.8)$$

where MM is the molar mass, σ is the specific conductivity and ρ is the density of the PIL. Results obtained for the estimated molar conductivity are reported in Table 2.12 and Figure 2.29.

Table 2.12. Molar conductivity Λ of the studied PILs.*

Temperature (K)	Molar conductivity (S.cm^2.mol^{-1})		
	DBUH-IM14	DBUH-TFO	DBUH-TFSI
298.15	0.060		
303.15	0.086		
308.15	0.130	0.108	
313.15	0.175	0.149	0.635
318.15	0.230	0.197	0.777
323.15	0.301	0.251	0.955
328.15	0.382	0.340	1.150
333.15	0.479	0.432	1.370
338.15	0.589	0.540	1.616
343.15	0.715	0.660	1.875
348.15	0.847	0.797	2.155
353.15	1.008	0.922	2.400
358.15	1.223	1.127	2.788
363.15	1.401	1.335	3.163
368.15	1.638	1.568	3.509
373.15	1.849	1.792	3.885

*Relative standard uncertainty of the specific conductivity is 0.12; standard uncertainty of the temperature is 0.05 K.

The VFT model (Equation 2.9) can also describe the molar conductivity when the density shows a linear dependence with temperature[84].

$$\Lambda = \Lambda_0 \exp\left[\frac{-B}{T - T_0}\right] \tag{2.8}$$

with Λ_o (S.cm^2.mol^{-1}), B (K), and T$_0$ (K) adjustable parameters. The best-fit VFT parameters for the molar conductivity of the studied DBUH-PILs are listed in Table 2.13 and the fit curves are plotted in Figure 2.29.

Table 2.13. VFT fit parameters of the molar conductivity Λ.

PIL	T range (K)	Λ_o (S.cm^2.mol^{-1})	B (K)	T$_0$ (K)	R^2
DBUH-TFSI	313 – 373	182.4	719.1	185.9	0.999
DBUH-TFO	308 – 373	358.7	992.2	185.7	0.999
DBUH-IM14	298 – 373	164.1	779.6	199.5	0.999
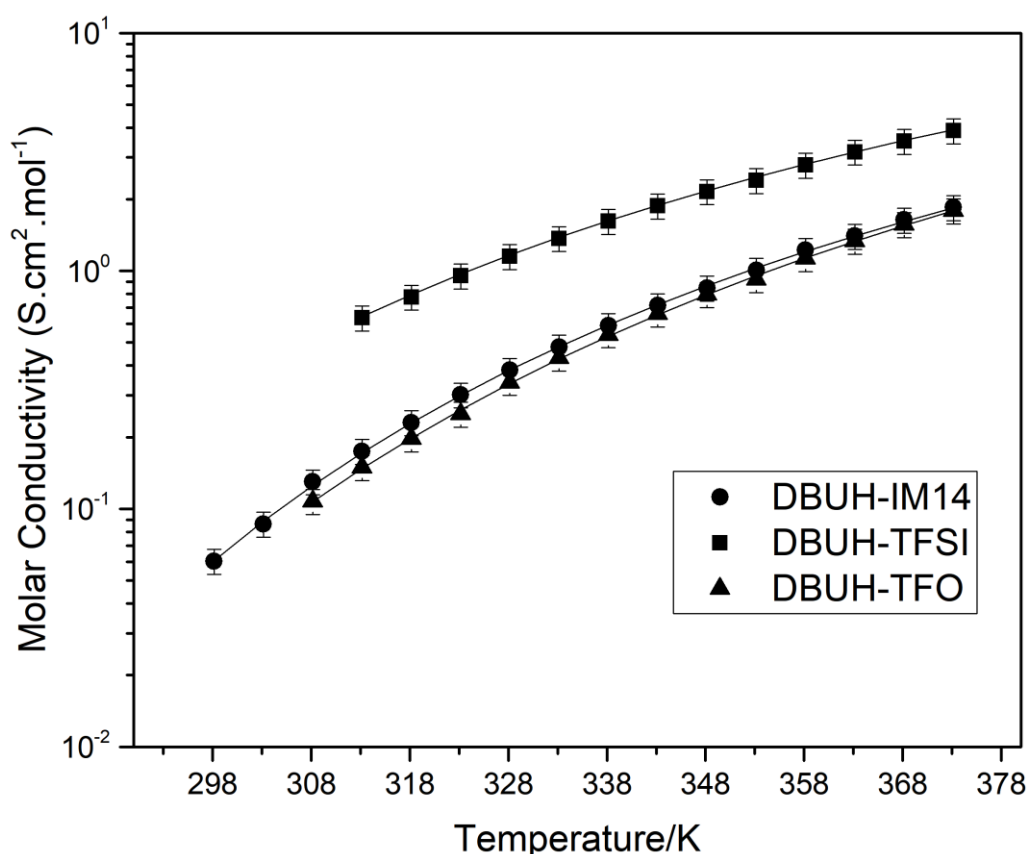
Figure 2.29. Molar conductivity Λ of the studied PILs.

The molar conductivity of the PILs studied follows the order DBUH-TFSI > DBUH-IM14 ≈ DBUH-TFO (Figure 2.29). Although DBUH-IM14 has lower viscosity than DBUH-TFO, both systems show a comparatively similar molar conductivity. Again, this fact may be related to the nature of the IM14$^-$ anion. Accordingly, despite DBUH-IM14 shows a softer H-bond network[76], long-range attractive

dispersive interactions among the fluorous tails[83] may be causing a decreasing on its molar conductivity. The net balance provides a comparable molar conductivity in the two cases, and a clear indication that the molecular volume, the structure, and the nature of interaction of the anions strongly influence the macroscopic property of this class of PILs.

2.3.9. The Walden Rule

A convenient way to get deeper insights into the transport properties of ILs is using the Walden rule [70]. Although the Walden rule is based on empirical observations of the properties of dilute aqueous solutions, it has been applied to describe the dynamic behavior of ILs[103]. According to the Walden rule, the liquid viscosity offers frictional resistance to charge mobility and consequently, the molar conductivity of a solution is proportional to its fluidity. Hence, in a log-log plot of molar conductivity (Λ) vs. fluidity (η^{-1}) (the "Walden plot"), this rule predicts a straight line according to Equation 2.9[70]:

$$\log \Lambda = \log C + \log \eta^{-1} \qquad (2.9)$$

where C is a constant.

Typically, a 0.01 M KCl solution is used as a calibration point (ideal situation), and the other electrolytes are compared with this "ideal" behavior. The choice of a 0.01 M KCl solution was arbitrary, and for such a case, the ions are considered well-dissociated and approximately equally mobile. Recently, it has been demonstrated that this concept should be applied with caution, especially in the case of ILs[103,104]. Still, deviations from the ideal line, termed ΔW, are taken as a convenient way to qualitatively access the ionicity (I_W) of an ionic system, i.e., the effective fraction of ions participating in the conduction process, according to Equation 2.10 [103,105]:

$$I_w = \frac{\Lambda_M}{\Lambda_M^0} = \frac{\Lambda_M}{1/\eta} = 10^{-\left(\log\frac{1}{\eta} - \log\Lambda\right)} = 10^{\Delta W} \qquad (2.10)$$

I_w values below unity indicates a reduction in the ionic character of the system compared to the ideal behavior of a 0.01 M KCl solution. Most ionic liquids fall below the line, and many PILs have I_w far below unity, i.e. highly deviating from the behavior of an ideal electrolyte system[103]. It should be noted that unreliable ionicity values can sometimes be found via the Walden rule, due to different factors such as the presence of aggregates[106,107], interacting ions present in the liquid structure[108], charge transfer between cation and anion[109], and anti-correlation motions[110].

Here the Walden plot and the ionicity values of the studied PILs are reported in Figure 2.30 and Table 2.14.
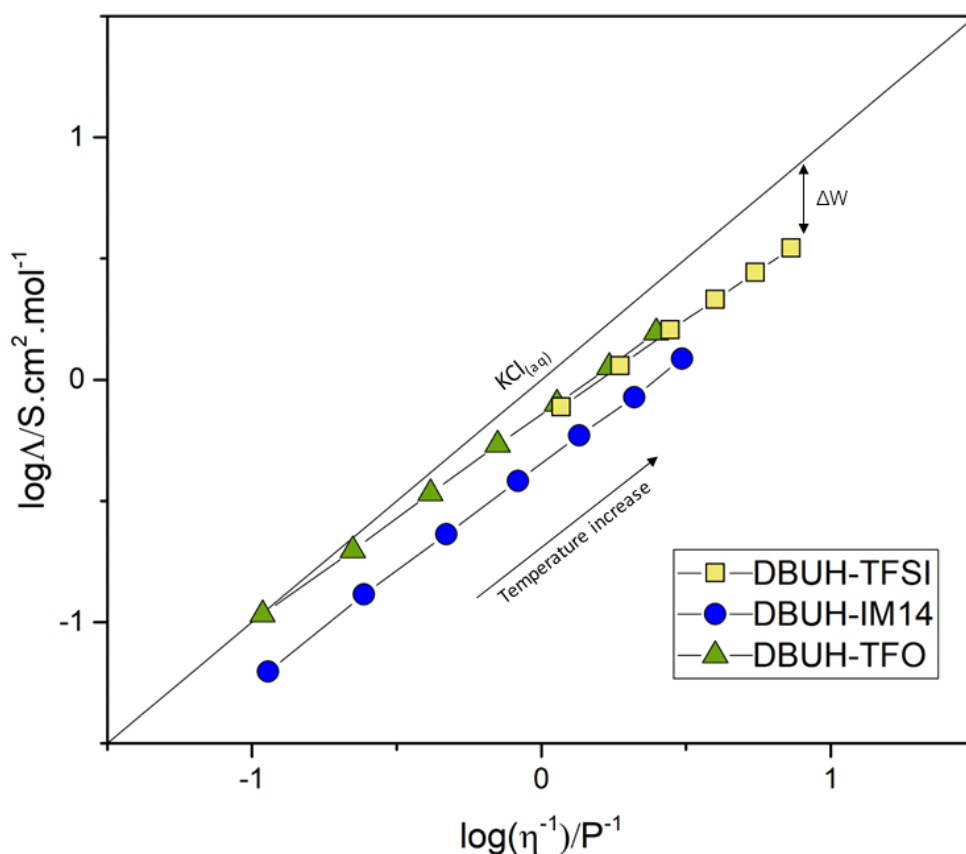
Figure 2.30. The Walden plot of the studied PILs.

Table 2.14. Ionicity values (I_w) estimated by the Walden approach for the studied PILs.

Temperature (K)	DBUH-TFO	DBUH-TFSI	DBUH-IM14
298			0.55
308	0.99		0.53
318	0.88	0.66	0.49
328	0.82	0.61	0.46
338	0.76	0.58	0.44
348	0.70	0.54	0.40
348	0.66	0.50	0.40
368	0.63	0.48	0.38

It can be observed that DBUH-TFO ($0.63 < I_w < 0.99$) and DBUH-TFSI ($0.48 < I_w < 0.66$) are more ionic systems than DBUH-IM14 ($0.38 < I_w < 0.55$).

When comparing DBUH-IM14 with DBUH-TFSI - that is systems with similar intermolecular interactions (i.e., "soft" hydrogen bonds) - the large difference between their ionic behavior is quite surprising. This notable discrepancy may be directly associated with the structural features of the IM14⁻ anion. Particularly, the presence of like-ion anticorrelations (cation-cation and anion-anion) is known to influence the conductivity of the system lowering its ionicity[111]. Such anion-anion effects may be reasonably more significant in IM14⁻ based PILs, due its geometrical nature, steric hindrance and the presence of fluorous domains via anion-anion interactions[76]. Given the similarity between the two sulfonylimide anions in terms of hydrogen bond strength, such difference in terms of anion-anion interactions may explain the difference observed in the I_w values.

Another relevant observation is the high ionicity found for DBUH-TFO. Although most ILs fall below the ideal line in the Walden plot, unexpectedly, some of them lie close to it having a good ionicity. This is the case, for instance, of DBUH-TFO at 308 K, which exhibits I_w=0.99. These high I_w values are counterintuitive as this PIL has a strong hydrogen bonding network, which would intuitively lead to strong ion interactions, thus decreasing the ionicity[76]. This intermolecular feature and the following unusual behavior may represent a limitation for the faithful use of the Walden rule to describe the real ionicity in such a viscous system[103,107,109,112,113]. Actually, additional models have been proposed to describe the dynamics of ions in ILs. Among them is the fractional Walden rule, which is built by introducing an additional exponent (α) to Equation 2.9, as shown in Equation 2.11[104].

$$\log \Lambda = \log C' + \alpha \log \eta^{-1} \qquad\qquad (2.11)$$

From the fractional Walden rule, notably, the fits for all the PILs investigated in this thesis produced α values in the range of 0.82-0.89 (Table 2.15), as typically observed for a variety of ILs[103,104]. Considering that the fractional Walden model uses macroscopic parameters, it qualitatively accesses the overall performance of an IL. In other words, higher log(C') values are attributed to highly conductive and most fluid systems[84]. Looking to the fitting parameters reported in Table 2.15, this approximation does not apply to the DBU-based PILs studied here. Indeed, DBUH-TFO is the most viscous and least conductive system, yet it shows the smallest magnitude for the log(C') parameter.

The above findings clearly show the limitation of Walden plot approach applied to the three DBU-based PILs studied in this thesis. From the one side, like-ion correlations appear to be a key factor when dealing with sulfonylimine anions (TFSI⁻ and IM14⁻). On the other both the original and fractional Walden rules fail in estimating the ionicity in the PIL with the strongest hydrogen bonding network

(DBUH-TFO). This encouraged further investigation, as it will be described in the next chapter.

Table 2.15. Values of the fitted α parameter (R² > 0.999) of the Fractional Walden Plot model for the studied PILs.

Parameter	DBUH-TFO	DBUH-TFSI	DBUH-IM14
α	0.85	0.82	0.89
log (C′)	-0.144	-0.166	-0.349
R²	0.9999	0.9999	0.9998

2.4. Conclusions

Protic ionic liquids (PILs) have been proposed as promising materials for electrolyte components in energy storage devices. Still, understanding the key factors governing their physicochemical properties is crucial when selecting those alternative materials for electrochemical applications. To this end, this chapter presented a set of novel DBU-based PILs. Their molecular features and physicochemical properties were widely investigated from a structural, thermal, rheological, and electrochemical viewpoint.

The PILs were synthesized and efficiently purified through a strict protocol. The purification procedure turned out to be fundamental to guarantee the proper thermal stability of the final material. From ^{1}H and ^{15}N NMR measurements, the ΔpK_a of DBUH-IM14 was estimated as comparable to that of DBUH-TFSI (23.4), and so far, this value is among the highest ΔpK_a reported in the literature. High ΔpK_a is a crucial parameter when accessing the proton transfer during the PIL formation. Indeed, all the systems studied showed a thermally stable N-H bond between the imino nitrogen of the DBU and the acidic proton, confirming that the status of protonation remains stable at elevated temperatures. By coupling constant measurements, it was shown that the N-H bond between the DBU base and the acidic proton is thermodynamically and kinetically stable under anhydrous conditions. However, the presence of water traces significantly influences the residence time of the acidic proton only in the imide-based PILs. This last finding experimentally confirms a distinct effect of water traces on the PIL according to the nature of the anion (triflate vs. sulfonylimide). From those results, it emerges the crucial role played by the anion on the intermolecular features of the selected PILs.

The thermal properties of the DBU-based PILs were also experimentally accessed. Firstly, the DSC analysis confirmed that DBUH-IM14 is the only system liquid at room temperature whereas

DBUH-TFO, apparently liquid, is actually in a glassy state. In perspective applications of the selected PILs as safer electrolyte components, their thermal stability was determined via TGA analysis. The three DBU-based PILs showed a very high thermal stability (i.e., $T_d > 710$ K), with a practical weight loss observed at least above 548 K. Consequently, all of the studied PILs can be considered eligible for high-temperature applications. The distinct thermal features of the selected DBU-based PILs also confirm that their thermal properties are driven by the structural characteristics of the anion, such as the asymmetrical perfluorinated butyl chain and the potential formation of fluorous domains via anion-anion interactions (in the case of DBUH-IM14) and the hydrogen bond network (in the case of DBUH-TFO).

Considering the potential application of the selected PILs as electrolyte components, their transport properties were investigated in terms of the macroscopic rheological and electrochemical properties. It is worth pointing out that DBUH-TFO is the most viscous system due to the strong hydrogen bond network of this liquid, reflecting on its lower ionic conductivity than the other PILs investigated. Noteworthy is the reduced molar conductivity detected for DBUH-IM14 concerning its fluidity. The complex interplay of different interaction types (H bond, Coulombic, dispersive) in DBUH-IM14 seems to affect its charge transport as revealed by the Walden plot.

Overall, the extensive characterization performed on the selected PILs demonstrate that the structural features of the PILs' constituents, especially of the anion, govern their physicochemical properties. These findings lead us to address a more detailed description of the DBU-based PILs at the molecular/atomic level and further investigate their transport properties, in order to promote their application as electrolytes.

CHAPTER 3

The transport properties of protic ionic liquids and protic ionic liquids electrolytes

3.1.   Introduction

Electrolytes based on protic ionic liquids (PILs) have been quoted as promising electrolyte components in combination with LIB electrodes[31,114,115]. Despite all the efforts to understand the key features ruling the properties of PILs for electrochemical applications, the dynamics of PIL-based electrolytes has been minimally discussed. So far, it is known that the presence of the acidic proton changes the intermolecular features of neat PILs, especially due to the presence of a hydrogen bond networking[22,45]. Moreover, *Chapter 2* has shown that the nature of the cation-anion pair strongly influences the intermolecular interactions of the studied PILs, formed by the DBUH$^+$ cation and the three anions IM14$^-$, TFSI$^-$ and TFO$^-$, thus affecting their physical-chemical properties.

The scenario is even more complicated in PIL electrolytes, i.e., PIL doped with a lithium salt, usually having the same anion as the neat PIL. Indeed, the addition of a third ionic species, Li$^+$, will have a relevant effect on the intermolecular interactions of the neat PIL, thus affecting drastically micro- and macroscopic properties. However, it is still unclear how the simultaneous presence of an acidic proton and a small positively charged ion change the intermolecular network and specifically the transport properties of PIL electrolytes in terms of ion mobilities[35].

Up to now, just a few studies have reported the behavior of PIL electrolytes mainly focused on TFSI-based PILs[32,35,116]. Considering that the nature of the anion (functional groups, size, structure) has a key role in driving intermolecular interactions in neat PILs, as highlighted in *Chapter 2*, it will have implications also in the translational and rotational dynamics of the ions[115,117], both in neat PILs and PIL electrolytes. Then, I extended my investigation toward understanding the molecular mobilities of PILs and their mixtures with a lithium salt sharing the same anion, aiming at their application as electrolyte components.

In this *Chapter*, I present a systematic study of the effects of lithium salt on the structure and dynamic properties of the DBU-based PILs previously introduced (DBUH-IM14, DBUH-TFI and DBUH-TFO). In this context, I prepared the corresponding PIL electrolytes (PIL doped with lithium salt), and I explored different NMR techniques as a unique and powerful tool to access the rotational and translational dynamics of the ions. The combination of relaxation and diffusion data provided me with information about the ionic mobilities from the molecular scale to an extremely local level[118]. Besides, density and conductivity, together with the diffusion coefficients, allowed the calculation of the ionicity to characterize the ionic behavior of the systems. Finally, electrophoretic NMR was employed to obtain ion drift information giving insights into the ionicity of the DBUH-IM14.

Overall, the investigation discussed in the following Sections attempted to (i) elucidate how the molecular interactions present in the neat PILs affect their ions' rotational and translational mobility and (ii) disentangle the effects at the molecular level of the lithium-ion on the overall mobility and ionic conductivity of the PIL electrolytes.

3.2. Theoretical background and methodology

3.2.1. Preparation of PIL electrolytes

Neat PILs (synthesized as described in *Chapter 2*) and their respective lithium salt sharing the same anion (LiIM14 and LiTFSI provided by 3M, and LiTFO from Sigma Aldrich) were blended in a closed vial using a thermoregulated bath and continuous agitation, keeping the molar ratio [DBUH$^+$]:[Li$^+$] equal to 10:1. The final PIL electrolytes (DBUH-IM14)$_1$(LiIM14)$_{0.1}$, (DBUH-TFSI)$_1$(LiTFSI)$_{0.1}$ and (DBUH-TFO)$_1$(LiTFO)$_{0.1}$, were vacuum dried (< 1 mbar) in an oil-free pump at 373 K for at least 18 hours.

For NMR measurements, the PIL electrolytes were placed in 5 mm NMR tubes and flame-sealed in a controlled environment (dry-room, relative humidity < 0.1% at 293 K) to prevent any contamination and

air contact. All the NMR tubes contained a flame-sealed capillary with deuterated DMSO (DMSO-d6) as a reference/lock solution.

3.2.2. Diffusion measurements

Translational diffusion is the most fundamental form of transport in chemical systems. The self-diffusion coefficients represent the random motion (Brownian motion) of molecules or ions driven by internal kinetic energy[119]. Then, it provides information not only about the translational ionic motion, but also about the molecular organization since diffusion rates are sensitive to structural changes, such as ions association[73].

Pulsed-field gradient (PFG) NMR spectroscopy is a unique and non-invasive tool for studying translational dynamics in IL systems. In the PFG NMR method, the self-diffusion coefficients D are measured through the attenuation of a spin echo signal resulting from the dephasing of the nuclear spins within imposition of field gradient pulses[119].

First, magnetic field gradients of different intensities are applied along the z-axis, resulting in position dependent local magnetic field across the macroscopic sample and then causing the dephasing of the magnetic moments. Weaker gradients lead to less dephasing and stronger gradients leads to greater dephasing. The gradients are applied to the sample in the form of short pulses that break the homogeneity in a predictable way. By convention, the center of the sample is set to zero on the z-axis, meaning that spins above the center experience larger magnetic fields and below zero experience smaller magnetic fields. Because the inhomogeneities in the magnetic field are predictable, the spins are spatially labeled as a function of position, i.e., marked depending on their position in the NMR tube[119]. After the encoding, molecules are let free to diffuse during a delay period (the diffusion time), after which a second gradient (partially) rephase the magnetic moments. If a molecule moves during the diffusion time, its new position can be decoded by the second gradient. Practically speaking, this means that the observed NMR signal will be attenuated depending on the diffusion. The fitting of the signal intensity decay as a function of gradient strength is commonly achieved by the Stejskal-Tanner equation[120] (Eq. 3.1), giving the self-diffusion coefficient D as fitting parameter:

$$\frac{I}{I_0} = exp\left(-\gamma^2 g^2 \delta^2 D \left(\Delta - \frac{\delta}{3}\right)\right) \tag{3.1}$$

where I and I_0 are the intensity with and without field gradient, γ is the gyromagnetic ratio, g and δ are the gradient strength and duration, and Δ is the diffusion time.

Diffusion spectra as measured by PFG NMR can be recorded and plotted as pseudo two-dimensional experiments called Diffusion-Ordered Spectroscopy (DOSY), in which a 1D spectrum is recorded over a range of gradient strengths, starting from the weaker to the stronger, and keeping the other parameters as constant, creating a series of 1D experiments with decaying signal intensity.

In the simplest case, PFG NMR diffusion experiment is performed using a spin echo (SE) pulse sequence (PFG SE). The pulse sequence of the PFG SE experiment, shown in Figure 3.1, begins with a 90° pulse, resulting in traverse magnetization. A first gradient pulse is then applied along the z-axis during a certain time δ, systematically varying the precession rates. The array of precession rates creates a spiraling magnetization along the z-axis, which directly depends on the area of the gradient pulse. Once the gradient pulse ends, the labeled spins feel a homogeneous magnetic field, and all the spins precess at the same rate with retained dephasing. Then a 180° pulse is applied, making the spins to rotate on the x-axis, creating a mirror image of the spiral created after the first gradient pulse. After that, the same gradient pulse is repeated, refocusing the spins into the positive y-axis, and creating the echo signal which is detected during acquisition. If the nuclei did not change position between the first and second gradient pulse (i.e., did not diffuse during the diffusion time Δ), the echo signal must have the same intensity as the initial signal observed. Contrarily, if the spins diffused into a new region along the z-axis, the magnitude of the refocussed signal would decrease. Therefore, monitoring the attenuation of the signal as a function of gradient strength, one can encode the diffusion along the z-axis. The fitting of the echo attenuation data for different values of the gradient eventually provides the observed diffusivity[119].
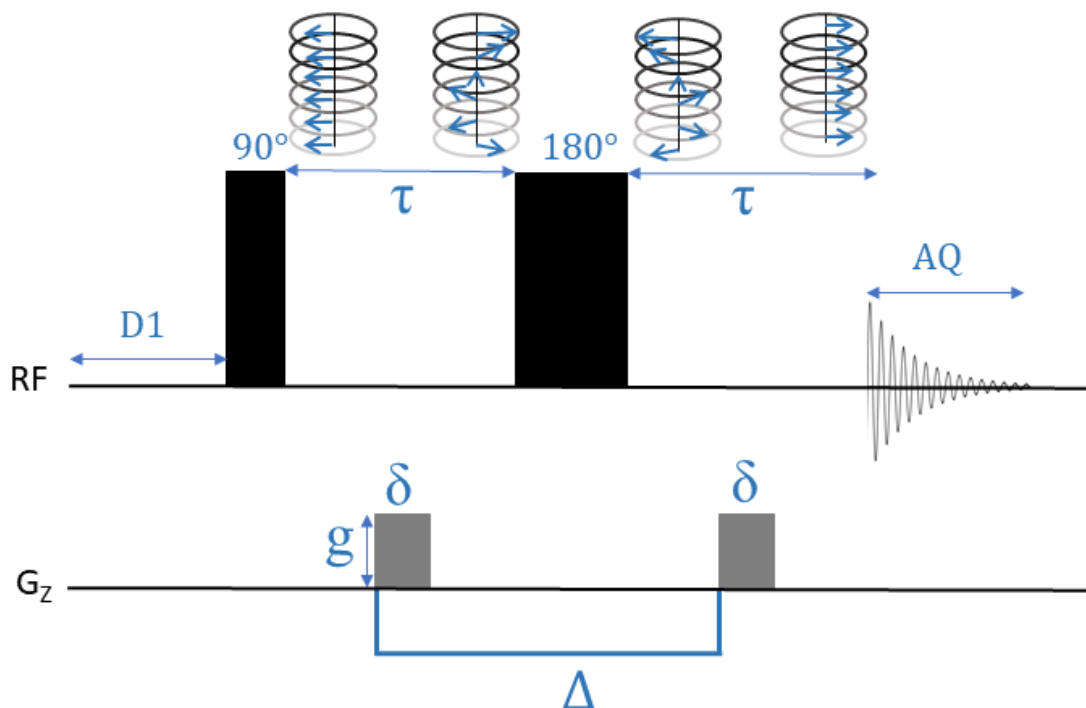
Figure 3.1. Spin Echo Pulsed Field Gradient (PFG SE) NMR pulse sequence. The radio frequency pulse (RF) is applied to a 90° or 180° rotation, separated by the time τ. A gradient (g) is applied along the z-axis for a duration of time (δ) to induce dephasing. The diffusion time (Δ) is the time between gradient pulses. D1 is the recycling delay and AQ is the acquisition time.

Even if the PFG SE is frequently applied to solutions, it is not uniformly applicable to more viscous and chemically complex systems. Annat et. al.[121] showed that in the case of ILs, PFG SE suffers from intrinsic internal gradients and can produce apparent diffusion coefficients, which vary by as much as 20% for different ^{1}H nuclei within a given molecule, which is inaccurate. In contrast, they showed that the Pulsed Field Gradient Stimulated Echo (PFG STE) pulse sequence (Figure 3.2) does not suffer from this problem to the same extent and produces self-consistent data to a high degree of accuracy. In addition, PFG STE allows to overcome some of the problems associated with the PFG SE experiments, in particular the loss of magnetization due to T_2 (spin-spin relaxation) effects. For spins having a short T_2 (e.g. in macromolecules), most of the signal disappears at the time of the echo. In the PFG STE pulse sequence, a second 90° pulse is applied after the first gradient, so that during the time T, the magnetization is along the z-axis and there is no T_2 relaxation which hampers the loss of magnetization. Hence, the PFG STE has the advantage of having an effective shorter time for T_2 relaxation (2τ).
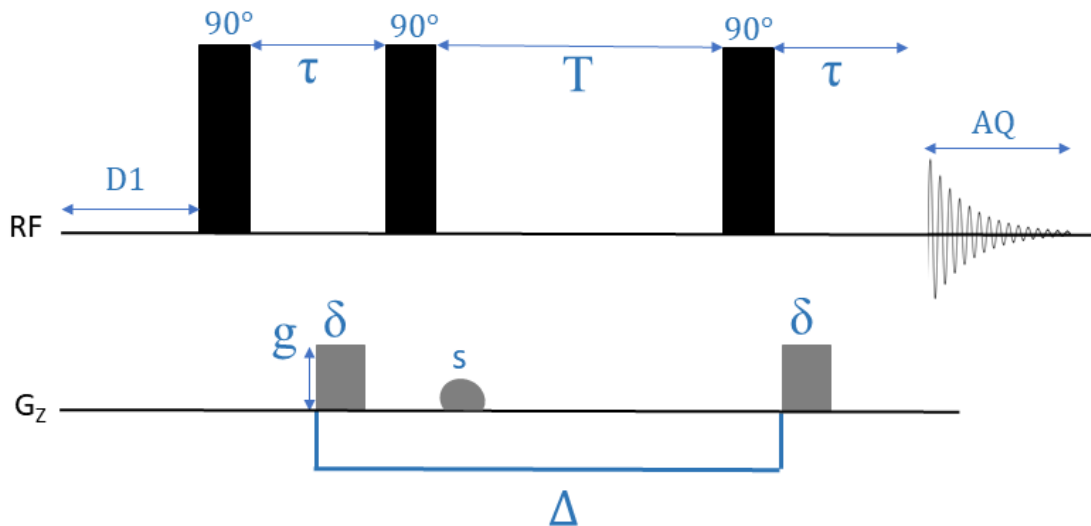
Figure 3.2. Pulsed Field Gradient Stimulated Echo (PFG STE) NMR pulse sequence. The RF pulse is applied to a 90° rotation. A gradient (g) is applied along the z-axis for a duration of time (δ) to induce dephasing. One additional spoiler magnetic field gradient pulse (s) is applied to remove unwanted phase coherence causing signal distortions. The diffusion time (Δ) is the time between gradient pulses. T and τ are the time where spin-lattice and spin-spin relaxation times take place, respectively.

From the simple PFG STE experiment other pulse sequences were developed. A modified PFG STE pulse sequence incorporates BiPolar Pulses (BPP-STE, Figure 3.3). Basically, the single gradient pulses of the PG STE sequence are split into a pair of two pulses with opposite signs enclosing a 180° pulse. This pulse sequence is used to remove the effect of internal gradients in the sample. The dephasing resulting from internal static gradients is removed by means of the 180° pulse.
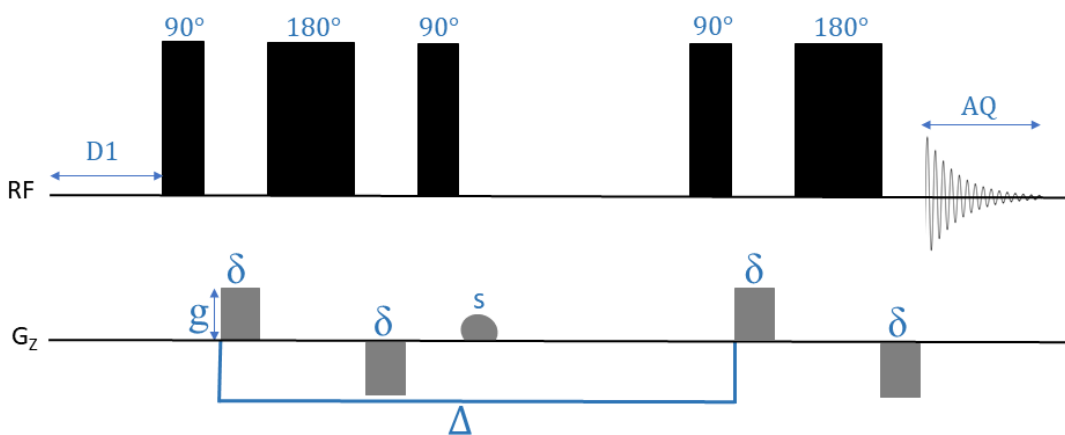
Figure 3.3. Stimulated Echo using BiPolar Pulses (BPP-STE)) NMR pulse sequence.

An alternative to the PFG STE experiment is the Longitudinal Eddy current Delay (LED, Figure 3.4), which is used to suppress eddy current effects. The LED sequence stores the magnetization for the time of the LED delay in the longitudinal direction waiting for the eddy currents to decay. From the practical viewpoint, the LED experiment allows the measurement of slower diffusing species where a longer diffusion time is required to detect attenuation of the signal[122]. An evolutionary improvement is the Longitudinal Eddy current Delay experiment using BiPolar Pulses (BPP-LED, Figure 3.5), which basically combines the advantages of the previous two sequences.
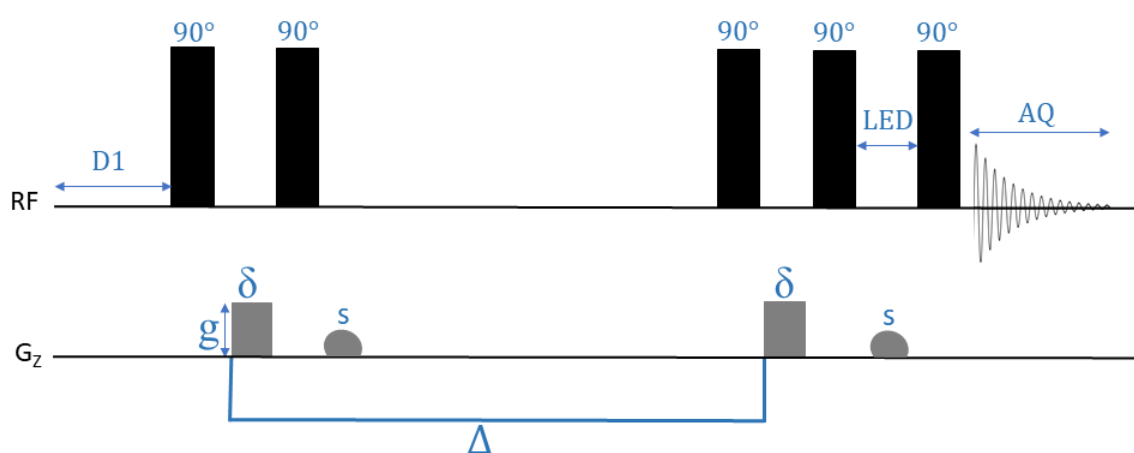
Figure 3.4. Longitudinal Eddy current Delay (LED) NMR pulse sequence.
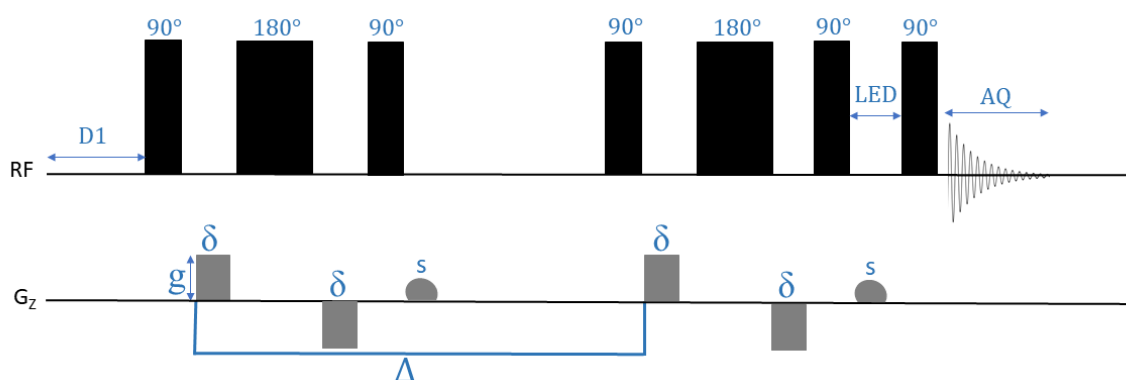
Figure 3.5. Longitudinal Eddy current Delay experiment using BiPolar Pulses (BPP-LED) NMR pulse sequence.

In the present *Chapter*, PFG NMR was applied to determine the self-diffusion coefficients (D_i) of the ionic species in the PILs and PIL electrolytes.

In the neat PIL, temperature-dependent diffusion coefficients were measured from a minimum temperature (i.e., 298 K for DBUH-IM14, 308 K DBUH-TFO, and 318 K for DBUH-TFSI) up 368 K, with a 10

K temperature step at 11.74 T with a Bruker NEO 500 console equipped with a direct observe 5 mm pulsed-field z-gradient BBFO iProbe by using the BPP-LED pulse sequence (ledbpgp2s in Bruker library), in the ^{1}H and ^{19}F frequency domains independently for DBUH$^+$ cation and TFSI$^-$ and TFO$^-$ anions, respectively. The temperature was controlled using a variable-temperature (VT) unity previously calibrated by a standard methodology using ethylene glycol as a reference solution. For the IM14$^-$ anion, self-diffusion coefficients were determined during my research stay in the University of Münster applying the STE pulse sequence (stegp1s in Bruker library) using a Bruker Advance 400 NMR instrument equipped with the diff30 probe head operating at a magnetic field of 9.4 T. In this case, the temperature was calibrated by the gradient cooling unit in conjunction with a PT100 thermocouple before each measurement. All experiments were carried out with a total of 8 transients per increment and over a spectral width of 12 ppm for ^{1}H. For the DBUH-TFO and DBUH-TFSI the spectral width of ^{19}F was 80 ppm, and for DBUH-IM14 it was 90 ppm. The relaxation delay was set to at least five times T_1, and 8 dummy scans were programmed prior to acquisition. The pulse gradients were incremented from 2 to 95% of the maximum gradient strength in a linear ramp with 16-32 steps. For each experiment, the duration of the magnetic field pulse gradients (δ) and the diffusion times (Δ) were optimized to obtain, where possible, 95% signal attenuation for the slowest diffusion species at the last step experiment. For ^{1}H and ^{19}F diffusion experiments, δ values were in the 3−6 ms range, while Δ values were 0.5−0.8 s long (gradient strength of 48.15 G.cm^{-1}). For the ^{19}F nucleus of the DBUH-IM14, δ and Δ values were fixed as 3 ms and 50 ms long varying the gradient strength in the range from 950 G.cm^{-1} to 150 G.cm^{-1}.

For the PIL electrolytes, the diffusion NMR experiments were performed during my research stay at the Hunter College – City University New York (CUNY) using a Bruker Advance 400 NMR instrument equipped with a direct observe 5 mm pulsed-field z-gradient BBFO probe, operating at a magnetic field of 9.4 T. The temperature was controlled using a variable-temperature (VT) unity previously calibrated by a standard methodology using ethylene glycol as a reference solution. The BPP-LED pulse sequence was used for all nuclei (^{1}H, ^{7}Li and ^{19}F) of (DBUH-TFO)$_1$(LiTFO)$_{0.1}$ and (DBUH-TFSI)$_1$(LiTFSI)$_{0.1}$, as well for the ^{1}H nucleus of (DBUH-IM14)$_1$(LiIM14)$_{0.1}$. Instead, for the ^{19}F nucleus of (DBUH-IM14)$_1$(LiIM14)$_{0.1}$, the STE pulse sequence was applied. The diffusion coefficients were measured from a minimum temperature (i.e., 298 K for DBUH-IM14, 308 K DBUH-TFO, and 318 K for DBUH-TFSI) up 368 K, with a 10 K. For the measurements at least 16 transients were used with optimized recycling delay (4 – 8 s). The gradient strength was varied in the range of 2 - 95% of a maximum

strength 50 G.cm^{-1}, with 16 increments, following a linear increase. The δ values were optimized in the 3−10 ms range, while Δ values were 0.5−0.8 s long, allowing the 95% signal attenuation of the diffusion species at the last step experiment.

The ^{7}Li nuclei of the (DBUH-IM14)$_1$(LiIM14)$_{0.1}$ suffers from a very short T$_2$ and the signal disappears at the time of the echo. The ^{7}Li diffusion coefficients were measured during my research stay at the Hunter College on a 300 MHz NMR spectrometer with Agilent/Varian DDR console operating at a magnetic field of 7 T (^{7}Li Larmor frequency of 116.6 MHz), equipped with a Doty Z-spec PFG NMR probe. The diffusion coefficients were measured as a function of temperature from 298 K to 367 K by using the BPP-LED pulse sequence. In this case, the temperature was controlled by a variable temperature (VT) unit in conjunction with a thermocouple before each measurement. At least 16 transients were used with optimized recycling delay (4 – 8 s). The diffusion time (Δ) and the diffusion pulse length (δ) were set as 100 ms and 2.5 ms, respectively. The gradient strength g was varied in 16 increments following a linear increase; values were in the range of 2-95% of a maximum strength, set in the range of 180-850 G.cm^{-1}, allowing, if possible, 95% signal attenuation of the diffusion species at the last step experiment.

Due to the heat exchange with the environment, temperature gradients may cause convective current (especially at high temperature experiments) which can potentially promote displacement z, interfering in the diffusion measurements. The diffusion coefficients were then determined at two different observation times (Δ) to check for the absence of convection artifacts. Indeed, no convection artefacts were detected during the diffusion experiments.

For the experiments acquired with Bruker spectrometers, the raw spectra were subjected to manual phasing and automatic baseline correction. Data were processed using an exponential filter in F2 dimension (LB = 0.3 Hz). Integrals were employed in the Bruker T1/T2 module of TopSpin to fit the Stejskal–Tanner relation. For the experiments performed using the Agilent/Varian DDR console, the diffusion coefficients were determined by a non-linear fitting entering a user function in the software *Origin-Pro 16*. Figure 3.6 exemplifies one series of DBUH$^+$ spectra showing the corresponding magnetization loss during the diffusion experiment.
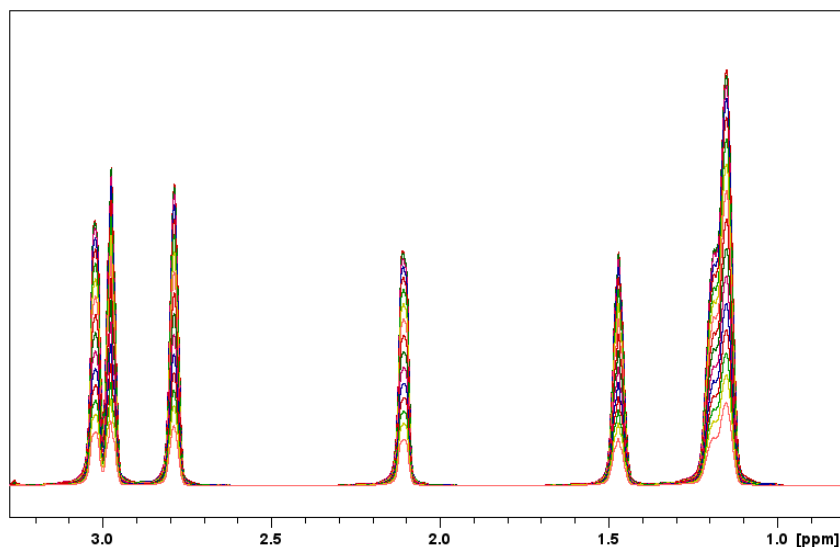
Figure 3.6. Series of spectra of the DBUH$^+$ and the corresponding magnetization loss during the PFG-NMR experiment.

3.2.3. Electrophoretic NMR (e-NMR)

When investigating the transport properties of systems containing changed species, advanced NMR methods can be exploited. Extremely interesting among them is electrophoretic NMR (e-NMR), a powerful method for the determination of the electrophoretic mobilities. The electrophoretic mobility μ represents the velocity of the motion of a charged species when an electric field is applied[123].

Basically, the e-NMR experiment consists of a Pulsed Field Gradient Double Stimulated Echo (PFG DSTE) NMR experiment in the presence of an external electric field applied between two electrodes parallel to the in z-direction of the static magnetic field B$_0$, as shown in Figure 3.7. The conventional PFG DSTE sequence is a duplicated version of PFG STE (Figure 3.2), typically used to compensate for convective flow in the sample. As explained in the previous section, the investigated nucleus undergoes self-diffusion during the diffusion time Δ, leading to the attenuation of the observed signal. However, in the e-NMR experiment, an additional electric field induces the drift of charged species i with a velocity v_i according to the strength of the electric field E applied and the electrophoretic mobility μ_i of the investigated species[124].
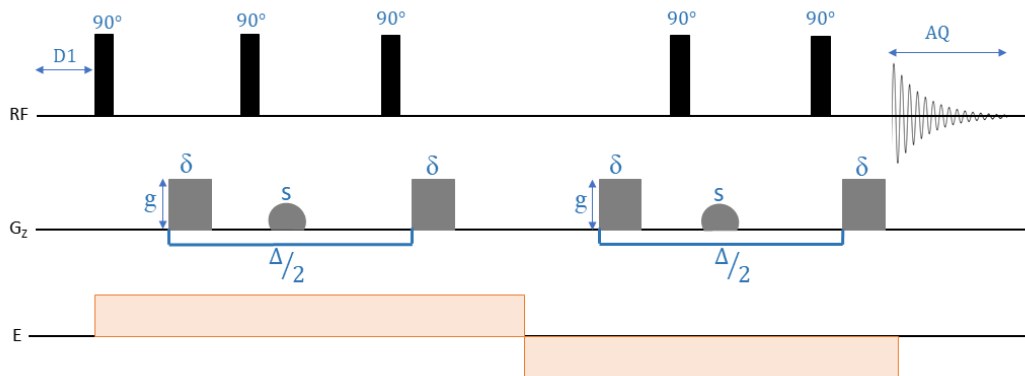
Figure 3.7. e-NMR pulse sequence consisting of a Double Stimulated Echo (DSTE) with two additional spoiler magnetic field gradient pulses s to remove unwanted phase coherence causing signal distortions. In each STE block, two phase encoding magnetic field gradient pulses g are applied with a duration δ separated at the observation time $\Delta/2$. Additional bipolar electric field pulses E are applied to the sample parallel to B_0 (Figure adapted from Gouverneur et al. [124]).

In the present thesis, the e-NMR measurements were carried out during my secondment at the University of Münster, by using a Bruker Advance 400 NMR instrument equipped with the diff30 probe head using a self-build e-NMR electrode tailored for 5 mm NMR tubes. A self-build pulse generator (V_{max} = 1 kV, I_{max} = 50 mA) was used to apply the electric field during the e-NMR measurements. The electrode and the wires are fixed on a polyimide (VESPEL) rod, which inhibits distortions by electrode vibration. The rod is hollow in the bottom to house coated capillaries with polyimide (Polymicro), preventing convection during the measurements. A Teflon cap is used to fix the NMR tube on the polyimide rod with a sealing ring, which protects the sample from air contact and moisture contamination (Figure 3.8).
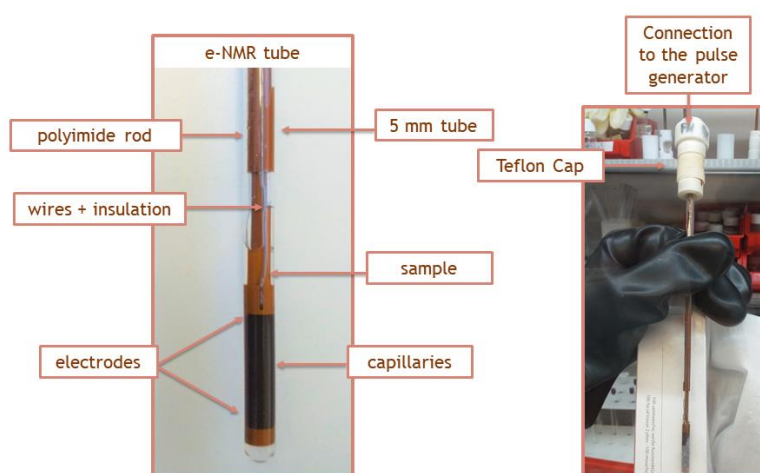
Figure 3.8. Self-built e-NMR electrode configuration for 5 mm NMR tubes (left picture is the bottom of the tube, right picture is the whole tube setup). The contacts are housed in a Teflon cap, in which the 5 mm NMR tube can be fixed with a Teflon screw. The connection to the pulse generator is in the internal part of the Teflon.

To record the ions mobilities, the DSTE pulse sequence and an electric field were simultaneously applied, switching the polarity during the echo pulse sequence. In a series of spectra, the gradient strength g is increased linearly, and the drift of the charged ions can be seen by a phase shift of the transformed NMR peak $\Delta\Phi = \Phi - \Phi_0$ in subsequent spectra which depends on the gradient strength (Eq. 3.2):

$$\Delta\Phi = \gamma\delta g\Delta_{\text{Drift}}\mu E_{dc} \qquad (3.2)$$

where μ is the electrophoretic mobility, E_{dc} is the applied electric field and Δ_{drift} is the drift time.

In a linear plot $\Phi(g)$, one can extract the electrophoretic mobility (μ) from the slope m if the drift time, gradient pulse length δ and the electric field strength are known (Eq. 3.3). Exemplification of the phase shift in dependence on the gradient strength of the DBUH$^+$ cation and IM14$^-$ anion is shown in Figure 3.9.

$$\mu = \frac{m}{\gamma\delta g\Delta_{\text{Drift}}} \qquad (3.3)$$
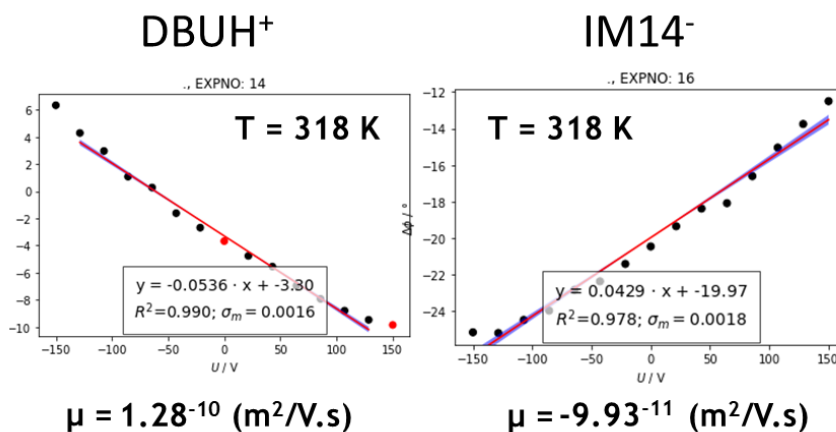
Figure 3.9. Exemplification of the phase shift in dependence on the gradient strength of the DBUH$^+$ cation and IM14$^-$ anion at 318 K. The electrophoretic mobilities (μ) were extracted from the slope m of the curves.

In the present thesis work the electrophoretic NMR experiments were performed only for the sample DBUH-IM14 at three different temperatures (318 K, 348K, 368K). The temperature was calibrated by the gradient cooling unit in conjunction with a PT100 thermocouple before each measurement. The experiments were performed in duplicates or triplicates. The gradient pulse length (δ) was set between 1 to 3 ms and the drift time was between 100 ms and 50 ms. The electric field strength was varied between 80 and 120 V. The gradient strength was selected allowing the drift time to have sufficient signal intensity in the range from 250 G.cm^{-1} to 80 G.cm^{-1}. The analysis of the phase shift was performed in TopSpin

3.2 with a self-written program which detects the phase shift at a given gradient strength. Figure 3.9 displays a series of acquired DBUH$^+$ spectra exemplifying the phase shift during the e-NMR experiment.
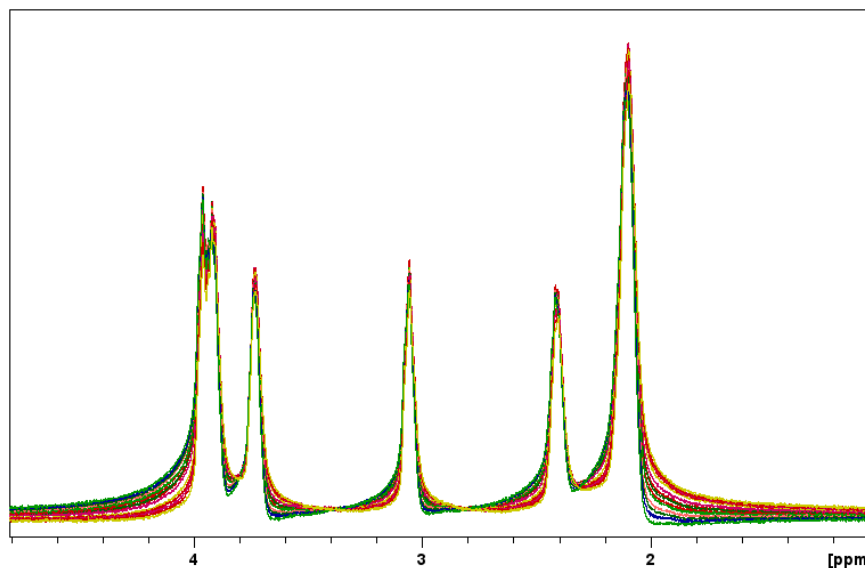
Figure 3.9. Series of spectra of the DBUH$^+$ and the corresponding phase shift during the e-NMR experiment.

During the e-NMR experiments, the application of a current may cause the Joule heating of the sample, resulting in artifacts due to the convection effects. Here, two main approaches were employed to overcome these issues: the using of capillaries between the electrodes (to work as a mechanical barrier), and convection compensated pulse program (the gradient nulling double stimulated echo pulse program, described above).

3.2.4. Spin-lattice T$_1$ relaxation measurements

In a semi-classic model (vector model), the equilibrium magnetization is aligned with the z-axis of the stray field B$_0$. Such a magnetization is commonly referred to as the longitudinal magnetization M_z. In thermal equilibrium conditions, the magnetization components on the xy plane (M_{xy}, the transverse magnetization) are null. The creation of a single-quantum coherence by a $\pi/2$ RF pulse turns the longitudinal magnetization into the free-precessing transverse magnetization. NMR relaxation is the process by which the transverse magnetization returns to the equilibrium state. The process schematically passes through the recovery of the M_z magnetization from null to the maximum value (spin-lattice relaxation) and the decay of the transverse magnetization M_{xy} from the actual value after excitation to null (spin-spin relaxation). In both relaxation pathways, the return of the magnetization to equilibrium

is described by an exponential law, with time constants T_1 (spin-lattice relaxation time) and T_2 (spin-spin relaxation time), respectively. The theoretical background of the NMR relaxometry is well described in the literature, and this technique is widespread to explain the ion dynamics in ILs[125–127].

T_1 characterizes the time constant for the recovery of the longitudinal M_z component of the magnetization towards thermodynamic equilibrium. In a simple way the rate of such phenomenon can be defined as the spin−lattice relaxation rate, $R_1 = 1/T_1$. In the case of null initial M_z, as after a $\pi/2$ rf pulse, the recovery is described by the following (Eq. 3.4)[52]:

$$M_z(t) = M_0 \left(1 - e^{-\frac{t}{T_1}}\right)$$
(3.4)

The experimental measurement of T_1 is commonly obtained by the inversion recovery (*IR*) pulse sequence, showed in Figure 3.10. The *IR* pulse sequence begins with a 180° pulse followed by a variable recovery time τ and a 90° pulse. The initial 180° pulse inverts the spin population (M_z) from its equilibrium value $+M_z$ to $-M_z$. Following the inverting pulse, the population can evolve during the recovery period τ. To measure a signal after the recovery period (τ), a 90° pulse is applied to create readable single quantum coherence. The associated FID reflects the degree of recovered magnetization (with respect to τ) and the signal is acquired.
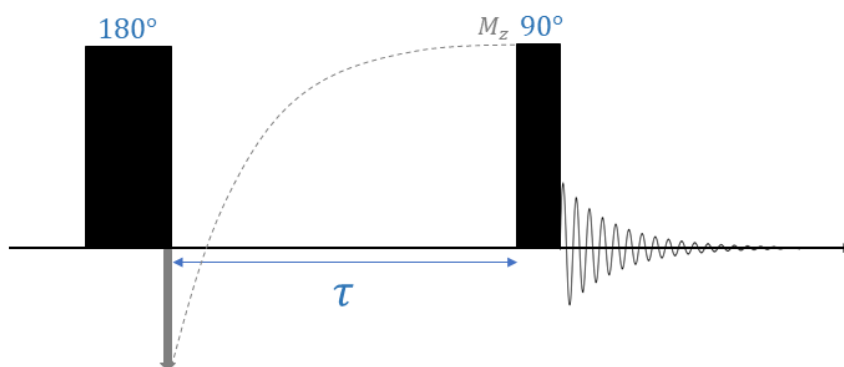
Figure 3.10. Inversion recovery pulse-sequence for measurement of T1 relaxation time.

T_1 Relaxation measurements of the neat PILs and PIL electrolytes were performed without sample spinning with a Bruker NEO 500 console (11.74 T) equipped with a direct observe BBFO iProbe and a variable-temperature unit (^{1}H, ^{19}F, and ^{7}Li resonance frequency of 500.13, 470.59 and 194.37 MHz, respectively). The instrument was carefully tuned, shimmed, and the 90° pulses calibrated before the measurements. ^{1}H, ^{19}F and ^{7}Li T_1 relaxation experiments were performed over a temperature range from 298-308K to 378 K, in 10

K increments, with a minimum of 15 min allowed for thermal equilibration.

Spectra were recorded using relaxation delays at least five times the longest T_1, four dummy scans prior to acquisition, and data matrices of 16384 (t_2) × 16 (τ), with 2 transients per increment, over a spectral width of 11.76 ppm for ^1H, 39 ppm for ^{19}F in the case of DBUH-TFSO and DBUH-TFSI, 15.2 ppm and 25.3 ppm for ^{19}F in the case of DBUH-IM14, and 19.79 ppm for ^7Li. The spin−lattice relaxation rates were measured for delay times ranging from 0.05−10 s to 0.05−12 s for ^1H; from 0.05−8 s to 0.05−15 s for ^{19}F; and from 0.05-8.0 s to 0.05-15 s for ^7Li, according to the temperature. The baselines of all arrayed T_1 spectra were corrected prior to processing the data using an exponential filter in F_2 dimension (with LB equal to 0.3 Hz). Relaxation times were computed using integrals from experimental raw data by means of the Bruker T_1/T_2 relaxation module using the manual integration option and applying the standard one-component fitting function.

Figure 3.11 shows the structures of DBUH$^+$ cation and IM14$^-$, TFSI$^-$ and TFO$^-$ anions and the labels referring to the different ^1H and ^{19}F nuclei whose signal intensity was used for T_1 determinations.
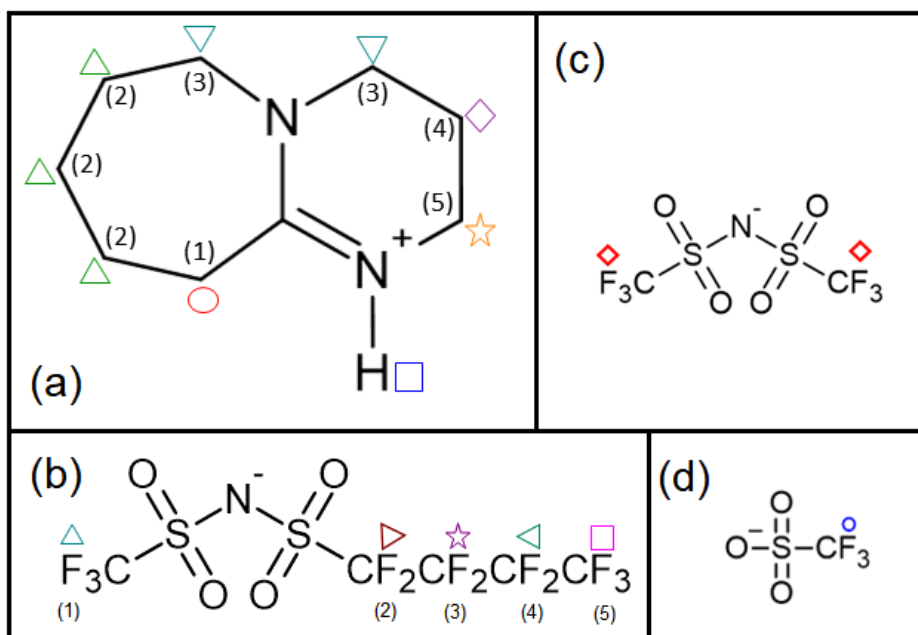
Figure 3.11. Grouping of the ^1H signal of the DBUH$^+$ cation and ^{19}F signals of the (b) IM14$^-$, (c) TFSI$^-$ and (d) TFO$^-$ anions

3.2.5. Ionic conductivity

The electrochemical impedance spectroscopy (EIS) is the usual approach for investigating the ionic conductivities for electrolytes. The basics of ESI are described in *Section 2.2.9* of *Chapter 2*.

The ionic conductivity of the neat PILs is presented and discussed in *Chapter 2* (*Section 2.3.8*). EIS measurements of the PIL electrolytes, that is PILs doped with lithium salt, were carried out at the facilities of the University of Münster. The temperature-controlled measurements were conducted using a Microcell HC cell stand from RHD Instruments with a TSC 70 closed cell. The cell was polished with a diamond paste before each experiment. The cell constant was determined via a reference measurement using an aqueous KCl standard solution exhibiting a conductivity of 147 µS cm^{-1}. The sample cell was filled with about 70 µL of each sample in a glove box under argon atmosphere. Each measurement temperature was equilibrated for 15 minutes prior to the actual measurement. The impedance was analyzed at frequencies ranging from 10 MHz to 1 Hz. The conductivity was then determined by extracting the Z' from the complex plot.

3.2.6. Density measurements

The basics of density measurements as well as the results obtained for the neat PILs are reported in *Chapter 2* (*Sections 2.2.7* and *2.3.6*, respectively). In this Chapter, I present measurements of density (ρ) carried out for the PIL electrolytes investigated during my secondment at the University of Campinas using the density meter DM45 Delta Range from Mettler Toledo. The experiments were performed from 298 K up to 358 K for (DBUH-IM14)$_1$(LiIM14)$_{0.1}$, from 308K up to 358 K for (DBUH-TFO)$_1$(LiTFO)$_{0.1}$ and from 318K up to 358 K for (DBUH-TFSI)$_1$(LiTFSI)$_{0.1}$, in 10 K steps, allowing 15 minutes for temperature equilibration before the measurements.

Density values allowed for the determination of the molar conductivity (Λ) of the PIL electrolytes (Eq. 3.5), as well as the composition of the electrolyte and its total molar mass MM:

$$\Lambda = \frac{\sigma}{\rho} MM \qquad (3.5)$$

The molar mass of the PIL electrolyte is determined by Eq. 3.6:

$$MM = x_{salt} MM_{salt} + x_{PIL} MM_{PIL} \qquad (3.6)$$

Where, x_i and MM_i are the molar fraction and molar mass of the species *i*, respectively.

3.3. Results

3.3.1. Self-diffusion coefficients

3.3.1.1. Self-diffusion coefficients of the neat PILs

Figure 3.12 displays the self-diffusion coefficient (D_i) of the ionic species in the neat PILs, cation (D_{cation}), anion (D_{anion}), and N-H proton (D_{N-H}), as a function of temperature (the raw data are reported in the Appendix A3, Tables A3.1-A3.3). The notation (D_{N-H}) is a synthetic way to report on the diffusion coefficient obtained by the fitting of the decay intensity of the signal assignable to the potentially exchangeable N-H proton. However, the discussion concerning the stability of N-H covalent bond reported in *Chapter 1* should be kept in mind to avoid any misinterpretation.

The temperature dependent values for the self-diffusion coefficients were fitted using the Vogel-Fulcher-Tammann (VFT) type relationship (Eq. 3.7) and Arrhenius equation (Eq. 3.8). Both models have been widely used for describing IL transport properties.

$$D = D_0 \exp\left[\frac{-B}{T - T_0}\right] \tag{3.7}$$

where D_0 (m^2.s^{-1}), B (K) and T_0 (K) are the VFT fitting parameters;

$$D = A \exp\left(\frac{-E_a^{trans}}{RT}\right) \tag{3.8}$$

with A a pre-exponential factor, E_a^{transl} the activation energy for the diffusive motion, R the gas constant, and T the absolute temperature for the Arrhenius model.

The best fitting parameters for the VFT and Arrhenius model for each ionic species are reported in the Appendix A, Table A3.4-A3.5, respectively.

In principle, high diffusivity is expected for PILs with low viscosity (high fluidity). The results obtained for the neat DBUH-TFSI and DBUH-TFO, the least and the most viscous system, respectively (see viscosity data of *Section 2.3.7, Chapter 2*), are in line with such a statement, showing the highest and smallest translational mobility, respectively. Indeed, for some DBU-based PILs it is already reported that the viscosity is well-correlated with the microscopic properties[46].

DBUH-IM14 behaves as an important exception to the viscosity statement since its diffusivity is almost equal to that of DBUH-TFO which is the most viscous system among the studied PILs. For instance, at 308 K, DBUH-IM14 shows diffusivities of 3.1·10^{-12} and 2.6·10^{-12} m^2.s^{-1} for cation and anion, respectively, which are very close to DBUH-TFO (2.9·10^{-12} and 2.5·10^{-12} m^2.s^{-1} for cation and anion, respectively). Yet, DBUH-TFO viscosity is more than twice the viscosity of DBUH-IM14 (919 vs. 410 mPa.s, at 308 K, respectively).
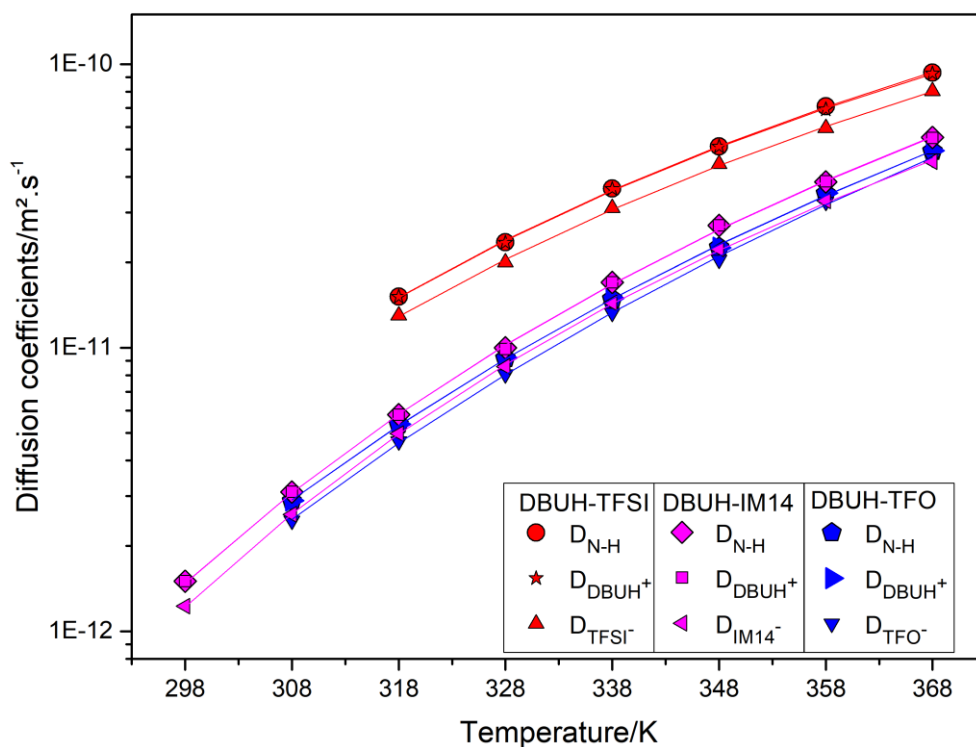
Figure 3.12. Self-diffusion coefficients of the neat PILs as a function of temperature. Solid lines correspond to the VFT fitting.

The self-diffusion coefficients make it possible also to characterize the mechanism of charge transport in the PILs. Commonly, the charge transport in neat PILs occurs by the vehicular and/or the Grotthuss mechanisms[128]. In the Grotthuss type mechanism, the proton diffuses hopping through the hydrogen-bonded network using its H-bonding ability. On the contrary, in the vehicular mechanism, the acidic proton moves attached to a carrier molecule as ionic species. The issue whether proton transport in ILs can occur via the Grotthuss mechanism is currently vividly debated, yet not conclusively verified[79]. Looking at the ratio between the diffusivities of the acidic proton and the cation (D_{N-H}/D_{DBUH+}), Figure 3.13 and Tables A3.6-A3.8), it can be observed that in all the systems, the acidic proton (D_{N-H}) moves at the same rate as the DBUH$^+$ cation ($D_{N-H}/D_{DBUH+} \approx 1$), indicating a charge transport based on the vehicular mechanism. Indeed, for other anhydrous PILs containing similar anions (TFO$^-$ and TFSI$^-$), it has been shown that Grotthuss mechanism is unlike to occur[79,128]. The data are fully consistent with the discussion on $^1J_{NH}$ of *Chapter 2*.

Looking at the cation/anion diffusion coefficient ratios (D_{cation}/D_{anion}) (Figure 3.13 and Tables A3.6-A3.8), we observe that D_{cation}/D_{anion} is higher than unity, indicating that the anions are always the slowest species in the PILs evaluated. Also, D_{cation}/D_{anion} different from the unity is quite intuitive as it is very well known by now that PIL (and IL in general) are not diffusing as long-lived ion pairs[101]. While D_{cation}/D_{anion} is almost constant in whole temperature range studied for the sulfonylimide-based PILs, it decreases for DBUH-TFO. This means that the temperature has a different effect on the cation and

anion of this PIL (i.e. the TFO$^-$ experiences a higher diffusivity enhancement with the temperature increasing than the DBUH$^+$ cation). Indeed, the diffusion of the two ionic species is very close at 368 K (D_{cation}/D_{anion} = 1.07). This difference between imide and triflate-based PIL might be related to the different interactions: TFO$^-$ has a strong H-bond component which is, *per se*, very sensitive to the temperature, while this is not the case for IM14$^-$ and TFSI$^-$. Perhaps the weakening of the hydrogen bond network may be responsible for the fastest diffusion of TFO$^-$ with increasing temperature.
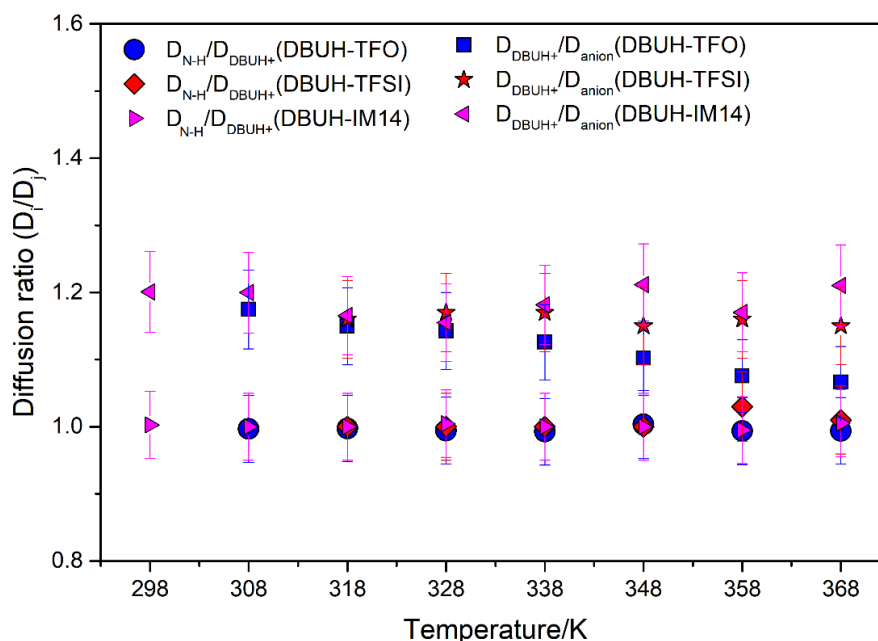
Figure 3.13. Self-diffusion ratios of the neat PILs as a function of temperature.

3.3.1.2. Self-diffusion coefficients of the PIL electrolytes

I then proceeded to study the effects of lithium doping in the translational motion and structural features of the PILs by evaluating the self-diffusion coefficients of the ion in the PIL electrolytes (Figure 3.14a-c). The raw data (Tables A3.1-A3.3) and best fitting parameters for the VFT (Table A3.4) and Arrhenius (Table A3.5) model for each ionic species are reported in the Appendix A3.

Looking at Figure 3.14a-c, it is worth mentioning that the presence of the Li$^+$ decreases the overall diffusion coefficients of the all the PILs' ions (filled vs. empty symbols). This is consistent with the visual increasing of the viscosity of the samples, and in agreement with results already reported for other ILs doped with lithium salts[129]. Besides, the relative diffusivities follow the order D_{cation} > D_{anion} > D_{Li+} and similar trends have been already reported for other ILs. The low values of D_{Li}^+ have been explained by molecular dynamics simulations[130] and experimental studies[131], which

demonstrated that Li⁺ cation is generally anion coordinated and exists as a distribution of complexes of varying sizes. Because of the coordination, the Li⁺ diffusivity is much lower than expected.
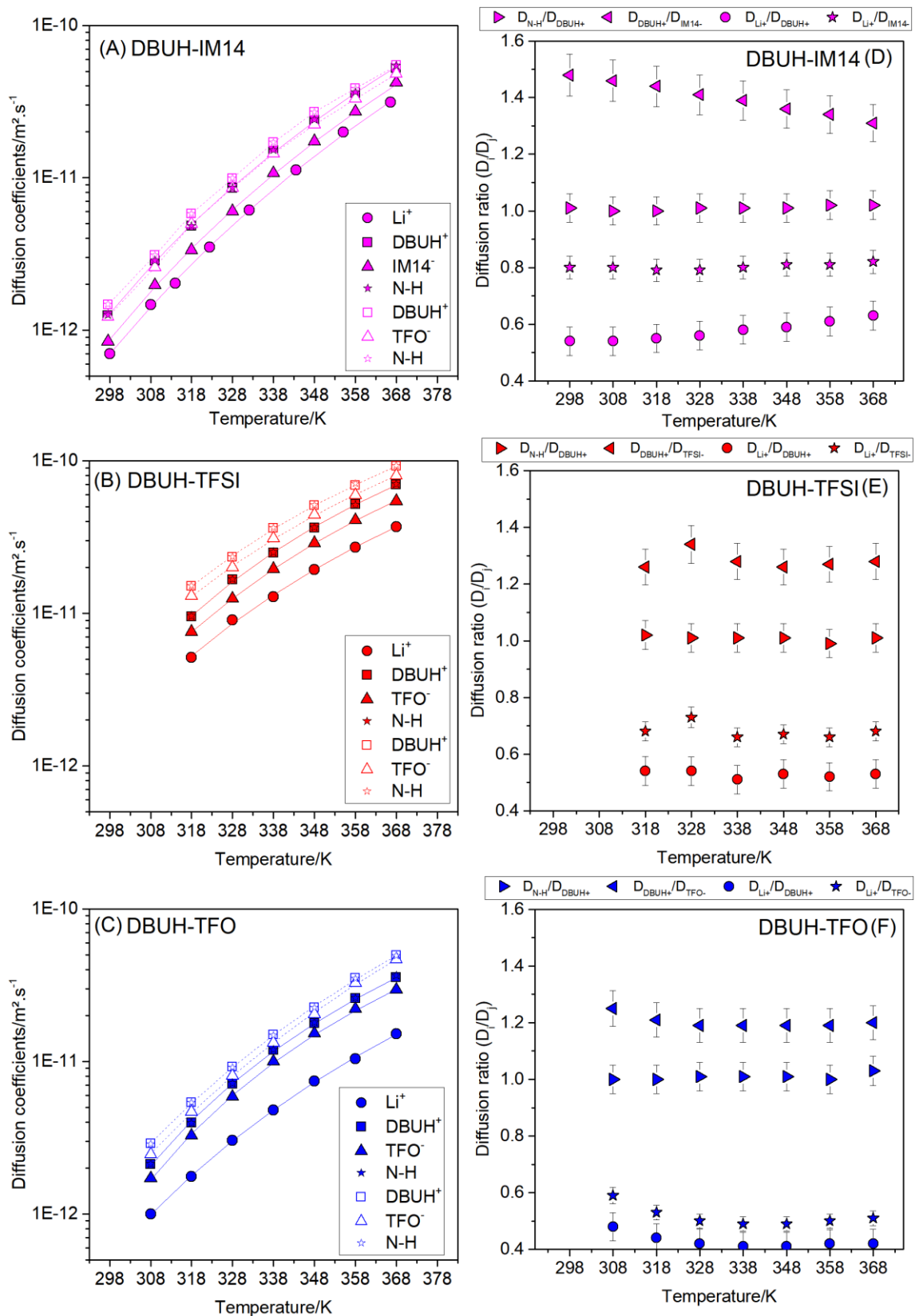
Figure 3.14. Self-diffusion coefficients of the (a) DBUH-IM14, (b) DBUH-TFSI (c) DBUH-TFO neat PILs (empty symbols) and PIL electrolytes (filled symbols), and diffusion ratios of the (d) DBUH-IM14, (e) DBUH-TFSI (f) DBUH-TFO PIL electrolytes as a function of temperature.

Interestingly, the relative diffusion (Figure 3.14d-f, Tables A3.6-A3.8) of the D_{Li+}/D_{anion} follows the order $D_{Li+}/D_{IM14-} > D_{Li+}/D_{TFSI-} > D_{Li+}/D_{TFO-}$. It seems that the size and shape of the large and asymmetrical anion IM14$^-$ favors the relatively faster Li$^+$ diffusion in respect to the anion. The distribution of the values observed for the diffusion of Li$^+$ relative to the anion of the PIL further suggests the dependence of Li$^+$ transport mechanism upon the structural features of the anion. From molecular dynamics (MD) simulations, it is known that the vehicular mechanism[130] (i.e., the diffusion of Li$^+$ with its solvation shell) contributes less to the net Li$^+$ diffusion, whereas structural diffusion mechanism[129] (i.e., Li$^+$ transport through exchange of the anions in the first solvation shell via the steps of disruption–diffusion–reformation of the solvation shell of Li$^+$) is more favored to occur[132]. To get a precise estimation of how much the structure diffusion and vehicular mechanism accounts for the Li$^+$ transport, MD simulations are highly recommended and will be part of a follow-up of the present work. However, the trend of the D_{Li+}/D_{anion} may provide a first indication of the dynamics of the disruption-reformation of the Li$^+$ first solvation shell, confirming the unique effects of the distribution of the fluorinated pool of IM14$^-$ anions on the overall transport of Li ions.

Finally, it is worth mentioning that DBUH-IM14 is the only system for which the ratio between the diffusion coefficients of the cation and anion is appreciably affected by the temperature (D_{cation}/D_{anion} equal to 1.48 at 298 K and 1.31 at 368 K). Considering the D_{Li+}/D_{IM14-} remains constant as the temperature rises ($D_{Li+}/D_{IM14} \approx 0.80$), whereas D_{Li+}/D_{cation} slightly increases (from 0.54 at 298 K to 0.63 at 368 K), one can rationalize that the mobility of the DBUH$^+$ cation is increased at a slower pace than the diffusivity of anion and Li$^+$. In other words, the effect of temperature on lithium and IM14$^-$ anion is comparable (i.e., D_{Li+}/D_{IM14-} is constant in the whole temperature range), but is less marked on the cation (i.e., IM14 diffusivity increases faster than DBUH$^+$ diffusivity, so that D_{cation}/D_{anion} appreciably decreases). Once again, MD simulations are expected to get more insight into these findings.

A related observation regarding the diffusion ratio is that, unlike the neat PIL, the ratio D_{cation}/D_{anion} is almost constant in whole temperature range for the Li-doped DBUH-TFO (from 1.25 at 298 K to 1.20 at 368 K). This means that the addition of lithium changes the dynamic response of DBUH$^+$ cation and TFO$^-$ anion to the temperature increase, probably due to the coordination Li-TFO. Although a clear-cut model is unrealistic at moment, it seems that the Li$^+$ solvation shell formation - disruption dynamics (see above) is different in DBUH-IM14 than in DBUH-TFSI and DBUH-TFO, thus highlighting again the unique structural features of the IM14$^-$ anion.

Similar considerations can be drawn from the translational activation energies (E_a^{transl}) extracted from the Arrhenius model (Table A3.5):

(i) In neat PILs, E_a^{transl} follows the order [E_a^{transl}(IM14⁻) = 47.01 kJ.mol⁻¹] ≈ [E_a^{transl}(TFO⁻) = 46.06 kJ.mol⁻¹] > [E_a^{transl}(TFSI⁻) = 35.31 kJ.mol⁻¹]. TFSI shows the lowest translational activation energy, in line with the highest diffusion coefficients in the explored T range. A possible explanation may be found in the two major sources of intermolecular interactions: anion-cation H-bond and fluorophilic dispersive forces. While in the IM14⁻ and TFO⁻ based PILs the two interactions mutually compensate (i.e. TFO⁻: strong H-bond and weak fluorophilic interactions, IM14⁻: weak H-bond and intense fluorophilic interactions), TFSI⁻ is in an imbalanced situation (weak H-bond and weak fluorophilic interactions) leading to low activation energy for the translation with respect to the other two PILs.

(ii) The effect of Li⁺ doping on the activation parameters of DBUH-TFSI is totally non-selective, as it affects in the same way the E_a^{transl} of all the components (ca. 3 kJ.mol⁻¹increase, see corresponding values in Table A3.5). The activation energy for Li⁺ translation is ca. 1 kJ.mol⁻¹ below that of TFSI⁻
.

(iii) DBUH-TFO shows a weak response to the Li salt doping and with different features compared to the TFSI-analogue: E_a^{transl} of the cation is not changed, that of the anions is slightly lowered (less than 1 kJ.mol⁻¹). Finally, the activation energy for Li⁺ translation is ca. 2.5 kJ.mol⁻¹ below that of TFO⁻ anion.

(iv) DBUH-IM14 electrolyte shows distinct patterns upon Li salt addition. Cation: is a moderate increase of E_a^{transl}(DBUH⁺) (ca. 1 kJ.mol⁻¹). Anion: the effect is higher than the one observed on the cation (ca. 3 kJ.mol⁻¹ increase). Noticeably, the activation energy determined for Li⁺ is the same as that of IM14⁻.

(v) Finally, it is worth summarizing the picture of the activation energy of the Li⁺. For the DBUH-TFSI and DBUH-TFO samples, E_a^{transl}(Li⁺) is smaller than the activation energy of the cation and anion (i.e. E_a^{transl}(Li⁺) = 37.77 and E_a^{transl}(Li⁺) = 42.60 for DBUH-TFSI and DBUH-TFO electrolytes, respectively). Instead, for the DBUH-IM14 electrolyte E_a^{transl}(Li⁺) is on the upper limit (very close to the activation energy of the anion; E_a^{transl}(Li⁺) = 50.46)

Therefore, the overall picture emerging from the diffusion data stress out the peculiarity of DBUH-IM14 and its electrolyte, once again suggesting a close relationship between the structural features of the IM14⁻ anion and the dynamic properties observed in the corresponding electrolyte. In turn, this again calls for a detailed

simulation work to provide further physical insights. Finally, to quantify the relative mobility of Li$^+$ ions with respect to other species in the mixture one can calculate the apparent transference number, which is the fractional contribution of an ion species to the overall conductivity[124]. Indeed, all ions in the system contribute to the total current, but Li$^+$ ion transport is crucial for the charge/discharge process of LIBs[133]. Under the assumption of the ideality of the investigated electrolyte (i.e., that all ionic species are free neglecting the presence of ion pairs and/or ion clustering), the apparent transference number for Li$^+$ (t_{Li+}) can be calculated from NMR diffusion experiments as given by Eq. 3.9:

$$t_{Li^+} = \frac{D_{Li}x_{Li}}{D_{Li}x_{Li} + D_{DBUH+}x_{Li} + D_{anion}x_{anion}} \tag{3.9}$$

with x$_i$ the molar fraction of the *i*-th component[133].

The t_{Li+} obtained for the PIL electrolytes investigated in this thesis are shown in Figure 3.15. Calculated transference numbers for all the ionic species in the neat and PIL electrolytes are reported in Table A3.9 of Appendix A3.
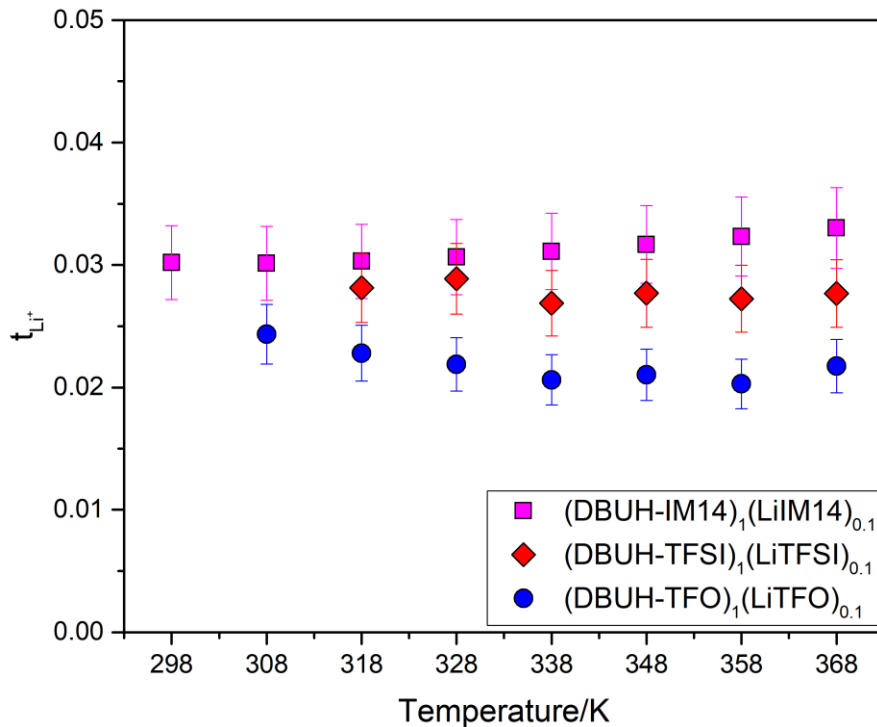
Figure 3.15. Apparent transference number t_{Li+} for the lithium ion in the investigated PIL electrolytes.

For all the studied PIL electrolytes (x$_{LiSalt}$ = 0.09), t_{Li+} < 0.04 with a negligible changing when increasing the temperature, and t_{Li+} follows the order t_{Li+}(DBUH-IM14)$_1$(LiIM14)$_{0.1}$ ≈ t_{Li+}(DBUH-TFSI)$_1$(LiTFSI)$_{0.1}$> t_{Li+}(DBUH-TFO)$_1$(LiTFO)$_{0.1}$. The low apparent

transference numbers calculated for the studied PIL electrolytes are in line with transference numbers found for other mixtures of ILs and lithium salts at similar concentrations (i.e, t_{Li+} is below 0.04 for $[PYR_{14+}][TFSI][134]$, $[Pyr_{12O1}][FTFSI][131]$ and $[emim][BF_4][135]$ containing x_{LiSalt} around 0.1). Typically, lower salt concentrations in IL-based electrolytes compared to organic solvent-based electrolytes, along with the higher viscosity and lower conductivity, contributes to the poorer rate performance of the Li-containing IL electrolytes in the same cell configuration[136]. As the salt concentration in the electrolyte increases, t_{Li+} also tends to increase significantly due to the higher Li^+ availability at the electrodes, which likely is the primary reason for the improved rate capability. Therefore, further investigations on developing other PIL electrolytes should consider higher salt concentrations.

3.3.2. Spin−lattice relaxation times T_1 for ^1H, ^{19}F, and ^7Li

To gather a more complete overview of ion dynamics in the studied system, ^1H, ^{19}F and ^7Li T_1 relaxation times were measured as a function of temperature, and are reported in Appendix C3, Tables C3.1-C3.4. The corresponding relaxation rates R_1 – which is simply $1/T_1$ – are displayed in Figures 3.16 and 3.18. Once again, I remind that the spin-lattice relaxation constant measured on the ^1H peak of the N-H proton is indicated with the short notation R_1(N-H).

3.3.2.1. ^1H spin−lattice relaxation times T_1

Employing spin-lattice relaxation times and rates, I could investigate the ion dynamics of the PILs and the effects of lithium doping on the dynamics of the systems. Figure 3.16 shows that R_1 of DBUH protons increases with increasing temperature, reaches a maximum at the temperature $T_{R1,max}$, and then, decreases. This indicates that these nuclei undergo a transition from the diffusion limit (slow motion, characteristic of viscous systems and/or low temperatures and/or molecules having large size) to the extreme narrowing (fast motion, characteristic of fluid systems and/or high temperatures and/or molecules having small size).

Figure 3.16. ^{1}H spin-lattice relaxation rates R_1, as a function of temperature, measured for neat (a) DBUH-IM14, (b) DBUH-TFSI and (c) DBUH-TFO PILs (empty symbols) and PILs electrolytes (filled symbols)

It is convenient here to define $R_{1,max}$, the maximum of R_1; $T_{R1,max}$, the temperature of $R_{1,max}$, as obtained by derivative method ($dR_1/dT = 0$); and $\Delta T_{R1,max}$, the temperature shift of $R_{1,max}$ from the neat PIL to the PIL electrolyte ($\Delta T_{R1,max} = T_{R1,max}$(PIL electrolyte) $-$ $T_{R1,max}$(neat PIL)). A first look at Figure 3.16 reveals that the amplitude of $R_{1,max}$ is not significantly influenced by the presence of Li$^+$ (except for the N-H of the DBUH-IM14, empty and filled blue squares in Figure 3.16a). However, $R_{1,max}$ is shifted to higher temperatures ($\Delta T_{R1,max} > 0$) in all PIL electrolytes (Table C3.5 in Appendix C). This means that the transition from a slow motion regime to a fast motion regime occurs at higher temperature when Li is added to the PILs. In other words, the presence of the additional Li$^+$ ion into the system slows down the rotational motion of the DBUH cation in the three PIL electrolytes.

From a closer look it can be observed that in the case of DBUH-TFSI and DBUH-TFO (Figure 3.16b and 3.16c, respectively), $\Delta T_{R1,max}$ is comparable for all the protons of the DBUH$^+$ cation ($\Delta T_{R1,max} \approx 6.7$ K and 6.6 K, respectively, Table C3.5 in Appendix C3). Contrarily, for DBUH-IM14 (Figure 3.16a), a significant difference is observed between the N-H proton and the methylene protons of the DBU ($\Delta T_{R1,max} = 17$ K and ≈ 2.5 K, respectively). This would indicate that the presence of Li$^+$ has a stronger, and selective effect on the N-H on DBUH-IM14.

To obtain more quantitative information about the relaxation process, the relaxation rates R_1 were fitted, if possible, to the Bloembergen, Purcell, and Pound (BPP) model. The BPP model description is presented in the Appendix B3. Briefly, the BPP fit yields valuable indicators of the rotational motion at each site, namely the correlation time τ_c and the activation energy for the rotational motion E_a^{rot}. The BPP fitting parameters are presented in Tables C3.6-C3.8 in Appendix C3. As indicated above, the correlation time of the N-H vector is shortly indicated as τ_c(N-H).

The BPP model describes very well the relaxation rate of the protons of the DBUH$^+$ cation (Figure 3.17). As discussed more in detail in Appendix B3, under a predominant ^{1}H-^{1}H dipolar relaxation mechanism, the corresponding correlation times τ_c can be rationalized as the time taken for the molecule to rotate by roughly 1 radian about any axis[137] in the course of its random, isotropic tumbling . In the case of small rigid molecules τ_c usually reflects the molecular reorientational time constant instead for flexible molecules it has to be rather considered as a combination of molecular reorientation and internal motions of each given segment[138]. As observed in Figure 3.17 for the neat PILs (empty symbols), all the CH$_2$ groups of the DBUH$^+$ cation show very similar

τ_c profile. Accordingly, τ_c describes the whole-molecular motion, with only minor differences coming from the contribution of local motions.
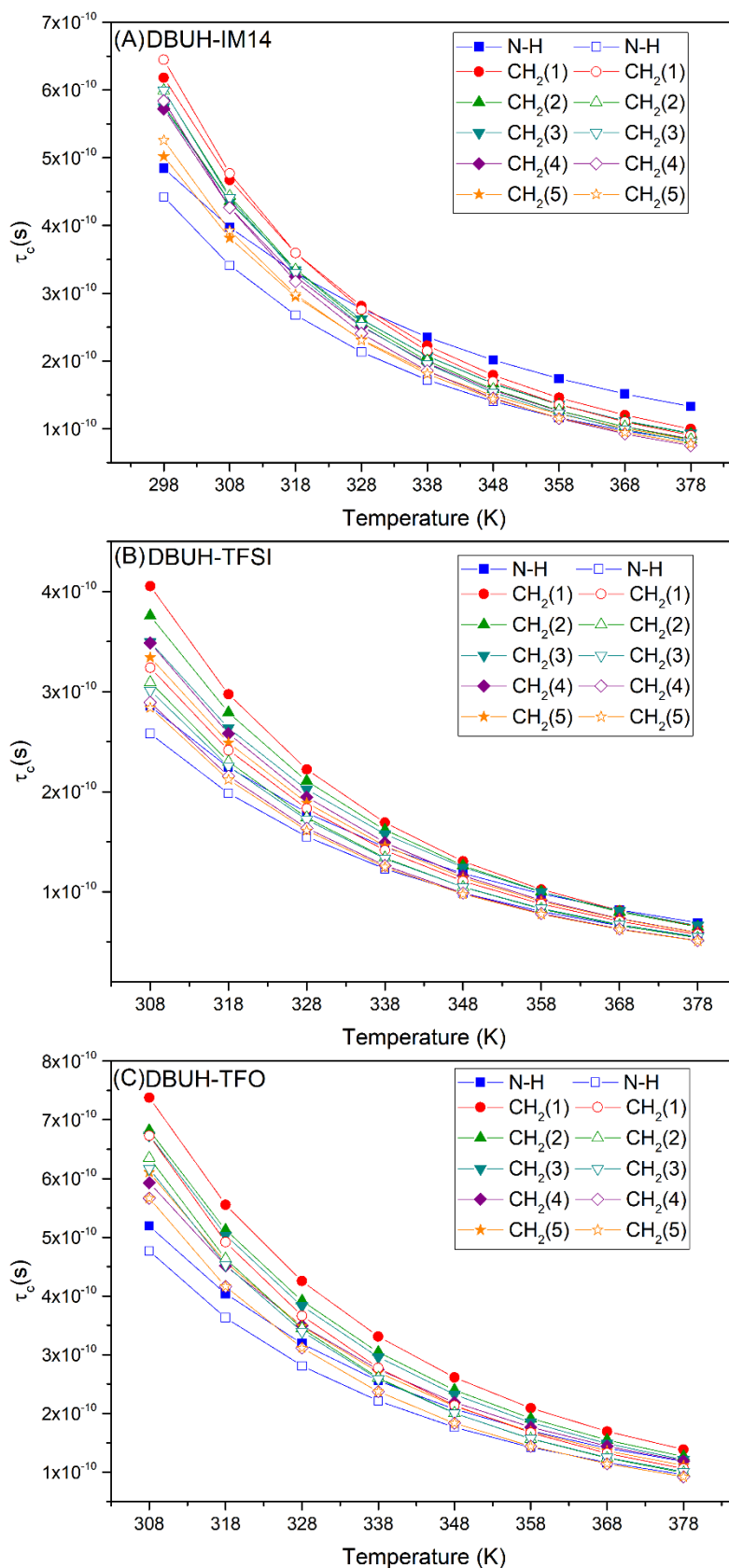
Figure 3.17. Reorientational correlation times τ_c as a function of temperature calculated for neat PILs (empty symbols) and PIL electrolytes (filled symbols), separated as follows: (a) ^{1}H of DBUH-IM14 and (DBUH-IM14)$_1$(LiIM14)$_{0.1}$. (b) ^{1}H of DBUH-TFSI and (DBUH-TFSI)$_1$(LiTFSI)$_{0.1}$; (c) ^{1}H of DBUH-TFO and (DBUH-TFO)$_1$(LiTFO)$_{0.1}$.

When considering the effects on the rotational motion of DBUH$^+$ cation upon addition of lithium salt (Figure 3.17, solid vs. empty symbols), it can be observed in all cases an increase of the correlation times describing the reorientational motion of the DBUH$^+$ cation (Tables C3.10-C3.11 in Appendix C3). As qualitatively deduced from Figure 3.17, the overall motion of the DBUH cation is reduced in the three PIL electrolytes. Such phenomenon is expected due to the viscosity effects, and similar findings have been already reported for other ILs[139]. In agreement with the above discussion on $\Delta T_{R1,max}$, for the PILs DBUH-TFSI and DBUH-TFO the slowing down of the rotational motion is comparable for all the protons (i.e., CH$_2$ groups of DBU and H$^+$) in the whole temperature range. Clearly, molecular motion of the DBUH$^+$ cation as a whole is maintained, and a homogeneous effect upon the lithium doping is detected. Surprisingly, for the DBUH-IM14, the effect of Li$^+$ into the system has a stronger impact in decreasing the rotational mobility of the N-H proton, than of the methylene protons of DBU, and at high temperatures (T > 328 K) τ_c(H$^+$) is even higher than τ_c(CH$_2$) (filled vs empty blue squares in Figure 3.17a). In other words, N-H is more responsive to the presence of Li$^+$ than the DBU as a whole, resulting in an anomalous increasing of N-H correlation time, and decreasing of its internal mobility. For the sake of clarity, let's consider these examples. Be the temperature T=368 K and let's evaluate the ratios τ_c(PIL electrolyte) / τ_c(neat PIL) in the case of N-H vs CH$_2$(1) of DBUH$^+$ in the three PILs studied (Tables C3.10-C3.12 in Appendix C3), the results are: 1.57 vs 1.09 for DBUH-IM14, 1.24 vs 1.15 for DBUH-TFSI, and 1.22 vs 1.28 for DBUH-TFO. In the case of the DBUH-TFSI and DBUH-TFO, the ratios between the correlation times are quite close for the N-H and the CH$_2$(1) of the DBUH$^+$. However, for the DBUH-IM14, there is a clear difference between the τ_c ratios of the N-H and CH$_2$(1), meaning that the N-H is more responsive to the presence of Li$^+$. These data suggest the pool effect of H-bond strength, amount of F atoms, size and distribution of the F atoms as factors affecting the responsivity of the N-H site of this set of PILs.

Comparing now the activation energy for the rotational motion (Tables C3.6-C3.8), E_a^{rot} of all the CH$_2$ protons of DBU is nearly the same in the three neat PILs (in the range 22-25 kJ.mol^{-1}), and remains almost unchanged upon lithium addition. A major effect on the E_a^{rot} due to the Li$^+$ was observed in the N-H proton of the DBUH-IM14. Indeed, a significant decrease of its activation energy is observed (ΔE_a^{rot}(N-H) = 4.6 kJ/mol). Contrarily, in the systems containing TFSI and TFO as the anion, E_a^{rot}(N-H) does not change markedly after Li addition (i.e., it remains in the range 20-22 kJ.mol^{-1}). These findings i) on the one hand confirm the unique behavior of IM14-based PILs and ii) on the other hand reinforce the model of the dynamic behavior of DBUH-IM14 modulated not only by the H-bond

properties of the N-H site, but also by the size and symmetry of the anion.

3.3.2.2. ^{19}F spin−lattice relaxation times T_1

Concerning ^{19}F R_1 relaxation rates, the BPP model describes quite well the relaxation profile of CF_3 groups of the DBUH-TFSI and DBUH-TFO PILs and PIL electrolytes (Figure 3.18, blue and red symbols). Note that the contribution of the internal rotation around the three symmetrical axes to the relaxation mechanism of the CF_3 groups has to be considered for TFSI$^-$ and of TFO$^-$ anions, as previously reported for TFSI-based ILs (see Appendix B3 for more details)[140]. Tables C3.11-C3.12 and Figure 3.19 show that τ_c(CF_3) DBUH-TFO > τ_c(CF_3) DBUH-TFSI, likely due to viscosity effects. In both cases, the addition of lithium salt causes an increase of R_1, mostly in the TFO (Figure 3.18b), and a corresponding increase of τ_c (Figure 3.19), suggesting that the ^{19}F rotational motion in the CF_3 groups was significantly reduced with respect to the neat PIL. Interestingly, this effect is stronger in the high temperature region, with τ_c at 308 K practically overlapping in the PIL and PIL electrolyte. Moreover, E_a^{rot} are reduced in both cases upon addition of lithium of 2-3 kJ.mol^{-1}. These counterintuitive observations suggest that even if the BPP model fits the R_1 profiles, the relaxation behavior cannot be easily interpreted.
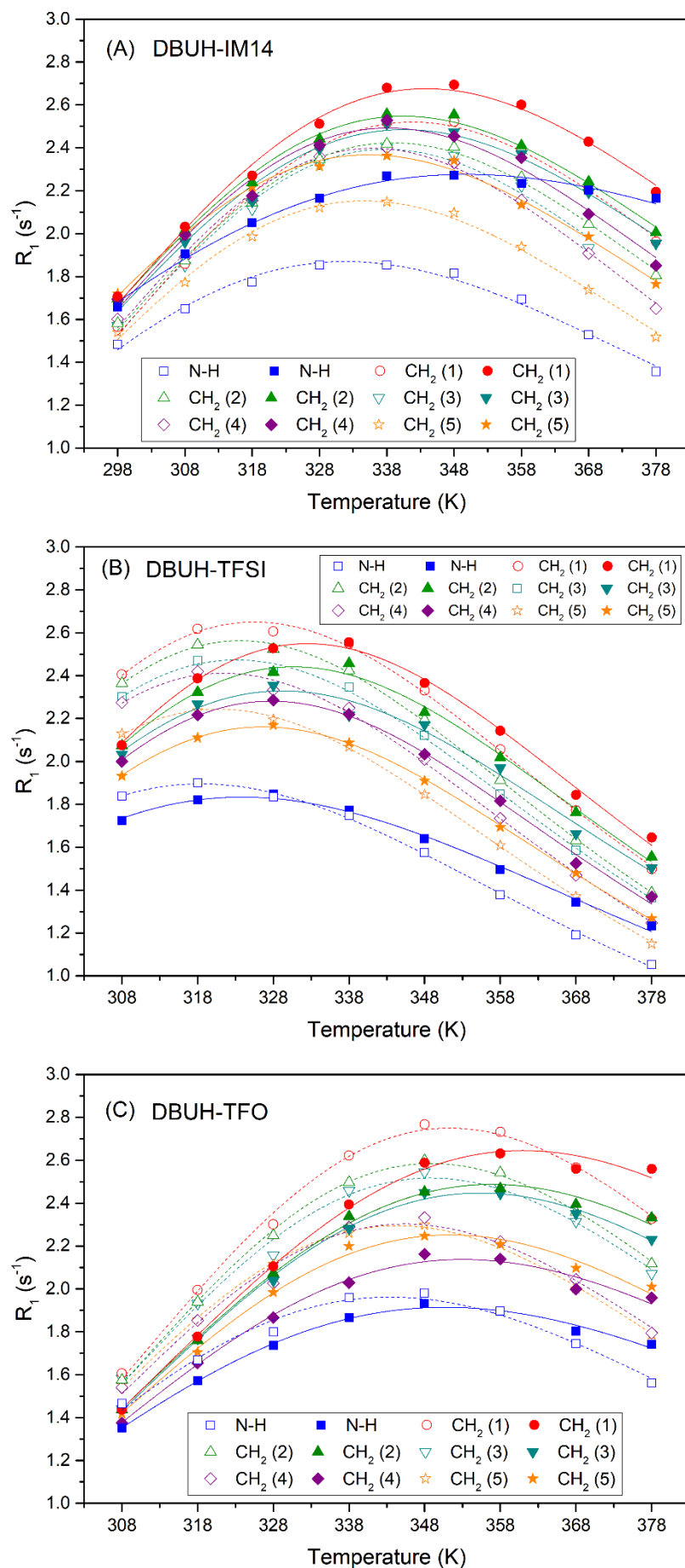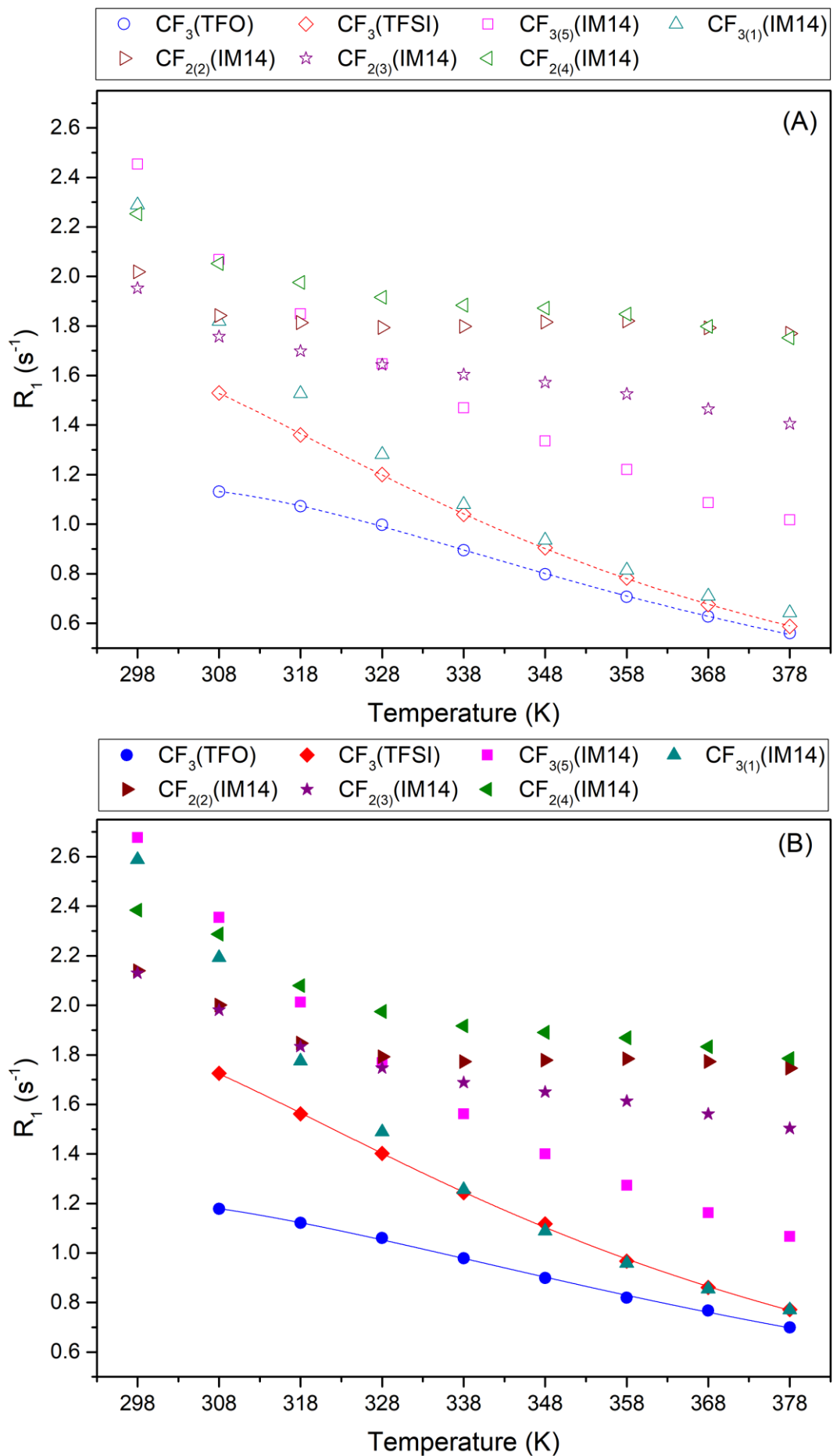
Figure 3.18. ^{19}F spin-lattice relaxation rates R_1, as a function of temperature, measured for neat (a) DBUH-IM14, (b) DBUH-TFSI and (c) DBUH-TFO PILs (empty symbols) and PILs electrolytes (filled symbols).
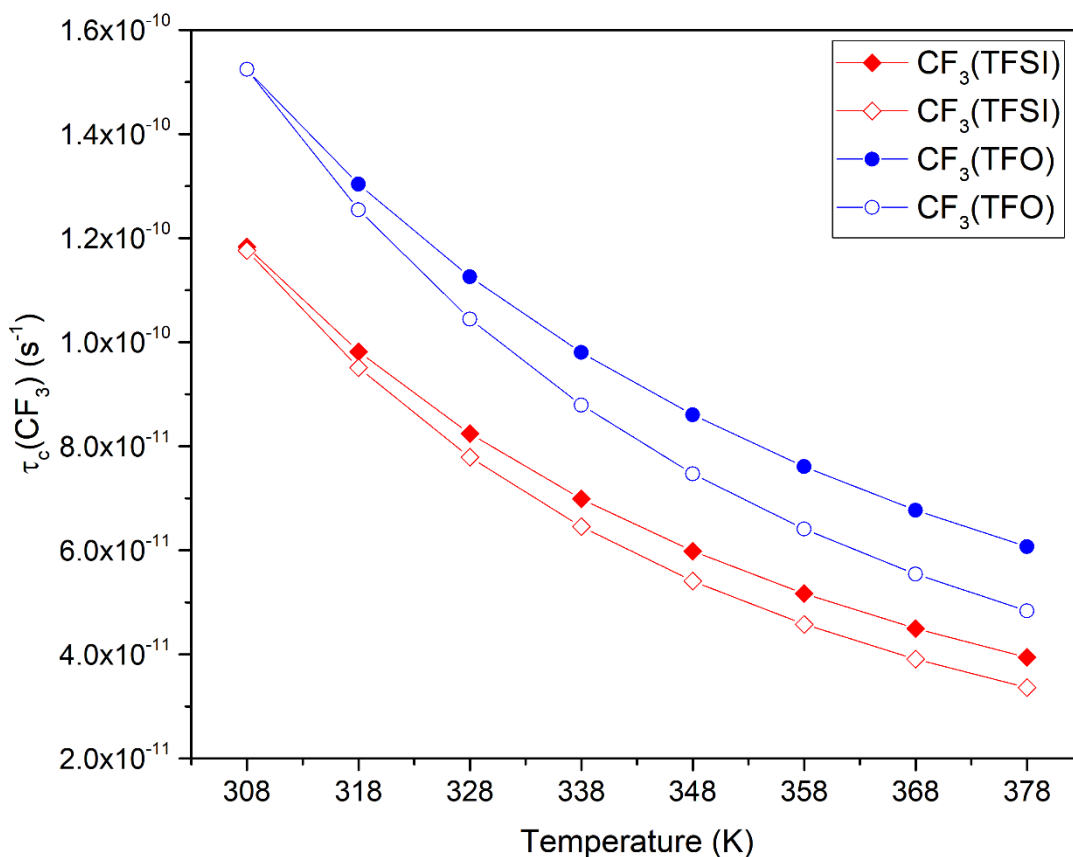
Figure 3.19. ^{19}F reorientational correlation times τ_c as a function of temperature calculated of for neat PILs (empty symbols) and PIL electrolytes (filled symbols).

For the CF_3 groups of the IM14, the BPP model fails to describe the ^{19}F relaxation behavior. Here, the trifluoromethyl group, labeled as $CF_3(5)$, located at the edge of the perfluoroalkyl chain, has shorter relaxation times than the $CF_3(1)$ (Table C3.2 in Appendix C3). Interestingly, the curves of the $CF_{3(1)}(IM14)$ and $CF_3(TFSI)$ almost overlap from 338 K on (Figure 3.18, green triangles and red diamonds, respectively), thus suggesting a change in the combination of relaxation mechanisms contributing to the relaxation profile, and a similarity in the relaxation mechanisms at higher temperatures between $CF_{3(1)}(IM14)$ and $CF_3(TFSI)$ in both PILs and PIL electrolytes. I then attempted to fit the R_1 profiles of $CF_3(1)$ and $CF_3(5)$ of IM14 in two portions (298-338 K and 348-37K), where the curves show a linear trend. In such extreme narrowing condition, an approximate approach can be applied (see Appendix B3) and the E_a^{rot} was directly estimated from the Arrhenius plot of the temperature-dependent T_1 values (Table C3.9). While two different E_a^{rot} are obtained for $CF_3(1)$ in both PIL and PIL electrolyte (ca. 15 and 13 kJ.mol^{-1}), very close values are extracted for $CF_3(5)$ (ca. 10 kJ.mol^{-1}). A clear explanation for such behavior is not available so

90

far, and more experimental points are needed to increase the accuracy of the extracted E_a^{rot} in the two temperature intervals.

Interpretation of the ^{19}F relaxation results of the CF_2 groups of IM14^{-} (Figure 3.18) is even less straightforward because the observed R_1 dependences are not symmetric with the temperature. The R_1 profiles do not obey to the BPP model and do not show wide enough linear regions for the extreme narrowing approximation to be applied. Concerning the effect of Li doping on ^{19}F local dynamics in both the methyl and methylene groups of the IM14^{-} anion, Figures 3.18(b) show that the addition of lithium salt causes an increase of R_1. Similarly to the methyl groups of TFSI[-] and TFO[-], this indicates that the ^{19}F rotational motion was reduced with respect to the neat PIL, as expected.

Some general qualitative considerations on the relaxation behavior of fluorine nuclei can be drawn if one considers the R_1 profiles all together (Figure 3.18). $CF_3(TFSI)$, $CF_3(TFO)$ and $CF_{3(1)}(IM14)$ exhibit the shortest R_1 (longest T_1, see Tables C3.2-C3.4) in both PILs and PIL electrolytes, and they almost overlap in the high temperature region. Given that short R_1 qualitatively translate into short τ_C, and that for flexible molecules τ_C is a combination of molecular reorientation and internal motions (Appendix B3), this would mean that the rotational motion of these methyl groups corresponds to (or is the closest to) the molecular reorientation. Other relaxation mechanisms add up when looking at $CF_{3(5)}(IM14)$ and the three CF_2 groups of IM14. Among them, spin diffusion likely plays a major role, considering the structure of the perfluorobutyl chain, and this holds true especially at low temperatures. Also, intermolecular dipole-dipole interactions may likely contribute, considering that IM14^{-} is known to create fluorophilic domains in ILs. However, other relaxation mechanisms can contribute to the higher R_1 measured at these fluorine sites, and at present we cannot formulate any hypothesis on the relative contribution of the different relaxation mechanisms to the observed R_1 profiles of each IM14^{-} fluorine sites. However, we may speculate that this behaviour relies again upon the peculiar features of the IM14^{-} anion and its known capability to generate fluorophilic domains in ILs.

3.3.2.3. [7]Li spin−lattice relaxation times T_1

The temperature dependences of $R_1(Li^+)$ in the three PIL electrolytes are shown in Figure 3.20. In all cases, the BPP equation for quadrupolar [7]Li was successfully applied, and the activation energy for the Li^{+} motion was estimated (Tables C3.8 in Appendix C3). For the DBUH-TFSI and DBUH-TFO, activation energies were 20.4 kJ.mol^{-1} and 23.4 kJ.mol^{-1}, respectively. For TFSI-based ILs, activation energies around 20 kJ.mol^{-1} are reported for a salt

concentration ranging from 0.16 mol.kg^{-1} to 0.86 mol.kg^{-1}.[141,142] These results are in good agreement with our findings.
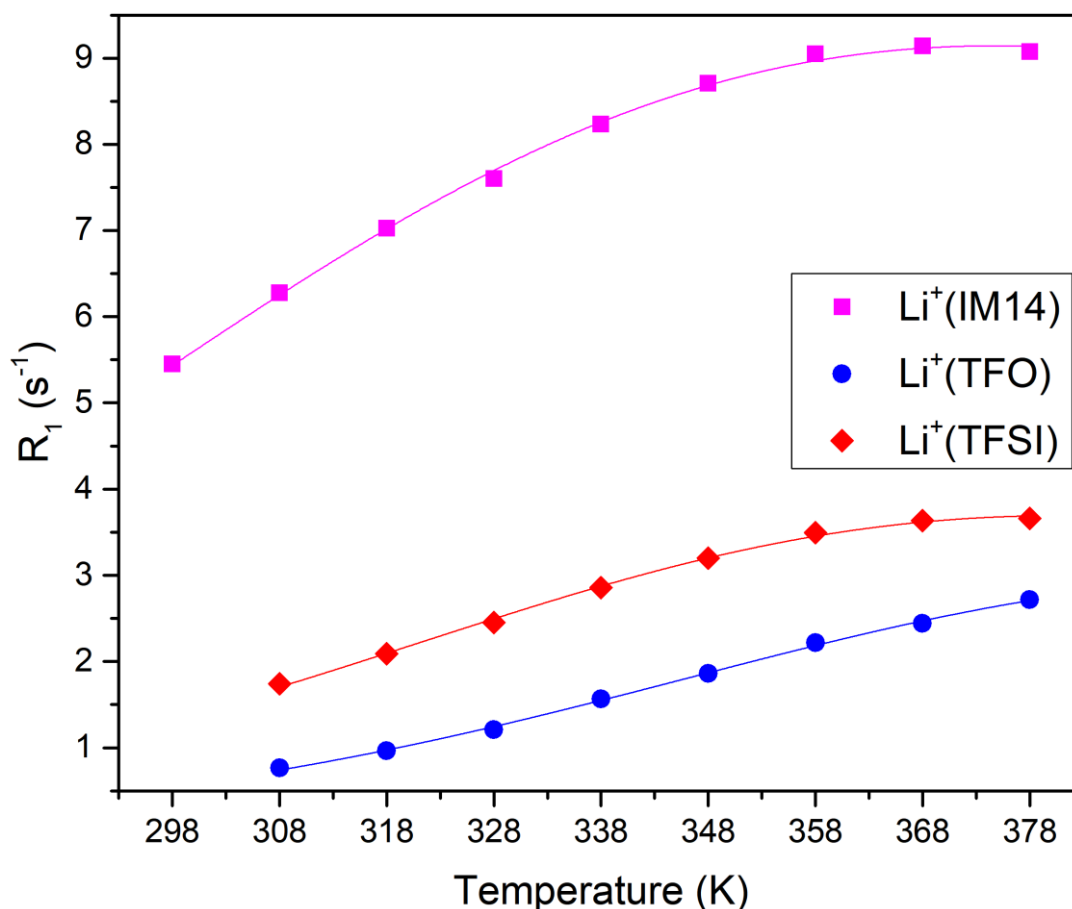
Figure 3.20. [7]Li spin-lattice relaxation rates R$_1$, as a function of temperature, measured for neat (a) DBUH-IM14, (b) DBUH-TFSI and (c) DBUH-TFO PILs electrolytes.

The most interesting finding comes from the DBUH-IM14 results. In this case, the activation energy of Li$^+$ motion is significantly lower than in the other PILs electrolytes (E$_a$ = 14.7 kJ.mol^{-1}). I wish to remind here the key concept of the interpretation of [7]Li relaxation data highlighted in Appendix B3. Indeed, τ_c([7]Li) (Figure 3.21a) obtained via T$_1$ measurements is related to the one-flip time of the translational displacement[140,143]. Thus, the activation energy for [7]Li τ_c refers to the energy barrier for the Li$^+$ jump. It is quite clear that the anion nature – IM14$^-$ on the one side, TFSI$^-$ and TFO$^-$ on the other – is driving the motion of Li$^+$ in the PILs' set examined here. Also, the findings on τ_c([7]Li) activation energies matches well with the diffusion coefficient discussion of the previous section and consolidate the conclusion that IM14$^-$ is favouring the motion of Li$^+$ ions.

Taking that the values of D$_{Li}$ obtained by the PFG NMR measurements correspond to the short-range diffusion, one can

consider τ_c(^{7}Li) as a descriptor of a single lithium jump from one place to another. The estimated average jump distances $\langle R_{one-flip} \rangle$, shown in Figure 3.21b, ranged for the three PIL electrolytes between 0.1 and 0.4 nm (Table C3.13), which is close to other Li-doped ILs[142,144]. $\langle R_{one-flip} \rangle$ became longer with increasing temperature, and below 358 K, it was in the order (DBUH-TFSI)$_1$(LiTFSI)$_{0.1}$ > (DBUH-TFO)$_1$(LiTFO)$_{0.1}$ > (DBUH-IM14)$_1$(LiIM14)$_{0.1}$. Notably, at high temperatures (i.e., from 358 K on), the averaged one jump distance of the Li$^+$ in (DBUH-IM14)$_1$(LiIM14)$_{0.1}$ significantly increases, getting longer than in (DBUH-TFO)$_1$(LiTFO)$_{0.1}$. Considering that the lithium jump takes place within the coordination sphere surrounded by anions[139–142,145], it seems that the coordination shell is significantly more responsive to the temperature in the PIL containing the anion with long perfluoroalkyl chain in comparison with the other two PILs with shorter fluorinated groups. This finding nicely matches also the previous relaxation results found for CF$_{3(1)}$(IM14), where a change in the relaxation behavior was observed on going from low to high temperatures.

Finally, plotting the self-diffusion coefficient measured for lithium, D_{Li}, versus $1/\tau_c$(^{7}Li) (Figure 3.22) one can evaluate the one-directional diffusional displacement of the Li$^+$ ion[142,145]. Figure 3.22 reveals a similar trend for DBUH-TFSI and DBUH-TFO. Both plots show separated linear regions with two different gradients (α). The distances obtained from the gradients $\sqrt{\alpha}$ correspond to the one-directional diffusional displacement of lithium per flip. For these PILs, the diffusional displacement ranges from 0.12 nm to 0.19 nm (Table 3.1), in accordance with previous reports for ILs[142,145]. For the DBUH-IM14, the plot is somehow non-linear. To get reasonable linear fittings, the data were thus divided into three different gradients. As shown in Table 3.1, the Li$^+$ diffusional displacement in DBUH-IM14 shows a remarkable increase at higher temperatures ($\sqrt{\alpha}$ = 0.24 nm in the temperature interval 358-378 K) and considering that lithium ion is always solvated by anions, this enhancement is a valuable experimental descriptor for validation of coming-up MD simulations.
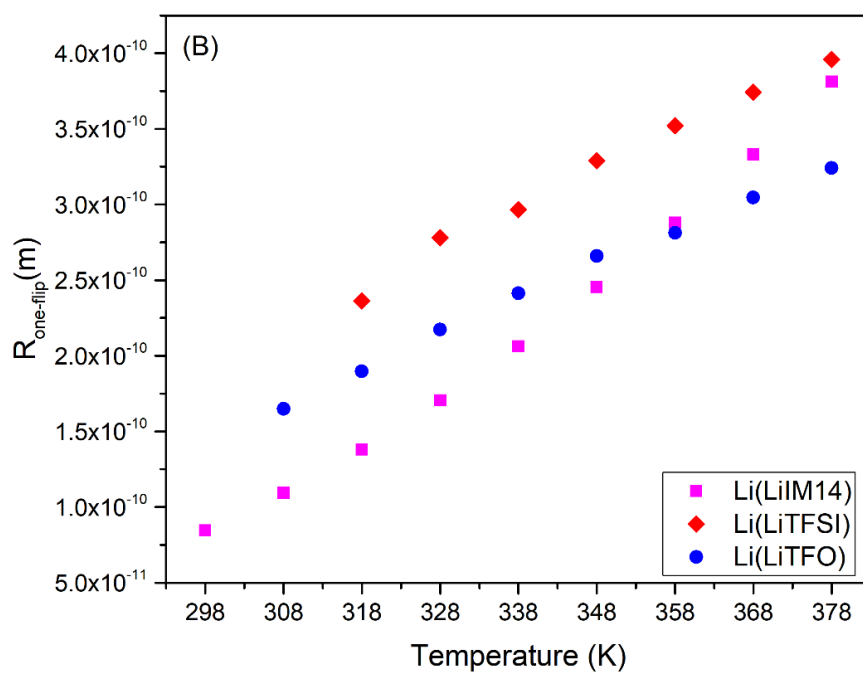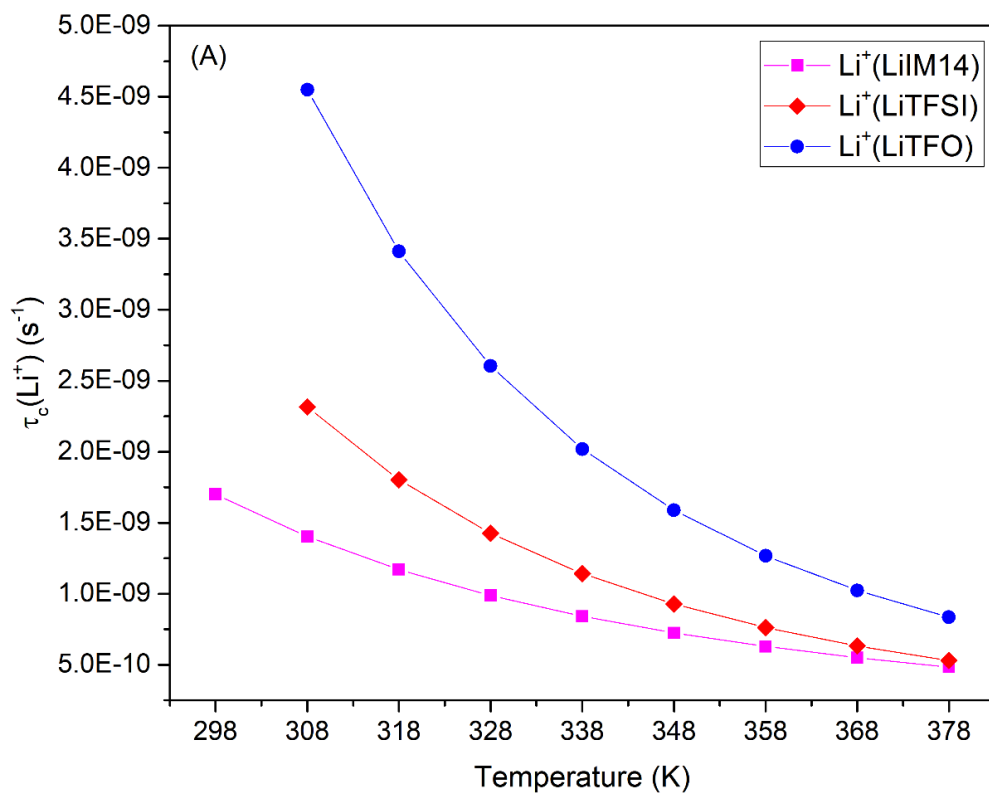
Figure 3.21. (a) [7]Li reorientational correlation times τ_c as a function of temperature calculated for all PIL electrolytes Li⁺; (b) Averaged Li⁺ one-jump distances.
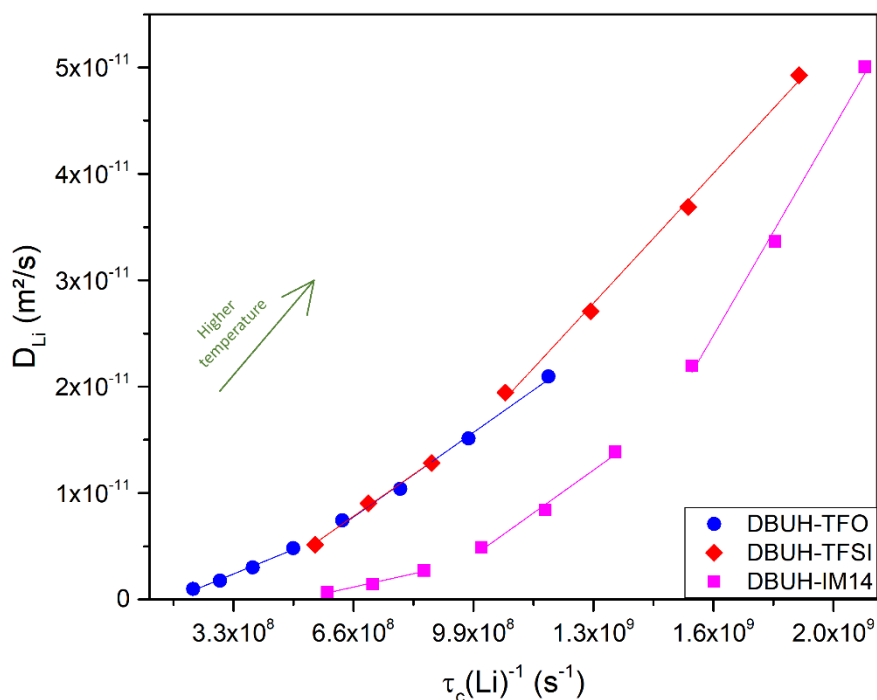
Figure 3.22. Plot of self-diffusion coefficient of lithium D_{Li} vs lithium jump rate $\tau_c(Li)^{-1}$

Table 3.1. Linear fitting gradients (α) and one-directional diffusional displacement ($\sqrt{\alpha}$) of lithium per flip.

	DBUH-TFO		DBUH-TFSI		DBUH-IM14		
T range (K)	308-338	348-378	318-338	348-378	298-318	328-348	358-378
α (m²)	1.39E-20	2.41E-20	2.39E-20	3.70E-20	7.60E-21	2.44E-20	5.91E-20
$\sqrt{\alpha}$ (m)	1.18E-10	1.55E-10	1.55E-10	1.92E-10	8.72E-11	1.56E-10	2.43E-10
R²	0.993	0.995	0.997	0.998	0.984	0.991	0.995

3.3.3. Density of the PIL electrolytes

The density (ρ) of the investigated PILs doped with lithium salts were measured as a function of temperature and experimental values are shown in Figure 3.23. The densities of all the samples show the typical linear decrease with rising temperature, and the linear fitting parameters as well as the raw data are reported in Table D3.1 and Table D3.2 in Appendix D3, respectively.

Comparing the density of PILs (section 2.3.6, Chapter 2) and PIL electrolytes, it is possible to see that ρ of DBUH-TFSI and DBUH-TFO is almost equally affected by the presence of Li salt ($\Delta\rho = \rho$(PIL electrolyte) – ρ(PIL) = 0.02 g.cm^{-3}). Contrarily, the density of DBUH-IM14 is almost unchanged upon lithium doping. According to the literature, a relatively large ρ increase upon the lithium salt addition is indicative of the efficient packing of anion around cations[130] (i.e., the presence of lithium results in smaller interionic separations and thus higher density[35]). Then, it seems that IM14$^-$, the largest and asymmetrical anion, has the least "packing" ability. This point

should not be underestimated, especially in view of possible application of these PILs as gas sorbent materials. Nevertheless, any naive interpretation on the capability of absorbing gas as purely dependent on the presence of "holes" in the liquid should be avoided. Rather, this first indication of the packing ability in the selected PILs may represent a starting point of deeper and targeted studies with multidisciplinary approaches.
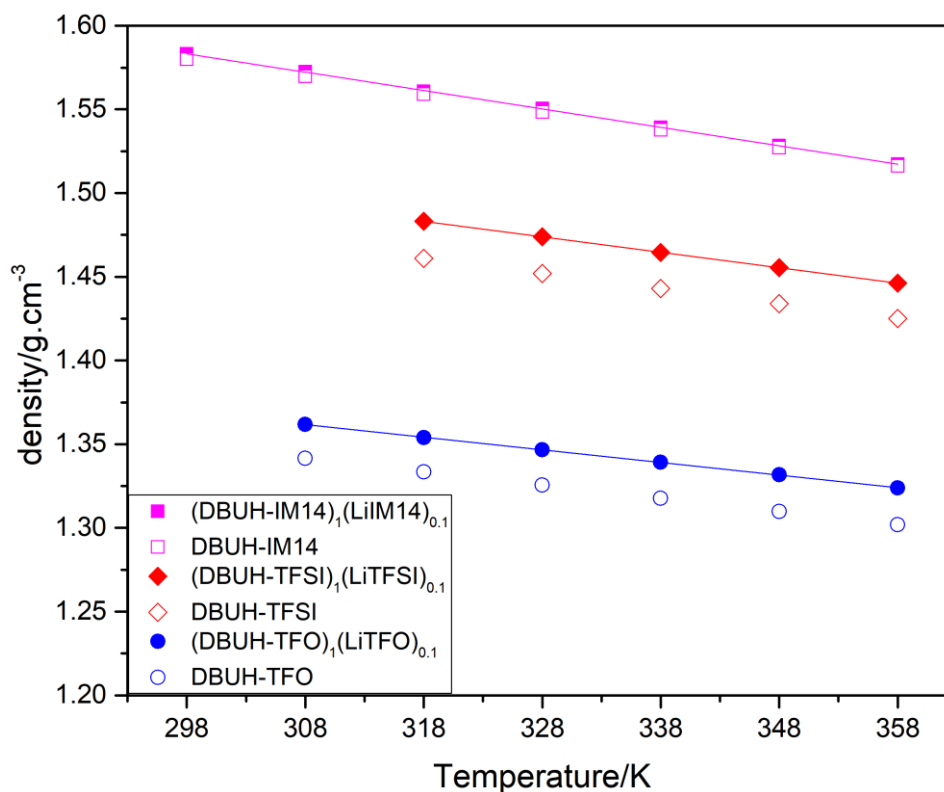
Figure 3.23. Density of the neat PILs and PIL electrolytes.

3.3.4. Specific and molar conductivity of the PIL electrolytes

The ionic conductivity of electrolytes is strongly influenced by the number and mobility of charge carriers throughout the system, which is, in principle, limited by the fluidity. As shown in *Chapter 2* (Section 2.3.8), the fluidity statement does not hold for the neat PIL DBUH-IM14, for which intermolecular interactions from the anion play a key role in lowering its ionic conductivity. A similar trend is observed here for the PIL electrolytes (experimental data reported in Table D3.3 and plotted in Figure 3.24). The specific conductivity σ follows the order: $\sigma[(DBUH\text{-}TFSI)_1(LiTFSI)_{0.1}] > \sigma[(DBUH\text{-}TFO)_1(LiTFO)_{0.1}] > \sigma[(DBUH\text{-}IM14)_1(LiIM14)_{0.1}]$.
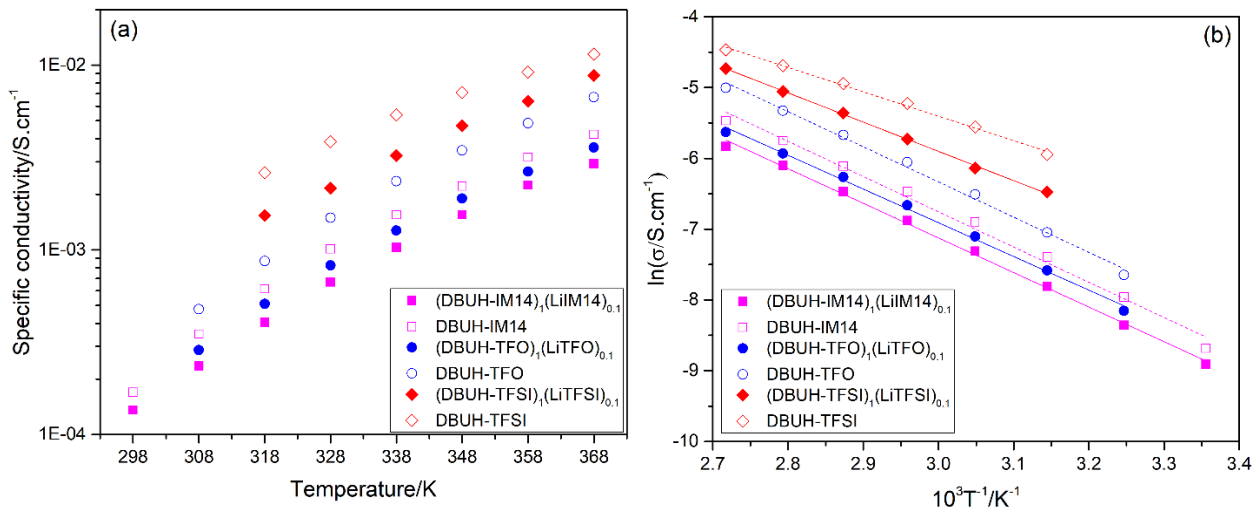
Figure 3.24. Specific conductivity (a) and its Arrhenius plot (b) of the PILs and PILs electrolytes as a function of temperature.

In all cases, the addition of lithium decreases the specific conductivity σ. When considering the effect of the lithium doping in the PILs, two factors must be accounted for as responsible of the lowering of the ionic conductivity: (i) viscosity increase due to the additional friction forces, (ii) decreased mobility of charge carriers due to the solvation of the ions. The Arrhenius fit of the ionic conductivity of both PILs and PIL electrolytes (Eq. 3.9), allowed us to isolate the effect of the lithium salt (Figure 3.24b and Table 3.2). Note that contrarily to the neat PIL, VFT model does not properly describe the ionic conductivity of the DBUH-TFSI electrolyte (the maximum number of interactions during the fitting is achieved and the parameters do not converge).

$$\ln\left(\sigma\right) = \ln\left(\sigma_0\right) - \frac{E_a}{RT} \tag{3.9}$$

Where E_a, R, T, and σ_0 are the activation energy for ion transport, universal gas constant, absolute temperature (K), and fitting parameter, respectively.

The specific conductivity of a liquid electrolyte is linked (i) to the fluidity which promotes ion diffusion, and (ii) to the available number of charge carriers[146,147]. When looking to the effect of the lithium salt on the activation energy of the ionic conductivity, obtained by the Arrhenius fitting, some assumption regarding the ion transport can be drawn. For instance, considering that the liquid electrolyte became more viscous when doping with lithium salt, an increasing in the activation energy would be expected (due to the reducing of fluidity). However, in the case of $(DBUH-TFO)_1(LiTFO)_{0.1}$ and $(DBUH-IM14)_1(LiIM14)_{0.1}$, a minor change in the activation energy upon the lithium addition is observed. This suggests that the conductivity and fluidity are not scaled as expected. In other words,

the fluidity is not the major factor responsible for the decreasing of the ionic conductivity of those PILs electrolytes, otherwise it would be reflected of the increasing of the activation energy. Consequently, the decreasing of the conductivity may arise from the interionic interactions (or the available number of charge carriers). Instead, DBUH-TFSI behaves as expected from its fluidity: a significant increase in the activation energy is detected when doping with lithium salt, probably due to a relevant change in the sample viscosity upon the lithium salt addition (i.e. the fluidity decrease and the activation energy of the ion conductivity became greater).

Table 3.2. Arrhenius fitting parameters for the temperature dependences on the ionic conductivity of the neat PILs and PILs electrolytes.

	E_a (kJ.mol^{-1})	σ_0 (S.cm^{-1})	R^2
DBUH-IM14	41.39	3.56E+03	0.993
(DBUH-IM14)$_1$(LiIM14)$_{0.1}$	40.64	1.89E+03	0.998
DBUH-TFSI	28.64	1.38E+02	0.997
(DBUH-TFSI)$_1$(LiTFSI)$_{0.1}$	34.32	6.55E+02	0.999
DBUH-TFO	41.28	5.23E+03	0.995
(DBUH-TFO)$_1$(LiTFO)$_{0.1}$	39.60	1.60E+03	0.997

Using the ionic conductivity and the density, the molar conductivity of the PIL electrolytes was calculated, as described in *Chapter 2 (Section 2.3.8)*. The obtained Λ values are listed in Table D3.4 and shown in Figure 3.25. The molar conductivity of both PILs and PIL electrolytes were fitted using the Arrhenius model (Eq. 3.10), with fitting parameters reported in Table 3.3.

$$\ln (\Lambda) = \ln (\Lambda_0) - \frac{E_a}{RT}$$

(3.10)

Where E_a, R, T, and Λ_0 are the activation energy for the molar transport, universal gas constant, absolute temperature (K), and fitting parameter, respectively.

Table 3.3. Arrhenius fitting parameters for the temperature dependences on the molar conductivity Λ of the neat PILs and PIL electrolytes.

	E_a (kJ.mol^{-1})	Λ_0 (S.cm^2.mol^{-1})	R^2
DBUH-IM14	42.00	1.69E+06	0.992
(DBUH-IM14)$_1$(LiIM14)$_{0.1}$	41.29	8.80E+05	0.998
DBUH-TFSI	29.24	5.11E+04	0.996
(DBUH-TFSI)$_1$(LiTFSI)$_{0.1}$	35.00	2.39E+05	0.999
DBUH-TFO	41.85	1.47E+06	0.995
(DBUH-TFO)$_1$(LiTFO)$_{0.1}$	40.13	4.19E+05	0.997

As stated before, the lowering in the molar conductivity due to the presence of the lithium salt is generally attributed to the enhancement of the ions interactions within the ionic liquid, which reduces the ion mobility or the number of active ion species. This point will be next discussed with the ionicity concept. From the Figure 3.25, it is clear that Li^+ has a stronger effect on lowering the molar conductivity in the DBUH-TFO than in the other PILs, probably due to the stronger Li^+ and TFO^- ion coordination.
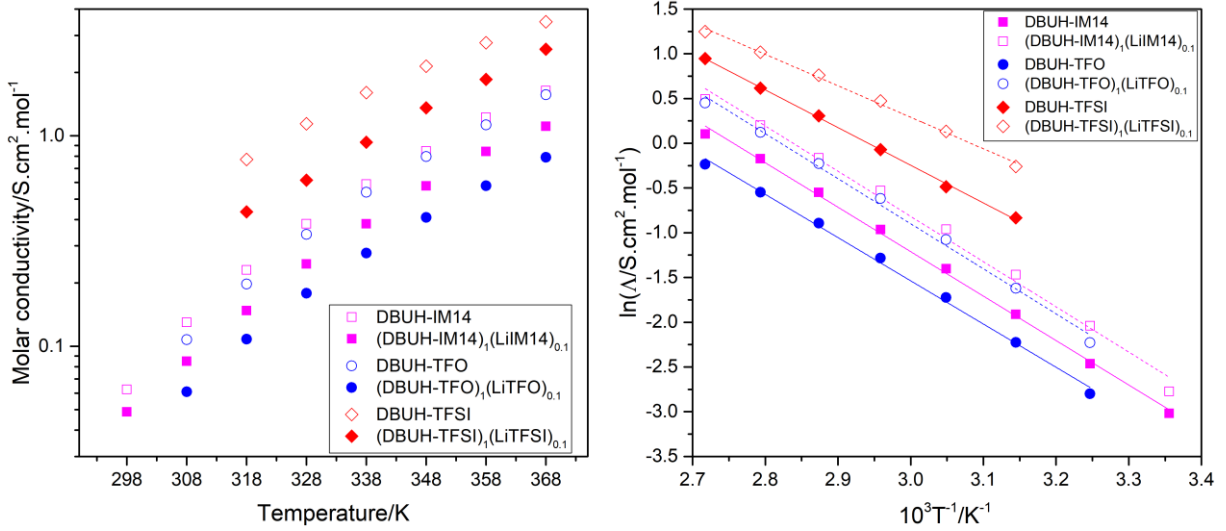
Figure 3.25. Molar conductivity (left panel) and Arrhenius plot (right panel) of the molar conductivity of the PILs and PILs electrolytes as a function of temperature.

3.3.5. Ionicity

In an ionic system, such as PIL and PIL electrolyte, the effective fraction of ions participating in the conduction process is estimated by the "ionicity"[103]. In *Chapter 2*, the ionicity obtained by the Walden plot has been introduced (*Section 2.3.9*). Here, the ionicity is quantitatively estimated using the inverse Haven ratio. According to this approach, the ionicity I_{HR} can be calculated by the ratio between the experimental molar conductivity Λ, which is derived from the EIS measurements, and the molar conductivity Λ_{NMR}, which is derived from the diffusion coefficients of the cation (D_+) and anion (D_-) of a neat PIL by the Nernst-Einstein equation (Eqs. 3.11-3.12)[107,148]:

$$I_{HR} = \frac{\Lambda}{\Lambda_{NMR}} \tag{3.11}$$

$$\Lambda_{NMR} = \frac{N_A e^2}{K_B T}(D_{DBUH+} + D_{anion-}) \tag{3.12}$$

with N_A being Avogadro's number, e the electronic charge on each ionic carrier, D_{DBUH+} and D_{anion-} the diffusion coefficients of the cation and anion, respectively, K_B the Boltzmann constant and T the absolute temperature.

Eq. (3.12) postulates that all the diffusing species detected by PFG NMR contribute to the molar conductivity. In contrast, the measured Λ relies on the net migration of charged species in an electric field. Therefore, the inverse Haven ratio accounts for the proportion of ions (charged species) that participate in ionic conduction from all the diffusing species on the time scale of the measurement and appears to be a good metric to identify the interionic interactions[149].

For the PIL electrolytes, Λ_{NMR} is calculated according to Nernst-Einstein equation in the form of Eq. 3.13[150]:

$$\Lambda_{NMR} = \frac{N_A e^2}{kT} \left(\frac{n_{DBUH+}}{n_{DBUH+} + n_{Li+}} D_{DBUH+} + \frac{n_{Li+}}{n_{DBUH+} + n_{Li+}} D_{Li+} \right. \tag{3.13}$$
$$\left. + D_{anion-} \right)$$

with n_{DBUH+} being the number of moles of PIL and n_{Li+} the number of moles of lithium salt.

The ionicity values calculated using the inverse Haven ratio for the PILs and PIL electrolytes are shown in Figure 3.26 and reported in Table D3.5. DBUH-TFSI is the most ionic system among the three neat PILs studied, with I_{HR} = 0.78 at 318 K. Indeed, it has been shown that TFSI-based AILs and PILs have considerable high ionicity values (e.g., I_{HR}(C_1mim-TFSI) = 0.76[150]; I_{HR}(C_1HTMG-TFSI) = 0.74[84]; I_{HR}(P_{4442}-TFSI) = 0.71[105]). DBUH-IM14 and DBUH-TFO show lower ionicity than DBUH-TFSI (I_{HR} = 0.61 and 0.56 at 318 K, respectively), and very close ionicity values with each other, especially at high temperature (I_{HR} = 0.54 at 368 K).
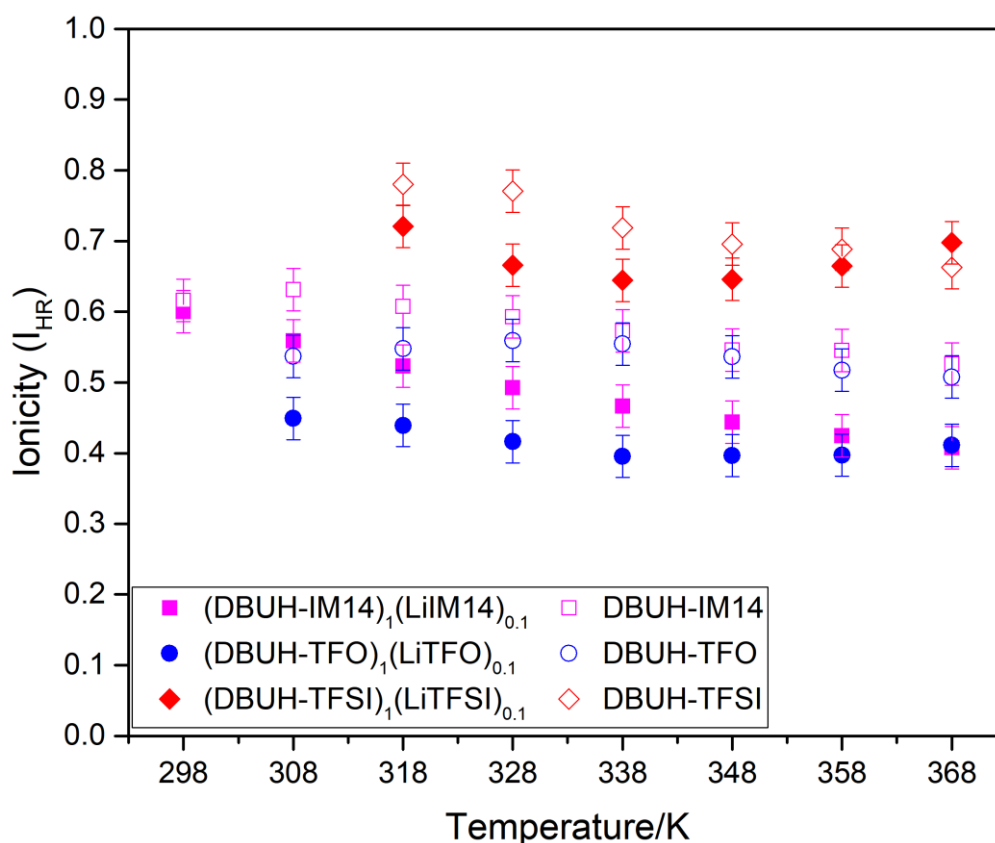
Figure 3.26. Ionicity calculated using the inverse Haven ratio for PILs and PIL electrolytes as a function of temperature.

It is worth mentioning that the cation-anion associations in PILs are very short lived to affect the ionicity to any significant extent[151]. Then, the lower ionicity values in the PILs may be related to other contributions such as interacting ions present in the liquid structure[108], charge transfer between cation and anion[109], and ionic mobilities[106]. Hence, the lowering of the ionicity of DBUH-IM14 and DBUH-TFO with respect to DBUH-TFSI may stem from the different factors associated to the TFO⁻ and IM14⁻ anions.

It is known from the literature that DBUH-TFO has a well-packed cation-anion solvation shell, and a highly oriented hydrogen bonding network[49]. This structural organization may contribute to the decrease of DBUH-TFO ionicity, because even if the hydrogen bond does not promote a long-lived ion association, it may influence the motion of the ions in the structured solvation shell. The situation is quite different for the DBUH-IM14, because this PIL has a weaker hydrogen bond network, resulting in a much less structured solvation shell[49]. Even if the F atoms of perfluorinated chain substituents do not tend to form H-bonds, they still undergo the formation of fluoroalkyl structural domains[49,152,153] Thus, this additional intermolecular F-F interaction may contribute to the lowering of the DBUH-IM14 ionicity, due to the presence of fluorous domains. Additional hints about the ionicity decrease in the DBUH-

IM14 were obtained via electrophoretic NMR, as shown in the next section.

An interesting point in the ionicity data of neat PILs is that while the ionicity of DBUH-TFO remains nearly constant within the experimental error with the temperature, for the DBUH-TFSI and DBUH-IM14, I_{HR} decreases with the temperature increase (from 0.78 to 0.66 in the temperature interval 318-368 K for DBUH-TFSI, and from 0.62 to 0.54 in the temperature interval 298-368 K for DBUH-IM14). At first inspection, one can think that it is counterintuitive because ion dissociation is expected to become larger at high temperatures, which would translate into an I_{HR} increase. However, as mentioned previously, long-lived cation-anion associations are unlikely to occur, especially at high temperatures, in order to significantly reducing their ionicity[151]. Hence, this is not a plausible reason to explain the ionicity decrease. Another hypothesis, that may explain such lowering effect is the inter movement of the ions (i.e., the anti-correlation motions). Indeed, the literature says that the inter movement of the ions may play a crucial role in the ionicity of the PILs[112]. It is known that the movement of oppositely charged ions increases the ionic conductivity, whereas the anticorrelated motion of ions of the same charge decreases the conductivity of an ionic liquid. It is plausible that the contribution of the anticorrelated motion of imide anions, such as TFSI⁻ and IM14⁻, increases with increasing temperature, thus preventing the ionic conductivity to increase as expected from the viscosity and ion diffusion coefficients[111,154]. Therefore, the ionicity of these PILs decreases when increasing the temperature. Similar findings have been reported for other TFSI-ILs[142,144], but more precise experimental and theoretical studies are still needed for deeper understanding the consequences of anticorrelated motions in ILs.

Previously, in Chapter 2 (*Section 2.3.9*), the Walden approach was applied to estimate the ionicity of the PILs. Despite the widespread application of the Walden plot, it lacks theoretical basis, consequently its proper application to describe the real ionic behavior of PILs is still questionable. Comparing the ionicity results (Table 3.4) obtained from the two different methodologies (I_W from Walden rule and I_{HR} from the inverse Haven ratio), there are some discrepancies between the data estimated using those approaches. For instance, lowering of the ionicity values due to strong intermolecular interactions, which probably slow down the diffusional motion, are not considered when using the Walden approach, consequently, an overestimation of the ionicity values may occur, as observed for DBUH-TFO: the system with strong hydrogen bond-network. In contrast, for the DBUH-IM14 and DBUH-TFSI the opposite effect was detected: the ionicity from the Walden plot was lower than the real ionicity determined by the inverse Haven ratio. As stated above, it is possible that the contribution of the

anticorrelated motion of the TFSI⁻ and IM14⁻ anions is lowering their ionic conductivity, more than expected from their respective viscosity, resulting in an underestimation of the ionicity values calculated by the Walden approach. From those consideration, it is evident that the capability of Walden method to describe the ionicity of PILs must be seen with caution, and here, it fails on describe the ionic behavior of the PILs selected in this study.

Table 3.4. Comparison between the ionicity of the PILs estimated by the inverse Haven ration (I_{HR}) and the Walden rule (I_W).

T (K)	(DBUH-IM14)		(DBUH-TFSI)		(DBUH-TFO)	
	I_{HR}	I_W	I_{HR}	I_W	I_{HR}	I_W
298	0.62	0.55				
308	0.63	0.53			0.55	0.99
318	0.61	0.49	0.78	0.66	0.56	0.88
328	0.61	0.46	0.77	0.61	0.58	0.82
338	0.57	0.44	0.72	0.58	0.58	0.76
348	0.53	0.40	0.70	0.54	0.58	0.70
358	0.55	0.40	0.69	0.50	0.53	0.66
368	0.54	0.38	0.66	0.48	0.54	0.63

Considering now the effect of the lithium salt on the ionicity of the PILs (Figure 3.26, filled symbols, and Table D3.5), it can be observed that (DBUH-TFSI)₁(LiTFSI)₀.₁ is again the most ionic system among the three PIL electrolytes, with I_{HR} = 0.73 at 318 K.

In the (DBUH-TFSI)₁(LiTFSI)₀.₁ the ionicity values of the lithium-free and doped systems are very close (I_{HR} in the range 0.78-0.66 and 0.73-0.65, respectively). Unlike the neat DBUH-TFSI, a progressively ionicity decreasing as a function of temperature is not observed in the Li-doped system. In the hypothesis that the ionicity mainly decreases because of the anion-anion anticorrelation, the presence of Li⁺ may work as a counterbalancing ion favoring the momentum conservation[110] and preventing the lowering of the ionicity.

For the (DBUH-TFO)₁(LiTFO)₀.₁ and (DBUH-IM14)₁(LiIM14)₀.₁ there is a decrease of the ionicity with the presence of Li⁺ with respect to the neat PILs ($\Delta \approx 0.1$). In the case of the triflate anion, probably, the Li⁺ is highly structured around TFO⁻ forming strongly bonded Li−TFO which contributes to the ionicity decrease. In the case of (DBUH-IM14)₁(LiIM14)₀.₁, I_{HR} values are also lower than in neat DBUH-IM14; moreover, this PIL electrolyte is the only one showing a strong decrease of the ionicity as a function of temperature (from 0.60 to 0.41 in the temperature interval 298-368 K). Unlike the system containing TFSI⁻, the ionicity decrease as a function of temperature is preserved in both (DBUH-IM14)₁(LiIM14)₀.₁ and (DBUH-IM14, suggesting that with IM14⁻ as the anion, the presence of Li⁺ is not

enough to counterbalance the anion-anion anticorrelation motion. An alternative hypothesis would consider an increase in cation−anion correlation induced by lithium doping, with consequent slowing down of the ions mobilities (i.e., the anticorrelated motion of oppositely charged ions is reduced), decrease of the ionic conductivity, and consequently, lowering of the ionicity. No clear conclusion about the temperature dependence of the ionicity in the DBUH-IM14 electrolyte can be drawn at this stage, and more investigations experimental and theoretical will address the subject.

3.3.6. Electrophoretic NMR of DBUH-IM14

DBUH-IM14 stood out in *Chapter 2* as a PIL with unique features stemming from the structure, size, shape and fluorine content of its anion. The experimental results presented in this Chapter unveiled even more the crucial role of this anion in driving intermolecular interactions and transport properties in both the neat PIL and its mixture with lithium salt. More specifically, the joint interpretation of conductivity and diffusion data outlined a peculiar temperature-dependent ionicity in both IM14-based PIL and PIL electrolyte, which is not observed in the other two systems. To gain additional information about the ion dynamics into the DBUH-IM14, and confirm the temperature dependent ionicity, I resorted to electrophoretic NMR. The electrophoretic mobilities (μ_i) corresponding to the anion, cation and N-H proton were determined at three different temperatures (318, 348 and 368 K) and are reported in Table D3.6 (Appendix D3). Here, the electrophoretic mobility of the N-H proton is indicated with the short notation μ_{N-H}.

As a first validation of the experimental e-NMR results, one can calculate the molar conductivity from the cation (μ_+) and anion (μ_-) mobility by Eq. 3.14:

$$\Lambda_{e-NMR} = zF(\mu_+ + \mu_-) \tag{3.14}$$

where z is the charge number and F is the Faraday constant

As shown in Table 3.5, the calculated molar conductivities from electrophoretic mobilities are in excellent agreement with the molar conductivities determined by impedance spectroscopy. Then, from a close inspection of the individual mobilities, the e-NMR results confirmed that the charge transport in the PIL occurs by the vehicular mechanisms since the mobilities of the N-H proton (μ_{N-H}) are the same as the mobilities of the cation (μ_{DBUH+}). Also, the results showed that the cation's mobilities are higher than the anion's (μ_{IM14-}), validating that these ionic species do not move as long-lived ion pairs.

Table 3.5. Electrophoretic mobilities of cation, anion and N-H proton in DBUH-IM14, and calculated ($\Lambda_{e\text{-NMR}}$) and experimental (Λ_{EIS}) molar conductivities.

T (K)	$\mu_{N\text{-}H}$ (m².V.s⁻¹)	μ_{cation}(m².V.s⁻¹)	μ_{anion}(m².V.s⁻¹)	$\Lambda_{e\text{-NMR}}$ (S.cm².s⁻¹)	Λ_{EIS}(S.cm².s⁻¹)
318	1.39E-10	1.35E-10	-9.56E-11	0.22	0.23
348	4.82E-10	4.70E-10	-3.99E-10	0.84	0.85
368	9.71E-10	9.51E-10	-8.26E-10	1.71	1.64

The real transference numbers t_i, (i.e., relative contribution of one type of ion i to the overall conductivity) were also obtained from the e-NMR results, using the Eq. 3.15 and are reported in Table 3.5.

$$t_+ = \frac{\mu_+}{\mu_+ + \mu_-} \; and \; t_- = \frac{\mu_-}{\mu_+ + \mu_-} \tag{3.15}$$

Often, in the literature, the apparent transference numbers ($t_+{}^{app}$) is extracted from the diffusion coefficients by the ratio $\frac{D_+}{D_+ + D_-}$. As shown in Table 3.6, the values for the transference numbers calculated by both methodologies (PFG-NMR and e-NMR) for the DBUH-IM14 are in good agreement, within the error. This comparison shows that even if apparent transference numbers are only an approximate concept, under certain circumstances (i.e., without significant ion clusters and ionic associations), PFG NMR can still provide valuable information about the ion dynamics in the bulk liquid.

For the cation, the transference number is slightly higher than that of the anion, meaning the former DBUH⁺ contributes more to the conduction process of this PIL.

The knowledge of both the self-diffusion coefficients and the electrophoretic mobilities of the ions allows one to calculate an effective charge for cations (εc_+) and anions (εc_-), (Eq 3.16).

$$\varepsilon_i = \frac{\mu_i}{\mu_{diff}} , and \; u_{diff} = \frac{zeD_i}{K_B T} \tag{3.15}$$

where e is the elementary charge and K_B the Boltzmann constant.

The effective charge can be understood as an apparent ion dissociation because it describes the transported charge concerning to the diffusive motions. In other words, the effective charge is equivalent to the ion specific ionicity. In the case of the DBUH-IM14 (Table 3.5), the effective charge of the cation slightly decreases with temperature, while for the anion it remains nearly constant. Considering that the effective charge of the cation decreases with the temperature, the overall ionicity of the system also decrease with the temperature, confirming the results previously showed for DBUH-IM14.

Table 3.6. Apparent transference number (t_+^{app}, t_-^{app}) measured by PFG-NMR, transference number (t_+, t_-) and effective charge measured by e-NMR of the DBUH-IM14.

T (K)	t_+^{app}	t_-^{app}	t_+	t_-	εc_+	εc_-
318	0.54 ± 0.03	0.46 ± 0.03	0.59 ± 0.02	0.41 ± 0.02	0.63 ± 0.03	0.53 ± 0.03
348	0.55 ± 0.03	0.45 ± 0.03	0.54 ± 0.05	0.46 ± 0.05	0.54 ± 0.05	0.54 ± 0.05
368	0.55 ± 0.03	0.45 ± 0.03	0.54 ± 0.02	0.46 ± 0.02	0.55 ± 0.03	0.55± 0.03

3.4. Conclusions

Protic ionic liquid electrolytes are attractive systems to improve the safety of lithium batteries. However, to promote their application, a deeper understanding of the features governing the transport properties of PILs electrolytes is still needed. Here, we investigated the transport properties of three different PILs (DBUH-IM14, DBUH-TFSI and DBUH-TFO) and the respective PIL electrolytes (DBUH-IM14)$_1$(LiIM14)$_{0.1}$, (DBUH-TFSI)$_1$(LiTFSI)$_{0.1}$ and (DBUH-TFO)$_1$(LiTFO)$_{0.1}$.

DBUH-IM14 is the system showing peculiar characteristics in terms of its transport properties. First, diffusion NMR detects lower diffusion coefficients than expected from its viscosity, probably due to occurrence of fluorous interactions between the asymmetrical fluorinated chains of the IM14 anion. Besides, the fluorine sites of the IM14$^-$ anion does not follow the same relaxation behavior of the CF$_3$ groups contained in the other PILs, revealing that other mechanisms play a crucial role on the IM14$^-$ rotational mobility. When looking at the transport properties, the DBUH-IM14 electrolyte showed an unusual and relatively faster translational mobility of the Li$^+$ and the highest lithium apparent transference number. Also, the relaxation data reveals that the lithium jump within the coordination sphere surrounded by anions is temperature responsive in the PIL containing the anion with long perfluoroalkyl chain in comparison with the other two PILs with shorter fluorinated groups. Overall, this unusual dynamics deserves further investigation.

Regarding the lithium salt effect in the ionic conductivity, in all investigated electrolytes the conductivity decreased with Li salt addition due to increasing viscosity, with the DBUH-TFSI electrolyte displaying higher ionic conductivity. Also, the ionicity is differently affected by the lithium salt in each PIL electrolyte. In the case of DBUH-TFSI, the ionicity seems to be constant upon the Li addition whereas for DBUH-TFO and DBUH-IM14 it shows a strong decreasing, which is probably related to the strong intermolecular interactions between the ions. A peculiar temperature-dependent ionicity decrease was detected in IM14-based PIL and PIL electrolyte, further confirmed by e-NMR data. The latter outlined a

decrease in the effective charge of the cation with temperature in DBUH-IM14, which is responsible for the overall decrease of ionicity of the system. For the DBUH-IM14 electrolyte, the origin of temperature dependent ionicity is still unclear and further investigations are required to evaluate such effects.

APPENDIX A3

Self-diffusion coefficients raw data and best fitting parameters

Table A3.1. Self-diffusion coefficients measured for DBUH-IM14 and (DBUH-IM14)1(LiIM14)0.1 as a function of temperature via PFG NMR.

DBUH-IM14				
T (K)	N-H (m².s⁻¹)	DBUH⁺ (m².s⁻¹)	IM14⁻ (m².s⁻¹)	
298.0	1.48E-12	1.47E-12	1.23E-12	
308.0	3.10E-12	3.10E-12	2.58E-12	
318.0	5.80E-12	5.80E-12	4.98E-12	
328.0	9.96E-12	9.91E-12	8.58E-12	
338.0	1.70E-11	1.70E-11	1.44E-11	
348.0	2.70E-11	2.70E-11	2.23E-11	
358.0	3.84E-11	3.86E-11	3.30E-11	
368.0	5.51E-11	5.48E-11	4.53E-11	

(DBUH-IM14)₁(LiIM14)₀.₁					
T (K)	N-H (m².s⁻¹)	DBUH⁺ (m².s⁻¹)	IM14⁻ (m².s⁻¹)	T (K)	Li⁺ (m².s⁻¹)
297.6	1.26E-12	1.25E-12	8.43E-13	298	7.02E-13
309.1	2.87E-12	2.86E-12	1.98E-12	308	1.47E-12
318.0	4.84E-12	4.82E-12	3.35E-12	314	2.04E-12
328.0	8.59E-12	8.55E-12	6.01E-12	322	3.50E-12
338.0	1.52E-11	1.50E-11	1.07E-11	332	6.15E-12
348.0	2.41E-11	2.38E-11	1.73E-11	344	1.12E-11
358.0	3.64E-11	3.59E-11	2.71E-11	355	1.99E-11
368.0	5.43E-11	5.25E-11	4.21E-11	367	3.12E-11

Table A3.2. Self-diffusion coefficients measured for DBUH-TFSI and (DBUH-TFSI)₁(LiTFSI)₀.₁ as a function of temperature via PFG NMR.

DBUH-TFSI				
T (K)	N-H (m².s⁻¹)	DBUH⁺ (m².s⁻¹)	TFSI⁻ (m².s⁻¹)	
318.0	1.52E-11	1.51E-11	1.29E-11	
328.0	2.35E-11	2.34E-11	2.05E-11	
338.0	3.64E-11	3.63E-11	3.07E-11	
348.0	5.13E-11	5.12E-11	4.39E-11	
358.0	7.10E-11	6.92E-11	6.03E-11	
368.0	9.33E-11	9.26E-11	8.02E-11	

(DBUH-TFSI)₁(LiTFSI)₀.₁				
T (K)	N-H (m².s⁻¹)	DBUH⁺ (m².s⁻¹)	TFSI⁻ (m².s⁻¹)	Li⁺ (m².s⁻¹)
318.0	9.64E-12	9.49E-12	7.56E-12	5.16E-12
328.0	1.68E-11	1.67E-11	1.25E-11	9.04E-12
338.0	2.52E-11	2.50E-11	1.95E-11	1.28E-11
348.0	3.67E-11	3.65E-11	2.89E-11	1.94E-11
358.0	5.15E-11	5.19E-11	4.08E-11	2.71E-11
368.0	7.06E-11	6.98E-11	5.44E-11	3.69E-11

Table A3.3. Self-diffusion coefficients measured for DBUH-TFO and (DBUH-TFO)$_1$(LiTFO)$_{0.1}$ as a function of temperature via PFG NMR.

DBUH-TFO			
T (K)	N-H (m².s^{-1})	DBUH$^+$ (m².s^{-1})	TFO$^-$ (m².s^{-1})
308.0	2.88E-12	2.89E-12	2.46E-12
318.0	5.36E-12	5.38E-12	4.68E-12
328.0	9.16E-12	9.21E-12	8.06E-12
338.0	1.48E-11	1.49E-11	1.33E-11
348.0	2.26E-11	2.25E-11	2.04E-11
358.0	3.49E-11	3.51E-11	3.27E-11
368.0	4.93E-11	4.96E-11	4.65E-11

(DBUH-TFO)$_1$(LiTFO)$_{0.1}$				
T (K)	N-H (m².s^{-1})	DBUH$^+$ (m².s^{-1})	TFO$^-$ (m².s^{-1})	Li$^+$ (m².s^{-1})
308.0	2.12E-12	2.12E-12	1.71E-12	9.97E-13
318.0	3.95E-12	3.95E-12	3.26E-12	1.76E-12
328.0	7.19E-12	7.09E-12	5.85E-12	3.03E-12
338.0	1.19E-11	1.18E-11	9.97E-12	4.80E-12
348.0	1.80E-11	1.78E-11	1.52E-11	7.42E-12
358.0	2.61E-11	2.60E-11	2.20E-11	1.04E-11
368.0	3.66E-11	3.55E-11	2.95E-11	1.51E-11

Table A3.4. Best VFT fitting parameters of the self-diffusion coefficients of the PILs and PILs electrolytes.

	$D_0(m^2.s^{-1})$	B (K)	T_0 (K)	R^2
DBUH-IM14				
N-H	5.56E-08	1404.26	164.72	0.999
DBUH+	5.46E-08	1401.47	164.76	0.999
IM14-	2.33E-08	1184.64	177.84	0.999
(DBUH-IM14)$_1$(LiIM14)$_{0.1}$				
N-H	8.80E-07	2432.17	116.80	0.999
DBUH+	5.66E-07	2260.99	123.95	0.999
IM14-	1.05E-06	2589.91	113.05	0.999
Li+	2.47E-06	3053.57	95.43	0.999
DBUH-TFSI				
N-H	1.49E-08	956.89	179.31	0.999
DBUH+	1.25E-08	908.61	182.89	0.999
TFSI-	1.35E-08	975.84	177.72	0.999
(DBUH-TFSI)$_1$(LiTFSI)$_{0.1}$				
N-H	9.96E-09	870.54	192.31	0.999
DBUH+	7.32E-09	780.39	200.39	0.999
TFSI-	1.06E-08	961.56	185.41	0.999
Li+	1.07E-08	1106.06	172.83	0.999
DBUH-TFO				
N-H	1.39E-07	1810.19	140.04	0.999
DBUH+	1.44E-07	1822.41	139.38	0.999
TFO-	3.09E-07	2106.68	128.44	0.999
(DBUH-TFO)$_1$(LiTFO)$_{0.1}$				
N-H	7.10E-09	902.97	197.00	0.999
DBUH+	6.60E-09	891.40	197.42	0.999
TFO-	3.54E-09	764.48	208.15	0.999
Li+	1.86E-08	1544.82	151.04	0.999

Table A3.5. Best Arrhenius fitting parameters of the self-diffusion coefficients of the PILs and PILs electrolytes.

DBUH-IM14			
	A (m².s^{-1})	E_a^{transl} (kJ.mol^{-1})	R^2
N-H	2.93E-04	47.05	0.996
DBUH$^+$	2.94E-04	47.06	0.996
IM14$^-$	2.43E-04	47.01	0.995
(DBUH-IM14)$_1$(LiIM14)$_{0.1}$			
	A (m².s^{-1})	E_a^{transl} (kJ.mol^{-1})	R^2
N-H	4.61E-04	48.61	0.999
DBUH$^+$	4.16E-04	48.35	0.998
IM14$^-$	5.93E-04	50.24	0.999
Li$^+$	5.16E-04	50.46	0.999
DBUH-TFSI			
	A (m².s^{-1})	E_a^{transl} (kJ.mol^{-1})	R^2
N-H	1.08E-05	35.53	0.997
DBUH$^+$	9.81E-06	35.29	0.997
TFSI$^-$	9.17E-06	35.31	0.997
(DBUH-TFSI)$_1$(LiTFSI)$_{0.1}$			
	A (m².s^{-1})	E_a^{transl} (kJ.mol^{-1})	R^2
N-H	1.93E-05	38.18	0.996
DBUH$^+$	2.06E-05	38.39	0.996
TFSI$^-$	1.68E-05	38.51	0.997
Li$^+$	8.80E-06	37.77	0.996
DBUH-TFO			
	A (m².s^{-1})	E_a^{transl} (kJ.mol^{-1})	R^2
N-H	1.07E-04	44.49	0.998
DBUH$^+$	1.09E-04	44.51	0.998
TFO$^-$	1.68E-04	46.06	0.999
(DBUH-TFO)$_1$(LiTFO)$_{0.1}$			
	A (m².s^{-1})	E_a^{transl} (kJ.mol^{-1})	R^2
N-H	9.06E-05	44.78	0.995
DBUH$^+$	8.08E-05	44.48	0.995
TFO$^-$	2.29E-04	45.11	0.993
Li$^+$	1.76E-05	42.60	0.998

Table A3.6. Diffusion ratios of the ions of the neat DBUH-IM14 and (DBUH-IM14)$_1$(LiIM14)$_{0.1}$ electrolyte.*

	DBUH-IM14			
T (K)	D_{N-H}/D_{DBUH+}	D_{DBUH+}/D_{IM14-}		
298	1.00	1.20		
308	1.00	1.20		
318	1.00	1.17		
328	1.00	1.16		
338	1.00	1.18		
348	1.00	1.21		
358	1.00	1.17		
368	1.01	1.21		
	(DBUH-IM14)$_1$(LiIM14)$_{0.1}$			
T (K)	D_{N-H}/D_{DBUH+}	D_{DBUH+}/D_{IM14-}	D_{Li+}/D_{DBUH+}	D_{Li+}/D_{IM14-}
298	1.01	1.48	0.54	0.80
308	1.00	1.46	0.54	0.80
318	1.00	1.44	0.55	0.79
328	1.01	1.41	0.56	0.79
338	1.01	1.39	0.58	0.80
348	1.01	1.36	0.59	0.81
358	1.02	1.34	0.61	0.81
368	1.02	1.31	0.63	0.82

*The values of the diffusion coefficients used in the calculation of (DBUH-IM14)$_1$(LiIM14)$_{0.1}$ ratios were estimated using the VFT fitting parameters to keep the same temperature range (298-368 K, with 10 K steps).

Table A3.7. Diffusion ratios of the ions of the DBUH-TFSI neat PIL and electrolyte.

	DBUH-TFSI			
T (K)	D_{N-H}/D_{DBUH+}	D_{DBUH+}/D_{TFSI-}		
318	1.00	1.16		
328	1.00	1.17		
338	1.00	1.17		
348	1.00	1.15		
358	1.03	1.16		
368	1.01	1.15		
	(DBUH-TFSI)$_1$(LiTFSI)$_{0.1}$			
T (K)	D_{N-H}/D_{DBUH+}	D_{DBUH+}/D_{TFSI-}	D_{Li+}/D_{TFSI-}	D_{Li+}/D_{TFSI-}
318	1.02	1.26	0.54	0.68
328	1.01	1.34	0.54	0.73
338	1.01	1.28	0.51	0.66
348	1.01	1.26	0.53	0.67
358	0.99	1.27	0.52	0.66
368	1.01	1.28	0.53	0.68

Table A3.8. Diffusion ratios of the ions of the DBUH-TFO neat PIL and electrolyte.

T (K)	D_{N-H}/D_{DBUH+}	D_{DBUH+}/D_{TFO-}		
		DBUH-TFO		
308	1.00	1.17		
318	1.00	1.15		
328	0.99	1.14		
338	0.99	1.13		
348	1.00	1.10		
358	0.99	1.08		
368	0.99	1.07		
		(DBUH-TFO)$_1$(LiTFO)$_{0.1}$		
T (K)	D_{N-H}/D_{DBUH+}	D_{DBUH+}/D_{TFO-}	D_{Li+}/D_{DBUH+}	D_{Li+}/D_{TFO-}
308	1.00	1.25	0.48	0.59
318	1.00	1.21	0.44	0.53
328	1.01	1.19	0.42	0.50
338	1.01	1.19	0.41	0.49
348	1.01	1.19	0.41	0.49
358	1.00	1.19	0.42	0.50
368	1.03	1.20	0.42	0.51

Table A3.9. Apparent transference numbers (t_i) of the ionic species in the neat PILs and PILs electrolytes.*

	DBUH-IM14			(DBUH-IM14)$_1$(LiIM14)$_{0.1}$	
T (K)	t_{DBUH+}	t_{IM14-}	t_{Li+}	t_{DBUH+}	t_{IM14-}
298	0.55	0.45	0.03	0.56	0.41
308	0.55	0.45	0.03	0.55	0.42
318	0.54	0.46	0.03	0.55	0.42
328	0.54	0.46	0.03	0.55	0.42
338	0.54	0.46	0.03	0.54	0.43
348	0.55	0.45	0.03	0.54	0.43
358	0.54	0.46	0.03	0.53	0.44
368	0.55	0.45	0.03	0.53	0.44
	DBUH-TFSI			(DBUH-TFSI)$_1$(LiTFSI)$_{0.1}$	
T (K)	t_{DBUH+}	t_{TFSI-}	t_{Li+}	t_{DBUH+}	t_{TFSI-}
318	0.54	0.46	0.03	0.52	0.45
328	0.54	0.46	0.03	0.53	0.44
338	0.54	0.46	0.03	0.52	0.45
348	0.53	0.47	0.03	0.52	0.45
358	0.54	0.46	0.03	0.52	0.45
368	0.54	0.46	0.03	0.52	0.45
	DBUH-TFO			(DBUH-TFO)$_1$(LiTFO)$_{0.1}$	
T (K)	t_{DBUH+}	t_{TFO-}	t_{Li+}	t_{DBUH+}	t_{TFO-}
308	0.54	0.46	0.02	0.52	0.46
318	0.53	0.47	0.02	0.51	0.46
328	0.53	0.47	0.02	0.51	0.47
338	0.53	0.47	0.02	0.51	0.47
348	0.52	0.48	0.02	0.50	0.47
358	0.52	0.48	0.02	0.51	0.47
368	0.52	0.48	0.02	0.51	0.47

*The values of the diffusion coefficients used in the calculation of (DBUH-IM14)$_1$(LiIM14)$_{0.1}$ transference numbers were estimated using the VFT fitting parameters to keep the same temperature range (298-368 K, with 10 K steps).

The Bloembergen, Purcell, and Pound (BPP) model

Several mechanisms can contribute to the NMR relaxation rate, including dipolar relaxation, chemical shift anisotropy, spin rotation, scalar relaxation, and chemical exchange [125–127,155]. In principle, the predominant relaxation mechanism determining ^{1}H and ^{19}F T_1 in liquid systems can be assumed to be the homonuclear ^{1}H-^{1}H or ^{19}F-^{19}F dipolar interactions. In the simplest cases, the Bloembergen, Purcell, and Pound (BPP) model can properly describe the NMR relaxation rate profile[156]. For ^{1}H and ^{19}F, both nuclei possessing spin ½, BPP equation can be written as follow (Eq. B3.1):

$$\frac{1}{T_1} = C \left(\frac{\tau_c}{1 + \omega_0^2 \tau_c^2} + \frac{4\tau_c}{1 + 4\omega_0^2 \tau_c^2} \right) \tag{B3.1}$$

where ω_0 is the observe frequency (rad s^{-1}) and τ_c is the correlation time. C is a parameter evaluated separately for each nucleus.

In the case of intramolecular dipolar relaxation, C can be defined as (Eq. B3.2)[140]:

$$C = \frac{3}{10} \gamma_i^4 \hbar^2 \sum \frac{1}{r^6} \tag{B3.2}$$

where γ_i is the gyromagnetic ratio of ^{1}H or ^{19}F atoms, $\hbar$ is the reduced Planck's constant $\left(\hbar = {h}/{2\pi} \right)$ and r is the H-H or F-F atomic distance, i.e., the distance between protons or fluorine nuclei over all interacting dipoles.

In the case of CF$_3$ groups, the additional contribution from the internal rotation around the three symmetrical axes of the CF$_3$ group of TFSI has be considered, and C was found as follows (Eq. B3.3)[140]:

$$C = \frac{9}{20} \gamma_F^4 \hbar^2 \sum \frac{1}{r^6} \tag{B3.3}$$

where γ_F is the ^{19}F gyromagnetic ratio, r is the F-F atomic distance in CF$_3$.[117].

For a quadrupolar nuclei such as ^{7}Li (spin = 3/2), the main relaxation mechanism is the quadrupolar coupling between the electrostatic quadrupolar moment of the nucleus and the electric field gradient (EFG) at the site of the nucleus. When applying the BPP equation

for describing the T_1(Li), the pre-factor C is given as follows (Eq. B3.4)[142]:

$$C = \frac{3\pi^2}{10} \frac{2I+3}{I^2(2I-1)} \left(1 + \frac{\eta^3}{3}\right) \omega_q^2 \tag{B3.4}$$

where I is the spin quantum number, $\omega_q = 2\pi\nu_q$ is the quadrupolar coupling constant in Hz, η is the asymmetry parameter of the electric field gradient[142]. When the EFG is axially symmetric, $\eta = 0$, and C can be described as follows (Eq. B3.5):

$$C = \frac{3\pi^2}{10} \frac{2I+3}{I^2(2I-1)} \omega_q^2 \tag{B3.5}$$

The temperature dependence of the correlation times (τ_c) is often described by the Arrhenius equation (Eq. B3.6)[138,157,158]:

$$\tau_C = \tau_0 exp\left(\frac{E_a^{rot}}{RT}\right) \tag{B3.6}$$

where τ_0 is a pre-exponential factor which so far has no clear physical meaning[126], R the gas constant, T the absolute temperature and E_a^{rot} the apparent activation energy for the rotational motion.

Owing to the term in brackets in Equation (B3.1), T_1 is minimum when, $\omega_0\tau_c = 2\pi\nu_0\tau_c = 0.616$. In the current study, the ^{1}H, ^{19}F and ^{7}Li observed frequencies ν_0 are 500.13 MHz, 470.59 MHz and 194.31 MHz, respectively. Then the τ_c(H), τ_c(F) and τ_c(Li) at the minimum can be easily calculated being 196 ps, 208 ps, and 504 ps, respectively. Then, such minimum T_1 value can be used to calculate C from Eq. (B3.1), enabling the estimation of τ_c values from the T_1 data acquired at any temperature. The temperature-dependent τ_c can be then used in Eq. (B3.6) to calculate the apparent activation energy for the rotational motion (E_a^{rot})[138,157,158]. Alternatively, the calculation of the correlation times τ_c for the reorientation motion can be done in a one-step approach using a non-linear least squares method. Substituting Equation (B3.6) into the BPP equation (Eq.B3.1), the combined equation can be directly solved by the nonlinear least squares method[159], entering C, τ_0 and E_a as iterative parameters and resulting in the same outputs of the T_1 minimum approach within the experimental error [160,161]. This latter method is precise, time saving and yields the desired parameters. Also, this method is feasible if the T_1 minimum is not fully achieved within the studied temperature range, but the curve seems to approach it. Therefore, it was applied in the present thesis work. The non-linear fitting was performed by using the software *Origin-Pro 16*.

In some cases, the T_1 minimum is not achieved in the explored temperature range and the T_1 curve shows a linear trend. In the present thesis, this situation was observed for the ^{19}F T_1 curves of CF_3 groups of DBUH-IM14 and $(DBUH-IM14)_1(LiIM14)_{0.1}$. In these cases, the extreme narrowing condition (i.e., $\omega_0\tau_c << 1$) may be assumed. As a result, Eq. (B3.1) reduces to (Eq. B3.7):

$$\frac{1}{T_1} = \frac{9}{4}\gamma_F^4\hbar^2\sum\frac{1}{r^6}\tau_C \qquad (B3.7)$$

and Eq. (B3.6) can be rewritten as[140]:

$$T_1 = T_{1,A}exp\left(\frac{E_a^{rot}}{RT}\right) \qquad (B3.8)$$

allowing the estimation of the activation energy of reorientational motion directly from the Arrhenius plot of the temperature dependent T_1 values.

Regarding the physical meaning of the correlation time τ_C, in theory, it represents the time required for the vector connecting the interacting nuclei to rotate through the angle of one radian[137]. For small rigid molecules, τ_c commonly reflects the molecular reorientational time constant τ_M. However, for the case of ILs, τ_c more accurately means a combination of the molecular reorientation τ_M and internal motions τ_i (Eq. B3.9) [138]:

$$\frac{1}{\tau_C} = \frac{1}{\tau_M} + \frac{1}{\tau_i} \qquad (B3.9)$$

In such cases, one correlation time is not enough to describe the experimental dependencies of relaxation rates. This may be due to the participation of studied nuclei simultaneously in two or more reorientation processes (a set of discrete correlation times), as well as the presence of the correlation time distribution that occurs due to different conditions for reorientation of nuclei in various local environments[162]. For internal motions that are very fast compared to the overall molecular motion, the second term of Eq. (B3.9) can be neglected[138]. For ILs, and for the PILs investigated here, τ_c more accurately describes a combination of the molecular reorientation and internal motions[163].

Considering that Li is a quadrupolar nucleus, the physical interpretation of its τ_c is less intuitive. In the case of Li, interaction arises from the coupling of the electric quadrupole moment, which is a property of the nucleus, with the EFG, which is a property of the sample. As τ_c (Li) reflects the fluctuations of the EFG, and given that the EFG is generated by the surroundings, a reasonable interpretation of τ_c (Li) takes into account the local environment of the ion, via the corresponding charge distribution, but also on the deformation of the electronic cloud of the ion itself induced by the

surroundings[137,164]. Usually, the τ_c (Li) is considered as the one-flip time of the translational displacement[140,143]. This approach is based on the assumption that the Li relaxation takes place by the quadrupolar mechanism for translational motion rather than rotational motion of Li atom[140,142]. Therefore, the physical meaning of τ_c (Li) is a single lithium jump from one place to another. The diffusion coefficients (D) measured via PFG NMR represents the translational motion during the time interval (Δ), and the average distance $\langle R \rangle = \sqrt{6D\Delta}$ is in the order of 10^{-6} m. Assuming that the Li diffusion coefficient measured by PFG NMR corresponds to the short-range diffusion (i.e., the diffusion for a jump is the same as the one in the μm space), the average distances for a Li one-flip jump can be calculated as follows (Eq. B3.10)[142,144]:

$$\langle R_{one-flip} \rangle = \sqrt{6D\tau_C(Li)} \tag{B10}$$

Relaxation data and best fitting parameters

Table C3.1. ^1H and ^7Li spin-lattice relaxation times (T_1) of DBUH-IM14 and (DBUH-IM14)$_1$(LiIM14)$_{0.1}$. The assignment is depicted in Figure 3.11.

T (K)	N-H (s)	CH$_{2(1)}$ (s)	CH$_{2(2)}$ (s)	CH$_{2(3)}$ (s)	CH$_{2(4)}$ (s)	CH$_{2(5)}$ (s)	Li$^+$ (s^1)
DBUH-IM14							
298	0.674	0.639	0.632	0.637	0.624	0.632	
308	0.606	0.538	0.534	0.540	0.529	0.534	
318	0.564	0.464	0.467	0.473	0.464	0.467	
328	0.539	0.416	0.426	0.430	0.424	0.426	
338	0.539	0.398	0.413	0.416	0.417	0.413	
348	0.551	0.397	0.416	0.423	0.429	0.416	
358	0.591	0.417	0.442	0.450	0.464	0.442	
368	0.655	0.455	0.489	0.517	0.524	0.489	
378	0.737	0.509	0.554	0.737	0.606	0.554	
(DBUH-IM14)$_1$(LiIM14)$_{0.1}$							
298	0.603	0.586	0.590	0.595	0.591	0.582	0.183
308	0.525	0.492	0.496	0.510	0.502	0.501	0.159
318	0.488	0.440	0.447	0.465	0.460	0.451	0.142
328	0.462	0.398	0.410	0.417	0.415	0.432	0.132
338	0.441	0.373	0.391	0.398	0.395	0.423	0.121
348	0.440	0.371	0.392	0.404	0.407	0.427	0.115
358	0.448	0.385	0.415	0.422	0.425	0.469	0.111
368	0.454	0.412	0.446	0.456	0.478	0.503	0.109
378	0.462	0.456	0.499	0.512	0.540	0.567	0.110

Table C3.2. ^{19}F spin-lattice relaxation times (T_1) of DBUH-IM14 and (DBUH-IM14)$_1$(LiIM14)$_{0.1}$. The assignment is depicted in Figure 3.11.

DBUH-IM14					
T (K)	CF$_{3(1)}$ (s)	CF$_{2(2)}$ (s)	CF$_{2(3)}$ (s)	CF$_{2(4)}$ (s)	CF$_{3(5)}$ (s)
298	0.437	0.495	0.512	0.444	0.408
308	0.550	0.543	0.569	0.487	0.483
318	0.655	0.551	0.589	0.506	0.541
328	0.780	0.557	0.608	0.522	0.607
338	0.926	0.556	0.624	0.531	0.680
348	1.068	0.551	0.636	0.534	0.749
358	1.227	0.549	0.656	0.541	0.819
368	1.409	0.558	0.683	0.556	0.920
378	1.556	0.565	0.712	0.571	0.982
(DBUH-IM14)$_1$(LiIM14)$_{0.1}$					
T (K)	CF$_{3(1)}$ (s)	CF$_{2(2)}$ (s)	CF$_{2(3)}$ (s)	CF$_{2(4)}$ (s)	CF$_{3(5)}$ (s)
298	0.386	0.500	0.505	0.437	0.374
308	0.456	0.541	0.545	0.481	0.425
318	0.563	0.558	0.572	0.506	0.497
328	0.671	0.564	0.592	0.522	0.565
338	0.796	0.562	0.606	0.529	0.640
348	0.919	0.560	0.620	0.535	0.714
358	1.043	0.564	0.640	0.546	0.785
368	1.170	0.573	0.665	0.560	0.860
378	1.299	0.500	0.505	0.437	0.938

Table C3.3. ^1H, ^{19}F and ^7Li spin-lattice relaxation times (T_1) of DBUH-TFSI and (DBUH-TFSI)$_1$(LiTFSI)$_{0.1}$. The assignment is depicted in Figure 3.11.

DBUH-TFSI							
T (K)	N-H (s)	CH$_{2(1)}$ (s)	CH$_{2(2)}$ (s)	CH$_{2(3)}$ (s)	CH$_{2(4)}$ (s)	CH$_{2(5)}$ (s)	CF$_3$ (s)
308	0.544	0.416	0.423	0.435	0.440	0.470	0.654
318	0.526	0.382	0.393	0.405	0.413	0.447	0.735
328	0.545	0.384	0.396	0.414	0.429	0.455	0.833
338	0.572	0.392	0.412	0.426	0.445	0.483	0.962
348	0.635	0.429	0.456	0.471	0.498	0.542	1.105
358	0.725	0.486	0.523	0.541	0.576	0.622	1.277
368	0.839	0.564	0.613	0.631	0.681	0.730	1.480
378	0.949	0.667	0.721	0.733	0.802	0.870	1.704

(DBUH-TFSI)$_1$(LiTFSI)$_{0.1}$								
T (K)	N-H (s)	CH$_{2(1)}$ (s)	CH$_{2(2)}$ (s)	CH$_{2(3)}$ (s)	CH$_{2(4)}$ (s)	CH$_{2(5)}$ (s)	CF$_3$ (s)	Li$^+$ (s)
308	0.580	0.482	0.482	0.492	0.500	0.518	0.580	0.574
318	0.549	0.419	0.430	0.441	0.451	0.474	0.640	0.478
328	0.542	0.396	0.414	0.424	0.438	0.461	0.713	0.408
338	0.565	0.391	0.407	0.451	0.451	0.479	0.804	0.350
348	0.610	0.423	0.449	0.460	0.492	0.524	0.895	0.312
358	0.669	0.467	0.495	0.508	0.551	0.590	1.034	0.286
368	0.744	0.542	0.568	0.601	0.656	0.676	1.161	0.275
378	0.812	0.608	0.643	0.665	0.730	0.789	1.296	0.273

Table C3.4. ^1H, ^{19}F and ^7Li spin-lattice relaxation times (T_1) of DBUH-TFO and (DBUH-TFO)$_1$(LiTFO)$_{0.1}$. The assignment is depicted in Figure 3.11.

				DBUH-TFO				
T (K)	N-H (s)	CH$_{2(1)}$ (s)	CH$_{2(2)}$ (s)	CH$_{2(3)}$ (s)	CH$_{2(4)}$ (s)	CH$_{2(5)}$ (s)	CF$_3$ (s)	
308	0.682	0.623	0.635	0.631	0.649	0.644	0.884	
318	0.599	0.501	0.516	0.518	0.539	0.538	0.932	
328	0.556	0.434	0.445	0.464	0.493	0.473	1.002	
338	0.511	0.381	0.400	0.407	0.437	0.442	1.118	
348	0.505	0.361	0.385	0.393	0.429	0.435	1.253	
358	0.527	0.366	0.393	0.405	0.450	0.453	1.414	
368	0.573	0.390	0.424	0.432	0.489	0.500	1.595	
378	0.641	0.430	0.472	0.483	0.649	0.560	1.785	
				(DBUH-TFO)$_1$(LiTFO)$_{0.1}$				
T (K)	N-H (s)	CH$_{2(1)}$ (s)	CH$_{2(2)}$ (s)	CH$_{2(3)}$ (s)	CH$_{2(4)}$ (s)	CH$_{2(5)}$ (s)	CF$_3$ (s)	Li$^+$ (s)
308	0.740	0.696	0.695	0.694	0.727	0.705	0.849	1.308
318	0.636	0.563	0.568	0.565	0.604	0.586	0.892	1.034
328	0.576	0.475	0.483	0.491	0.536	0.504	0.943	0.826
338	0.536	0.418	0.428	0.438	0.493	0.455	1.022	0.639
348	0.518	0.386	0.408	0.408	0.462	0.445	1.112	0.537
358	0.528	0.380	0.405	0.409	0.467	0.453	1.221	0.451
368	0.555	0.391	0.418	0.425	0.500	0.477	1.303	0.409
378	0.574	0.391	0.429	0.448	0.510	0.497	1.429	0.368

Table C3.5. Temperature where R_1 is maximum ($T_{R1,max}$) and temperature shift ($\Delta T_{R1,max}$) of the $R_{1,max}$ from the neat PIL to the PIL electrolyte upon the lithium salt addition*.

	DBUH-IM14			DBUH-TFSI			DBUH-TFO		
	PIL	PIL electrolyte		PIL	PIL electrolyte		PIL	PIL electrolyte	
	$T_{R1,max}$	$T_{R1,max}$	$\Delta T_{R1,max}$	$T_{R1,max}$	$T_{R1,max}$	$\Delta T_{R1,max}$	$T_{R1,max}$	$T_{R1,max}$	$\Delta T_{R1,max}$
Group	(K)	(K)	(K)	(K)	(K)	(K)	(K)	(K)	(K)
N-H	334.37	351.37	17.00	317.54	323.18	5.64	345.66	352.57	6.91
CH$_2$(1)	344.59	346.31	1.73	326.35	333.97	7.62	352.49	359.79	7.30
CH$_2$(2)	341.70	343.24	1.54	324.16	331.76	7.60	350.64	357.24	6.60
CH$_2$(3)	339.72	343.23	3.50	323.40	330.29	6.89	350.50	356.10	5.60
CH$_2$(4)	338.56	340.81	2.26	321.76	328.25	6.49	347.62	354.45	6.82
CH$_2$(5)	337.30	338.18	0.88	321.28	327.29	6.00	346.88	353.25	6.37
CF$_3$	-	-	-	281.95	270.29	-11.66	288.89	271.06	-17.83
Li$^+$	-	365.57	-	-	-	370.30	-	374.50	-

*$\Delta T_{R1,max} = T_{R1,max}$(PIL electrolyte) – $T_{R1,max}$(neat PIL)); $T_{R1,max}$ is the temperature where R_1 is maximum obtained by derivative method ($dR_1/dT = 0$).

Table C3.6. BPP fitting parameters for the ^{1}H nuclei of the PILs and PILs elecrolytes.* The assignment is depicted in Figure 3.11.

DBUH-IM14				
[1]H	C (s^{-2})	τ_0 (s^{-1})	E_a^{rot} (kJ.mol^{-1})	R^2
N-H	4.12E+09	1.52E-13	19.75	0.987
CH$_2$(1)	5.6E+09	5.97E-14	23.00	0.995
CH$_2$(2)	5.3E+09	5.69E-14	22.93	0.995
CH$_2$(3)	5.3E+09	4.62E-14	23.45	0.986
CH$_2$(4)	5.3E+09	3.63E-14	23.99	0.994
CH$_2$(5)	4.7E+09	6.38E-14	22.33	0.992
(DBUH-IM14)$_1$-(LiIM14)$_{0.1}$				
[1]H	C (s^{-2})	τ_0 (s^{-1})	E_a^{rot} (kJ.mol^{-1})	R^2
N-H	5.01E+09	1.07E-12	15.13	0.990
CH$_2$(1)	5.9E+09	1.12E-13	21.34	0.991
CH$_2$(2)	5.6E+09	1.00E-13	21.44	0.992
CH$_2$(3)	5.5E+09	1.06E-13	21.30	0.984
CH$_2$(4)	5.5E+09	6.99E-14	22.31	0.977
CH$_2$(5)	5.2E+09	1.06E-13	20.95	0.992
DBUH-TFSI				
[1]H	C (s^{-2})	τ_0 (s^{-1})	E_a^{rot} (kJ.mol^{-1})	R^2
N-H	4.18E+09	6.05E-14	21.39	0.998
CH$_2$(1)	5.80E+09	2.83E-14	23.92	0.998
CH$_2$(2)	5.65E+09	2.48E-14	24.13	0.999
CH$_2$(3)	5.45E+09	3.07E-14	23.53	0.998
CH$_2$(4)	5.31E+09	2.51E-14	23.94	0.998
CH$_2$(5)	4.94E+09	2.64E-14	23.76	0.999
(DBUH-TFSI)$_1$(LiTFSI)$_{0.1}$				
[1]H	C (s^{-2})	τ_0 (s^{-1})	E_a^{rot} (kJ.mol^{-1})	R^2
N-H	4.04E+09	1.35E-13	19.6	0.995
CH$_2$(1)	5.62E+09	2.12E-14	25.23	0.995
CH$_2$(2)	5.38E+09	2.83E-14	24.3	0.983
CH$_2$(3)	5.13E+09	4.42E-14	22.97	0.984
CH$_2$(4)	5.03E+09	2.44E-14	24.48	0.993
CH$_2$(5)	4.76E+09	2.90E-14	23.94	0.996
DBUH-TFO				
[1]H	C (s^{-2})	τ_0 (s^{-1})	E_a^{rot} (kJ.mol^{-1})	R^2
N-H	4.18E+09	8.29E-14	22.16	0.985
CH$_2$(1)	6.04E+09	3.10E-14	25.56	0.997
CH$_2$(2)	5.68E+09	2.80E-14	25.67	0.998
CH$_2$(3)	5.53E+09	3.44E-14	25.07	0.994
CH$_2$(4)	5.06E+09	3.10E-14	25.12	0.989
CH$_2$(5)	5.03E+09	3.44E-14	24.74	0.996
(DBUH-TFO)$_1$(LiTFO)$_{0.1}$				
[1]H	C (s^{-2})	τ_0 (s^{-1})	E_a^{rot} (kJ.mol^{-1})	R^2
N-H	4.22E+09	1.75E-13	20.46	0.994
CH$_2$(1)	5.83E+09	8.85E-14	23.11	0.995
CH$_2$(2)	5.48E+09	7.64E-14	23.28	0.997
CH$_2$(3)	5.39E+09	6.35E-14	23.73	0.988
CH$_2$(4)	4.71E+09	1.01E-13	22.2	0.993
CH$_2$(5)	4.76E+09	6.19E-14	23.94	0.998

*C, τ_0, E_a^{rot} are the fitting constants obtained by the nonlinear regression of R_1 curves (Eqs. B3.1,B3.6); R^2 is the coefficient of determination.

Table C3.7. BPP fitting parameters for the ^{19}F nuclei of the PILs and PILs elecrolytes.* The assignment is depicted in Figure 3.11.

(CF$_3$)	C (s^{-2})	τ_0 (s^{-1})	E_a^{rot} (kJ.mol^{-1})	R²
DBUH-TFSI	3.62E+09	1.36E-13	17.30	0.999
(DBUH-TFSI)$_1$(LiTFSI)$_{0.1}$	4.08E+09	3.14E-13	15.18	0.999
DBUH-TFO	2.48E+09	3.08E-13	15.88	0.999
(DBUH-TFO)$_1$(LiTFO)$_{0.1}$	2.55E+09	1.05E-12	12.74	0.999

*C, τ_0, E_a^{rot} are the fitting constants obtained by the nonlinear regression of R$_1$ curves (Eqs. B3.1,B3.6); R² is the coefficient of determination.

Table C3.8. BPP fitting parameters for the ^{7}Li nuclei of PILs elecrolytes.*

Li$^+$	C (s^{-2})	ω_q (kHz)	τ_0 (s^{-1})	E_a^{rot} (kJ.mol^{-1})	R²
(DBUH-IM14)$_1$(LiIM14)$_{0.1}$	7.83E+09	44.53	4.48E-12	14.71	0.998
(DBUH-TFSI)$_1$(LiTFSI)$_{0.1}$	3.16E+09	28.29	8.08E-13	20.37	0.998
(DBUH-TFO)$_1$(LiTFO)$_{0.1}$	2.56 E+09	25.46	4.83 E-13	23.42	0.999

*C, τ_0, E_a^{rot} are the fitting constants obtained by the nonlinear regression of R$_1$ curves (Eqs. B3.1,B3.6); ω_q is the quadrupolar coupling constant calculated from Eq. (B3.5); R² is the coefficient of determination.

Table C3.9. Activation Energies (E_a^{rot}) for the rotational motions of the CF$_3$ groups of the DBUH-IM14 neat PIL and electrolyte obtained from the ^{19}F T$_1$.* The assignment is depicted in Figure 3.11.

DBUH-IM14	T$_{range}$ (K)	E_a^{rot} (kJ.mol^{-1})	R²	E_a^{rot} (kJ.mol^{-1})	R²	T$_{range}$ (K)
CF$_3$(1)	298-338	15.52	1.00	348-378	13.88	0.997
CF$_3$(2)	298-338	10.51	0.996	348-378	10.19	0.992
(DBUH-IM14)$_1$-(LiIM14)	T$_{range}$ (K)	E_a^{rot} (kJ.mol^{-1})	R²	E_a^{rot} (kJ.mol^{-1})	R²	T$_{range}$ (K)
CF$_3$(1)	298-338	15.34	0.998	348-378	12.36	0.999
CF$_3$(2)	298-338	11.42	0.999	348-378	9.95	0.993

*E_a^{rot} is the fitting constant obtained by the nonlinear regression of R$_1$ curves (Eqs. B3.7).

Table C3.10. ^{1}H and ^{7}Li rotational correlation times τ_c of DBUH-IM14 and (DBUH-IM14)$_1$(LiIM14)$_{0.1}$. The assignment is depicted in Figure 3.11.

DBUH-IM14						
T (K)	N-H (s^{-1})	CH$_{2(1)}$ (s)	CH$_{2(2)}$ (s)	CH$_{2(3)}$ (s)	CH$_{2(4)}$ (s^1)	CH$_{2(5)}$ (s)
298	4.42E-10	6.45E-10	5.99E-10	6.00E-10	5.84E-10	5.26E-10
308	3.41E-10	4.77E-10	4.44E-10	4.41E-10	4.26E-10	3.92E-10
318	2.68E-10	3.59E-10	3.35E-10	3.31E-10	3.18E-10	2.98E-10
328	2.13E-10	2.76E-10	2.57E-10	2.52E-10	2.41E-10	2.31E-10
338	1.72E-10	2.15E-10	2.00E-10	1.95E-10	1.86E-10	1.81E-10
348	1.41E-10	1.70E-10	1.58E-10	1.54E-10	1.45E-10	1.44E-10
358	1.16E-10	1.36E-10	1.27E-10	1.23E-10	1.15E-10	1.16E-10
368	9.70E-11	1.10E-10	1.03E-10	9.90E-11	9.25E-11	9.46E-11
378	8.18E-11	9.03E-11	8.44E-11	8.08E-11	7.52E-11	7.80E-11

(DBUH-IM14)$_1$(LiIM14)$_{0.1}$							
T (K)	N-H (s)	CH$_{2(1)}$ (s)	CH$_{2(2)}$ (s)	CH$_{2(3)}$ (s)	CH$_{2(4)}$ (s)	CH$_{2(5)}$ (s)	Li$^+$ (s)
298	4.85E-10	6.18E-10	5.77E-10	5.75E-10	5.72E-10	5.02E-10	1.70E-09
308	3.97E-10	4.67E-10	4.36E-10	4.35E-10	4.27E-10	3.81E-10	1.40E-09
318	3.30E-10	3.59E-10	3.35E-10	3.35E-10	3.25E-10	2.95E-10	1.17E-09
328	2.77E-10	2.81E-10	2.62E-10	2.62E-10	2.51E-10	2.32E-10	9.88E-10
338	2.35E-10	2.23E-10	2.07E-10	2.08E-10	1.97E-10	1.85E-10	8.42E-10
348	2.01E-10	1.79E-10	1.66E-10	1.67E-10	1.57E-10	1.49E-10	7.24E-10
358	1.74E-10	1.46E-10	1.35E-10	1.36E-10	1.26E-10	1.22E-10	6.28E-10
368	1.52E-10	1.20E-10	1.11E-10	1.12E-10	1.03E-10	1.00E-10	5.49E-10
378	1.33E-10	9.98E-11	9.24E-11	9.31E-11	8.50E-11	8.38E-11	4.84E-10

Table C3.11. ^1H, ^{19}F and ^7Li rotational correlation times τ_c of DBUH-TFSI and (DBUH-TFSI)$_1$(LiTFSI)$_{0.1}$. The assignment is depicted in Figure 3.11.

DBUH-TFSI							
T (K)	N-H (s)	CH$_{2(1)}$ (s)	CH$_{2(2)}$ (s)	CH$_{2(3)}$ (s)	CH$_{2(4)}$ (s)	CH$_{2(5)}$ (s)	CF$_3$ (s)
308	2.58E-10	3.24E-10	3.09E-10	3.01E-10	2.89E-10	2.84E-10	1.18E-10
318	1.98E-10	2.41E-10	2.30E-10	2.26E-10	2.16E-10	2.12E-10	9.51E-11
328	1.55E-10	1.83E-10	1.74E-10	1.72E-10	1.64E-10	1.61E-10	7.79E-11
338	1.23E-10	1.41E-10	1.34E-10	1.33E-10	1.26E-10	1.25E-10	6.45E-11
348	9.87E-11	1.11E-10	1.05E-10	1.05E-10	9.87E-11	9.77E-11	5.41E-11
358	8.03E-11	8.78E-11	8.29E-11	8.34E-11	7.83E-11	7.76E-11	4.58E-11
368	6.60E-11	7.06E-11	6.65E-11	6.73E-11	6.30E-11	6.25E-11	3.91E-11
378	5.49E-11	5.74E-11	5.40E-11	5.49E-11	5.12E-11	5.09E-11	3.36E-11

(DBUH-TFSI)$_1$(LiTFSI)$_{0.1}$								
T (K)	N-H (s)	CH$_{2(1)}$ (s)	CH$_{2(2)}$ (s)	CH$_{2(3)}$ (s)	CH$_{2(4)}$ (s)	CH$_{2(5)}$ (s)	CF$_3$ (s)	Li$^+$ (s)
308	2.85E-10	4.06E-10	3.76E-10	3.50E-10	3.49E-10	3.34E-10	1.18E-10	2.32E-09
318	2.24E-10	2.97E-10	2.79E-10	2.64E-10	2.58E-10	2.49E-10	9.82E-11	1.80E-09
328	1.79E-10	2.22E-10	2.11E-10	2.02E-10	1.95E-10	1.89E-10	8.24E-11	1.43E-09
338	1.45E-10	1.69E-10	1.62E-10	1.58E-10	1.49E-10	1.46E-10	6.99E-11	1.14E-09
348	1.18E-10	1.31E-10	1.26E-10	1.25E-10	1.16E-10	1.14E-10	5.98E-11	9.28E-10
358	9.79E-11	1.02E-10	9.98E-11	9.98E-11	9.17E-11	9.05E-11	5.17E-11	7.62E-10
368	8.19E-11	8.13E-11	8.00E-11	8.09E-11	7.33E-11	7.27E-11	4.50E-11	6.33E-10
378	6.91E-11	6.53E-11	6.48E-11	6.63E-11	5.93E-11	5.91E-11	3.94E-11	5.30E-10

Table C3.12. ^1H, ^{19}F and ^7Li rotational correlation times τ_c of DBUH-TFO and (DBUH-TFO)$_1$(LiTFO)$_{0.1}$. The assignment is depicted in Figure 3.11.

DBUH-TFO							
T (K)	N-H (s)	CH$_{2(1)}$ (s)	CH$_{2(2)}$ (s)	CH$_{2(3)}$ (s)	CH$_{2(4)}$ (s)	CH$_{2(5)}$ (s)	CF$_3$ (s)
308	4.77E-10	6.73E-10	6.35E-10	6.17E-10	5.67E-10	5.43E-10	1.52E-10
318	3.63E-10	4.92E-10	4.63E-10	4.53E-10	4.16E-10	4.01E-10	1.25E-10
328	2.81E-10	3.66E-10	3.45E-10	3.39E-10	3.11E-10	3.01E-10	1.04E-10
338	2.21E-10	2.77E-10	2.61E-10	2.59E-10	2.37E-10	2.30E-10	8.79E-11
348	1.76E-10	2.14E-10	2.01E-10	2.00E-10	1.83E-10	1.79E-10	7.47E-11
358	1.42E-10	1.67E-10	1.57E-10	1.57E-10	1.44E-10	1.41E-10	6.41E-11
368	1.16E-10	1.32E-10	1.24E-10	1.25E-10	1.14E-10	1.12E-10	5.54E-11
378	9.59E-11	1.06E-10	9.91E-11	1.01E-10	9.20E-11	9.07E-11	4.83E-11

(DBUH-TFO)$_1$(LiTFO)$_{0.1}$								
T (K)	N-H (s)	CH$_{2(1)}$ (s)	CH$_{2(2)}$ (s)	CH$_{2(3)}$ (s)	CH$_{2(4)}$ (s)	CH$_{2(5)}$ (s)	CF$_3$ (s)	Li$^+$ (s)
308	5.19E-10	7.38E-10	6.82E-10	6.74E-10	5.93E-10	6.11E-10	1.52E-10	4.55E-09
318	4.04E-10	5.55E-10	5.12E-10	5.03E-10	4.51E-10	4.57E-10	1.30E-10	3.41E-09
328	3.19E-10	4.25E-10	3.92E-10	3.83E-10	3.49E-10	3.48E-10	1.13E-10	2.60E-09
338	2.55E-10	3.31E-10	3.04E-10	2.96E-10	2.75E-10	2.70E-10	9.80E-11	2.02E-09
348	2.07E-10	2.61E-10	2.40E-10	2.32E-10	2.19E-10	2.12E-10	8.60E-11	1.59E-09
358	1.70E-10	2.09E-10	1.91E-10	1.85E-10	1.77E-10	1.69E-10	7.61E-11	1.27E-09
368	1.41E-10	1.69E-10	1.55E-10	1.49E-10	1.44E-10	1.36E-10	6.77E-11	1.02E-09
378	1.18E-10	1.39E-10	1.27E-10	1.21E-10	1.19E-10	1.11E-10	6.07E-11	8.36E-10

Table C3.13. The estimated average jump distances $\langle R_{one-flip} \rangle$ of the PILs electrolytes.

Temperature (K)	(DBUH-IM14)$_1$(LiIM14)$_{0.1}$ $\langle R_{one-flip} \rangle$ (m)	(DBUH-TFSI)$_1$(LiTFSI)$_{0.1}$ $\langle R_{one-flip} \rangle$ (m)	(DBUH-TFO)$_1$(LiTFO)$_{0.1}$ $\langle R_{one-flip} \rangle$ (m)
298	8.46E-11		
308	1.09E-10		1.65E-10
318	1.38E-10	2.36E-10	1.90E-10
328	1.70E-10	2.78E-10	2.17E-10
338	2.06E-10	2.97E-10	2.41E-10
348	2.45E-10	3.29E-10	2.66E-10
358	2.88E-10	3.52E-10	2.81E-10
368	3.33E-10	3.74E-10	3.05E-10
378	3.81E-10	3.96E-10	3.24E-10

Temperature (K)	(DBUH-IM14)$_1$(LiIM14)$_{0.1}$ $\langle R_{one-flip} \rangle$ (m)	(DBUH-TFSI)$_1$(LiTFSI)$_{0.1}$ $\langle R_{one-flip} \rangle$ (m)	(DBUH-TFO)$_1$(LiTFO)$_{0.1}$ $\langle R_{one-flip} \rangle$ (m)

Density, specific conductivity, molar conductivity, ionicity and e-NMR data

Table D3.1. Density values of the PIL electrolytes.

T (K)	$(DBUH\text{-}IM14)_1(LiIM14)_{0.1}$	$(DBUH\text{-}TFSI)_1(LiTFSI)_{0.1}$	$(DBUH\text{-}TFO)_1(LiTFO)_{0.1}$
298.0	1.5833		
308.0	1.5725		1.3618
318.0	1.5607	1.4832	1.3540
328.0	1.5505	1.4738	1.3467
338.0	1.5393	1.4646	1.3393
348.0	1.5283	1.4554	1.3317
358.0	1.5173	1.4463	1.3239

The density values were fitted to a linear equation (Eq. D3.1).

$$\rho = \rho_0 - \alpha T \tag{D3.1}$$

Table D3.2. Linear fitting parameters for the density data of the PILs doped with lithium salt samples.

	ρ_0	α (10^{-5} g.cm^3.K^{-1})	R^2
$(DBUH\text{-}IM14)_1(LiIM14)_{0.1}$	1.9112	1.100	0.9999
$(DBUH\text{-}TFSI)_1(LiTFSI)_{0.1}$	1.7765	0.992	0.9999
$(DBUH\text{-}TFO)_1(LiTFO)_{0.1}$	1.5939	0.754	0.9999

Table D3.3. Specific conductivity values σ in S.cm^{-1} of the PIL electrolytes.

T (K)	$(DBUH\text{-}IM14)_1(LiIM14)_{0.1}$	$(DBUH\text{-}TFSI)_1(LiTFSI)_{0.1}$	$(DBUH\text{-}TFO)_1(LiTFO)_{0.1}$
298	1.36E-04		
308	2.35E-04		2.87E-04
318	4.05E-04	1.54E-03	5.10E-04
328	6.69E-04	2.16E-03	8.23E-04
338	1.03E-03	3.25E-03	1.28E-03
348	1.55E-03	4.70E-03	1.90E-03
358	2.24E-03	6.38E-03	2.65E-03
368	2.93E-03	8.81E-03	3.59E-03

Table D3.4. Molar conductivity values Λ in S.cm².mol^{-1} of the PILs electrolytes.

T (K)	(DBUH-IM14)$_1$(LiIM14)$_{0.1}$	(DBUH-TFSI)$_1$(LiTFSI)$_{0.1+}$	(DBUH-TFO)$_1$(LiTFO)$_{0.1}$
298	0.049		
308	0.085		0.061
318	0.148	0.435	0.108
328	0.246	0.615	0.178
338	0.381	0.932	0.277
348	0.578	1.357	0.409
358	0.842	1.853	0.579
368	1.109	2.578	0.790

Table D3.5. Ionicity values calculated using the inverse Haven ratio for PILs and PIL electrolytes.*

T (K)	(DBUH-IM14)	(DBUH-IM14)$_1$ (LiIM14)$_{0.1}$	(DBUH-TFSI)	(DBUH-TFSI)$_1$ (LiTFSI)$_{0.1}$	(DBUH-TFO)	(DBUH-TFO)$_1$ (LiTFO)$_{0.1}$
298	0.62	0.60				
308	0.63	0.56			0.55	0.45
318	0.61	0.52	0.78	0.73	0.56	0.44
328	0.61	0.49	0.77	0.66	0.58	0.42
338	0.57	0.47	0.72	0.65	0.58	0.40
348	0.53	0.44	0.70	0.65	0.58	0.40
358	0.55	0.42	0.69	0.66	0.53	0.40
368	0.54	0.41	0.66	0.70	0.54	0.41

*The values of the diffusion coefficients used in the calculation of (DBUH-IM14)$_1$(LiIM14)$_{0.1}$ transference numbers were estimated using the VFT fitting parameters to keep the same temperature range (298-368 K, with 10 K steps).

Table D3.6. e-NMR experimental data of the DBUH-IM14*.

318 K Experiment n⁰	μ_{N-H}	μ_{DBUH+}	μ_{IM14-}
1	1.48E-10	1.42E-10	-9.19E-11
2	1.29E-10	1.28E-10	-9.94E-11
Average	1.39E-10	1.35E-10	-9.56E-11

348 K Experiment n⁰	μ_{H+}	μ_{DBUH+}	μ_{IM14-}
1	4.33E-10	4.26E-10	-4.27E-10
2	4.80E-10	4.67E-10	-4.07E-10
3	5.34E-10	5.17E-10	-3.64E-10
Average	4.82E-10	4.70E-10	-3.99E-10

368 K Experiment n⁰	μ_{H+}	μ_{DBUH+}	μ_{IM14-}
1	9.53E-10	9.43E-10	-8.19E-10
2	9.38E-10	9.25E-10	-7.85E-10
3	1.02E-09	9.85E-10	-8.74E-10
Average	9.71E-10	9.51E-10	-8.26E-10

*Experiment n° means the replication of the experiment at a certqain temperature; and average refers to the average of the values obtained in each experiment.

Structure and dynamics of PIL-based polymer electrolytes

4.1. Introduction

The previous *Chapters* of this thesis emphasized the benefits of the use of protic ionic liquids (PILs) as electrolyte components to improve the safety issues related to the flammability of the current state-of-art organic solvents used as electrolyte components[165]. I have shown that PILs are potential candidates to replace organic solvents in electrochemical applications due to their unique physicochemical properties such as high thermal stability and acceptable conductivity. Among the investigated PILs, namely DBUH-TFO, DBUH-TFSI and DBUH-IM14, I have unveiled the favourable influence of DBUH-IM14 on the mobility of Li$^+$ ions, thus making this PIL a highly interesting one for LIB applications.

Further developments of PILs for electrochemical applications include their use in polymer electrolytes, both solid polymer electrolytes (SPE) and gel-like, quasi-solid, systems. Polymer electrolytes have been extensively explored for use in LIBs because of their ability to address the safety issues and at the same time improve the volumetric design concerns associated with liquid electrolytes[166]. However, SPE typically exhibit resistive interfaces and a low ionic conductivity. Enhanced conductivity of SPE can be achieved by immobilizing ILs inside a polymeric network and to date, many investigations have been dedicated to the development of SPE containing ILs[167]. A further conductivity enhancement can be obtained moving to gel systems, known as ionogels or iongels, consisting of an IL confined in a structured gel-like matrix. Ionogels have attracted the attention of the scientific community as they

exhibit high mechanical stability while preserving a liquid state ionic conductivity[168]. Blended with lithium salts, ionogels are promising quasi-solid electrolytes, thanks to their high ionic conductivity, stability, and solution processability. Macroscopically, the gel electrolytes behave as a solid, but at microscopic scale the liquid nature is retained[169].

Most of the studies related to the use of SPE and gel electrolytes was performed using aprotic ionic liquids (AILs). However, very recently, it was shown that PIL-based polymer electrolytes are also suitable for stable operations[39]. The immobilization of PILs inside of a polymer network is appealing to overcome the limitation related to the PIL reactivity toward alkali metals[34], which is presently hindering the practical use of PIL-based electrolytes in high energy/power density alkali metal batteries. Still, to promote the application of these materials as electrolyte components, the features ruling the transport properties of PIL-based polymer electrolytes need to be well defined.

The present *Chapter* reports on the preparation and characterization of PIL-based polymeric systems in terms of their structural features and molecular interactions. The first part of this work was focused on the investigation of solid polymeric systems based on poly(methyl methacrylate) (PMMA, Figure 4.1) as a host for the PILs formed by the DBUH$^+$ cation and the three different anions TFO$^-$, TFSI$^-$ and IM14$^-$.

The complex and distinguished interactions between DBUH-IM14 and the PMMA matrix detected via thermogravimetric analysis and solid-state NMR prompted me to extend the studies to DBUH-IM14 polymer electrolytes with a significantly lower polymer content. I specifically targeted the system containing 10% wt of PMMA, which is a highly viscous quasi-gel system. These latter investigations intended to fully address the nature of the ion interaction and ion dynamics in the complex polymeric systems.

As a last step towards the development of PIL polymer electrolytes, I prepared and studied the ternary systems made of PMMA, DBUH-IM14 and Li salt. Understanding how the lithium ions behave inside the matrix is crucial for improving the ionic conductivity and the Li$^+$ transference number. Therefore, this last part of the thesis combined diffusion and fast-field cycling relaxation NMR techniques to elucidate the ions' dynamics (translational and rotational diffusion) as a function of temperature.
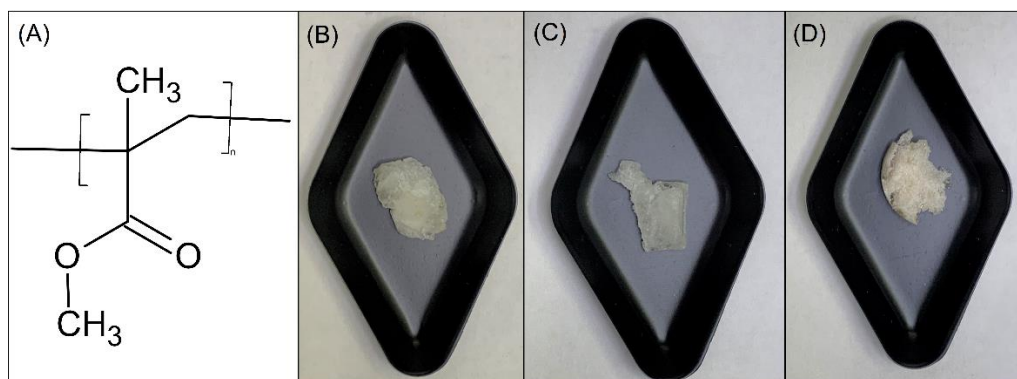
Figure 4.1. Structure picture of the (a) PMMA; picture of the solid materials (b) (PMMA + DBUH-IM14), (c) (PMMA + DBUH-TFSI), and (d) (PMMA + DBUH-TFO)

4.2. Methodology and theoretical background

4.2.1. Samples preparation

This *Chapter* is focused on studying two different sets of samples (Table 4.1):

(i) solid binary polymeric systems based on PMMA and PIL;

(ii) highly viscous binary and ternary polymeric systems, containing DBUH-IM14 and DBUH-IM14 electrolyte (i.e. PIL + Li salt having the same anion) blended with lower amount of PMMA.

Table 4.1. Summary of the samples investigated in the present chapter*.

Solid polymeric systems						
	Mass Fraction (%)		Molar Fraction (%)			
Sample Acronym	MMA	PIL	MMA	PIL		
$P(MMA)_{0.91}$-$(IM14)_{0.09}$	0.63	0.37	0.91	0.09		
$P(MMA)_{0.91}$-$(TFSI)_{0.09}$	0.70	0.30	0.91	0.09		
$P(MMA)_{0.91}$-$(TFO)_{0.09}$	0.77	0.23	0.91	0.09		
Highly viscous binary polymeric systems						
	Mass Fraction (%)		Molar Fraction (%)			
Sample Acronym	MMA	PIL	MMA	PIL		
$(DBUH-IM14)_{0.60}$-$P(MMA)_{0.40}$	0.90	0.10	0.40	0.60		
Highly viscous ternary polymeric systems						
	Mass Fraction (%)			Molar Fraction (%)		
Sample Acronym	MMA	PIL	LiIM14	MMA	PIL	LiIM14
$(DBUH)_{0.55}$-$(Li)_{0.06}$-$P(MMA)_{0.39}$	0.10	0.84	0.06	0.39	0.55	0.06

*The subscripts in the acronyms correspond to the molar fraction of the respective component.

The preparation of the samples was performed as follows:

(I) *Solid binary polymeric systems:* The binary solid mixtures P(MMA)$_{0.91}$-(PIL)$_{0.09}$ were prepared through a solvent-free process. The three PILs (DBUH-TFSI, DBUH-TFO, and DBUH-IM14, synthesized as described in *Chapter 2*) and the PMMA (MW = 996,000), purchased from Sigma-Aldrich, were first vacuum-dried for at least 48 hours at 353-373 K. Then, PMMA and PIL were blended in a fixed molar ratio MMA:PIL equal to 10:1, inside a glass vial using a micromixer, and vacuum annealed at 373 K for 5 days. The final mixtures were cooled down at ambient temperature, and homogenous solid samples were formed hereafter referred to as P(MMA)$_{0.91}$-(IM14)$_{0.09}$, P(MMA)$_{0.91}$-(TFSI)$_{0.09}$ and P(MMA)$_{0.91}$-(TFO)$_{0.09}$. The procedure was performed inside a glove box (VAC, [O$_2$] < 1 ppm, [H$_2$O] < 1 ppm).

(II) *Highly viscous binary and ternary polymeric systems:* Neat DBUH-IM14 (synthesized as described in *Chapter 1*) and (DBUH-IM14)$_1$(LiIM14)$_{0.1}$ (hereafter DBUH-LiIM14, synthesized as described in *Chapter 3*) were mixed with the proper amount of PMMA (10 % wt), under continuous stirring at high temperature (T > 100 °C), using a thermoregulated bath, until a clear and homogenous solution is formed. The final samples, (DBUH-IM14)$_{0.60}$P(MMA)$_{0.40}$ and (DBUH)$_{0.55}$-(Li)$_{0.06}$-P(MMA)$_{0.39}$, were then vacuum-dried (< 1 mbar) in an oil-free pump at 373 K for at least 48 hours. Finally, they were transferred to an argon glove box and housed in 10 mm and 5 mm NMR tubes for the FFC NMR and PFG NMR experiments, respectively. All the tubes were flame sealed to avoid air exposure and moisture contamination.

4.2.2. Differential scanning calorimetry (DSC) and thermogravimetric analysis (TGA)

DSC and TGA are common techniques to determine the phase transitions and thermal stability of polymeric systems. These two techniques are detailed described in *Chapter 2* and were employed to investigate the solid binary polymeric systems P(MMA)$_{0.91}$-(PIL)$_{0.09}$ during my secondment at the University of Campinas – Brazil.

Thermal transitions of each P(MMA)$_{0.91}$-(PIL)$_{0.09}$ were evaluated using a DSC 1 instrument (Mettler Toledo) , equipped with a liquid nitrogen cooling system. About 10 mg of the PIL samples were weighted using a microanalytical balance MX5 (Mettler Toledo) and tightly sealed in standard aluminum crucible. For the DSC analysis, each P(MMA)$_{0.91}$-(PIL)$_{0.09}$ sample was heated from 298 K up to 443 K at 10 K.min^{-1}, with isothermal treatment at this temperature for 5 minutes. Then, the sample was cooled down to 153 K 10 K.min^{-1} and kept at this temperature for 15 minutes. Finally, the sample was

heated up to 443 K 10 K.min^{-1}. For all samples investigated, the DSC trace was measured in the last heating scan.

The thermal stability of the three polymeric systems P(MMA)$_{0.91}$-(PIL)$_{0.09}$ was assessed in a nitrogen atmosphere using the instrument TGA/DSC1 from Mettler Toledo with the STARe Thermal Analysis Software 10.00. During the experiment, the gas flow rate was set at 100 ml.min^{-1} to avoid external contamination from the atmosphere. Then, open alumina crucibles containing 10–15 mg of PMMA-PIL were scanned. The thermal stability was investigated by heating the samples from room temperature to 873 K at the heating scan of 10 K.min^{-1}. The decomposition temperature (T$_d$) was estimated by taking the minimum of the TGA derivative curve (DTG).

4.2.3. Solid-state NMR

Solid-state NMR (ssNMR) methods have been extensively used in structure and dynamic characterization for a wide range of polymeric systems[170]. For an introduction to ssNMR spectroscopy, the interested reader is referred to the literature[171,172], while here, we briefly describe the ssNMR experiments applied in this chapter to probe the local dynamics and the structure of the solid binary polymeric systems P(MMA)$_{0.91}$-(PIL)$_{0.09}$.

The NMR transition frequencies are sensitive to the electron distribution around the nucleus, which shields the nucleus from the applied magnetic field. Moreover, NMR frequencies are modified by a series of interactions: spin–spin scalar couplings, which depend on covalent bonding; spin–spin dipolar couplings, which depend on internuclear distances, and, for nuclear spins greater than 1/2, quadrupolar couplings between the electric field gradient at the nucleus and the charge distribution of the nucleus. All of these NMR interactions have anisotropic components, that is, they depend on the sample orientation relative to the magnetic field direction[173].

In liquids, these anisotropic interactions are partially averaged by the rapid isotropic molecular tumbling, and the NMR spectra are then affected only by the isotropic components of chemical shift and scalar coupling. In solids, molecular rotations are absent or much slower, and the orientation dependence of NMR frequencies causes powder patterns for each nuclear spin. In most cases, this anisotropic contribution is (partially) removed by magical angle spinning (MAS), where samples are physically spun around an axis that is tilted by 54.74° – the magic angle –from the static magnetic field. The choice of this angle stems from the fact that the anisotropy of NMR interactions is given by a second- rank tensor, whose time average vanishes at 54.74°[173]. Broadly speaking, MAS averages out the anisotropic chemical shift and dipolar interactions, thus

making it possible to get spectra with narrower lines and then access valuable spectral information.

^{13}C is a nucleus of choice in ssNMR. The homonuclear ^{13}C-^{13}C dipolar coupling is usually insignificant due to its low abundance, and the heteronuclear ^{1}H-^{13}C dipolar coupling can be decoupled with high-power. This basic experiment called high power decoupling (HPDEC) is based on a continuous high power RF pulse applied on the ^{1}H channel for the whole duration of ^{13}C data acquisition (Figure 4.2a). Such applied RF pulse averages (partially) the dipolar ^{13}C-^{1}H couplings according to the strength of the interactions[174]. This means that a 1D ^{13}C HPDEC MAS experiment run on polymeric systems will show only the resonances of carbon atoms of the polymer backbone where the dipolar interactions are partially averaged by molecular motion[175].

The most common pulse sequences in solids are based on cross polarization (CP). CP exploits a polarization transfer via strong dipolar couplings from an abundant magnetization (typically ^{1}H, but also ^{19}F) to a weaker one (e.g., ^{13}C), to overcome the low sensitivity of the latter, which is due to its small gyromagnetic ratio $(\gamma(^{1}H) = 4 \cdot \gamma(^{13}C))$, low natural abundance (1% for ^{13}C), and long spin-lattice relaxation times (several seconds to several minutes for ^{13}C). By using CP, the sensitivity of each scan can be (theoretically) enhanced by the ratios of the gyromagnetic ratio of the two nuclei, that is ~ 4 for CP from ^{1}H to ^{13}C. Technically, the CP is achieved by irradiating simultaneously the abundant spin reservoir (^{1}H) and the rare spins (^{13}C) with RF reaching the Hartmann-Hahn matching condition (vide ultra). This "spin-lock" condition allows the magnetization transfer to occur from protons to ^{13}C nuclei, thus enhancing the spectral sensitivity. In general, CP between abundant and rare spins is achievable provided the hardware is suitably designed. For example, in the course of this work also ^{19}F to ^{13}C CP has been used. Along with the beneficial magnetization transfer obtainable by using CP, also the repetition rate for multiple scans is determined by the much shorter spin-lattice relaxation time of the abundant nuclei - protons or fluorines –, thus requiring shorter relaxation delays and allowing to collect more scans in the same amount of time.

The basic CPMAS experiment (Figure 4.2b) starts with a 90° pulse on the abundant spin (in our case ^{1}H or ^{19}F) which is followed by a spin-lock pulse of the abundant spin (^{1}H or ^{19}F) along the y-axis[176]. During this time, a spin-lock of same length is applied on the dilute spin (^{13}C), placing both magnetization vectors along the y-axis in a way that magnetization (polarization) transfer can occur[176]. The time during which the two spin-lock fields are applied is named contact time. After the spin lock pulse, the radio frequency on the dilute spin (^{13}C) is turned off allowing the signal

acquisition while the abundant spin is decoupled[176]. For polarization transfer to occur, the Hartmann-Hahn matching condition[177], where both nuclei nutate at the same frequency and have equal effective energies, must be met (Eq. 4.1).

$$\omega_{1(^1H)} = \omega_{1(^{13}C)} \implies \gamma_{(^1H)}B_{1(^1H)} = \gamma_{(^{13}C)}B_{1(^{13}C)} \qquad (4.1)$$

The theory of CP combined with MAS is a bit tricky. Basically, the sample spinning introduces a time dependence into the dipolar coupling. Fortunately, the modified Hartman-Hahn matching condition for the case of CP combined with MAS is rather easy (Eq. 4.2):

$$\omega_{1(^1H)} = \omega_{1(^{13}C)} + n\omega_{rot} \qquad (4.2)$$

with $n = 0, \pm 1, \pm 2, ...$

This condition is obtained by setting the effective field B₁ on each channel such that the difference between the product of the effective magnetic field and the gyromagnetic ratio is equal to n times the MAS rate in kHz [178] (Eq. 4.3).

$$\gamma_{(^1H)}B_{1(^1H)} - \gamma_{(^{13}C)}B_{1(^{13}C)} = nMAS \qquad (4.3)$$

Then, the efficiency of the polarization transfer is different for different values of n, depending on the spinning speed. Therefore, it is recommended to use shaped contact pulses (on one or both nuclei) to cover a range of RF fields in a single contact pulse. Figure 4.2c shows the CPMAS pulse sequence with ramp-shaped contact pulse on proton used in this thesis work. The use of a linear variation of $B_{1(^1H)}$ over the contact time compensates for the spinning speed and makes the matching more robust.
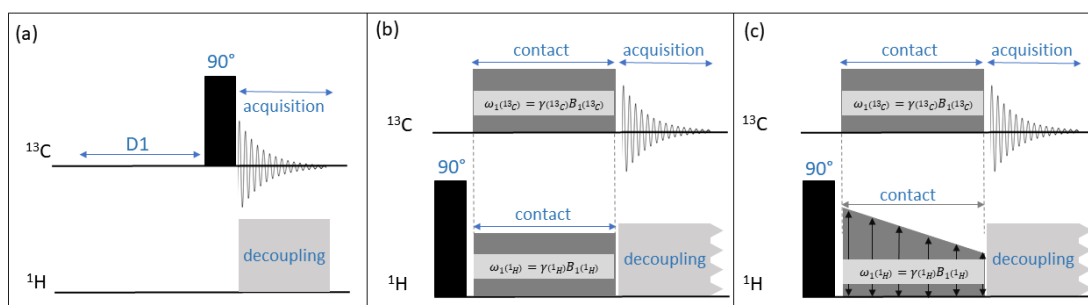
Figure 4.2. Schematic representation of the pulse sequences (a) 1D ^{13}C HPDEC MAS, (b) ^{1}H-^{13}C cross polarization (CP) with rectangular contact pulses on both ^{1}H and ^{13}C, and (c) ^{1}H-^{13}C cross polarization (CP) with ramped contact pulse on ^{1}H and rectangular contact pulse on ^{13}C.

As magnetization transfer between spins during CP is dependent on the strength of the dipolar coupling interaction, the resultant spectral intensities can be used to get information regarding the distances

between chemical environments (i.e., stronger signals are indicative of spin environments being closer together in space) and site mobility (increased motion decreases the strength of the dipolar coupling interaction leading to weaker signals)[178].

In this thesis, ssNMR experiments were performed to get structural and dynamic information of the solid binary $P(MMA)_{0.91}$-$(PIL)_{0.09}$ polymeric systems. The sample were manipulated as a powder and packed in a 4 mm rotor (volume 50 µl) closed with a VESPEL cap inside a glove bag under nitrogen atmosphere. 1D ^{13}C HPDEC MAS, ^{1}H-^{13}C and ^{19}F-^{13}C CPMAS NMR spectra were collected on a Bruker NEO 500 MHz console (^{1}H, ^{19}F and ^{13}C Larmor frequencies of 500.0 MHz, 470.385 MHz and 125.721 MHz, respectively) equipped with a 4 mm CPMAS iProbe operating at a magnetic field of 11.74 T. ^{1}H-^{13}C and ^{19}F-^{13}C CPMAS experiments were performed by fulfilling the Hartmann-Hahn condition by using optimized contact time of 2 ms and 5 ms, respectively. For the PMMA the optimized contact time was 0.5 ms. The samples were spun at 12 kHz and the spectra were collected over 2-18 k scans with 2-10 s recycling delay. In both HPDEC and CPMAS experiments, the SPINAL64 decoupling sequence was used, with a power of 215 W and 230 W for ^{1}H and ^{19}F, respectively. All measurements were performed at room temperature.

4.2.4. PFG NMR measurements

The theoretical background the PFG NMR was already described in the *Chapter 3*. Here, the same technique was used to determine the self-diffusion coefficients of the highly viscous binary and ternary polymeric samples, $(DBUH-IM14)_{0.60}P(MMA)_{0.40}$ and $(DBUH)_{0.55}$-$(Li)_{0.06}$-$P(MMA)_{0.39}$. The experiments were performed during my secondment at the Hunter College – CUNY, on a 300 MHz NMR spectrometer with Agilent/Varian DDR console two channel solids configuration operating at a magnetic field of 7 T (^{1}H, ^{19}F and ^{7}Li Larmor frequencies of 300.0, 282.4 and 116.6 MHz, respectively) equipped with a Doty Z-spec PFG NMR probe. The diffusion coefficients were measured as a function of temperature by using BPP-LED pulse sequence. The temperature was controlled by a variable temperature (VT) unit in conjunction with a thermocouple before each measurement. At least 16 transients were used with optimized recycling delay (4–8 s). The gradient strength was varied in the range of 50–850 G.cm^{-1} for 16 increments, allowing, if possible, 95% of the signal attenuation at the last step experiment. The diffusion time (Δ) and the diffusion pulse length (δ) were set as the range of 50–100 ms and 2–3 ms, respectively. The raw spectra acquired were subjected to manual phasing and automatic baseline correction. Data were processed using an exponential filter in F2

dimension (LB = 0.3 Hz). Integrals were employed to fit the Stejskal–Tanner relation[120] using the software *Origin Pro 16*:

4.2.5. Fast Field Cycling Relaxometry (FFC) NMR

Fast field cycling relaxometry NMR (FFC NMR) is a powerful tool for the identification and characterization of molecular dynamics in a complex polymeric system covering different frequencies with the same instrument[179]. The two typical FFC sequences used to measure T_1 are the so-called prepolarized (PP) and nonpolarized (NP) techniques (Fig. 4.3a and b, respectively). The PP consists of a first step of polarization of the sample in a magnetic field with a flux density B_p as high as technically feasible; in this step the equilibrium magnetization builds up during the polarization time (d_p). After switching to the low relaxation field B_r, the spin system relaxes to a new equilibrium state imposed by the new magnetic field value. Finally, the magnetic field is switched up to B_d, again as high as possible, to detect the NMR signal in the detection field through the application of a radio-frequency (RF) pulse. The RF unit is tuned to a predetermined frequency irrespective of the relaxation field chosen. The time needed by the field to jump between different levels is contained in the switching time (s_w). Then, an extended recycle delay for the restoration of thermal equilibrium and polarization follows until the next cycle begins. In the NP sequence, the only difference is that the magnetization built up during relaxation in the field B_r is sampled in the detection field B_d. When the relaxation B_r approaches the polarization one B_p, the magnetization evolution takes place between close initial and final values, incrementing thus the error of the measurement. In such a case the NP sequence is preferable, where the magnetization growth from an initial zero value is sampled[180].
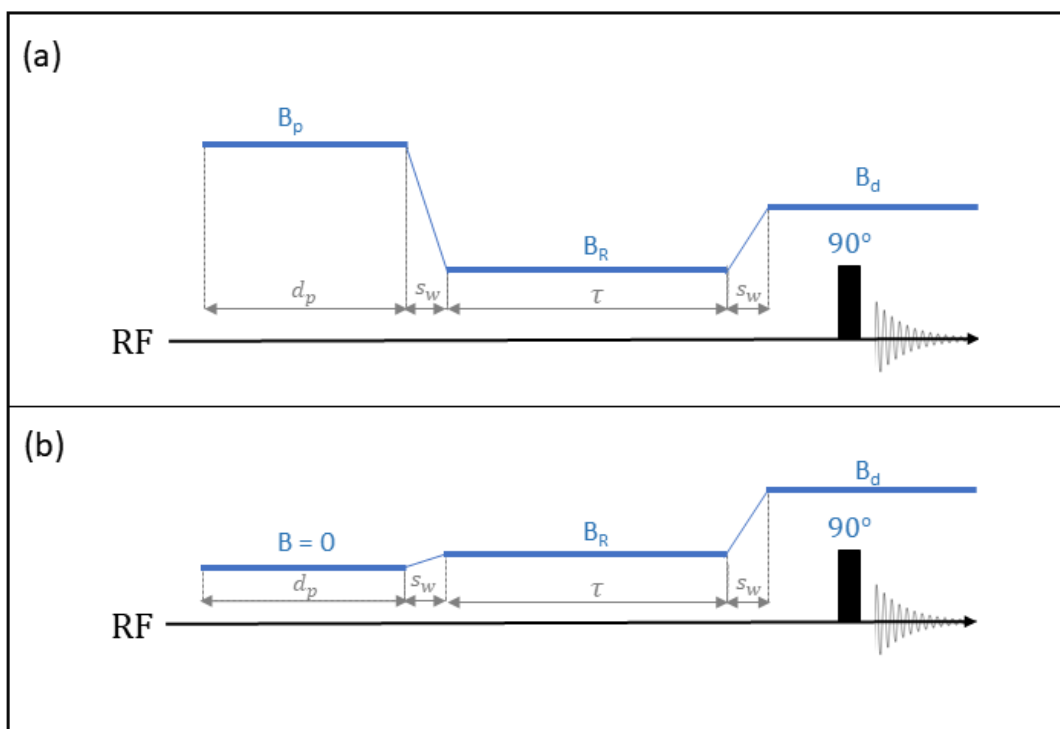
Figure 4.3. Schematic representation of the basic (a) prepolarized (PP) and (b) nonpolarized (NP) FFC NMR sequences.

In this thesis, the FFC NMR was used to acquire the ^{1}H and ^{19}F spin-lattice relaxation rate (R_1) dispersions for the neat DBUH-IM14, the DBUH-IM14 electrolyte (DBUH-LiIM14), and the two highly viscous binary and ternary polymeric systems ((DBUH-IM14)$_{0.60}$P(MMA)$_{0.40}$ and (DBUH)$_{0.55}$-(Li)$_{0.06}$-P(MMA)$_{0.39}$. The experiments were carried out during my secondment at the Hunter College – City University New York (CUNY) using a Spinmaster FFC2000 CDC Relaxometer (Stelar; Italy). The spin-lattice relaxation rate R_1 was determined by using the standard prepolarized (PP) and non-polarized (NP) sequences. In all cases, the polarization magnetic field was 0.353 T (equivalent to 15 MHz for ^{1}H Larmor frequency). The acquisition magnetic field was 0.383 T (equivalent to 16.3 MHz for ^{1}H Larmor frequency) and 0.432 T (equivalent to 17.3 MHz for ^{1}H Larmor frequency) for ^{1}H and ^{19}F relaxation measurements, respectively. Relaxation dispersion curves were measured with 20 points distributed in a window ranging from 30 kHz to 20 MHz in ^{1}H Larmor frequencies (relaxation magnetic field values). The field slew rate was 13 MHz.ms^{-1} and the switching time was 3 ms. Typically, 4-8 signal scans were accumulated at each delay τ (16 different values) and frequency. R_1 was calculated from the magnetization recovery curves and were not sensitive to the time window over which the NMR signal was acquired (after a 90° pulse). The spin relaxation profiles were tabulated with respect to τ for a given B_R, and T_1 by fitting the mono-exponential profiles with Equation 4.4[180], at all frequencies.

$$M_z(\tau) = M_0(B_r) + \left[M_0\left(B_p\right) - M_0(B_r)\right]e^{-\frac{\tau}{t_1(B_R)}} \qquad (4.4)$$

Relaxation profiles were measured at four different temperatures: 298 K, 313 K, 328 K, and 343 K. The sample temperature was controlled within ±1°C using a Stelar variable temperature controller (VTC). For the electrolyte samples, the ^{7}Li relaxation rate profiles could not be measured due to the poor signal to noise ratio attributed in part to the very short spin-spin relaxation time T_2 (in the range of μs) which was even shorter than the switching time (3 ms).

4.3. Results

4.3.1. DSC and TGA analysis

The glass transition temperature (T_g) is important in designing polymeric materials because it distinguishes between the hard, glassy region and the rubbery plateau in the DSC curve, thereby determining the temperature range where a polymer will have the flexibility, processability, and workability of plastics[181]. Figure 4.4a displays the DSC thermograms of the pure PMMA and the investigated solid binary polymeric P(MMA)$_{0.91}$-(PIL)$_{0.09}$ samples. The DSC thermograms indicate the full miscibility and a single-phase morphology of the PMMA and PILs in the blended systems due to the presence of a very broad glass transition feature (magnified in Figure 4.4b). For the neat PMMA, the DSC shows a glass transition at 391 K, in agreement with values already reported in the literature[182]. When housing the PILs, the glass transition is shifted toward lower temperatures around 330 K, suggesting a *plasticizing* effect due to the presence of the PIL[182]. In DSC curves, the T_g of the samples is defined as the middle point of the temperature range in which the heat flow jumps from the value of the glassy state to that of the rubbery state. The T_g values of all investigated systems are summarized in Table 4.2.
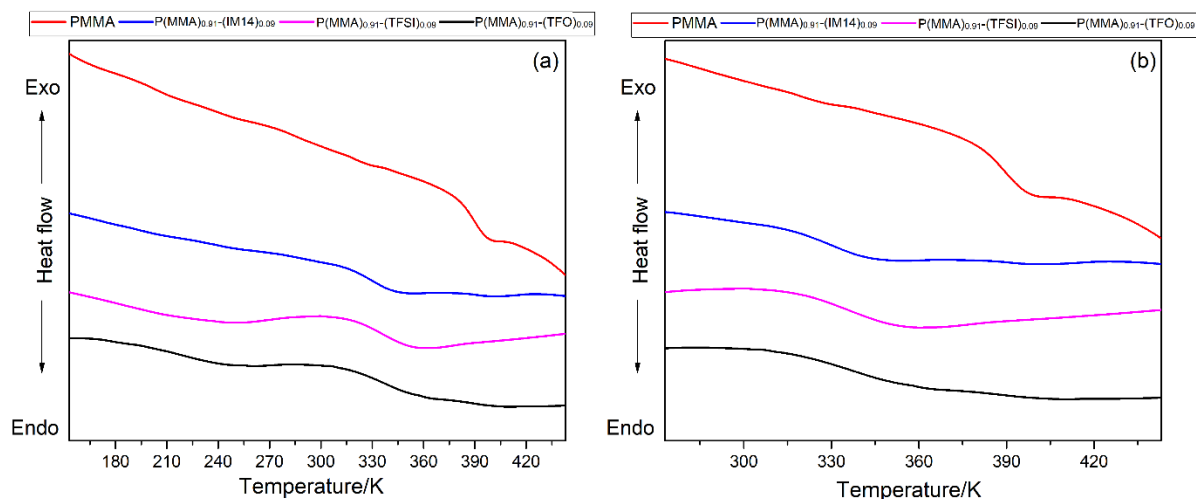
Figure 4.4. DSC thermograms of the PMMA and P(MMA)$_{0.91}$-(PIL)$_{0.09}$ systems investigated (a) in the full range of temperature evaluated and (b) in the magnified region from 273 to 443 K.

Figures 4.5(a-b) show the TGA and DTG curves of the studied systems, respectively. According to the literature, PMMA exhibits a degradation stage (i.e., at 572 K) attributed to the decomposition of its side chain, followed by a second degradation plateau (i.e., at 653 K) relative to the decomposition of the PMMA main chain[183].

The two PMMA-related degradation stages are preserved in the TGA curves of the solid binary polymeric systems P(MMA)$_{0.91}$-(PIL)$_{0.09}$ (Table 4.2). Moreover, an additional decomposition plateau is observed above 700K for the samples P(MMA)$_{0.91}$-(PIL)$_{0.09}$, representing the main decomposition of the PIL itself. A similar behavior has already been reported for other PMMA:IL systems[184,185]. For the P(MMA)$_{0.91}$-(TFO)$_{0.09}$ sample (green line in Figure 4.5(b)), there is an initial degradation stage at 493 K, probably due to the decomposition of impurities trapped in the PMMA matrix (equivalent to 1.5 % weight loss) coming from the annealing procedure.

A few considerations can be drawn from TGA/DTG data of Table 4.2:

- The weight loss (w_1) of the first degradation stage (around 570 K), attributed to the decomposition of the PMMA side chain, is lower for the P(MMA)$_{0.91}$-(PIL)$_{0.09}$ than for the PMMA itself. Actually, the expected first weight loss (w_1) considering the amount of PMMA present in the system would be nearly 25%, 27%, 30% for P(MMA)$_{0.91}$-(IM14)$_{0.09}$, P(MMA)$_{0.91}$-(TFSI)$_{0.09}$ and P(MMA)$_{0.91}$-(TFO)$_{0.09}$, respectively. However, the respective w_1 detected was 21%, 9% and 3%.
- Interestingly, the degradation temperatures of the second plateau observed in (PMMA)$_{0.91}$-(PIL)$_{0.09}$ samples were 14-20 K higher than the neat PMMA. When housing the PILs, the PMMA samples became more thermally stable than the PMMA itself, probably due to the interaction between the

polymer and the PIL. Similar findings have been already reported in the literature[184,186].

- The degradation temperature of the PIL in the solid polymeric sample is very close to the T_d of the neat PIL, i.e., the immobilization in the solid support does not have a significant effect on the PIL thermal stability.
- The weight loss of the third plateau, i.e., corresponding to the PIL in the solid sample (w_3) does not correspond to the total weight fraction of the PIL in binary system (w_{PIL}). This indicates that a fraction of the PIL degrades in the previous stages at lower temperatures, due to interactions between the PIL and the PMMA.
- Finally, it is worth mentioning that DBUH-IM14 seems to have stronger interactions with the PMMA than the other PILs, reflecting on the higher weight loss of the DBUH-IM14 occurring at the initial plateaus (for instance the difference w_3 to w_{PIL} is 9% for while is 5% for DBUH-TFO and DBUH-TFSI).
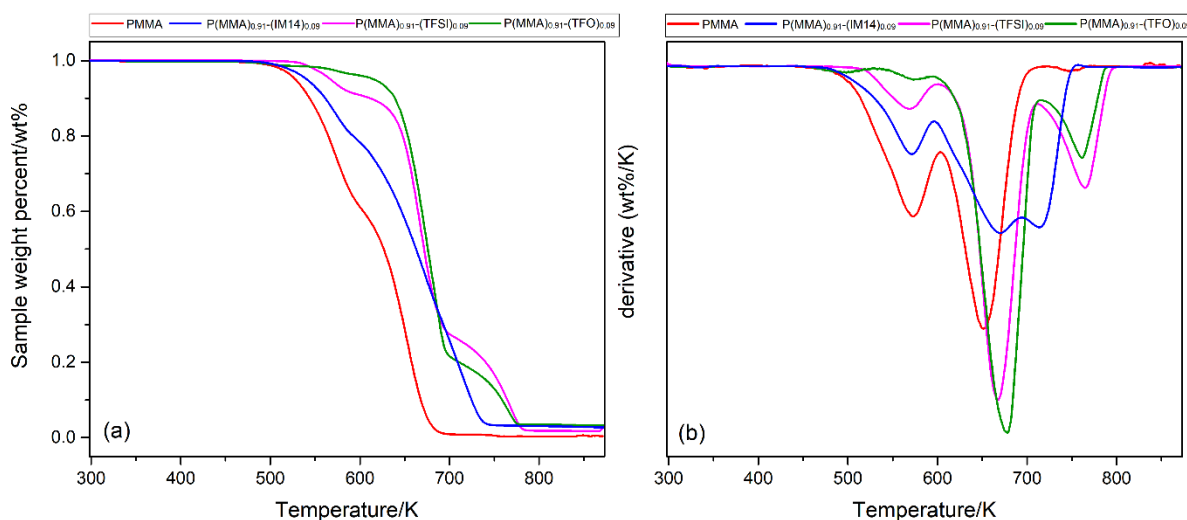
Figure 4.5. (a) TGA and (b) DTG plot of the PMMA and P(MMA)$_{0.91}$-(PIL)$_{0.09}$ samples.

Table 4.2. Glass transition T_g and degradation temperature T_d of the studied PMMA and solid binary polymeric P(MMA)$_{0.91}$-(PIL)$_{0.09}$ systems*. Degradation temperature of the neat PIL is also listed for comparison.

Sample	T_g (K)	T_{d1}(K)	w_1 (%)	T_{d2} (K)	w_2 (%)	T_{d3} (K)	w_3 (%)	w_{PIL} (%)	$T_{d\text{-}PIL}$ (K)
PMMA	391	572	39	653	61				
P(MMA)$_{0.91}$-(IM14)$_{0.09}$	332	570	21	670	48	714	28	37	
P(MMA)$_{0.91}$-(TFSI)$_{0.09}$	337	571	9	667	65	768	25	30	
P(MMA)$_{0.91}$-(TFO)$_{0.09}$	330	575	3	673	76	766	17	23	
DBUH-IM14									712
DBUH-TFSI									762
DBUH-TFO									760

*T_{di} corresponds to the degradation temperature at the i plateau; w_i corresponds to the weight loss percent at the i plateau; w_{PIL} corresponds to the total weight fraction of the PIL in binary system, $T_{d\text{-}PIL}$ corresponds to the degradation temperature of the neat PIL, as described in *Section 2.3.5* of *Chapter 2*.

4.3.2. Solid state NMR

To further investigate the structural features of the solid binary polymeric $P(MMA)_{0.91}$-$(PIL)_{0.09}$ systems, I used different ssNMR techniques. The ^{13}C HPDEC spectra (Figure 4.6) spectra clearly show the PMMA peaks, which means that the polymer exhibits non-negligible mobility. This may be related to the internal mobility of the long polymer chain segments between crosslinking points, as previously detected for other polymeric systems[175]. In the ^{13}C HPDEC spectra of the blended systems, signals corresponding to the DBUH$^+$ cation and the anions (TFO$^-$, TFSI$^-$ and IM14$^-$) can be detected. This indicates that all PILs retained some internal mobility when housed by the PMMA polymer.
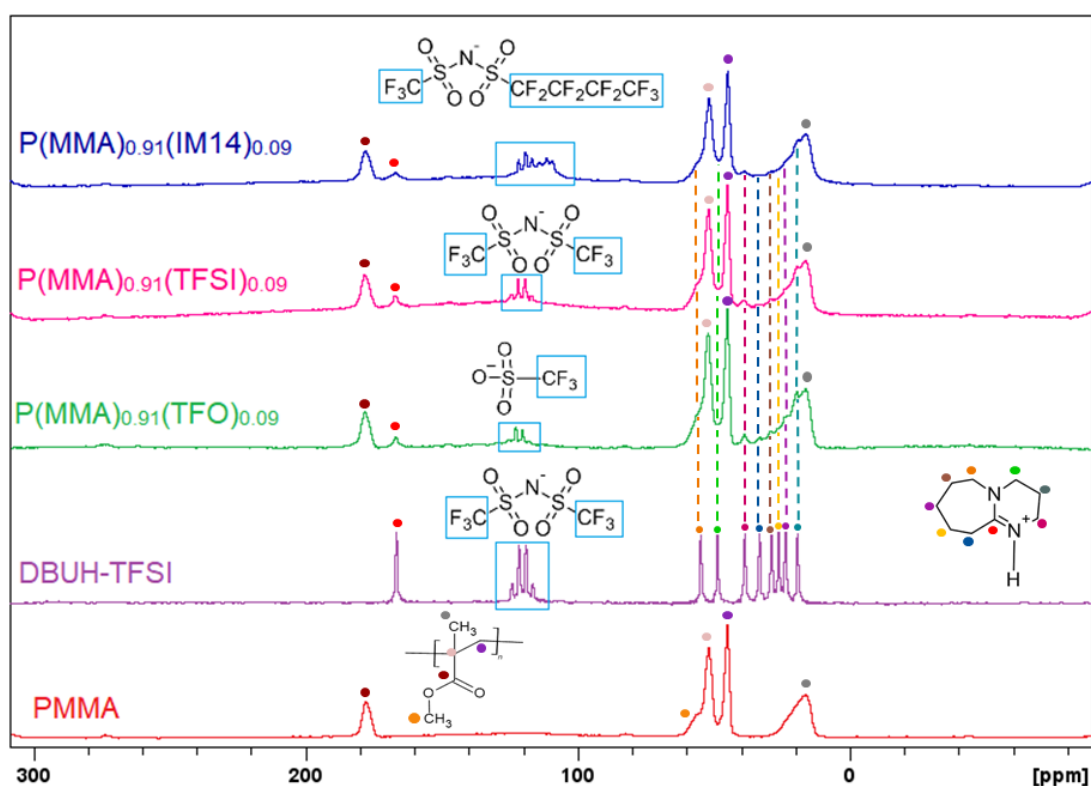
Figure 4.6. ^{13}C HPDEC spectra recorded at 298 K for the PMMA and the solid binary polymeric $P(MMA)_{0.91}$-$(PIL)_{0.09}$ systems, at a spinning speed of 12kHz. The ^{13}C HPDEC spectra of the DBUH-TFSI recorded at 293 K is also reported as a comparison purpose.

To get more information about the interactions between the polymer and the PILs, I performed ^{19}F-^{13}C CPMAS (Figure 4.7) and ^{1}H-^{13}C CPMAS (Figure 4.8) experiments. As explained in *Section 4.2.3*, CP allows to identify sites based on the strength of the heteronuclear dipolar coupling interaction that exists between nuclei. Given, the transfer of magnetization from ^{1}H or ^{19}F to ^{13}C depends on the dipolar through-space interaction[176], stronger signals are

indicative of stronger dipolar couplings (i.e., the nuclei are closer in space), whereas weaker signals indicate weaker dipolar couplings[178]. Besides, the intensity of CP spectra is also associated with ion mobility, as increased mobility tends to reduce the strength of the dipolar coupling interaction[187].

The ^{1}H-^{13}C CPMAS spectra (Figure 4.7) display all characteristic signals of PMMA, but no signal corresponding to the DBU cation is visible, even with 6K scans. This would indicate that the DBU cations are relatively mobile in the solid polymeric samples, so that the heteronuclear dipolar interactions are partially averaged out and do not markedly contribute to the ^{13}C signal enhancement.

More interesting findings emerged from the ^{19}F-^{13}C CPMAS spectra shown in Figure 4.8. It is evident that in all systems there is a signal enhancement due to the ^{19}F-^{13}C cross-polarization from the anion's fluorine nuclei and the PMMA carbons, and this transfer is more effective for IM14$^-$ than TFSI$^-$ and TFO$^-$. Although this is a qualitative observation, it is a first ranking of the interactions of the anions with the polymeric matrix (i.e., spatial proximity and mobility of the anions). Accordingly, the results indicate that IM14$^-$ is closer in space to the polymer backbone and less mobile compared to the other anions. This is also in agreement with the findings of the TGA analysis, reported in the *section 4.3.1*.
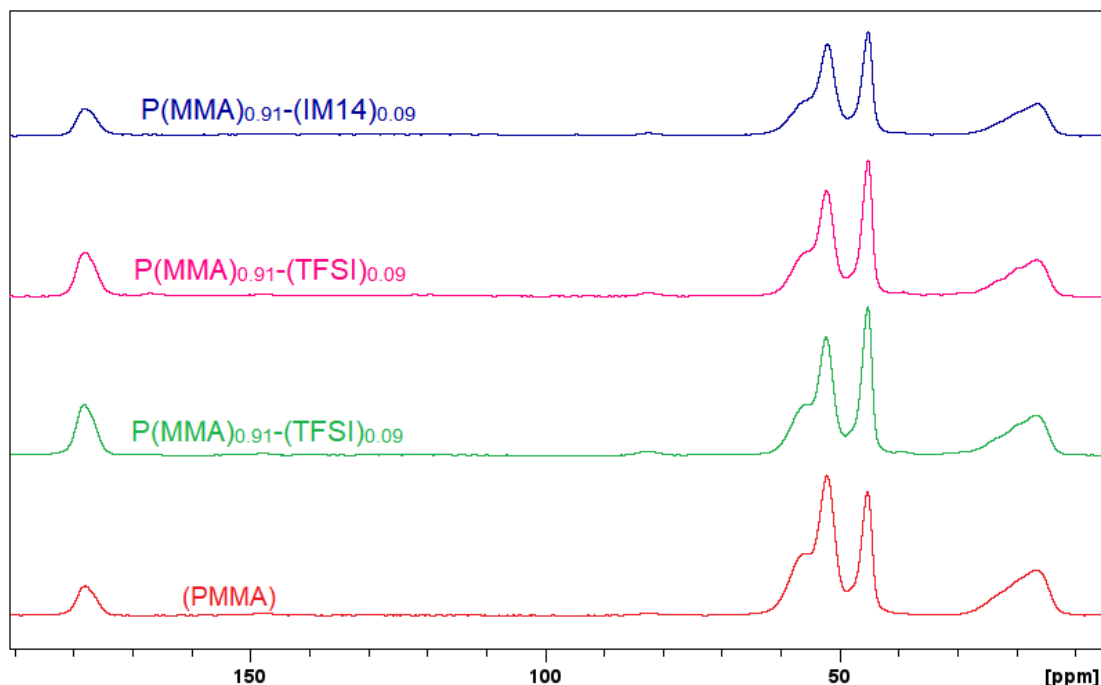
Figure 4.7. ^{1}H-^{13}C CPMAS spectra of the solid polymeric binary P(MMA)$_{0.91}$-(PIL)$_{0.09}$ systems, acquired with a contact time of 2 ms, and ^{1}H-^{13}C CPMAS spectrum of the PMMA acquired with a contact time of 0.5 ms. All spectra were acquired at 298 K at a spinning speed of 12 kHz.
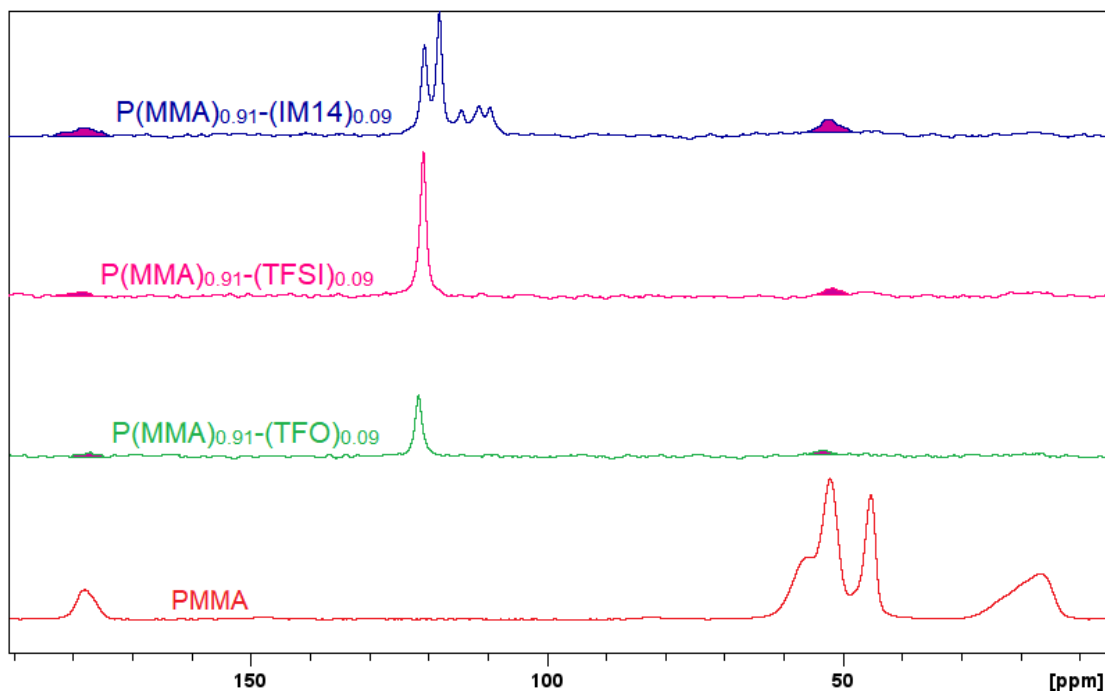
Figure 4.8. ^{19}F-^{13}C CPMAS spectra of the solid polymeric binary P(MMA)$_{0.91}$-(PIL)$_{0.09}$ systems, acquired with a contact time of 5 ms, and ^{1}H-^{13}C CPMAS spectrum of the PMMA acquired with a contact time of 0.5 ms. All spectra were acquired at 298 K at a spinning speed of 12 kHz. The shaded areas are a guide for the eyes to stress the amount of cross-polarization between ^{19}F (anion) and ^{13}C (polymer backbone).

4.3.3. PFG NMR measurements

Both TGA and ssNMR unveiled a peculiar behavior of the solid polymeric binary system containing DBUH-IM14 trapped in PMMA, with stronger PIL-polymer interactions compared to the parent systems containing the TFSI$^-$ and TFO$^-$ as the anions. This is also in line with the unique features of neat DBUH-IM14 in terms of intermolecular interactions already observed in *Chapters 2 and 3*.

Given the peculiarities of the P(MMA)$_{0.91}$-(IM14)$_{0.09}$ system, a blended sample with a much lower PMMA concentration was prepared and investigated to gain more insights into the intermolecular interactions, structure and dynamics of the system. More in detail, I blended DBUH-IM14 with PMMA at 10% wt in the attempt of forming a gel-like system. Viewing the potential application of gels as safer electrolytes in energy storage devices, a ternary polymeric sample was also prepared blending DBUH-LiIM14 with PMMA at 10% wt. Note that this low concentration of PMMA selected as a preliminary study drastically increased the viscosity of the systems with respect to the neat DBUH-IM14, but did not form free-standing systems to be classified as a gels.

The highly viscous binary and ternary polymeric systems (DBUH-IM14)$_{0.60}$P(MMA)$_{0.40}$ and (DBUH)$_{0.55}$-(Li)$_{0.06}$-P(MMA)$_{0.39}$ were investigated via PFG NMR and FFC NMR to disentangle the effect

of polymer and lithium salt in the rotational and translational mobility of the ionic species blended with the polymeric matrix. Self-diffusion measurements will be presented in this section, while the FFC experiments will be discussed in *Section 4.3.4*.

The self-diffusion coefficients of the $(DBUH-IM14)_{0.60}P(MMA)_{0.40}$ and $(DBUH)_{0.55}-(Li)_{0.06}-P(MMA)_{0.39}$ are shown in Figure 4.9 as a function of temperature. The diffusion data for the neat DBUH-IM14 and DBUH-LiIM14 are also plotted for comparison purposes. The raw data are compiled in Table 4.2. At 298 K, neither the cation nor anion self-diffusion coefficients could be obtained because the maximum gradient strength (850 G.cm^{-1}) was not enough to obtain sufficient signal attention. The Li$^+$ self-diffusion coefficient could not be measured for the system $(DBUH)_{0.55}-(Li)_{0.06}-P(MMA)_{0.39}$ due to its short T_2.
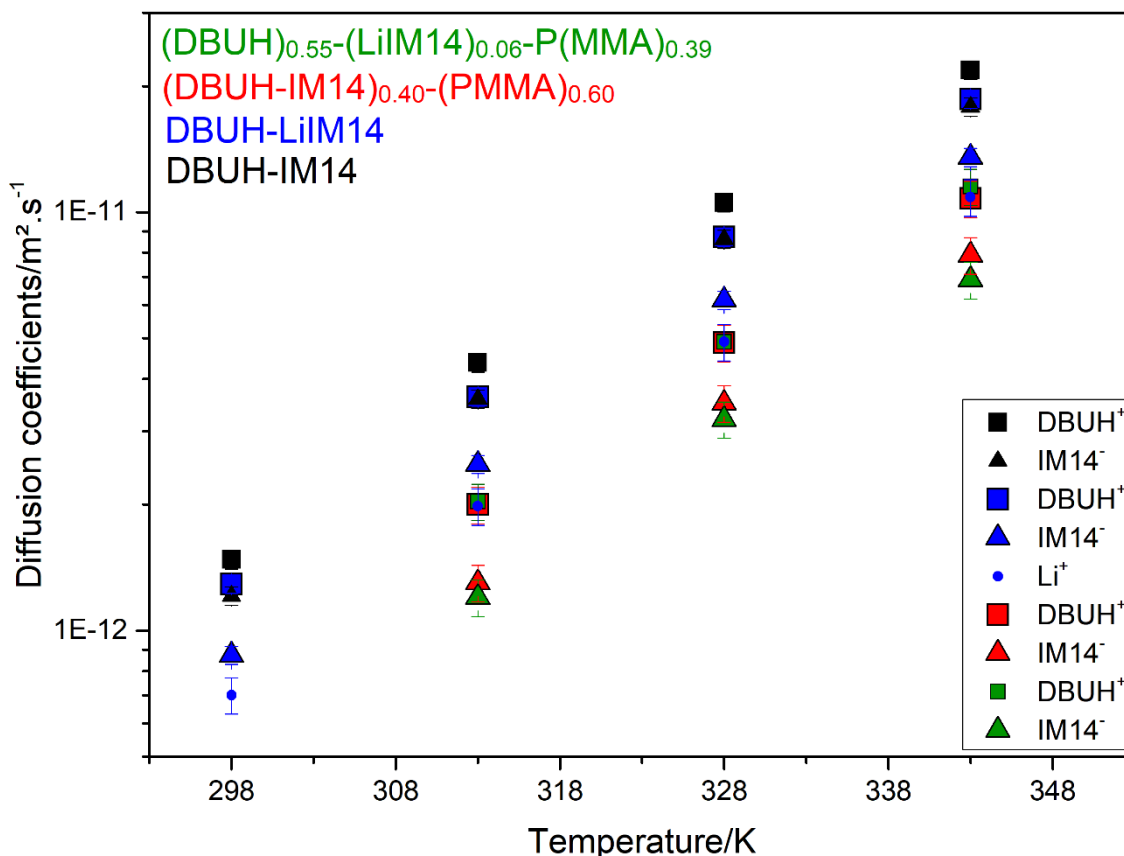
Figure 4.9. Temperature dependence of the self-diffusion coefficients of DBUH$^+$ cation and IM14$^-$ anion in the DBUH-IM14-based systems.

When blending the DBUH-IM14 and DBUH-LiIM14 with the PMMA, the diffusion of both DBUH$^+$ cation and IM14$^-$ anion drastically reduces. No significant differences are detected for the self-diffusion of the ions in the $(DBUH-IM14)_{0.60}P(MMA)_{0.40}$ and $(DBUH)_{0.55}-(Li)_{0.06}-P(MMA)_{0.39}$, meaning that the PMMA plays the major effect on driving the translational mobilities of the ions due to confinement effects. Note that the self-diffusion of the DBUH$^+$ is slightly higher in

the neat PIL (black square) than in the PIL electrolyte (blue square). However, upon the polymer addition, self-diffusion for the DBUH$^+$ cation in both systems (DBUH-IM14)$_{0.60}$P(MMA)$_{0.40}$ and the (DBUH)$_{0.55}$-(Li)$_{0.06}$-P(MMA)$_{0.39}$ fall in the same range. In the case of IM14$^-$ anion, the effect of confinement also plays a crucial role in decreasing this ion mobility, and the presence of Li$^+$ slightly contributes to the lowering of the IM14$^-$ diffusion in the (DBUH)$_{0.55}$-(Li)$_{0.06}$-P(MMA)$_{0.39}$.

Table 4.3. Self-diffusion coefficients of DBUH$^+$ cation and IM14$^-$ anion in the DBUH-IM14-based systems as a function of temperature. Uncertainties of the values are 10%.

Temperature (K)	(DBUH-IM14)$_{0.60}$P(MMA)$_{0.40}$		(DBUH)$_{0.55}$-(Li)$_{0.06}$-P(MMA)$_{0.39}$	
	DBUH$^+$	IM14$^-$	DBUH$^+$	IM14$^-$
313	2.0E-12	1.3E-12	2.0E-12	1.2E-12
328	4.9E-12	3.5E-12	4.9E-12	3.2E-12
343	1.1E-11	7.9E-12	1.1E-11	6.9E-12

4.3.4. FFC NMR

To get more information about the internal mobilities of the ions, I obtained the relaxation rates (R$_1$) of the DBUH-IM14-based highly viscous polymeric systems as a function of temperature (raw data are reported in Appendix A4). Overall, the FFC curves can be properly fitted to a model to disentangle the intra- and intermolecular relaxation contributions. The mathematical modeling of the FFC data is in progress together with our collaborators from Hunter College – CUNY. So far, there is already a model available in the literature to describe the relaxation profile of PILs[188–190], as described in *Section 4.3.4.1*. However, for polymeric systems, more complex relaxation mechanisms are involved[191,192]. Consequently, the development of an appropriated model is still ongoing.

The ^{19}F and ^{1}H relaxation profile of the neat DBUH-IM14 (square symbols in Figure 4.10) shows a significant decreasing of the R$_1$ relaxation rates with increasing of temperature. This is expected from the increase of the fluidity with the temperature which reflects on the decreasing of the correlation times (τ_R) and enhancement of the diffusion coefficients of the PIL[188,189]. Note that the relaxation profile becomes flatter with the temperature increase due to the decreasing of the viscosity[192].

Comparing the effect of the lithium doping in the neat PIL, we observed that ^{1}H relaxation profile is slightly higher upon the addition of the lithium salt until 328 K, whereas at 343 K the ^{1}H relaxation

rates are nearly the same within the error for both DBUH-IM14 and DBUH-LiIM14. The minor increase of the ^{1}H relaxation rates upon addition of the lithium salt may be attributed to the increasing of viscosity. The situation is different for the IM14$^-$anion: Upon LiIM14 doping, ^{19}F relaxes significantly faster as the frequency decreases and as the temperature increases. This is directly connected to the strong Li$^+$ and IM14$^-$ association, where the quadrupolar interaction may serve as an extra source of relaxation for ^{7}Li and in turn affecting the ^{19}F relaxation by means of intermolecular dipolar coupling[192]. Finally, it is worth mentioning that for DBUH-IM14 and DBUH-LiIM14, ^{1}H and ^{19}F the relaxation profiles show a plateau at the lowest frequencies and highest temperature.
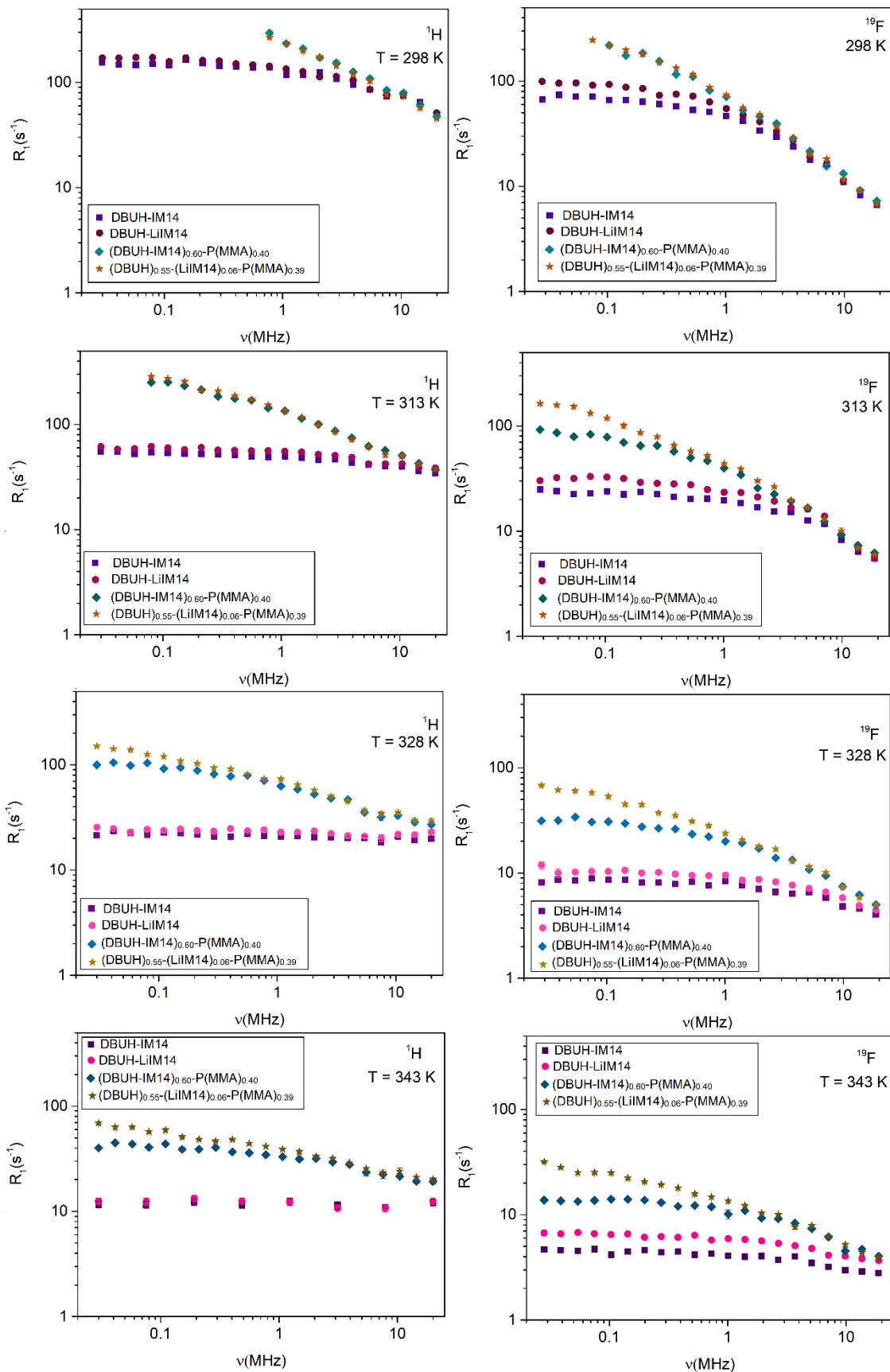
Figure 4.10. ^1H and ^{19}F relaxation rate dispersions (R_1) for DBUH-IM14, DBUH-LiIM14, (DBUH-IM14)$_{0.60}$-P(MMA)$_{0.40}$ and (DBUH)$_{0.55}$-(Li)$_{0.06}$-P(MMA)$_{0.39}$ recorded at 298 K, 313 K, 328 K and 343 K.

When the PIL is mixed with the polymer, the molecular dynamics of the ions become more complex for the confinement effects. Since both cations and anions can interact with the polymer chains, their translational displacements become restricted taking different local orientations determined by the topology of the polymer network. These molecular reorientations mediated by translational displacements (RMTD) of the molecules, which occur on a much slower time scale than bulk rotational or translational diffusion, have shown to be an efficient relaxation mechanism taking place in polymeric systems[193,194].

When blending the DBUH-IM14 and DBUH-LiIM14 with the PMMA, a strong increase of the relaxation rate is observed. ^1H and ^{19}F in the (DBUH-IM14)$_{0.60}$-P(MMA)$_{0.40,}$ show a monotonic R_1 increase when the frequency decrease, followed by a plateau as the temperature increases (as detected for DBUH-IM14 and DBUH-LiIM14). Instead, (DBUH)$_{0.55}$-(Li)$_{0.06}$-P(MMA)$_{0.39}$ shows a monotonic increase when frequencies decrease without reaching the plateau, resulting in a splitting of the (DBUH-IM14)$_{0.60}$-P(MMA)$_{0.40}$ and (DBUH)$_{0.55}$-(Li)$_{0.06}$-P(MMA)$_{0.39}$ relaxation profiles. This different behavior is a clear indication that a new relaxation mechanism is activated in the polymer electrolyte system because of confinement of the PIL and the presence of Li$^+$. Even though a model is under development to explain the relaxation profiles and therefore the dynamics of these systems, we can certainly state that structural features and nature of the intermolecular interaction are playing a crucial role in the transport properties of the DBUH-IM14 polymer electrolytes.

4.3.4.1. Analysis of ^1H and ^{19}F relaxation profiles in the DBUH-IM14

The spin−lattice relaxation of ^1H and ^{19}F (spins of quantum number I = 1/2) in ionic liquids (ILs) is mainly due to the dipole−dipole interactions through space which can be divided into intra- and intermolecular ones[179]. In the case of DBUH-IM14, ^1H nuclei can be found solely in the cation, whereas ^{19}F nuclei are only found in the anion. Thus, homonuclear interactions are either intramolecular or intermolecular between the same species (co-ions) and heteronuclear interactions are solely between cation and anion (counter-ions). As a first approach, the ^1H and ^{19}F spin−lattice relaxation dispersions of ILs can be modeled by considering translational diffusion plus a Lorentzian term accounting for molecular rotations[192]. This model was already successfully applied to describe the molecular dynamics of the aprotic ionic liquid 1-butyl-3-methylimidazolium bis(trifluoromethylsulfonyl)imide BMIM-TFSI[192].

In the present thesis, the translational diffusion was modeled using the so-called force-free-hard-sphere (FFHS) model, which considers that the molecular motion can be compared to that of a rigid sphere following the Fick's diffusion equation[195,196]. According to this assumption, the spins are positioned in the center of the molecules, and there is a uniform distribution of the molecules outside the distance d of the closest approach which should be of the order of the ion size. The FFHS diffusion model, which considers an excluded volume effect because of the last assumption, is resolved by including an extra term in the relative diffusion equation, representing the potential from averaged forces between the spin-bearing molecules. The homonuclear (Eq 4.5) and heteronuclear (Eq 4.6) translational relaxation rates R_1 are given as:

$$R_{1Diff}^{ii}(\omega_i) = \frac{A_D^{ii}}{d_{ii}D_{ii}}\left[\tilde{J}(z(\omega_i))\right.$$
$$\left. + 4\tilde{J}(z(2\omega_i))\right]$$
(4.5)

$$R_{1Diff}^{ij}(\omega_i) = \frac{A_D^{ij}}{d_{ij}D_{ij}}\left[\tilde{J}\left(z(\omega_i - \omega_j)\right) + 3\tilde{J}(z(\omega_i))\right.$$
$$\left. + 6\tilde{J}\left(z(\omega_i + \omega_j)\right)\right]$$
(4.6)

where A_D^{ii}, A_D^{ij} and the spectral density $\tilde{J}(z)$ are given by:

$$A_D^{ii} = \frac{8}{45}\pi\gamma_i^4\hbar^2\left(\frac{\mu_0}{4\pi}\right)^2 n_i$$
(4.7)

$$A_D^{ij} = \frac{8}{135}\pi\gamma_i^2\gamma_j^2\hbar^2\left(\frac{\mu_0}{4\pi}\right)^2 n_j$$
(4.8)

$$\tilde{J}(z) = \frac{1 + \frac{5}{8}z + \frac{z^2}{8}}{1 + z + \frac{z^2}{2} + \frac{z^3}{6} + \frac{z^5}{81} + \frac{z^6}{648}}$$
(4.9)

Here, n_i is the nuclear density (calculated by Eq. 4.10), $\hbar$ is Plank's constant divided by 2π, and μ_0 is the vacuum magnetic permeability.

$$n_i = \frac{N\rho N_A}{MM}$$
(4.10)

Where *MM* is the molecular mass, ρ is the density of the IL, *N* is the number of spins (i.e., number of protons or fluorine nuclei) per molecule, and N_A is Avogadro's number.

$z(\omega_i)$ is given by Eq 4.11:

$$z(\omega_i) \equiv \sqrt{2\omega_i d_{ij}^2 \Big/ D_{ij}}$$
(4.11)

And $\omega_i = 2\pi\nu_0$, where ν_0 is the observed frequency

D_{ij} is defined as the sum of the self-diffusion coefficients of the pair of molecules involved in the intermolecular iinteractions (Eq. 4.12); d_{ij} is the closest distance between two nuclei located in different molecules:

$$D_{ij} = D_i + D_j \qquad (4.12)$$

For the contribution of the rotational dynamics, isotropic molecular rotations with an average correlation time were assumed as a first approach[156]. Hence, a Lorentzian form can, in principle, describes the contribution of molecular rotations to the spin−lattice relaxation rate (Eq. 4.13)

$$R_{1Rot}^{ii}(\omega_i) = A_R \left[\frac{\tau_R}{1 + (\omega_i)^2 \tau_R^2} + \frac{4\tau_R}{1 + (2\omega_i)^2 \tau_R^2} \right] \qquad (4.13)$$

$$A_R = \frac{3}{10} \gamma_i^4 \hbar^2 \left(\frac{\mu_0}{4\pi} \right)^2 \frac{1}{r_i^6} \qquad (4.14)$$

where A_R is the corresponding amplitude reflecting the strength of the relevant $^1H-^1H$ ($^{19}F-^{19}F$) dipolar interactions, r_i is the effective $^1H-^1H$ ($^{19}F-^{19}F$) distance between two nuclei located in the same molecule, and τ_R is the average rotational correlation time.

If the two processes described above, translational diffusion and molecular rotations, are assumed statistically independent and/or dominant in different time scales, the total spin−lattice relaxation rate of the DBUH-IM14 will be given by Eq. 4.15:

$$R_1^I(\omega) = R_{1intra}(\omega) + R_{1inter}(\omega) \qquad (4.15)$$

$$R_1^I(\omega) = R_{1Rot}^{ii}(\omega) + R_{1Diff}^{ii}(\omega) + R_{1Diff}^{ij}(\omega)$$

Here, we employed the equation 4.15 to model the ^1H and ^{19}F relaxation rate dispersions of the DBUH-IM14 at 298 K as a first trial.

All the physical parameters involved in these models were estimated from data fitting by means of fixing them within their most probable intervals obtained from the literature. The diffusion parameters and the proton and fluorine densities n_i were calculated as given by Eq 4.10 and 4.12, respectively. Using them in Equations 4.7 and 4.8, A_D^{ii} and A_D^{ij} could also be estimated. The calculated constants and the obtained best fitting parameters are reported in Table 4.4 and 4.5, respectively.

Table 4.4. Calculated constants for fitting of the ^{1}H and ^{19}F at 298 K.

Constant	Value
n_H (m^{-3})	2.77E+28
n_F (m^{-3})	1.96E+28
A^{HH}_D (m^{3}s^{-2})	8.82E-21
A^{FF}_D (m^{3}s^{-2})	4.89E-21
A^{HF}_D (m^{3}s^{-2})	1.84E-21
A^{FH}_D (m^{3}s^{-2})	2.60E-21
D_{HH} (m^{2}s^{-1})	2.94E-12
D_{FF} (m^{2}s^{-1})	2.46E-12
D_{HF} (m^{2}s^{-1})	2.70E-12
D_{FH} (m^{2}s^{-1})	2.70E-12

Table 4.5. Best fitting parameters for the ^{1}H and ^{19}F at 298 K.

Parameter	^{1}H	^{19}F
d_{HH} (m)	2.1E-10	-
d_{FF} (m)	-	4.4 E-10
d_{HF} (m)	2.1E-10	3.4E-10
D_H (m^{2}s^{-1})	1.45E-12	1.45E-12
D_F (m^{2}s^{-1})	1.2E-12	1.2E-12
A_R (s^{-2})	9.8E+08	0.7E+08
τ_R (s)	9.6E-09	65.4E-09

As a first inspection, the fitting seems to describe well the relaxation profiles of the cation and anion (Figure 4.11). However, a close inspection in the physical meaning of the best fitting parameters (Table 4.5) reveals some few inconsistencies. For example, d_{HF} should have the same value for the ^{1}H and ^{19}F fittings. However, in the present curves this condition could not be satisfied. This may be an indication that the current model, already used for modelling other ILs, does not properly work for fluorine in the case of IM14$^-$. Then, future improvements for modeling the dispersion curves of the IM14$^-$ are currently in progress.
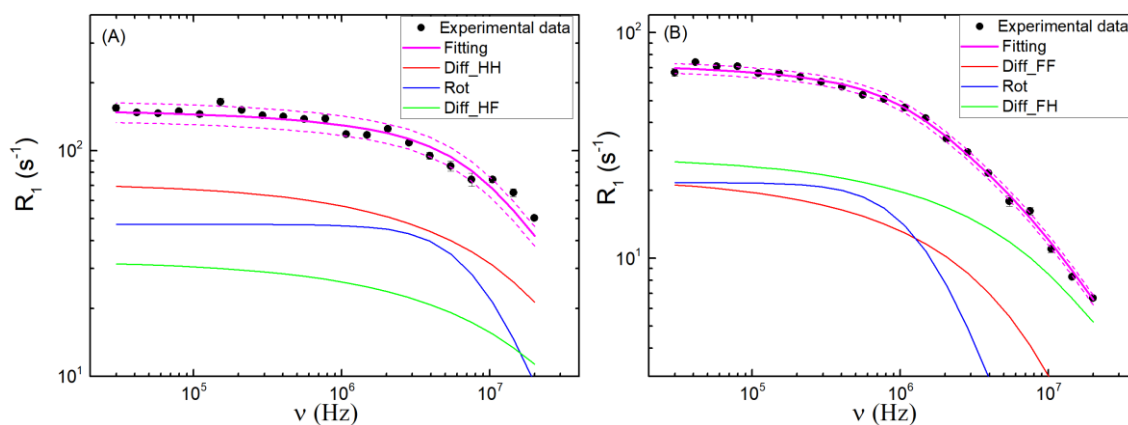
Figure 4.11. 1H(a) and 19F (b) relaxation rate dispersions for DBUH-IM14 and their corresponding fittings using the models given by Eq. 4.15.

Figure 4.11 (a) shows that the relaxation for DBUH$^+$ is dominated by homonuclear translational diffusion in the whole frequency range. In addition, it is worth noting that the rotational contribution is quite important especially from 10 MHz on, and the heteronuclear translational diffusion also contributes to the relaxation mechanism in contrast to other ILs. This is because the higher density of fluorine in IM14$^-$ when compared to other anions (for instance N(TFSI$^-$) = 6 vs N(IM14$^-$) = 12 nuclei per ion). In the case of TFSI-based ILs, the heteronuclear translational diffusion barely contributes to the ^{1}H relaxation mechanism[117,188,190–192].

Now, considering that the best fitting for the ^{19}F relaxation profiles for IM14$^-$ where physically inconsistencies were detected, further improvements of the mathematical model to explain the relaxation profile is still needed. Then, we cannot rely on the obtained curves to describe the specific contributions to the relaxation profile. For instance, the ^{19}F relaxation dispersion of the PIL triethylammonium bis(trifluoromethylsulfonyl)-imide TEA-TFSI, molecular dynamics simulations combined with FFC results suggest that the reorientational dynamics is substantially anisotropic. Hence its intramolecular ^{19}F relaxation rate needs to be expressed by at least two correlation times[190]. Hence, we seek to further improve the mathematical model to properly describe the ^{19}F relaxation profile in DBUH-IM14 and the other DBUH-IM14 based systems.

4.4. Conclusions

In this *Chapter*, thermal analysis, solid state NMR, PFG-NMR and FFC-NMR relaxometry techniques were combined to study the thermal and structural features as well the molecular dynamics of the cations and anions in polymeric systems containing PIL and PIL electrolytes.

In the first set of solid polymeric binary P(MMA)$_{0.91}$-(PIL)$_{0.09}$ systems, it emerged that DBUH-IM14 strongly interact with the PMMA matrix, in contrast to the other PILs (DBUH-TFO and DBUH-TFSI). Such interaction is reflected in the thermal properties changing the degradation profile and in the lowering mobility of the IM14$^-$ anion. Due to the peculiarities of the P(MMA)$_{0.91}$(IM14)$_{0.09}$ system, the investigation was extended to systems containing the DBUH-IM14 PIL but having lower PMMA content.

Studying the translational and rotational mobilities of the systems (DBUH-IM14)$_{0.60}$-P(MMA)$_{0.40}$ and and (DBUH)$_{0.55}$-(Li)$_{0.06}$-P(MMA)$_{0.39}$ I could draw the following conclusions:

(i) the effect of confinement plays a key role in lowering the translational mobilities of the DBUH$^+$ cation and IM14$^-$ anion, considering that the diffusion coefficients were in the same range in both systems despite the presence of Li$^+$;

(ii) A new relaxation mechanism is activated in the polymer electrolyte system because of confinement of the PIL and the presence of Li$^+$. Mathematical modeling of the FFC profiles is still ongoing in order to disentangle the intra- and intermolecular relaxation contributions, and so far, the models available in the literature do not properly describe the ^{19}F relaxation of the fluorine in the IM14$^-$ anion.

FFC raw data

Table A4.1. ^{1}H R_1 relaxation rates obtained for the studied DBUH-IM14, DBUH-LiIM14(DBUH-IM14)$_{0.60}$-P(MMA)$_{0.40}$ and and (DBUH)$_{0.55}$-(Li)$_{0.06}$-P(MMA)$_{0.39}$ systems at 298 K.

ω_{1H} (MHz)	DBUH-IM14 R_1 (s^{-1})	% error	DBUH-LiIM14 R_1 (s^{-1})	% error
20.003	50.38	2.1	51.18	3.13
14.452	65.26	3.9	61.38	3.25
10.440	74.41	2.8	76.83	2.25
7.541	74.46	6.7	74.39	5.84
5.449	85.42	5.2	85.59	4.43
3.937	95.02	3.6	105.09	2.86
2.845	108.38	2.2	113.83	2.22
2.055	124.96	2.4	112.81	2.94
1.484	117.39	1.9	126.97	1.85
1.072	118.45	2.0	134.60	3.05
0.774	138.96	3.7	142.60	1.51
0.560	138.14	1.2	146.93	3.16
0.404	141.79	1.7	150.24	2.54
0.292	143.36	1.2	160.27	1.82
0.211	151.54	2.4	161.67	3.70
0.152	164.36	3.9	170.66	6.78
0.110	145.31	2.6	157.65	2.21
0.080	149.37	2.9	172.57	2.94
0.058	146.76	1.3	172.98	2.26
0.041	147.47	2.2	170.56	4.26
0.030	154.88	3.2	170.72	2.65
ω_{1H} (MHz)	(DBUH-IM14)$_{0.60}$-P(MMA)$_{0.40}$ R_1 (s^{-1})	% error	(DBUH)$_{0.55}$-(Li)$_{0.06}$-P(MMA)$_{0.39}$ R_1 (s^{-1})	% error
20.003	47.59	3.71	45.57	2.45
14.452	61.56	3.52	57.29	2.91
10.440	79.64	4.41	73.63	4.14
7.541	84.43	4.22	77.06	4.28
5.449	108.67	4.62	102.83	4.69
3.937	125.92	2.49	121.09	3.52
2.845	153.53	5.16	144.04	5.54
2.055	172.05	3.94	174.73	2.57
1.484	210.51	3.03	200.74	1.64
1.072	234.24	2.57	236.79	3.01
0.774	295.54	4.13	269.91	2.23

Table A4.2. ^{19}F R_1 relaxation rates obtained for the studied DBUH-IM14, DBUH-LiIM14, $(DBUH-IM14)_{0.60}-P(MMA)_{0.40}$ and and $(DBUH)_{0.55}-(Li)_{0.06}-P(MMA)_{0.39}$ systems at 298 K.

	DBUH-IM14		DBUH-LiIM14	
ω_{19F} (MHz)	R_1 (s^{-1})	% error	R_1 (s^{-1})	% error
18.83	6.67	1.99	7.14	2.21
13.60	8.28	1.23	9.11	3.51
9.83	11.01	3.72	11.18	1.19
7.10	16.20	3.84	16.16	2.38
5.13	17.95	5.08	19.11	2.65
3.71	23.92	2.27	27.31	1.16
2.68	29.57	1.50	33.37	1.84
1.93	33.92	2.63	41.19	1.47
1.40	41.71	1.62	47.40	2.18
1.01	46.49	2.75	54.83	2.19
0.73	50.90	1.68	63.20	1.90
0.53	53.10	1.90	71.90	1.95
0.38	57.65	2.16	75.10	2.09
0.27	60.60	2.63	73.46	2.62
0.20	63.65	2.40	85.04	1.53
0.14	66.02	1.22	87.35	3.41
0.10	66.13	2.33	93.05	2.40
0.08	71.02	1.24	91.33	3.36
0.05	70.95	2.71	96.01	1.83
0.04	74.08	1.29	95.44	1.16
0.03	66.73	4.02	99.29	2.33
	$(DBUH-IM14)_{0.60}-P(MMA)_{0.40}$		$(DBUH)_{0.55}-(Li)_{0.06}-P(MMA)_{0.39}$	
ω_{19F} (MHz)	R_1 (s^{-1})	% error	R_1 (s^{-1})	% error
18.83	7.27	1.97	6.83	2.70
13.60	9.16	1.70	9.20	2.33
9.83	13.23	1.47	11.65	3.03
7.10	15.50	5.79	18.19	3.46
5.13	21.58	5.26	20.19	3.15
3.71	28.60	2.71	28.97	1.49
2.68	39.54	3.61	36.74	1.85
1.93	46.22	2.59	48.43	1.72
1.40	53.07	3.41	55.73	2.85
1.01	70.67	3.61	73.90	3.11
0.73	81.79	2.84	87.30	1.39
0.53	110.25	3.54	115.41	3.23
0.38	116.08	3.04	133.92	0.90
0.27	154.44	0.72	151.67	1.52
0.20	184.86	4.30	180.20	3.92
0.14	174.25	5.23	197.21	3.65
0.10	219.29	7.12	219.19	4.37
0.08			246.15	3.08

Table A4.3. ^1H R_1 relaxation rates obtained for the studied DBUH-IM14, DBUH-LiIM14, (DBUH-IM14)$_{0.60}$-P(MMA)$_{0.40}$ and and (DBUH)$_{0.55}$-(Li)$_{0.06}$-P(MMA)$_{0.39}$ systems at 313 K.

ω_{1H} (MHz)	DBUH-IM14 R_1 (s^{-1})	% error	DBUH-LiIM14 R_1 (s^{-1})	% error
20.003	34.32	3.01	38.49	3.90
14.452	35.91	3.85	39.00	4.33
10.440	39.72	3.47	42.31	4.17
7.541	40.14	5.22	42.24	5.79
5.449	41.63	1.83	41.93	3.60
3.937	43.50	2.37	48.56	2.00
2.845	46.57	1.20	50.62	2.65
2.055	46.09	1.65	51.88	1.22
1.484	48.39	1.67	54.47	1.65
1.072	49.24	0.93	55.57	2.00
0.774	49.17	1.41	56.26	1.56
0.560	49.78	1.37	56.03	1.06
0.404	50.89	0.82	56.55	1.49
0.292	51.75	0.96	56.87	0.88
0.211	52.24	1.10	60.32	1.29
0.152	52.84	1.15	57.36	1.39
0.110	53.53	1.06	59.76	0.79
0.080	54.13	1.17	61.67	1.61
0.058	52.22	1.49	58.67	0.90
0.041	55.02	1.13	57.87	0.60
0.030	55.02	0.58	61.40	0.93

ω_{1H} (MHz)	(DBUH-IM14)$_{0.60}$-P(MMA)$_{0.40}$ R_1 (s^{-1})	% error	(DBUH)$_{0.55}$-(Li)$_{0.06}$-P(MMA)$_{0.39}$ R_1 (s^{-1})	% error
20.003	37.04	3.19	37.47	3.82
14.452	42.66	2.53	41.93	3.24
10.440	50.71	4.51	49.94	4.19
7.541	56.62	3.41	51.38	5.01
5.449	62.03	4.31	61.22	5.33
3.937	74.23	1.97	72.49	1.93
2.845	86.87	0.82	85.50	2.20
2.055	100.51	2.00	100.07	2.00
1.484	113.88	2.38	117.38	1.90
1.072	134.54	2.15	134.93	2.16
0.774	143.28	3.25	152.34	2.09
0.560	169.21	2.73	172.46	1.88
0.404	176.20	1.50	188.24	1.16
0.292	183.81	1.67	209.13	1.10
0.211	214.09	1.79	214.54	2.16
0.152	233.96	2.66	254.59	3.83
0.110	253.16	2.45	274.15	1.08
0.080	251.02	3.89	287.15	0.98

Table A4.4. ^{19}F R_1 relaxation rates obtained for the studied DBUH-IM14, DBUH-LiIM14, (DBUH-IM14)$_{0.60}$-P(MMA)$_{0.40}$ and and (DBUH)$_{0.55}$-(Li)$_{0.06}$-P(MMA)$_{0.39}$ systems at 313 K.

	DBUH-IM14		DBUH-LiIM14	
ω_{1H} (MHz)	R_1 (s^{-1})	% error	R_1 (s^{-1})	% error
18.83	5.52	1.93	5.50	2.32
13.60	6.40	3.04	7.03	2.62
9.83	8.24	3.39	9.27	2.81
7.10	11.71	1.63	13.83	4.92
5.13	12.62	2.25	16.16	3.23
3.71	15.08	2.23	16.76	1.54
2.68	15.45	1.67	19.27	2.36
1.93	16.82	2.05	21.13	2.64
1.40	18.46	1.84	23.21	2.77
1.01	19.53	2.34	23.41	2.12
0.73	20.38	1.59	24.86	2.35
0.53	20.25	1.91	27.58	1.50
0.38	21.24	2.80	28.15	1.53
0.27	22.43	1.98	28.45	1.53
0.20	23.64	1.64	29.14	1.26
0.14	22.34	1.84	31.70	2.78
0.10	23.81	3.39	32.63	3.65
0.08	22.79	2.53	32.94	2.25
0.05	22.53	2.63	31.71	1.50
0.04	24.01	2.45	32.29	2.29
0.03	24.84	1.47	30.24	1.42
	(DBUH-IM14)$_{0.60}$-P(MMA)$_{0.40}$		(DBUH)$_{0.55}$-(Li)$_{0.06}$-P(MMA)$_{0.39}$	
ω_{1H} (MHz)	R_1 (s^{-1})	% error	R_1 (s^{-1})	% error
18.83	6.21	1.76	5.98	1.92
13.60	7.33	3.63	6.93	2.84
9.83	9.23	4.46	10.05	6.48
7.10	12.36	4.70	13.13	3.02
5.13	16.64	3.20	16.81	2.50
3.71	19.22	4.00	19.72	2.90
2.68	22.49	1.56	26.55	2.47
1.93	25.69	2.78	30.20	1.99
1.40	34.31	2.70	39.06	2.71
1.01	39.77	3.62	43.80	2.55
0.73	46.55	3.63	52.24	2.20
0.53	49.78	2.47	57.63	1.66
0.38	57.27	3.43	65.80	1.75
0.27	65.13	2.33	79.31	2.74
0.20	64.84	1.72	86.73	2.24
0.14	69.77	3.98	100.37	4.12
0.10	78.52	2.90	119.26	2.28
0.08	83.09	2.88	132.65	2.86
0.05	79.01	3.59	153.21	3.64
0.04	86.26	3.62	157.70	2.34
0.03	92.37	2.39	163.75	3.23

Table A4.5. ^{1}H R_1 relaxation rates obtained for the studied DBUH-IM14, DBUH-LiIM14, (DBUH-IM14)$_{0.60}$-P(MMA)$_{0.40}$ and and (DBUH)$_{0.55}$-(Li)$_{0.06}$-P(MMA)$_{0.39}$ systems at 328 K.

	DBUH-IM14		DBUH-LiIM14	
ω_{1H} (MHz)	R_1 (s^{-1})	% error	R_1 (s^{-1})	% error
20.003	19.94	4.31	22.97	5.96
14.452	19.18	4.54	21.62	5.36
10.440	21.12	7.01	21.84	6.66
7.541	18.29	4.98	20.16	7.47
5.449	20.30	4.10	20.86	3.20
3.937	20.11	2.02	21.27	3.07
2.845	20.44	1.63	22.25	2.49
2.055	20.60	2.03	23.44	2.21
1.484	20.97	2.04	22.76	2.73
1.072	20.76	1.63	22.86	1.43
0.774	21.20	2.02	24.13	2.16
0.560	22.02	1.48	23.53	2.48
0.404	20.64	1.36	24.78	1.86
0.292	20.73	1.10	23.40	1.25
0.211	21.66	1.39	23.71	1.96
0.152	22.43	1.82	24.59	1.96
0.110	22.70	2.14	23.77	2.40
0.080	21.64	0.94	24.34	0.53
0.058	22.59	1.52	22.90	1.84
0.041	23.47	2.19	24.76	1.51
0.030	21.33	2.56	25.61	1.17
	(DBUH-IM14)$_{0.60}$-P(MMA)$_{0.40}$		(DBUH)$_{0.55}$-(Li)$_{0.06}$-P(MMA)$_{0.39}$	
ω_{1H} (MHz)	R_1 (s^{-1})	% error	R_1 (s^{-1})	% error
20.003	27.17	5.16	29.29	5.34
14.452	28.47	5.00	29.68	5.35
10.440	32.98	6.99	35.19	5.66
7.541	31.93	7.85	34.34	4.56
5.449	35.31	5.09	36.71	5.57
3.937	46.85	3.18	45.41	2.58
2.845	48.13	3.04	50.37	1.05
2.055	52.76	3.24	57.35	2.81
1.484	58.78	2.24	64.56	2.60
1.072	62.85	2.90	73.54	2.07
0.774	70.86	2.24	73.63	3.07
0.560	79.27	1.47	80.80	2.33
0.404	77.88	1.69	91.19	2.97
0.292	81.59	1.82	93.64	2.14
0.211	88.41	3.19	103.31	1.91
0.152	94.26	3.74	108.99	2.31
0.110	92.19	3.56	120.58	1.38
0.080	104.43	2.22	126.08	1.69
0.058	98.63	2.06	139.30	1.27
0.041	105.35	3.09	141.42	2.30
0.030	99.74	3.87	150.54	2.20

Table A4.6. ^{19}F R_1 relaxation rates obtained for the studied DBUH-IM14, DBUH-LiIM14, (DBUH-IM14)$_{0.60}$-P(MMA)$_{0.40}$ and and (DBUH)$_{0.55}$-(Li)$_{0.06}$-P(MMA)$_{0.39}$ systems at 328 K.

	DBUH-IM14		DBUH-LiIM14	
ω_{19F} (MHz)	R_1 (s^{-1})	% error	R_1 (s^{-1})	% error
18.83	4.04	2.75	4.45	1.95
13.60	4.59	3.72	4.90	2.61
9.83	4.79	3.57	5.80	2.54
7.10	5.83	4.58	6.59	3.22
5.13	6.53	3.54	7.10	2.50
3.71	6.37	1.69	7.65	2.29
2.68	6.61	2.76	8.22	2.26
1.93	7.03	2.21	8.69	1.43
1.40	7.68	2.68	8.53	0.97
1.01	8.35	2.27	9.54	1.52
0.73	7.60	2.40	9.44	2.16
0.53	8.23	2.91	9.47	1.52
0.38	7.88	2.81	9.74	2.30
0.27	8.13	2.04	10.09	1.05
0.20	8.13	1.85	9.98	1.60
0.14	8.58	2.22	10.61	2.34
0.10	8.62	3.36	10.33	2.32
0.08	8.91	2.99	10.34	2.44
0.05	8.46	2.02	10.17	1.43
0.04	8.59	2.39	10.01	1.71
0.03	8.15	1.67	11.88	5.00
	(DBUH-IM14)$_{0.60}$-P(MMA)$_{0.40}$		(DBUH)$_{0.55}$-(Li)$_{0.06}$-P(MMA)$_{0.39}$	
ω_{19F} (MHz)	R_1 (s^{-1})	% error	R_1 (s^{-1})	% error
18.83	4.99	2.76	5.00	2.35
13.60	6.19	4.40	5.86	2.22
9.83	7.43	5.47	7.35	3.73
7.10	9.44	4.18	10.10	3.34
5.13	10.80	3.89	11.37	3.95
3.71	13.36	2.33	13.08	2.23
2.68	13.93	2.16	16.94	1.33
1.93	17.14	1.54	17.91	2.87
1.40	19.35	2.35	20.72	1.96
1.01	20.00	3.77	23.84	2.57
0.73	22.09	2.40	28.24	1.43
0.53	23.43	3.00	30.99	1.53
0.38	26.16	2.44	35.25	2.08
0.27	26.59	2.63	37.62	1.42
0.20	27.52	2.48	44.73	3.28
0.14	29.55	1.52	45.11	2.98
0.10	30.71	3.21	53.47	2.70
0.08	30.55	2.51	58.09	1.32
0.05	34.08	2.23	60.55	1.28
0.04	31.50	1.87	61.62	2.34
0.03	31.34	2.04	68.13	0.87

Table A4.7. ^{1}H R_1 relaxation rates obtained for the studied DBUH-IM14, DBUH-LiIM14, (DBUH-IM14)$_{0.60}$-P(MMA)$_{0.40}$ and and (DBUH)$_{0.55}$-(Li)$_{0.06}$-P(MMA)$_{0.39}$ systems at 343 K.

ω_{1H} (MHz)	DBUH-IM14		DBUH-LiIM14	
	R_1 (s^{-1})	% error	R_1 (s^{-1})	% error
20.00	12.09	4.81	12.51	5.86
7.90	10.78	5.71	10.79	9.48
3.12	11.45	4.48	10.68	2.50
1.23	12.40	0.59	12.23	2.39
0.49	11.56	2.83	12.43	1.08
0.19	12.30	1.05	13.24	0.75
0.08	11.55	1.66	12.36	2.93
0.03	11.52	1.14	12.47	1.56
	(DBUH-IM14)$_{0.60}$-P(MMA)$_{0.40}$		(DBUH)$_{0.55}$-(Li)$_{0.06}$-P(MMA)$_{0.39}$	
ω_{1H} (MHz)	R_1 (s^{-1})	% error	R_1 (s^{-1})	% error
20.003	19.25	5.28	20.19	5.54
14.452	19.37	4.78	21.07	5.87
10.440	21.49	6.58	24.07	6.97
7.541	22.50	8.48	23.24	7.12
5.449	23.51	7.40	25.56	4.67
3.937	27.88	4.96	29.01	4.41
2.845	29.50	2.79	31.82	3.13
2.055	31.78	2.92	33.36	3.19
1.484	31.43	4.68	36.83	4.08
1.072	33.03	2.17	39.01	1.43
0.774	34.48	3.38	41.47	1.22
0.560	35.97	2.70	44.12	1.59
0.404	36.69	2.14	48.16	1.71
0.292	40.39	2.33	46.63	1.54
0.211	38.83	1.28	48.52	1.07
0.152	38.82	4.78	50.98	1.57
0.110	43.74	1.71	59.34	1.82
0.080	40.59	1.96	57.16	2.12
0.058	43.55	1.99	63.44	1.67
0.041	44.77	1.62	63.17	2.16
0.030	40.03	3.07	69.16	2.50

Table A4.8. ^{19}F R_1 relaxation rates obtained for the studied DBUH-IM14, DBUH-LiIM14, (DBUH-IM14)$_{0.60}$-P(MMA)$_{0.40}$ and and (DBUH)$_{0.55}$-(Li)$_{0.06}$-P(MMA)$_{0.39}$ systems at 343 K.

	DBUH-IM14		DBUH-LiIM14	
ω_{19F} (MHz)	R_1 (s^{-1})	% error	R_1 (s^{-1})	% error
18.83	2.80	2.95	3.67	2.84
13.60	2.89	2.71	3.83	1.94
9.83	2.98	4.38	4.03	3.30
7.10	3.19	4.35	4.13	3.45
5.13	3.48	3.89	4.79	1.71
3.71	4.02	3.17	5.08	0.92
2.68	3.71	1.61	5.36	2.79
1.93	4.05	1.68	5.63	1.56
1.40	3.99	1.23	5.81	2.09
1.01	4.08	2.01	5.91	1.45
0.73	4.27	3.29	5.74	1.51
0.53	4.17	2.74	6.36	1.38
0.38	4.47	2.64	6.09	1.84
0.27	4.40	1.11	6.21	3.57
0.20	4.63	2.66	6.11	2.42
0.14	4.48	1.58	6.55	0.92
0.10	4.17	2.44	6.49	2.01
0.08	4.70	3.27	6.61	1.38
0.05	4.53	1.24	6.78	1.71
0.04	4.60	1.98	6.57	0.84
0.03	4.67	2.91	6.70	1.30
	(DBUH-IM14)$_{0.60}$-P(MMA)$_{0.40}$		(DBUH)$_{0.55}$-(Li)$_{0.06}$-P(MMA)$_{0.39}$	
ω_{19F} (MHz)	R_1 (s^{-1})	% error	R_1 (s^{-1})	% error
18.83	4.04	2.16	3.95	2.22
13.60	4.72	1.75	4.37	2.39
9.83	4.53	3.81	5.19	3.93
7.10	6.16	3.67	6.17	2.39
5.13	7.39	3.25	7.88	1.39
3.71	8.35	1.59	7.65	4.63
2.68	9.15	1.66	10.02	2.53
1.93	9.31	2.86	10.36	2.04
1.40	10.94	2.49	12.26	2.50
1.01	10.11	2.39	13.56	2.02
0.73	11.93	2.61	14.74	1.40
0.53	12.24	2.06	15.78	2.99
0.38	12.01	2.79	17.97	1.58
0.27	13.06	2.39	19.45	1.13
0.20	13.78	1.95	20.67	2.65
0.14	14.02	3.28	22.38	2.72
0.10	14.06	3.90	25.05	2.79
0.08	13.69	3.41	25.24	3.05
0.05	13.40	2.00	25.15	3.01
0.04	13.58	2.36	28.16	3.30
0.03	13.81	2.57	31.76	1.54

Summary and Outlook

5.1. Summary

The current state-of-art electrolytes present safety drawbacks due to the use of organic carbonates as electrolyte components. Considering that those organic solvents are highly flammable and volatile, under misuse conditions, they can end up in an uncontrolled chain of events, such as thermal runaway, cell venting, fire, and, sometimes, explosion[8]. Therefore, developing safer electrolytes is needed for further improvements in the safety of the lithium-ion battery (LIB) technology and the growth of this technology. In this regard, researchers were highly oriented towards the replacement of the organics carbonates, and since the last decade, protic ionic liquids (PILs) have been quoted for electrolytes application[32–35].

In this framework, this PhD research was devoted to investigating protic ionic liquids (PILs) as alternative electrolyte components to improve the safety of LIBs. During this PhD work, three DBU-based PILs (DBUH-TFSI, DBUH-TFO, and DBUH-IM14) were extensively characterized in view of their potential application as electrolyte components. The initial work, reported in *Chapter 2*, was focused on accessing the protonation status of the PILs, as well as on the characterization of the physical chemical properties of the neat systems. From an extensive 1D ^{1}H and ^{15}N NMR investigation it was concluded that all the PILs studied showed a thermodynamically and kinetically stable N-H covalent bond between the imino nitrogen of the DBU and the acidic proton. Also, from the temperature dependent ^{15}N NMR analysis, it was evidenced the stability of the N-H covalent bond in all the range of temperature evaluated, meaning that the status of protonation remains constant at elevated

temperatures. Besides, the physical chemical properties of the DBU-based PILs were experimentally accessed in terms of thermal, electrochemical, and rheological properties. From the distinct behavior of PILs, it was unveiled that the structural features of the anions are playing an important role on dictating their macroscopic features. For instance, the asymmetrical perfluorinated butyl chain and the potential formation of fluorous domain lower the DBUH-IM14 thermal stability and ionic conductivity. Whereas the strong hydrogen bonding network of DBUH-TFO reduces its ionic conductivity and increases its thermal stability.

After having a clear picture of the features governing the physical chemical properties of the PILs, this PhD work was extended to the investigation of the transport properties of the PILs and PILs electrolytes: $(DBUH\text{-}IM14)_1(LiIM14)_{0.1}$, $(DBUH\text{-}TFSI)_1(LiTFSI)_{0.1}$ and $(DBUH\text{-}TFO)_1(LiTFO)_{0.1}$, as reported in *Chapter 3*. Specifically, the systems were studied using conductivity, diffusion and relaxation NMR techniques. From the translational diffusion and relaxation measurements, it was observed that DBUH-IM14 is the system showing peculiar characteristics in terms of its ion dynamics. First, the PFG NMR detects slower diffusion coefficients of the DBUH-IM14 ions than expected from its viscosity, probably due to the occurrence of fluorous interactions between the asymmetrical fluorinated chains. Besides, the fluorinated chains of $IM14^-$ anion clearly do not follow the same relaxation profile as the other CF_3-containing PILs, revealing that other mechanisms play a crucial role in the $IM14^-$ rotational mobility. When looking at the transport properties of the DBUH-IM14 electrolyte, an unusual and relatively faster translational mobility of the Li^+ was found. Besides, the presence of Li^+ showed a peculiar effect on the rotational dynamics of N-H group of the DBUH-IM14. This odd internal motion may be related to the structural features of the $IM14^-$ anion and it deserves further investigation for an exhaustive clarification.

Still considering the transport properties of the PIL electrolytes, reported in *Chapter 3*, the ionicity of the systems was studied as a function of temperature. Basically, the ionicity reflects the real fraction of ions participating to the conduction process. From the results, it was observed that the intermolecular interaction of the PILs and PIL electrolytes may be playing a crucial role in driving their ionicity behavior. More in detail, in the case of DBUH-TFSI and DBUH-IM14 (systems with weaker hydrogen bonding) the ionicity decreases with the temperature. Whereas for the DBUH-TFO (system with strong hydrogen bonding network) the ionicity is nearly constant with the temperature increasing. Upon the Li addition, DBUH-TFSI electrolyte behaves differently (i.e., the ionicity remains almost constant with the temperature increasing). Whereas, for DBUH-TFO (system with stronger hydrogen bond network) and DBUH-IM14 (system with potential formation of fluorous domains)

the ionicity suffers from a marked decreasing with the temperature increasing. Probably, this thermal dependency of the ionicity is related to the intermolecular interactions and the relative motion of the ions, which may be enhanced due to the presence of Li in the case of DBUH-TFO and DBUH-IM14, and potentially diminished in the case of DBUH-TFSI. Yet, further investigations are required to better explain the different thermal effects on the ionicity of some PILs and PIL electrolytes found in this work.

Further improvements of the safety of LIBs can be achieved by immobilizing the ionic liquid electrolyte in a polymeric matrix, forming a polymer electrolyte or ionogel. Besides, polymer-based electrolytes are shapable materials and can improve the volumetric design concerns associated with liquid electrolytes. In this regard, the final activities of this PhD work, reported in *Chapter 4*, were devoted to exploring the application of PILs as polymer electrolytes components using poly(methyl methacrylate) (PMMA) as a polymer host. Firstly, the structural features and intermolecular interaction of the polymer-PIL binary systems $P(MMA)_{0.91}$-$(PIL)_{0.09}$ was probed by thermal analysis and solid stated NMR. Both techniques unveiled a stronger interaction between PMMA host with the DBUH-IM14 than with the other PILs.

Considering the peculiarities of the DBUH-IM14 polymeric systems, still on *Chapter 4*, the investigations were further extended to polymeric systems with lower PMMA content (10% wt). In particular, the studies were focused on understanding the effect of confinement on the ion dynamics using fast-field cycling (FFC) and diffusion NMR. Overall, the experimental results revealed that the dynamics of both, $DBUH^+$ cation and $IM14^-$ anion, is strongly reduced by the presence of polymer. In the case of the polymer electrolyte system, Li^+ shows a minor effect on the $DBUH^+$ dynamics, whereas rotational and translational dynamics of the $IM14^-$ anion was quite responsive to the presence of Li^+. Currently, a mathematical model is under development to explain the relaxation profiles and physically describe their internal mobility. Yet, the experimental results clearly indicated that the structural features and the nature of the intermolecular interaction in the $IM14^-$ anion is playing a crucial role in the transport properties of the DBUH-IM14 polymer electrolytes.

Summarizing, this PhD work combines a broad set of experimental techniques to obtain a clear picture of the features governing the transport properties of: (i) the selected PILs, (ii) the related PIL electrolytes, and (iii) PILs-based polymeric systems. Overall, after all the achievements of this thesis, a major finding must be highlighted: *the structural features of the anions play a crucial role on driven the intermolecular interaction of the PILs, which in turn affect their macroscopic and microscopic properties*. Figure 5.1 summarize and illustrate the structural feature of the PILs studied,

in terms of their intermolecular interactions. From the accomplishments of this thesis, I hope I contributed to the improvement of the current electrolytes' technologies giving general insights into how to tailor and scale the transport properties of PILs containing electrolytes.
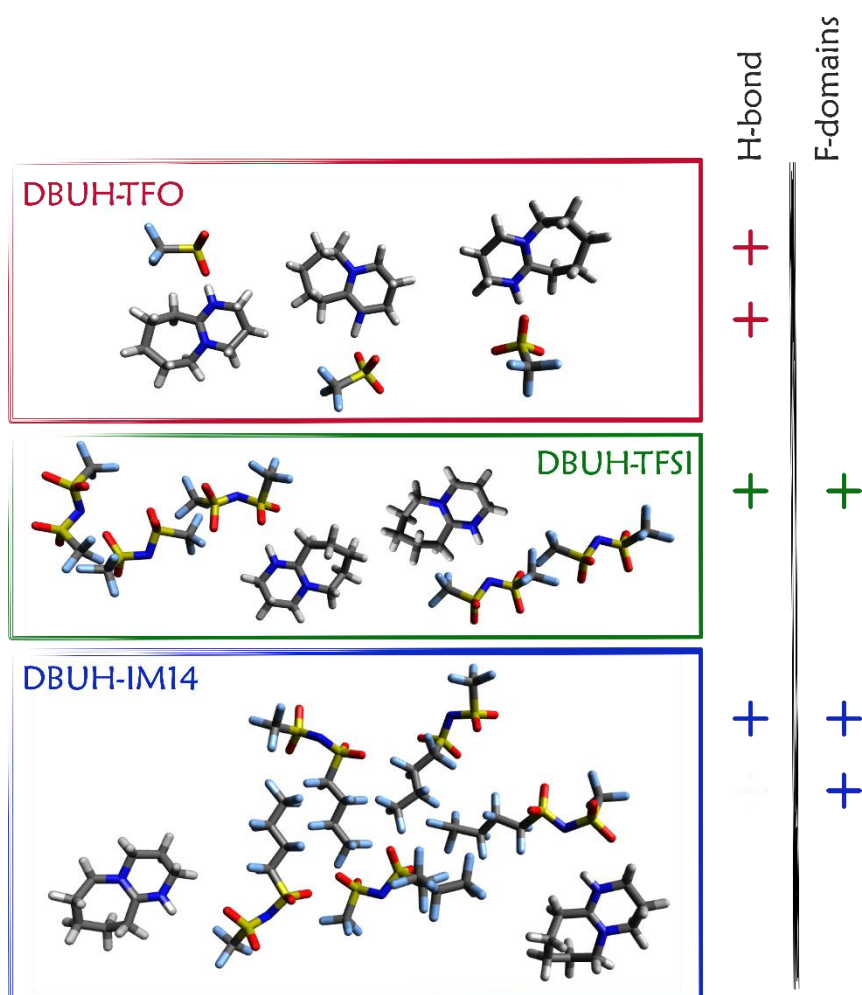

Figure 5.1. Illustration of the main intermolecular interactions present in each PIL due to the structural features of the anion.

5.2. Outlook

Although the experimental achievements of this PhD work provide a deep characterization of the selected PILs as electrolytes, some scientific contributions are still required to address certain findings related to the transport properties of the PILs electrolytes. For instance, unusual relatively faster diffusion of the Li^+ and enhanced correlation times of the N-H group upon Li salt doping were detected for the DBUH-IM14 electrolyte. Considering that Li^+ is always solvated by the anions the nature of (i) the enhancement of the diffusivity and (ii) the selective effect of Li^+ on the N-H relaxation pattern are still open questions. Thus, the synergistic effects of the Li^+ on the translational and rotational mobilities of the DBUH-IM14

electrolyte deserve further exploration through molecular dynamics (MD) simulations.

Rheological studies are a powerful tool to provide information about the macroscopic behavior of the PILs. So far, viscosity data for the investigated PIL electrolytes are not available in the literature. However, further works can be done in this regard to provide additional information about the Li salt effect on the activation energy of the internal flow. Consequently, joining information about the microscopic and macroscopic dynamics may provide a consistent picture of the Li salt effects on the transport properties of the PIL electrolytes.

Regarding the ionic behavior of the PIL electrolytes, the experimental results obtained via diffusion and conductivity measurements show that the nature of the anion seems to play an important role in driving the thermal-dependent ionicity. Theoretical explanations for the thermal ionicity behavior may stem from the anti-correlation/correlation motion of the ions. Still, further investigations on this topic may be considered as a follow-up of the present studies to provide supplementary information about the interionic mobilities. These considerations are of prime importance to further understanding the transport properties of the PIL electrolytes.

When quoting PILs as novel liquid electrolyte components for LIBs, additional experiments should be performed to evaluate the practical cell conditions. For instance, the understanding of the interaction at the electrode interfaces and in particular the solid electrolyte interface (SEI) formation process is of great importance to assess the real applicability of PILs-based electrolytes in LIBs.

To date, only a few studies have been dedicated to the use of PILs as polymer electrolyte components. From the investigations presented here on the structural features and ion dynamics of the PIL-based polymeric system, DBUH-IM14 was unveiled as an appealing polymer electrolyte component. Then, additional experimental and theoretical investigations should be performed to evaluate the overall performance of DBUH-IM14-based polymer electrolytes in a viewing of its successfully application in LIBs.

Finally, when proposing PIL as a competitive electrolyte component, sustainability, and economical metrics should be considered. Even if PIL is claimed as "cheaper" than AILs due to their simple synthesis, the cost of the fluorinated acids used as precursors can still be considered a drawback. Then, it will be of prime importance to verify whether it is possible to realize cheap and sustainable PIL electrolytes, which can be produced on large scale.

Bibliography

[1]A. Kalair, N. Abas, M.S. Saleem, A.R. Kalair, N. Khan, Role of energy storage systems in energy transition from fossil fuels to renewables, Energy Storage. 3 (2021) 1–27. https://doi.org/10.1002/est2.135.

[2]N. Abas, A. Kalair, N. Khan, Review of fossil fuels and future energy technologies, Futures. 69 (2015) 31–49. https://doi.org/10.1016/j.futures.2015.03.003.

[3]M. Armand, P. Axmann, D. Bresser, M. Copley, K. Edstr, C. Ekberg, D. Guyomard, B. Lestriez, P. Nov, M. Petranikova, W. Porcher, S. Trabesinger, M. Wohlfahrt-mehrens, Lithium-ion batteries – Current state of the art and anticipated developments, 479 (2020).

[4]M. Armand, Issues and challenges facing rechargeable lithium batteries, Nature. 414 (2001) 359–367. http://www.ncbi.nlm.nih.gov/pubmed/11713543.

[5]J. Wen, Y. Yu, C. Chen, A review on lithium-ion batteries safety issues: Existing problems and possible solutions, Mater. Express. 2 (2012) 197–212. https://doi.org/10.1166/mex.2012.1075.

[6]M. Schmidt, U. Heider, A. Kuehner, R. Oesten, M. Jungnitz, N. Ignat'ev, P. Sartori, Lithium fluoroalkylphosphates: A new class of conducting salts for electrolytes for high energy lithium-ion batteries, J. Power Sources. 97–98 (2001) 557–560. https://doi.org/10.1016/S0378-7753(01)00640-1.

[7]R. Fong, U. von Sacken, J.R. Dahn, Studies of Lithium Intercalation into Carbons Using Nonaqueous Electrochemical Cells, J. Electrochem. Soc. 137 (1990) 2009–2013. https://doi.org/10.1149/1.2086855.

[8]S. Passerini, M. Montanino, G.B. Appetecchi, Lithium Polymer Batteries Based on Ionic Liquids, Polym. Energy Storage Convers. (2013) 53–101. https://doi.org/10.1002/9781118734162.ch3.

[9]J. Wen, Y. Yu, C. Chen, A Review on Lithium-Ion Batteries Safety Issues: Existing Problems and Possible Solutions, Mater. Express. 2 (2012) 197–212. https://doi.org/10.1166/mex.2012.1075.

[10]L. Zheng, H. Zhang, P. Cheng, Q. Ma, J. Liu, J. Nie, W. Feng, Z. Zhou, Li[(FSO2)(n-C4F9SO2)N] versus LiPF6 for graphite/LiCoO2 lithium-ion cells at both room and elevated temperatures: A comprehensive understanding with chemical, electrochemical and XPS analysis, Electrochim. Acta. 196 (2016) 169–188. https://doi.org/10.1016/j.electacta.2016.02.152.

[11]J. Kalhoff, D. Bresser, M. Bolloli, F. Alloin, J.Y. Sanchez, S. Passerini, Enabling LiTFSI-based electrolytes for safer lithium-ion batteries by Using linear fluorinated carbonates as (Co)solvent, ChemSusChem. 7 (2014) 2939–2946. https://doi.org/10.1002/cssc.201402502.

[12]H.B. Han, S.S. Zhou, D.J. Zhang, S.W. Feng, L.F. Li, K. Liu, W.F. Feng, J. Nie, H. Li, X.J. Huang, M. Armand, Z. Bin Zhou, Lithium bis(fluorosulfonyl)imide (LiFSI) as conducting salt for nonaqueous liquid electrolytes for lithium-ion batteries: Physicochemical and electrochemical properties, J. Power Sources. 196 (2011) 3623–3632. https://doi.org/10.1016/j.jpowsour.2010.12.040.

[13]M. Armand, P. Axmann, D. Bresser, M. Copley, K. Edström, C. Ekberg, D. Guyomard, B. Lestriez, P. Novák, M. Petranikova, W. Porcher, S. Trabesinger, M. Wohlfahrt-Mehrens, H. Zhang, Lithium-ion batteries – Current state of the art and anticipated developments, J. Power Sources. 479 (2020) 26. https://doi.org/10.1016/j.jpowsour.2020.228708.

[14]C. Chiappe, D. Pieraccini, Ionic liquids: Solvent properties and organic reactivity, J. Phys. Org. Chem. 18 (2005) 275–297. https://doi.org/10.1002/poc.863.

[15]N. V. Plechkova, K.R. Seddon, Applications of ionic liquids in the chemical industry, Chem. Soc. Rev. 37 (2008) 123–150. https://doi.org/10.1039/b006677j.

[16]J.P. Hallett, T. Welton, Room-temperature ionic liquids: Solvents for synthesis and catalysis. 2, Chem. Rev. 111 (2011) 3508–3576. https://doi.org/10.1021/cr1003248.

[17]F. Jutz, J.M. Andanson, A. Baiker, Ionic liquids and dense carbon dioxide: A beneficial biphasic system for catalysis, Chem. Rev. 111 (2011) 322–353. https://doi.org/10.1021/cr100194q.

[18]J.S. Wilkes, A short history of ionic liquids - From molten salts to neoteric solvents, Green Chem. 4 (2002) 73–80. https://doi.org/10.1039/b110838g.

[19]T. Welton, Ionic liquids: a brief history, Biophys. Rev. 10 (2018) 691–706. https://doi.org/10.1007/s12551-018-0419-2.

[20]D.R. MacFarlane, N. Tachikawa, M. Forsyth, J.M. Pringle, P.C. Howlett, G.D. Elliott, J.H. Davis, M. Watanabe, P. Simon, C.A. Angell, Energy applications of ionic liquids, Energy Environ. Sci. 7 (2014) 232–250. https://doi.org/10.1039/c3ee42099j.

[21]G.B. Appetecchi, M. Montanino, S. Passerini, Ionic liquid-based electrolytes for high energy, safer lithium batteries, in: ACS Symp. Ser., 2012: pp. 67–128. https://doi.org/10.1021/bk-2012-1117.ch004.

[22]T.L. Greaves, C.J. Drummond, Protic Ionic Liquids: Evolving Structure-Property Relationships and Expanding Applications, Chem. Rev. 115 (2015) 11379–11448. https://doi.org/10.1021/acs.chemrev.5b00158.

[23]G.B. Appetecchi, S. Scaccia, C. Tizzani, F. Alessandrini, S. Passerini, Synthesis of Hydrophobic Ionic Liquids for Electrochemical Applications, J. Electrochem. Soc. 153 (2006) A1685. https://doi.org/10.1149/1.2213420.

[24]T. Beyersdorff, T.J.S. Schubert, U. Welz-Biermann, W. Pitner, A.P. Abbott, K.J. McKenzie, K.S. Ryder, Synthesis of Ionic Liquids, 1st ed., WILEY-VCH Verlag GmbH & Co, Weinheim, 2008. https://doi.org/10.1002/9783527622917.ch2.

[25]T.L. Greaves, A. Weerawardena, C. Fong, I. Krodkiewska, C.J. Drummond, Protic ionic liquids: Solvents with tunable phase behavior and physicochemical properties, J. Phys. Chem. B. 110 (2006) 22479–22487. https://doi.org/10.1021/jp0634048.

[26]W. Silva, M. Zanatta, A.S. Ferreira, M.C. Corvo, E.J. Cabrita, Revisiting ionic liquid structure-property relationship: A critical analysis, Int. J. Mol. Sci. 21 (2020) 1–37. https://doi.org/10.3390/ijms21207745.

[27]N. Böckenfeld, M. Willeke, J. Pires, M. Anouti, A. Balducci, On the Use of Lithium Iron Phosphate in Combination with Protic Ionic Liquid-Based Electrolytes, J. Electrochem. Soc. 160 (2013) A559–A563. https://doi.org/10.1149/2.027304jes.

[28]K. Karuppasamy, J. Theerthagiri, D. Vikraman, C.J. Yim, S. Hussain, R. Sharma, T. Maiyalagan, J. Qin, H.S. Kim, Ionic liquid-based electrolytes for energy storage devices: A brief review on their limits and applications, Polymers (Basel). 12 (2020) 1–37. https://doi.org/10.3390/POLYM12040918.

[29]T. Stettner, A. Balducci, Protic ionic liquids in energy storage devices: past, present and future perspective, Energy Storage Mater. 40 (2021) 402–414. https://doi.org/10.1016/j.ensm.2021.04.036.

[30]T. Vogl, S. Menne, R.S. Kühnel, A. Balducci, The beneficial effect of protic ionic liquids on the lithium environment in electrolytes

for battery applications, J. Mater. Chem. A. 2 (2014) 8258–8265. https://doi.org/10.1039/c3ta15224c.

[31]S. Menne, J. Pires, M. Anouti, A. Balducci, Protic ionic liquids as electrolytes for lithium-ion batteries, Electrochem. Commun. 31 (2013) 39–41. https://doi.org/10.1016/j.elecom.2013.02.026.

[32]T. Stettner, F.C. Walter, A. Balducci, Imidazolium-Based Protic Ionic Liquids as Electrolytes for Lithium-Ion Batteries, (2019) 55–59. https://doi.org/10.1002/batt.201800096.

[33]T. Stettner, S. Gehrke, P. Ray, B. Kirchner, A. Balducci, Water in Protic Ionic Liquids: Properties and Use of a New Class of Electrolytes for Energy-Storage Devices, ChemSusChem. 12 (2019) 3827–3836. https://doi.org/10.1002/cssc.201901283.

[34]T. Vogl, C. Vaalma, D. Buchholz, M. Secchiaroli, R. Marassi, S. Passerini, A. Balducci, The use of protic ionic liquids with cathodes for sodium-ion batteries, J. Mater. Chem. A. 4 (2016) 10472–10478. https://doi.org/10.1039/c6ta02277d.

[35]A.T. Nasrabadi, V. Ganesan, Structure and Transport Properties of Lithium-Doped Aprotic and Protic Ionic Liquid Electrolytes: Insights from Molecular Dynamics Simulations, J. Phys. Chem. B. 123 (2019) 5588–5600. https://doi.org/10.1021/acs.jpcb.9b04477.

[36]J. Wang, L. Xu, G. Jia, J. Du, Challenges and Opportunities of Ionic Liquid Electrolytes for Rechargeable Batteries, Cryst. Growth Des. 22 (2022) 5770–5784. https://doi.org/10.1021/acs.cgd.2c00706.

[37]R. Jamil, D.S. Silvester, Ionic liquid gel polymer electrolytes for flexible supercapacitors: Challenges and prospects, Curr. Opin. Electrochem. 35 (2022) 101046. https://doi.org/10.1016/j.coelec.2022.101046.

[38]C.A. Angell, Polymer electrolytes—Some principles, cautions, and new practices, Electrochim. Acta. 250 (2017) 368–375. https://doi.org/10.1016/j.electacta.2017.07.118.

[39]T. Stettner, G. Lingua, M. Falco, A. Balducci, C. Gerbaldi, Protic Ionic Liquids-Based Crosslinked Polymer Electrolytes: A New Class of Solid Electrolytes for Energy Storage Devices, Energy Technol. 8 (2020). https://doi.org/10.1002/ente.202000742.

[40]A. Marie, B. Said, A. Galarneau, T. Stettner, A. Balducci, M. Bayle, B. Humbert, J. Le Bideau, Silica based ionogels: Interface effects with aprotic and protic ionic liquids with lithium, Phys. Chem. Chem. Phys. 22 (2020) 24051–24058. https://doi.org/10.1039/d0cp03599h.

[41]J.S. Seenath, D. Pech, D. Rochefort, Investigation of protic ionic liquid electrolytes for porous RuO2 micro-supercapacitors, J. Power

Sources. 548 (2022) 232040. https://doi.org/10.1016/j.jpowsour.2022.232040.

[42]K. Fumino, A. Wulf, R. Ludwig, The potential role of hydrogen bonding in aprotic and protic ionic liquids, Phys. Chem. Chem. Phys. 11 (2009) 8790–8794. https://doi.org/10.1039/b905634c.

[43]P.A. Hunt, C.R. Ashworth, R.P. Matthews, Hydrogen bonding in ionic liquids, Chem. Soc. Rev. 44 (2015) 1257–1288. https://doi.org/10.1039/c4cs00278d.

[44]J.W. Wiench, L. Stefaniak, E. Grech, E. Bednarek, Two amidine derivatives studied by 1H, 13C, 14N, 15N NMR and GIAO-CHF calculations, J. Chem. Soc. Perkin Trans. 2. (1999) 885–889. https://doi.org/10.1039/a806259e.

[45]M.S. Miran, H. Kinoshita, T. Yasuda, M.A.B.H. Susan, M. Watanabe, Hydrogen bonds in protic ionic liquids and their correlation with physicochemical properties, Chem. Commun. 47 (2011) 12676–12678. https://doi.org/10.1039/c1cc14817f.

[46]M.S. Miran, H. Kinoshita, T. Yasuda, M.A.B.H. Susan, M. Watanabe, Physicochemical properties determined by $\Delta pK a$ for protic ionic liquids based on an organic super-strong base with various Brønsted acids, Phys. Chem. Chem. Phys. 14 (2012) 5178–5186. https://doi.org/10.1039/c2cp00007e.

[47]F.M.S. Ribeiro, C.F.R.A.C. Lima, A.M.S. Silva, L.M.N.B.F. Santos, Experimental Evidence for Azeotrope Formation from Protic Ionic Liquids, ChemPhysChem. 19 (2018) 2364–2369. https://doi.org/10.1002/cphc.201800335.

[48]M.S. Miran, M. Hoque, T. Yasuda, S. Tsuzuki, K. Ueno, M. Watanabe, Key factor governing the physicochemical properties and extent of proton transfer in protic ionic liquids: ΔpKa or chemical structure?, Phys. Chem. Chem. Phys. 21 (2019) 418–426. https://doi.org/10.1039/c8cp06973e.

[49]A. Triolo, F. Lo Celso, C. Ottaviani, P. Ji, G.B. Appetecchi, F. Leonelli, D.S. Keeble, O. Russina, Structural features of selected protic ionic liquids based on a super-strong base, Phys. Chem. Chem. Phys. 21 (2019) 25369–25378. https://doi.org/10.1039/c9cp03927a.

[50]A. Triolo, A. Paolone, A. Sarra, F. Trequattrini, O. Palumbo, G. Battista Appetecchi, F. Lo Celso, P. Chater, O. Russina, Structure and vibrational features of the protic ionic liquid 1,8-diazabicyclo[5.4.0]-undec-7-ene-8-ium bis(trifluoromethanesulfonyl)amide, [DBUH][TFSI], J. Mol. Liq. 347 (2021) 117981. https://doi.org/10.1016/j.molliq.2021.117981.

[51]M. Picollo, M. Aceto, T. Vitorino, UV-Vis spectroscopy, Phys. Sci. Rev. 4 (2018) 20180008. https://doi.org/doi:10.1515/psr-2018-0008.

[52]J. Keeler, Understanding NMR Spectroscopy, 2nd Edition | Wiley, Wiley. (2010) 190–200. https://www.wiley.com/en-us/Understanding+NMR+Spectroscopy%2C+2nd+Edition-p-9781119964933.

[53]G.A. Morris, Sensitivity enhancement in nitrogen-15 NMR: polarization transfer using the INEPT pulse sequence, J. Am. Chem. Soc. 102 (1980) 428–429.

[54]E. Gómez, N. Calvar, Á. Domínguez, Thermal Behaviour of Pure Ionic Liquids, in: Ion. Liq. - Curr. State Art, 2015: pp. 200–228. https://doi.org/10.5772/59271.

[55]C. Schick, Differential scanning calorimetry (DSC) of semicrystalline polymers, Anal. Bioanal. Chem. 395 (2009) 1589–1611. https://doi.org/10.1007/s00216-009-3169-y.

[56]K. Chrissafis, Kinetics of thermal degradation of polymers : CComplementary use of isoconversional and model-fitting methods, J. Therm. Anal. Calorim. 95 (2009) 273–283. https://doi.org/10.1007/s10973-008-9041-z.

[57]R. Bottom, Thermogravimetric Analysis, Princ. Appl. Therm. Anal. 1 (2008) 87–118. https://doi.org/10.1002/9780470697702.ch3.

[58]C. Maton, N. De Vos, C. V. Stevens, Ionic liquid thermal stabilities: Decomposition mechanisms and analysis tools, Chem. Soc. Rev. 42 (2013) 5963–5977. https://doi.org/10.1039/c3cs60071h.

[59]A. Mariani, M. Bonomo, X. Gao, B. Centrella, A. Nucara, R. Buscaino, A. Barge, N. Barbero, L. Gontrani, S. Passerini, The unseen evidence of Reduced Ionicity: The elephant in (the) room temperature ionic liquids, J. Mol. Liq. 324 (2021) 115069. https://doi.org/10.1016/j.molliq.2020.115069.

[60]METTLER TOLEDO, Density Meters, in: DE40/DE45 DeltaRange/DE51 Density Meters, 2007: p. 106.

[61]I. BROOKFIELD ENGINEERING LABORATORIES, BROOKFIELD DV1 Digital Viscometer Operating Instructions, M07-022-D0 (2017) 71.

[62]P. Vadhva, J. Hu, M.J. Johnson, R. Stocker, M. Braglia, D.J.L. Brett, A.J.E. Rettie, Electrochemical Impedance Spectroscopy for All-Solid-State Batteries: Theory, Methods and Future Outlook, ChemElectroChem. 8 (2021) 1930–1947. https://doi.org/10.1002/celc.202100108.

[63] E. Von Hauff, Impedance Spectroscopy for Emerging Photovoltaics, J. Phys. Chem. C. 123 (2019) 11329–11346. https://doi.org/10.1021/acs.jpcc.9b00892.

[64] Y. Zhao, W.E. Tenhaeff, Thermally and Oxidatively Stable Polymer Electrolyte for Lithium Batteries Enabled by Phthalate Plasticization, ACS Appl. Polym. Mater. 2 (2020) 80–90. https://doi.org/10.1021/acsapm.9b00986.

[65] R.D. Howells, J.D. Mc Cown, Trifluoromethanesulfonic Acid and Derivatives, Can. J. Chem. 56 (1977) 1832–1835. https://doi.org/10.1021/cr60305a005.

[66] M. De Francesco, E. Simonetti, G. Gorgi, G. Appetecchi, About the Purification Route of Ionic Liquid Precursors, Challenges. 8 (2017) 11. https://doi.org/10.3390/challe8010011.

[67] P. Nockemann, K. Binnemans, K. Driesen, Purification of imidazolium ionic liquids for spectroscopic applications, Chem. Phys. Lett. 415 (2005) 131–136. https://doi.org/10.1016/j.cplett.2005.08.128.

[68] H.J. Liaw, C.C. Chen, Y.C. Chen, J.R. Chen, S.K. Huang, S.N. Liu, Relationship between flash point of ionic liquids and their thermal decomposition, Green Chem. 14 (2012) 2001–2008. https://doi.org/10.1039/c2gc35449g.

[69] H. Niedermeyer, J.P. Hallett, I.J. Villar-Garcia, P.A. Hunt, T. Welton, Mixtures of ionic liquids, Chem. Soc. Rev. 41 (2012) 7780–7802. https://doi.org/10.1039/c2cs35177c.

[70] M. Yoshizawa, W. Xu, C.A. Angell, Ionic Liquids by Proton Transfer: Vapor Pressure, Conductivity, and the Relevance of ΔpKa from Aqueous Solutions, J. Am. Chem. Soc. 125 (2003) 15411–15419. https://doi.org/10.1021/ja035783d.

[71] D.R. MacFarlane, J.M. Pringle, K.M. Johansson, S.A. Forsyth, M. Forsyth, Lewis base ionic liquids, Chem. Commun. (2006) 1905–1917. https://doi.org/10.1039/b516961p.

[72] S.K. Davidowski, F. Thompson, W. Huang, M. Hasani, S.A. Amin, C.A. Angell, J.L. Yarger, NMR Characterization of Ionicity and Transport Properties for a Series of Diethylmethylamine Based Protic Ionic Liquids, J. Phys. Chem. B. 120 (2016) 4279–4285. https://doi.org/10.1021/acs.jpcb.6b01203.

[73] P. Judeinstein, C. Iojoiu, J.Y. Sanchez, B. Ancian, Proton conducting ionic liquid organization as probed by NMR: Self-diffusion coefficients and heteronuclear correlations, J. Phys. Chem. B. 112 (2008) 3680–3683. https://doi.org/10.1021/jp711298g.

[74] M. Hasani, J.L. Yarger, C.A. Angell, On the Use of a Protic Ionic Liquid with a Novel Cation To Study Anion Basicity, Chem. - A Eur.

J. 22 (2016) 13312–13319. https://doi.org/10.1002/chem.201601428.

[75]G.B. Appetecchi, M. Montanino, M. Carewska, M. Moreno, F. Alessandrini, S. Passerini, Chemical-physical properties of bis(perfluoroalkylsulfonyl)imide-based ionic liquids, Electrochim. Acta. 56 (2011) 1300–1307. https://doi.org/10.1016/j.electacta.2010.10.023.

[76]A. Triolo, F. Lo Celso, C. Ottaviani, P. Ji, G.B. Appetecchi, F. Leonelli, D.S. Keeble, O. Russina, Structural features of selected protic ionic liquids based on a super-strong base., Phys. Chem. Chem. Phys. 21 (2019) 25369–25378. https://doi.org/10.1039/c9cp03927a.

[77]M. Hasani, L. Nordstierna, A. Martinelli, Molecular dynamics involving proton exchange of a protic ionic liquid-water mixture studied by NMR spectroscopy, Phys. Chem. Chem. Phys. 21 (2019) 22014–22021. https://doi.org/10.1039/c9cp03563j.

[78]M. Anouti, J. Jacquemin, P. Porion, Transport properties investigation of aqueous protic ionic liquid solutions through conductivity, viscosity, and NMR self-diffusion measurements, J. Phys. Chem. B. 116 (2012) 4228–4238. https://doi.org/10.1021/jp3010844.

[79]N. Yaghini, L. Nordstierna, A. Martinelli, Effect of water on the transport properties of protic and aprotic imidazolium ionic liquids-an analysis of self-diffusivity, conductivity, and proton exchange mechanism, Phys. Chem. Chem. Phys. 16 (2014) 9266–9275. https://doi.org/10.1039/c4cp00527a.

[80]T.M. Chang, L.X. Dang, R. Devanathan, M. Dupuis, Structure and dynamics of N, N -diethyl- N -methylammonium triflate ionic liquid, neat and with water, from molecular dynamics simulations, J. Phys. Chem. A. 114 (2010) 12764–12774. https://doi.org/10.1021/jp108189z.

[81]C.P. Fredlake, J.M. Crosthwaite, D.G. Hert, S.N.V.K. Aki, J.F. Brennecke, Thermophysical properties of imidazolium-based ionic liquids, J. Chem. Eng. Data. 49 (2004) 954–964. https://doi.org/10.1021/je034261a.

[82]L.V.N.R. Ganapatibhotla, J. Zheng, D. Roy, S. Krishnan, PEGylated imidazolium ionic liquid electrolytes: Thermophysical and electrochemical properties, Chem. Mater. 22 (2010) 6347–6360. https://doi.org/10.1021/cm102263s.

[83]O. Russina, F. Lo Celso, M. Di Michiel, S. Passerini, G.B. Appetecchi, F. Castiglione, A. Mele, R. Caminiti, A. Triolo, Mesoscopic structural organization in triphilic room temperature

ionic liquids, Faraday Discuss. 167 (2013) 499–513. https://doi.org/10.1039/c3fd00056g.

[84]D. Rauber, F. Philippi, J. Zapp, G. Kickelbick, H. Natter, R. Hempelmann, Transport properties of protic and aprotic guanidinium ionic liquids, RSC Adv. 8 (2018) 41639–41650. https://doi.org/10.1039/C8RA07412G.

[85]I. Bandrés, F.M. Royo, I. Gascón, M. Castro, C. Lafuente, Anion influence on thermophysical properties of ionic liquids: 1-Butylpyridinium tetrafluoroborate and 1-butylpyridinium triflate, J. Phys. Chem. B. 114 (2010) 3601–3607. https://doi.org/10.1021/jp9120707.

[86]M. Kunze, M. Montanino, G.B. Appetecchi, S. Jeong, M. Schönhoff, M. Winter, S. Passerini, Melting behavior and ionic conductivity in hydrophobic ionic liquids, J. Phys. Chem. A. 114 (2010) 1776–1782. https://doi.org/10.1021/jp9099418.

[87]B. Tang, R. Gondosiswanto, D.B. Hibbert, C. Zhao, Critical assessment of superbase-derived protic ionic liquids as electrolytes for electrochemical applications, Electrochim. Acta. 298 (2019) 413–420. https://doi.org/10.1016/j.electacta.2018.12.100.

[88]J. Kalhoff, G.G. Eshetu, D. Bresser, S. Passerini, Safer Electrolytes for Lithium-Ion Batteries : State of the Art and Perspectives, ChemSusChem 2015,. 8 (2015) 2154–2175. https://doi.org/10.1002/cssc.201500284.

[89]Y. Huang, Z. Chen, J.M. Crosthwaite, S. N.V.K. Aki, J.F. Brennecke, Thermal stability of ionic liquids in nitrogen and air environments, J. Chem. Thermodyn. 161 (2021) 106560. https://doi.org/10.1016/j.jct.2021.106560.

[90]J. Salgado, M. Villanueva, J.J. Parajó, J. Fernández, Long-term thermal stability of five imidazolium ionic liquids, J. Chem. Thermodyn. 65 (2013) 184–190. https://doi.org/10.1016/j.jct.2013.05.049.

[91]S. Sowmiah, V. Srinivasadesikan, M.C. Tseng, Y.H. Chu, On the chemical stabilities of ionic liquids, 2009. https://doi.org/10.3390/molecules14093780.

[92]W.H. Awad, J.W. Gilman, M. Nyden, R.H. Harris, T.E. Sutto, J. Callahan, P.C. Trulove, H.C. DeLong, D.M. Fox, Thermal degradation studies of alkyl-imidazolium salts and their application in nanocomposites, Thermochim. Acta. 409 (2004) 3–11. https://doi.org/10.1016/S0040-6031(03)00334-4.

[93]M. Bellusci, E. Simonetti, M. De Francesco, G.B. Appetecchi, Ionic liquid electrolytes for safer and more reliable sodium battery systems, Appl. Sci. 10 (2020) 6323. https://doi.org/10.3390/APP10186323.

[94]J. Salgado, J.J. Parajó, J. Fernández, M. Villanueva, Long-term thermal stability of some 1-butyl-1-methylpyrrolidinium ionic liquids, J. Chem. Thermodyn. 74 (2014) 51–57. https://doi.org/10.1016/j.jct.2014.03.030.

[95]K.R. Seddon, A. Stark, M.J. Torres, Influence of chloride, water, and organic solvents on the physical properties of ionic liquids, Pure Appl. Chem. 72 (2000) 2275–2287. https://doi.org/10.1351/pac200072122275.

[96]C. Kolbeck, J. Lehmann, K.R.J. Lovelock, T. Cremer, N. Paape, P. Wasserscheid, A.P. Fröba, F. Maier, H.P. Steinrück, Density and surface tension of ionic liquids, J. Phys. Chem. B. 114 (2010) 17025–17036. https://doi.org/10.1021/jp1068413.

[97]Z. Bin Zhou, H. Matsumoto, K. Tatsumi, Low-melting, low-viscous, hydrophobic ionic liquids: Aliphatic quaternary ammonium salts with perfluoroalkyltrifluoroborates, Chem. - A Eur. J. 11 (2005) 752–766. https://doi.org/10.1002/chem.200400817.

[98]W.D. Amith, J.C. Araque, C.J. Margulis, A Pictorial View of Viscosity in Ionic Liquids and the Link to Nanostructural Heterogeneity, J. Phys. Chem. Lett. 11 (2020) 2062–2066. https://doi.org/10.1021/acs.jpclett.0c00170.

[99]G. Tammann, W. Hesse, Die Abhängigkeit der Viscosistat von der Temperatur bei unterkühlten Flüssigkeiten', Allg. Chemie. 156 (1926) 245–257.

[100]F.M. Gaciño, T. Regueira, L. Lugo, M.J.P. Comuñas, J. Fernández, Influence of molecular structure on densities and viscosities of several ionic liquids, J. Chem. Eng. Data. 56 (2011) 4984–4999. https://doi.org/10.1021/je200883w.

[101]O. Nordness, J.F. Brennecke, Ion Dissociation in Ionic Liquids and Ionic Liquid Solutions, Chem. Rev. 120 (2020) 12873–12902. https://doi.org/10.1021/acs.chemrev.0c00373.

[102]M. Hasani, S.A. Amin, J.L. Yarger, S.K. Davidowski, C.A. Angell, Proton Transfer and Ionicity: An 15 N NMR Study of Pyridine Base Protonation, J. Phys. Chem. B. 123 (2019) 1815–1821. https://doi.org/10.1021/acs.jpcb.8b10632.

[103]D.R. MacFarlane, M. Forsyth, E.I. Izgorodina, A.P. Abbott, G. Annat, K. Fraser, On the concept of ionicity in ionic liquids, Phys. Chem. Chem. Phys. 11 (2009) 4962–4967. https://doi.org/10.1039/b900201d.

[104]C. Schreiner, S. Zugmann, R. Hartl, H.J. Gores, Fractional walden rule for ionic liquids: Examples from recent measurements and a critique of the so-called ideal KCl line for the walden plot, J. Chem. Eng. Data. 55 (2010) 1784–1788. https://doi.org/10.1021/je900878j.

[105]F. Philippi, D. Rauber, J. Zapp, R. Hempelmann, Transport properties and ionicity of phosphonium ionic liquids, Phys. Chem. Chem. Phys. 19 (2017) 23015–23023. https://doi.org/10.1039/c7cp04552b.

[106]K.R. Harris, Relations between the fractional stokes-einstein and Nernst-Einstein equations and velocity correlation coefficients in ionic liquids and molten salts, J. Phys. Chem. B. 114 (2010) 9572–9577. https://doi.org/10.1021/jp102687r.

[107]K. Ueno, H. Tokuda, M. Watanabe, Ionicity in ionic liquids: correlation with ionic structure and physicochemical properties, Phys. Chem. Chem. Phys. 12 (2010) 1649–1658. https://doi.org/10.1039/c001176m.

[108]R. Ludwig, The effect of dispersion forces on the interaction energies and far infrared spectra of protic ionic liquids, Phys. Chem. Chem. Phys. 17 (2015) 13790–13793. https://doi.org/10.1039/c5cp00885a.

[109]O. Hollóczki, F. Malberg, T. Welton, B. Kirchner, On the origin of ionicity in ionic liquids. Ion pairing versus charge transfer, Phys. Chem. Chem. Phys. 16 (2014) 16880–16890. https://doi.org/10.1039/c4cp01177e.

[110]H.K. Kashyap, H.V.R. Annapureddy, F.O. Raineri, C.J. Margulis, How is charge transport different in ionic liquids and electrolyte solutions?, J. Phys. Chem. B. 115 (2011) 13212–13221. https://doi.org/10.1021/jp204182c.

[111]K.R. Harris, Scaling the transport properties of molecular and ionic liquids, J. Mol. Liq. 222 (2016) 520–534. https://doi.org/10.1016/j.molliq.2016.07.029.

[112]K.R. Harris, Can the transport properties of molten salts and ionic liquids be used to determine ion association?, J. Phys. Chem. B. 120 (2016) 12135–12147. https://doi.org/10.1021/acs.jpcb.6b08381.

[113]K.R. Harris, On the Use of the Angell-Walden Equation to Determine the "Ionicity" of Molten Salts and Ionic Liquids, J. Phys. Chem. B. 123 (2019) 7014–7023. https://doi.org/10.1021/acs.jpcb.9b04443.

[114]A. Brandt, J. Pires, M. Anouti, A. Balducci, An investigation about the cycling stability of supercapacitors containing protic ionic liquids as electrolyte components, Electrochim. Acta. 108 (2013) 226–231. https://doi.org/10.1016/j.electacta.2013.06.118.

[115]T. Stettner, A. Balducci, Protic ionic liquids in energy storage devices: past, present and future perspective, Energy Storage Mater. 40 (2021) 402–414. https://doi.org/10.1016/j.ensm.2021.04.036.

[116]T. Vogl, S. Menne, K. Ruben-simon, A. Balducci, The bene fi cial e ff ect of protic ionic liquids on the lithium environment in electrolytes for battery applications, J. Mater. Chem. A. 2 (2014) 8258–8265. https://doi.org/10.1039/c3ta15224c.

[117]V. Overbeck, A. Appelhagen, R. Rößler, T. Niemann, R. Ludwig, Rotational correlation times, diffusion coefficients and quadrupolar peaks of the protic ionic liquid ethylammonium nitrate by means of 1H fast field cycling NMR relaxometry, J. Mol. Liq. 322 (2021) 114983. https://doi.org/10.1016/j.molliq.2020.114983.

[118]H. Weingärtner, NMR studies of ionic liquids: Structure and dynamics, Curr. Opin. Colloid Interface Sci. 18 (2013) 183–189. https://doi.org/10.1016/j.cocis.2013.04.001.

[119]W.S. Price, Pulsed-field gradient nuclear magnetic resonance as a tool for studying translational diffusion: Part II. Experimental aspects, Concepts Magn. Reson. 10 (1998) 197–237. https://doi.org/10.1002/(SICI)1099-0534(1998)10:4<197::AID-CMR1>3.0.CO;2-S.

[120]E.O. Stejskal, J.E. Tanner, Spin diffusion measurements: Spin echoes in the presence of a time-dependent field gradient, J. Chem. Phys. 42 (1965) 288–292. https://doi.org/10.1063/1.1695690.

[121]G. Annat, D.R. MacFarlane, M. Forsyth, Transport properties in ionic liquids and ionic liquid mixtures: The challenges of NMR pulsed field gradient diffusion measurements, J. Phys. Chem. B. 111 (2007) 9018–9024. https://doi.org/10.1021/jp072737h.

[122]S.J. Gibbs, C.S. Johnson, A PFG NMR experiment for accurate diffusion and flow studies in the presence of eddy currents, J. Magn. Reson. 93 (1991) 395–402. https://doi.org/10.1016/0022-2364(91)90014-K.

[123]P. Stilbs, 8. Electrophoretic NMR (eNMR), in: Diffus. Electrophor. NMR, De Gruyter, Berlin, Boston, 2019: pp. 266–302. https://doi.org/doi:10.1515/9783110551532-008.

[124]M. Gouverneur, J. Kopp, L. Van Wüllen, M. Schönhoff, Direct determination of ionic transference numbers in ionic liquids by electrophoretic NMR, Phys. Chem. Chem. Phys. 17 (2015) 30680–30686. https://doi.org/10.1039/c5cp05753a.

[125]N. V. Plechkova, K.R. Seddon, Ionic Liquids Completely UnCOILed: Critical Expert Overviews, in: Ion. Liq. Complet. UnCOILed Crit. Expert Overviews, 2015: pp. 13–37. https://doi.org/10.1002/9781118840061.

[126]V. V. Matveev, K. V. Tyutyukin, Peculiarities of NMR relaxation in ionic liquids: Difficulties in interpretation and novel possibilities, Springer Proc. Phys. 197 (2018) 51–66. https://doi.org/10.1007/978-3-319-61109-9_4.

[127]R. Nanda, K. Damodaran, A review of NMR methods used in the study of the structure and dynamics of ionic liquids, Magn. Reson. Chem. 56 (2018) 62–72. https://doi.org/10.1002/mrc.4666.

[128]J.W. Blanchard, J.P. Belières, T.M. Alam, J.L. Yarger, G.P. Holland, NMR determination of the diffusion mechanisms in triethylamine-based protic ionic liquids, J. Phys. Chem. Lett. 2 (2011) 1077–1081. https://doi.org/10.1021/jz200357j.

[129]F. Chen, M. Forsyth, Elucidation of transport mechanism and enhanced alkali ion transference numbers in mixed alkali metal-organic ionic molten salts, Phys. Chem. Chem. Phys. 18 (2016) 19336–19344. https://doi.org/10.1039/c6cp01411a.

[130]J.B. Haskins, W.R. Bennett, J.J. Wu, D.M. Hernández, O. Borodin, J.D. Monk, C.W. Bauschlicher, J.W. Lawson, Computational and experimental investigation of li-doped ionic liquid electrolytes: [pyr14][TFSI], [pyr13][FSI], and [EMIM][BF4], J. Phys. Chem. B. 118 (2014) 11295–11309. https://doi.org/10.1021/jp5061705.

[131]G.A. Giffin, A. Moretti, S. Jeong, K. Pilar, M. Brinkkötter, S.G. Greenbaum, M. Schönhoff, S. Passerini, Connection between Lithium Coordination and Lithium Diffusion in [Pyr12O1][FTFSI] Ionic Liquid Electrolytes, ChemSusChem. 11 (2018) 1981–1989. https://doi.org/10.1002/cssc.201702288.

[132]O. Borodin, G.D. Smith, W. Henderson, Li+ cation environment, transport, and mechanical properties of the LiTFSI doped N-methyl-N-alkylpyrrolidinium+TFSI- Ionic liquids, J. Phys. Chem. B. 110 (2006) 16879–16886. https://doi.org/10.1021/jp061930t.

[133]H. Ye, J. Huang, J.J. Xu, A. Khalfan, S.G. Greenbaum, Li Ion Conducting Polymer Gel Electrolytes Based on Ionic Liquid/PVDF-HFP Blends, J. Electrochem. Soc. 154 (2007) A1048. https://doi.org/10.1149/1.2779962.

[134]F. Castiglione, E. Ragg, A. Mele, G.B. Appetecchi, M. Montanino, S. Passerini, Molecular environment and enhanced diffusivity of Li+ ions in lithium-salt-doped ionic liquid electrolytes, J. Phys. Chem. Lett. 2 (2011) 153–157. https://doi.org/10.1021/jz101516c.

[135]K. Hayamizu, Y. Aihara, H. Nakagawa, T. Nukuda, W.S. Price, Ionic conduction and ion diffusion in binary room-temperature ionic liquids composed of [emim][BF4] and LiBF4, J. Phys. Chem. B. 108 (2004) 19527–19532. https://doi.org/10.1021/jp0476601.

[136]P. Nürnberg, E.I. Lozinskaya, A.S. Shaplov, M. Schönhoff, Li Coordination of a Novel Asymmetric Anion in Ionic Liquid-in-Li Salt Electrolytes, J. Phys. Chem. B. 124 (2020) 861–870. https://doi.org/10.1021/acs.jpcb.9b11051.

[137]W.R. Carper, P.G. Wahlbeck, A. Dölle, 13C NMR relaxation rates: Separation of dipolar and chemical shift anisotropy effects, J. Phys. Chem. A. 108 (2004) 6096–6099. https://doi.org/10.1021/jp031300g.

[138]J.H. Antony, D. Mertens, A. Dölle, P. Wasserscheid, W.R. Carper, Molecular reorientational dynamics of the neat ionic liquid 1-butyl-3-methylimidazolium hexafluorophosphate by measurement of 13C nuclear magnetic relaxation data, ChemPhysChem. 4 (2003) 588–594. https://doi.org/10.1002/cphc.200200603.

[139]K. Hayamizu, S. Tsuzuki, S. Seki, Transport and electrochemical properties of three quaternary ammonium ionic liquids and lithium salts doping effects studied by NMR spectroscopy, J. Chem. Eng. Data. 59 (2014) 1944–1954. https://doi.org/10.1021/je500065k.

[140]K. Hayamizu, S. Tsuzuki, S. Seki, Molecular motions and ion diffusions of the room-temperature ionic liquid 1,2-dimethyl-3-propylimidazolium bis(trifluoromethylsulfonyl)amide (DMPImTFSA) studied by1H, 13C, and19F NMR, J. Phys. Chem. A. 112 (2008) 12027–12036. https://doi.org/10.1021/jp802392t.

[141]S. Tsuzuki, K. Hayamizu, S. Seki, Y. Ohno, Y. Kobayashi, H. Miyashiro, Quaternary ammonium room-temperature ionic liquid including an oxygen atom in side chain/lithium salt binary electrolytes: Ab initio molecular orbital calculations of interactions between ions, J. Phys. Chem. B. 112 (2008) 9914–9920. https://doi.org/10.1021/jp803866u.

[142]K. Hayamizu, S. Tsuzuki, S. Seki, Y. Umebayashi, Nuclear magnetic resonance studies on the rotational and translational motions of ionic liquids composed of 1-ethyl-3-methylimidazolium cation and bis(trifluoromethanesulfonyl)amide and bis(fluorosulfonyl)amide anions and their binary systems including li, J. Chem. Phys. 135 (2011). https://doi.org/10.1063/1.3625923.

[143]A. Carof, M. Salanne, T. Charpentier, B. Rotenberg, On the microscopic fluctuations driving the NMR relaxation of quadrupolar ions in water, J. Chem. Phys. 143 (2015). https://doi.org/10.1063/1.4935496.

[144]K. Hayamizu, S. Tsuzuki, S. Seki, K. Fujii, M. Suenaga, Y. Umebayashi, Studies on the translational and rotational motions of ionic liquids composed of N -methyl- N -propyl-pyrrolidinium (P13) cation and bis(trifluoromethanesulfonyl)amide and bis(fluorosulfonyl)amide anions and their binary systems including lithium salts, J. Chem. Phys. 133 (2010). https://doi.org/10.1063/1.3505307.

[145]K. Hayamizu, S. Tsuzuki, S. Seki, Y. Umebayashi, Multinuclear NMR studies on translational and rotational motion for two ionic

liquids composed of BF4 anion, J. Phys. Chem. B. 116 (2012) 11284–11291. https://doi.org/10.1021/jp306146s.

[146]J. Chidiac, L. Timperman, M. Anouti, Small dissymmetry, yet large effects on the transport properties of electrolytes based on imide salts: Consequences on performance in Li-ion batteries, J. Energy Chem. 65 (2021) 352–366. https://doi.org/10.1016/j.jechem.2021.05.054.

[147]C.L. Berhaut, P. Porion, L. Timperman, G. Schmidt, D. Lemordant, M. Anouti, LiTDI as electrolyte salt for Li-ion batteries: Transport properties in EC/DMC, Electrochim. Acta. 180 (2015) 778–787. https://doi.org/10.1016/j.electacta.2015.08.165.

[148]H. Tokuda, S. Tsuzuki, M.A.B.H. Susan, K. Hayamizu, M. Watanabe, How ionic are room-temperature ionic liquids? An indicator of the physicochemical properties, J. Phys. Chem. B. 110 (2006) 19593–19600. https://doi.org/10.1021/jp064159v.

[149]K. Ueno, K. Yoshida, M. Tsuchiya, N. Tachikawa, K. Dokko, M. Watanabe, Glyme-lithium salt equimolar molten mixtures: Concentrated solutions or solvate ionic liquids?, J. Phys. Chem. B. 116 (2012) 11323–11331. https://doi.org/10.1021/jp307378j.

[150]H. Srour, M. Traïkia, B. Fenet, H. Rouault, M.F. Costa Gomes, C.C. Santini, P. Husson, Effect of nitrile-functionalization of imidazolium-based ionic liquids on their transport properties, both pure and mixed with lithium salts, J. Solution Chem. 44 (2015) 495–510. https://doi.org/10.1007/s10953-014-0280-2.

[151]B. Kirchner, F. Malberg, D.S. Firaha, O. Hollóczki, Ion pairing in ionic liquids, J. Phys. Condens. Matter. 27 (2015). https://doi.org/10.1088/0953-8984/27/46/463002.

[152]O. Russina, F. Lo Celso, N. Plechkova, C.J. Jafta, G.B. Appetecchi, A. Triolo, Mesoscopic organization in ionic liquids, in: Faraday Discuss., 2017: pp. 247–263. https://doi.org/10.1007/978-3-319-89794-3_9.

[153]H. Weber, O. Hollóczki, A.S. Pensado, B. Kirchner, Side chain fluorination and anion effect on the structure of 1-butyl-3-methylimidazolium ionic liquids, J. Chem. Phys. 139 (2013). https://doi.org/10.1063/1.4818540.

[154]K.R. Harris, M. Kanakubo, Self-diffusion coefficients and related transport properties for a number of fragile ionic liquids, J. Chem. Eng. Data. 61 (2016) 2399–2411. https://doi.org/10.1021/acs.jced.6b00021.

[155]C.A. Rumble, A. Kaintz, S.K. Yadav, B. Conway, J.C. Araque, G.A. Baker, C. Margulis, M. Maroncelli, Rotational dynamics in ionic liquids from NMR relaxation experiments and simulations: Benzene

and 1-ethyl-3-methylimidazolium, J. Phys. Chem. B. 120 (2016) 9450–9467. https://doi.org/10.1021/acs.jpcb.6b06715.

[156]N. Bloembergen, E.M. Purcell, R. V. Pound, Relaxation effects in nuclear magnetic resonance absorption, Phys. Rev. 73 (1948) 679–712. https://doi.org/10.1103/PhysRev.73.679.

[157]Y. Shimizu, Y. Wachi, K. Fujii, M. Imanari, K. Nishikawa, NMR study on ion dynamics and phase behavior of a piperidinium-based room-temperature ionic liquid: 1-butyl-1-methylpiperidinium bis(fluorosulfonyl)amide, J. Phys. Chem. B. 120 (2016) 5710–5719. https://doi.org/10.1021/acs.jpcb.6b04095.

[158]M. Imanari, K. Fujii, T. Mukai, N. Mizushima, H. Seki, K. Nishikawa, Anion and cation dynamics of sulfonylamide-based ionic liquids and the solid-liquid transitions, Phys. Chem. Chem. Phys. 17 (2015) 8750–8757. https://doi.org/10.1039/c5cp00302d.

[159]P.M. Bayley, A.S. Best, D.R. MacFarlane, M. Forsyth, The effect of coordinating and non-coordinating additives on the transport properties in ionic liquid electrolytes for lithium batteries, Phys. Chem. Chem. Phys. 13 (2011) 4632–4640. https://doi.org/10.1039/c0cp02084b.

[160]M.E. Di Pietro, F. Castiglione, A. Mele, Polar/apolar domains' dynamics in alkylimidazolium ionic liquids unveiled by the dual receiver NMR 1H and 19F relaxation experiment, J. Mol. Liq. 322 (2021) 114567. https://doi.org/10.1016/j.molliq.2020.114567.

[161]M.E. Di Pietro, F. Castiglione, A. Mele, Polar / apolar domains ' dynamics in alkylimidazolium ionic liquids unveiled by the dual receiver NMR 1 H and 19 F relaxation experiment, J. Mol. Liq. 322 (2021) 114567. https://doi.org/10.1016/j.molliq.2020.114567.

[162]S.S. Bystrov, V. V. Matveev, Y.S. Chernyshev, V. Balevičius, V.I. Chizhik, Molecular Mobility in a Set of Imidazolium-Based Ionic Liquids [bmim]+A- by the NMR-Relaxation Method, J. Phys. Chem. B. 123 (2019) 2362–2372. https://doi.org/10.1021/acs.jpcb.8b11250.

[163]T.M. Alam, D.R. Dreyer, C.W. Bielwaski, R.S. Ruoff, Measuring molecular dynamics and activation energies for quaternary acyclic ammonium and cyclic pyrrolidinium ionic liquids using 14N NMR spectroscopy, J. Phys. Chem. A. 115 (2011) 4307–4316. https://doi.org/10.1021/jp200630k.

[164]A. Carof, M. Salanne, T. Charpentier, B. Rotenberg, Collective water dynamics in the first solvation shell drive the NMR relaxation of aqueous quadrupolar cations, J. Chem. Phys. 145 (2016). https://doi.org/10.1063/1.4963682.

[165]B. Scrosati, J. Garche, Lithium batteries: Status, prospects and future, J. Power Sources. 195 (2010) 2419–2430. https://doi.org/10.1016/j.jpowsour.2009.11.048.

[166]G.B. Appetecchi, Safer electrolyte components for rechargeable batteries, Phys. Sci. Rev. 4 (2019) 1–25. https://doi.org/10.1515/psr-2017-0150.

[167]M. Forsyth, L. Porcarelli, X. Wang, N. Goujon, D. Mecerreyes, Innovative Electrolytes Based on Ionic Liquids and Polymers for Next-Generation Solid-State Batteries, Acc. Chem. Res. 52 (2019) 686–694. https://doi.org/10.1021/acs.accounts.8b00566.

[168]J. Le Bideau, L. Viau, A. Vioux, Ionogels, ionic liquid based hybrid materials, Chem. Soc. Rev. 40 (2011) 907–925. https://doi.org/10.1039/c0cs00059k.

[169]D.S. Ashby, R.H. DeBlock, C.H. Lai, C.S. Choi, B.S. Dunn, Patternable, Solution-Processed Ionogels for Thin-Film Lithium-Ion Electrolytes, Joule. 1 (2017) 344–358. https://doi.org/10.1016/j.joule.2017.08.012.

[170]S. Munoz, S. Greenbaum, Review of recent nuclear magnetic resonance studies of ion transport in polymer electrolytes, Membranes (Basel). 8 (2018) 1–23. https://doi.org/10.3390/membranes8040120.

[171]K. Müller, M. Geppi, Solid State NMR: Principles, Methods, and Applications, Wiley, 2021.

[172]M.J. Duer, Introduction to solid-state NMR spectroscopy, Oxford, UK, 2004.

[173]B. Reif, S.E. Ashbrook, L. Emsley, M. Hong, Solid-state NMR spectroscopy, Nat. Rev. Methods Prim. 1 (2021) 2. https://doi.org/10.1038/s43586-020-00002-1.

[174]M. Ernst, Heteronuclear spin decoupling in solid-state NMR under magic-angle sample spinning, J. OfMagnetic Reson. 162 (2003) 1–34. https://doi.org/10.1016/S1090-7807(03)00074-0.

[175]Y.S. Yang, E. Lafontaine, B. Mortaigne, NMR characterisation of dicyclopentadiene resins and polydicyclopentadienes, J. Appl. Polym. Sci. 60 (1996) 2419–2435. https://doi.org/10.1002/(sici)1097-4628(19960627)60:13<2419::aid-app14>3.3.co;2-m.

[176]W. Kolodziejski, J. Klinowski, Kinetics of cross-polarization in solid-state NMR: A guide for chemists, Chem. Rev. 102 (2002) 613–628. https://doi.org/10.1021/cr000060n.

[177]S.R. Hartmann, E.L. Hahn, Nuclear double resonance in the rotating frame, Phys. Rev. 128 (1962) 2042–2053. https://doi.org/10.1103/PhysRev.128.2042.

[178]G. Foran, N. Verdier, D. Lepage, C. Malveau, N. Dupré, M. Dollé, Use of solid-state NMR spectroscopy for the characterization of molecular structure and dynamics in solid polymer and hybrid electrolytes, Polymers (Basel). 13 (2021). https://doi.org/10.3390/polym13081207.

[179]E. Anoardo, G. Galli, G. Ferrante, Fast-Field-Cycling NMR : Applications and Instrumentations, Appl. Magn. Reson. 404 (2014) 365–404.

[180]R. Kimmich, E. Anoardo, Field-cycling NMR relaxometry, 2004. https://doi.org/10.1016/j.pnmrs.2004.03.002.

[181]M.P. Scott, M.G. Benton, M. Rahman, C.S. Brazel, Plasticizing effects of imidazolium salts in PMMA: High-temperature stable flexible engineering materials, ACS Symp. Ser. 856 (2003) 468–477. https://doi.org/10.1021/bk-2003-0856.ch037.

[182]K. Jeddi, N.T. Qazvini, D. Cangialosi, P. Chen, Correlation between segmental dynamics, glass transition, and lithium ion conduction in poly(methyl methacrylate)/ionic liquid mixture, J. Macromol. Sci. Part B Phys. 52 (2013) 590–603. https://doi.org/10.1080/00222348.2012.725640.

[183]Z. Gao, W. Xie, J.M. Hwu, L. Wells, W.P. Pan, The characterization of organic modified montmorillonite and its filled PMMA nanocomposite, J. Therm. Anal. Calorim. 64 (2001) 467–475. https://doi.org/10.1023/A:1011514110413.

[184]N.A.M. Zailani, F.A. Latif, A.M.M. Ali, M.A.A. Rani, M.Z.A. Yahya, Synthesis of flexible acrylates films, AIP Conf. Proc. 2030 (2018). https://doi.org/10.1063/1.5066760.

[185]M.A.B.H. Susan, T. Kaneko, A. Noda, M. Watanabe, Ion gels prepared by in situ radical polymerization of vinyl monomers in an ionic liquid and their characterization as polymer electrolytes, J. Am. Chem. Soc. 127 (2005) 4976–4983. https://doi.org/10.1021/ja045155b.

[186]M. Tosoni, M. Schulz, T. Hanemann, Novel conductive gel polymers based on acrylates and ionic liquids, Int. J. Electrochem. Sci. 9 (2014) 3602–3617.

[187]G.Y. Foran, D.H. Brouwer, G.R. Goward, Quantifying Site-Specific Proton Dynamics in Phosphate Solid Acids by 1H Double Quantum NMR Spectroscopy, J. Phys. Chem. C. 121 (2017) 25641–25650. https://doi.org/10.1021/acs.jpcc.7b06034.

[188]V. Overbeck, H. Schröder, A.M. Bonsa, K. Neymeyr, R. Ludwig, Insights into the translational and rotational dynamics of cations and anions in protic ionic liquids by means of NMR fast-field-cycling relaxometry, Phys. Chem. Chem. Phys. 23 (2021) 2663–2675. https://doi.org/10.1039/d0cp05440b.

[189] V. Overbeck, A. Appelhagen, R. Rößler, T. Niemann, R. Ludwig, Rotational correlation times, diffusion coefficients and quadrupolar peaks of the protic ionic liquid ethylammonium nitrate by means of 1H fast field cycling NMR relaxometry, J. Mol. Liq. 322 (2021). https://doi.org/10.1016/j.molliq.2020.114983.

[190] V. Overbeck, B. Golub, H. Schröder, A. Appelhagen, D. Paschek, K. Neymeyr, R. Ludwig, Probing relaxation models by means of Fast Field-Cycling relaxometry, NMR spectroscopy and molecular dynamics simulations: Detailed insight into the translational and rotational dynamics of a protic ionic liquid, J. Mol. Liq. 319 (2020) 114207. https://doi.org/10.1016/j.molliq.2020.114207.

[191] M.N. Garaga, N. Jayakody, C.C. Fraenza, B. Itin, S. Greenbaum, Molecular-level insights into structure and dynamics in ionic liquids and polymer gel electrolytes, J. Mol. Liq. 329 (2021) 115454. https://doi.org/10.1016/j.molliq.2021.115454.

[192] N.K. Jayakody, C.C. Fraenza, S.G. Greenbaum, D. Ashby, B.S. Dunn, NMR Relaxometry and Diffusometry Analysis of Dynamics in Ionic Liquids and Ionogels for Use in Lithium-Ion Batteries, J. Phys. Chem. B. 124 (2020) 6843–6856. https://doi.org/10.1021/acs.jpcb.0c02755.

[193] A. Rachocki, E. Andrzejewska, A. Dembna, J. Tritt-Goc, Translational dynamics of ionic liquid imidazolium cations at solid/liquid interface in gel polymer electrolyte, Eur. Polym. J. 71 (2015) 210–220. https://doi.org/10.1016/j.eurpolymj.2015.08.001.

[194] J. Tritt-Goc, A. Rachocki, M. Bielejewski, The solvent dynamics at pore surfaces in molecular gels studied by field-cycling magnetic resonance relaxometry, Soft Matter. 10 (2014) 7810–7818. https://doi.org/10.1039/c4sm01140f.

[195] J.H. Freed, Dynamic effects of pair correlation functions on spin relaxation by translational diffusion in liquids. II. Finite jumps and independent T 1 processes, J. Chem. Phys. 68 (1978) 4034–4037. https://doi.org/10.1063/1.436302.

[196] L.P. Hwang, J.H. Freed, Dynamic effects of pair correlation functions on spin relaxation by translational diffusion in liquids, J. Chem. Phys. 63 (1975) 4017–4025. https://doi.org/10.1063/1.431841.